



Understanding Fluid Rock Interactions and Their Impact on Rock Properties as a Result of CO₂ Injection in the SW Hub

ANLEC Project 7-0314-0233
Final Project Report

Ali Saeedi¹, Claudio Delle Piane², Lionel Esteban², Ryan Noble², David Gray², Stefan Iglauer¹, Maxim Lebedev¹, Linda Stalker²

¹Curtin University

²CSIRO

July 2016

Australian National Low Emissions Coal Research and Development (ANLEC R&D)



Citation

Saedi, A., Delle Piane, C., Esteban, L., Noble, R., Gray, D., Iglauer, S., Lebedev, M., and Stalker, L. 2016. Understanding Fluid Rock Interactions and Their Impact on Rock Properties as a Result of CO₂ Injection in the SW Hub. Final Project Report, SCRIPT Project RES-SE-DPE-AS-53419-2, Curtin University

Contents

LIST OF FIGURES	IV
LIST OF TABLES	XIII
ACKNOWLEDGEMENT	XVI
EXECUTIVE SUMMARY	XVII
NOTES	XIX
SECTION 1: INTRODUCTION AND SAMPLE SELECTION AND PREPARATION	1
INTRODUCTION	2
THE RATIONALE BEHIND THE PROJECT	2
SAMPLE SELECTION AND PREPARATION	3
SECTION 2: CORE-FLOOD EXPERIMENTS	7
INTRODUCTION	8
EXPERIMENTAL SETUP	8
MATERIAL	9
EXPERIMENTAL CONDITIONS	9
EXPERIMENTAL PROCEDURE	10
OBSERVATIONS AND RESULTS	13
SUMMARY AND CONCLUSION	15
SECTION 3: PETROPHYSICAL CHARACTERISATION	16
INTRODUCTION	17
PRINCIPLES AND METHODOLOGIES	17
<i>X-ray Medical CT Imaging</i>	17
<i>Nitrogen Gas Porosity-Permeability</i>	18
<i>Bulk and Grain Density</i>	20
<i>Nuclear Magnetic Resonance</i>	21
<i>Electrical Resistivity Spectroscopy</i>	23
Low frequency electrical resistivity	23
Electrical Impedance Spectroscopy	24
<i>Ultrasonic Velocities</i>	25
<i>Simultaneous Electrical and Acoustic Acquisition</i>	26
Temperature monitoring.....	26
Electrical impedance spectroscopy (EIS) and time scan	26
Ultrasonic P- and S-wave velocities	27
<i>Mercury Porosimetry</i>	27
MEASUREMENT RESULTS	27
<i>Medical CT images</i>	27
<i>Gas porosity-permeability and density results</i>	43
Harvey-1	44
Harvey-3	53
Harvey-4	55
<i>Nuclear Magnetic Resonance Spectrometry</i>	58
Harvey-1	58
Harvey-3	61

Harvey-4	63
<i>Simultaneous Electrical and Acoustic Measurement under Confining Pressure- Harvey-1 Samples</i>	67
Ultrasonic velocity measurement	67
Electrical resistivity measurement	70
<i>Electrical Resistivity Results- Harvey-3 and 4</i>	83
<i>Benchtop Ultrasonic Results</i>	93
Harvey-3	93
Harvey-4	93
<i>Summary and Conclusions</i>	95
SECTION 4: MICROSTRUCTURAL EVALUATIONS	102
INTRODUCTION	103
METHODOLOGY	103
ANALYTICAL RESULTS	107
<i>Harvey-1</i>	107
<i>Harvey-3</i>	114
<i>Harvey-4</i>	118
SUMMARY AND CONCLUSIONS	121
SECTION 5: GEOCHEMICAL ANALYSIS OF EFFLUENT FLUIDS	123
METHODS AND ANALYSIS	124
<i>Core flood experiment set up and core materials</i>	124
<i>Synthetic brine selection</i>	124
<i>Chemical analysis</i>	125
<i>Modelling and mass balance</i>	126
RESULTS	128
<i>Data</i>	128
<i>Major elements</i>	129
<i>Trace elements</i>	136
<i>Modelled injection of CO₂</i>	145
Modelled fluid chemistry	146
Modelled mineral dissolution and precipitation	150
SUMMARY	154
CONCLUSIONS	155
SECTION 6: MICRO COMPUTED TOMOGRAPHY (MICRO-CT) IMAGING	157
INTRODUCTION	158
HARVEY-1 SAMPLES	158
<i>Experimental procedure</i>	158
Ex-situ imaging	158
In-situ imaging	158
<i>Experimental results</i>	158
Ex-Situ coreflooding	158
In-Situ coreflooding	165
<i>Conclusions</i>	171
HARVEY-4 SAMPLES	171
<i>Experimental procedure</i>	171
Ex-situ imaging	171
In-situ imaging	171
<i>Experimental Results</i>	172
Ex-situ imaging	172

In-situ imaging	179
<i>Quantitative analysis</i>	183
<i>Conclusions</i>	185
<i>Overall Conclusions</i>	185
SECTION 7: SUMMARY, CONCLUSIONS AND RECOMMENDATIONS	186
REFERENCES	191

List of Figures

Figure 1. Surface geology of the Perth Basin, the red dashed box indicates the approximate location of the proposed South-West Hub; (B) Stratigraphy of the Central and Southern Perth Basin, the studied section is highlighted in red (modified after Olierook et al., 2014).....	5
Figure 2. Examples of sample assemblies (composite cores) prepared using core-plugs from well Harvey-4.....	6
Figure 3. The schematic diagram of the core-flood apparatus.....	11
Figure 4. Schematic cross-sectional illustration of the core-holder assembly	12
Figure 5. Differential pressure evolution for the second sample assembly (plugs 3 and 4) of Harvey-4	14
Figure 6. Calculated differential pressure across the second sample assembly (plugs 3 and 4) of Harvey-1	15
Figure 7. Example of a XCT transversal image from a plug with the green circle representing the area where the CT mean is computed.....	19
Figure 8. Visual display of the medical CT images before and after flooding (salt cleaned) under dry conditions for the Harvey-1 plugs 1 and 2. The top images represent a transversal image of the plug in its middle part; the middle images are longitudinal XY plane and the bottom images are longitudinal YZ plan along the core axis. The grey and stern CLUTS along with their corresponding CT scale are presented.....	29
Figure 9. Visual display of the medical CT images before and after flooding (salt cleaned) under dry conditions for the Harvey-1 plugs 3 and 4. The top images represent a transversal image of the plug in its middle part; the middle images are longitudinal XY plan and the bottom images are longitudinal YZ plan along the core axis. The grey and stern CLUTS along with their corresponding CT scale are presented.....	30
Figure 10. 3D snapshot views from medical x-ray CT image processing on all the plugs from Harvey-1 before (blue background) and after flooding (orange background). The left images represent a surface rendering of the full plug using a STERN CLUT to highlight the bedding and visible macro-pores. The red images are 3D view of low density materials with CT < 1400; therefore, anything black in such images represent denser layers. A third type of 3D image was added in Plug 3 as a flat layer full of pyrite along the core axis was detected. The white/yellow dots represent pyrite visually enhanced by using a stern CLUT. Note how the bedding is oriented in all the plugs: along the core axis. Plug 1 also integrates a specific layer with inclined bedding.....	31
Figure 11. Transversal and longitudinal medical X-ray CT images for pre- and post-flood Harvey-3 plug 1. The visual representation of the pores in 3D after segmentation for the whole plug is also presented with pores coloured in red.....	32
Figure 12. Transversal and longitudinal medical X-ray CT images for pre- and post-flood Harvey-3 plug 2. The visual representation of the pores in 3D after segmentation for the whole plug is also presented with pores coloured in red.....	33
Figure 13. Transversal and longitudinal medical X-ray CT images on pre- and post-flood Harvey 4 plug 1. The visual representation of the pores in 3D after segmentation for the whole plug is also presented with pores shown in red.	34
Figure 14. Transversal and longitudinal medical X-ray CT images for pre- and post-flood Harvey-4 plug 2. The visual representation of the pores in 3D after segmentation for the whole plug is also presented with pores coloured in red.....	35

Figure 15. Transversal and longitudinal medical X-ray CT images for pre- and post-flood Harvey-4 plug 3. The visual representation of the pores in 3D after segmentation for the whole plug is also presented with pores coloured in red..... 36

Figure 16. Transversal and longitudinal medical X-ray CT images for pre- and post-flood Harvey-4 plug 4. The visual representation of the pores in 3D after segmentation for the whole plug is also presented with pores coloured in red..... 37

Figure 17. X-ray CT calibration for bulk density and porosity using the mean CT computed from all the transversal XCT images (with their standard deviation error bars), the dry bulk density from Harvey-1 plugs and the helium gas porosity extrapolated at 0 psi confining pressure. The data fitting can be used to convert the CT profile along the core axis into bulk density and porosity profile. 38

Figure 18. X-ray CT profile along the cores axis for each plug from Harvey-1 before (blue curves) and after flooding (salt cleaned) under dry condition (red curves). The XCT scale was converted into bulk density and porosity using the calibration equations from Figure 17. The blue and red dashed vertical lines mark the mean CT value for each plug before and after flooding, respectively. The red dashed and red dotted vertical lines differentiate plug segments A and B mean CT, respectively. The injection direction is from the bottom to the top of the graph. 41

Figure 19. Computed porosity profiles derived from the mean XCT and pore segmentation methods on the XCT images before (blue colors) and after flooding experiment (red & orange colors) on plugs from Harvey-3. 42

Figure 20. Computed porosity profiles derived from the mean CT within each transversal XCT image before (blue colors) and after (red & orange colors) flooding for all four plugs from Harvey-4..... 43

Figure 21. Evolution of the gas porosity at different confining pressures before (blue curves) and after flooding without salt cleaned (red curves) and with salt cleaned (green curves) in Harvey-1 plugs. The dashed curves correspond to the plug segments B (i.e. 2B and 4B) while the plain curves are full plugs (i.e. 1 and 3) and plug segments A (i.e. 2A and 4A). Note how the salt cleaning tends to slightly increase the porosity: the green curves are always above the red curves. Some plugs are marked by a decrease in porosity after flooding: plugs 1 and 3 (full plugs) while the other plugs record an increase after flooding. 45

Figure 22. Evolution of the gas permeability at different confining pressures before (blue curves) and after flooding without salt cleaned (red curves) and with salt cleaned (green curves) in Harvey-1 plugs. The dashed curves correspond to the plug segments B (i.e. 2B and 4B) while the solid curves are full plugs (i.e. 1 and 3) and plug segments A (i.e. 2A and 4A). Note how the salt cleaning tends to slightly increase the permeability but for plug 3, the green curves are always above the red curves. All the samples record a decrease in permeability after flooding. 45

Figure 23. Comparison of gas porosity (a) and gas permeability (b) variations at each confining pressure stage between the initial state (before flooding experiments) and after the flooding experiments for Harvey-1 samples. The label colours correspond to the confining pressure range: blue for a pressure up to 2000 psi, green up to 3500 psi and orange up to 4500 psi for only plugs 3 and 4. The circle symbols are the comparison between initial state and after flooding experiments while the triangle symbols compare the initial state with the post flooding after removing the residual salts from the pores. Note how the porosity of plug segments 2A/B and 4B are much more stress sensitive after flooding experiments (dashed areas). The plug segment 4A marks such sensitivity only after salt cleaning. The black dashed curves define “unchanged” porosity or permeability between the initial and post flooding. 47

Figure 24. Variations of gas porosity (a) and gas permeability (b) between the initial state and post-flooding without salt cleaning (red bars) and after salt cleaning (green bars) at each confining pressure for all the plugs from well Harvey-1. 48

Figure 25. X-ray CT images and mercury injection results of three previous samples from Harvey-1. Top left: Medical XCT image from the 3 tested plugs along with their bulk density, gas porosity and permeability and depth. Top right: pie charts representing the relative percentage of pore space subdivided in three pore throat size classes from mercury injection porosimetry data. Bottom: pore size distribution as measured by mercury injection porosimetry on offcuts of the three samples. 51

Figure 26. Validation of proper water saturation of the plugs from Harvey-1 in the pre- and post-flood stages by comparing the helium gas porosity (extrapolated to 0 psi) with water imbibition mass porosity method (WIP). Note however that water saturation is slightly less effective on the post-flood plugs (red symbols) than the pre-flood plugs (blue symbols). 52

Figure 27. Nitrogen gas porosity (top graph) and permeability (bottom graph) measured for Harvey-3 plugs under various overburden pressures with the extrapolation of the porosity-permeability from 500 psi to 0 psi (room conditions). The blue curves represent the pre-flood plugs and the red curves the post-flood plugs. 54

Figure 28. Nitrogen gas porosity (top graph) and permeability (bottom graph) measured on Harvey-4 samples under various overburden pressures with the extrapolation of the porosity-permeability from 500 psi to 0 psi (room conditions). The blue curves represent the pre-flood plugs and the red curves the post-flood plugs. 57

Figure 29. Helium gas porosity (at 0 psi confining pressure) versus NMR water-porosity computed from amplitude (circles) and T2 distribution (triangles) methods, on all the plugs from Harvey-1 before (blue colours) and after (red colours) flooding. Note how the linear fit of the pre-flooded plugs (red linear curves) are similar on both NMR methods and very close to 1:1 ratio with gas porosity. 59

Figure 30. NMR T2 distribution from CPMG sequence on the Harvey-1 plugs before (a) and after (b) flooding. The volume of water measured by NMR was normalised to the sample volume assuming a water density of 1 g/cm³ to convert the y axis into incremental porosity. The integration of all the T2 distribution will give the total water porosity of the plug. Note how the plugs 1 and 2 are different from the plugs 3 and 4 before flooding. 60

Figure 31. Comparison of NMR T2 distribution from CPMG sequence before and after flooding for each plug from Harvey-1. The volume of water measured by NMR was normalised to the sample volume assuming a water density of 1 g/cm³ to convert the y axis into incremental porosity. The integration of all the T2 distribution will give the total water porosity of the plug. 61

Figure 32. NMR T2 distribution for the pre-flood (blue curves) and post-flood (red/orange curves) plugs from Harvey-3. 63

Figure 33. NMR T2 pore distribution for the pre- (blue curves) and post-flood (red/orange curves) plugs from well Harvey-4. 66

Figure 34. Ultrasonic P- and S-wave measurements on plugs from well Harvey-1 before and after flooding experiments. (a) and (c) correspond to velocities on plugs 1 and 3 respectively before (blue) and after (red) flooding. P-wave velocities are represented by circle symbols while the triangle symbols define the S-wave velocities. The elastic parameters derived from P- and S-wave velocities before flooding are compared with the post-flooding for the plug 1 (b) and plug 3 (d) with red symbols for the bulk modulus, blue symbols for the shear modulus and triangle symbols for the Young modulus. 69

Figure 35. Histograms of P- and S-wave velocities before (blue bars) and after (red bars) flooding for plugs from Harvey-1. (a) velocities at no confining pressure; (b) velocities at 2000 psi confining pressure and (c) Difference (in %) between the velocities recorded at 0 and 2000 psi. Note that the poor S-wave velocities recording at 0 psi confining pressure for the post-flooding experiments did not allow the computation of such variation between 0 and 2000 psi (i.e. no red bars for the post-flooded plugs on histogram (c)). 70

Figure 36. EIS spectrum from 10 Hz to 10 kHz before and after flooding under various confining pressures for samples from Harvey-1: Plug 1 before (a) and after (b) flooding; and Plug 2 before (c) and after (d) flooding. The circle symbols represent the 2 electrodes mode and the triangles are the 4 electrodes mode. The blue curves represent 0 psi confining pressure, the red are for 2000 psi (or 100 psi) and the green curves are recorded at 1000 psi. 73

Figure 37. EIS spectrum from 10 Hz to 10 kHz before and after flooding under various confining pressures for samples from Harvey-1: Plug 3 before (a) and after (b) flooding; and Plug 4 before (c) and after (d) flooding. The circle symbols represent the 2 electrodes mode and the triangles are the 4 electrodes mode. The blue curves represent 0 psi confining pressure, the red are for 2000 psi (or 100 psi) and the green curves are recorded at 1000 psi. 74

Figure 38. Electrical resistivity at 1 kHz with time recorded with 2 electrodes under progressive increase of confining pressure stages of plug 1 of Harvey-1 before flooding. The red curves represents the temperature monitoring with time while the other curves are successive recording of resistivity with time. 77

Figure 39. Electrical resistivity at 1 kHz with time recorded with 2 electrodes under progressive increase of confining pressure stages of plug 1 of Harvey-1 after flooding. The red curves represent the temperature monitoring with time while the other curves are successive recording of resistivity with time. 78

Figure 40. Electrical resistivity at 1 kHz with time recorded with 4 electrodes under progressive increase of confining pressure stages of plug 2 of Harvey-1 before flooding. The red curves represents the temperature monitoring with time while the other curves are successive recording of resistivity with time. 79

Figure 41. Electrical resistivity at 1 kHz with time recorded with 4 electrodes under progressive increase of confining pressure stages of plug 3 of Harvey-1 before flooding. The red curves represents the temperature monitoring with time while the other curves are successive recording of resistivity with time. 80

Figure 42. Electrical resistivity at 1 kHz with time recorded with 2 electrodes under progressive increase of confining pressure stages of plug 3 of Harvey-1 after flooding. The red curves represents the temperature monitoring with time while the other curves are successive recording of resistivity with time. 81

Figure 43. Electrical resistivity at 1 kHz with time recorded with 4 electrodes under progressive increase of confining pressure stages of plug 4 of Harvey-1 before flooding. The red curves represents the temperature monitoring with time while the other curves are successive recording of resistivity with time. 82

Figure 44. Electrical Impedance spectroscopy of saturated plug 2 of Harvey-3 before (blue curves) and after flooding (red curves) between 10 and 10 kHz (top graph). Note the strong polarization from 100 Hz to 100 kHz: high values with a linear trend. The bottom plot shows a magnification of the top graph only between 10 and 100 Hz free of polarization effect. 86

Figure 45. Electrical Impedance spectroscopy of saturated plugs 1 and 2 before (blue curves) and after flooding experiment (red/orange curves) between 10 and 10 kHz (top graph). Note the strong polarization from 100 Hz to 100 kHz: high values with a linear trend. The bottom plot shows a magnification of the top graph only between 10 and 100 Hz free of polarization effect. 91

Figure 46. Electrical Impedance spectroscopy of saturated plugs 3 and 4 before (blue curves) and after flooding experiment (red/orange curves) between 10 and 10 kHz (top graph). Note the strong polarization from 100 Hz to 100 kHz: high values with a linear trend. The bottom plot shows a magnification of the top graph only between 10 and 100 Hz free of polarization effect. 92

Figure 47. Ultrasonic P- and S-wave forms on pre- (blue curves) and post-flood (red/green curves) plugs 1 and 2 of Harvey-3. 94

Figure 48. Comparison of gas porosity and permeability before and after flooding for all the tested three Harvey wells. 96

Figure 49 Left: Reflected light image of a polished surface of a disc belonging to H1-Plug4, diameter of the circular surface is 38 mm. Right: overlay showing the grid of images acquired with the SEM.... 103

Figure 50 Flow chart illustrating the acquisition, treatment and analysis steps performed on the SEM mosaics acquired on the Wonnerup samples..... 104

Figure 51 Mosaics of the surface of a disc belonging to H1-Plug4 imaged using the SEM in back scattered electron (BSE) and elemental mapping mode. Each image is composed of a matrix of 42 tiles stitched together in a single file of 8532 × 9055 pixels (27.05 × 28.70 mm; 1pixel = 3.17 microns).. 105

Figure 52 Schematic drawing illustrating the importance of proper sample preparation quantitative analysis. Left: rough sample surface affecting the propagation of X-rays emitted (yellow arrows) from the interaction volume (orange teardrop) excited by the incident electron beam (blue arrow). Right: smooth sample surface. Image modified from <http://www.ammr.org.au/myscope/analysis/eds/quantitative/>. 106

Figure 53. (A-B) Positions of selected plugs and distribution of lithofacies and rock properties in the Wonnerup Member cored intervals of Harvey 1: (A) Core 5, 1896-1847.7 m, and; (B) Core 6, 2480-2532.5 m. Gamma was taken at 5 cm intervals on whole core. Porosity (Por.) and permeability (Perm.) were determined from wireline logs (continuous lines) and from helium-injection on core plugs (black dots). Short-wavelength infrared (SWIR) spectra from the HyLogger were binned every 20 cm. (C) Pie chart showing the relative abundance of each facies of the Wonnerup Member. Modified after Olierook et al., 2014..... 108

Figure 54. BSE image of the disc cut from H1-Plug2 (depth 1924.84 m) illustrating the main mineral phases of the sediment and their geometry. 110

Figure 55. Grain size and shape of quartz and K-feldspar grains identified in the disc cut from H1-Plug2 (depth 1924.84 m). Left: Histogram of equivalent circular diameter of quartz and K-feldspar grains. Right scatter plot of the shape factor as a function of the grain size of quartz and feldspar grains.. 110

Figure 56. BSE images of the core surface before and after core flooding tests, sample is oriented so that bedding is vertical. Black scale bar is 1 cm (the disc cut from H1-Plug4; depth 2505.52 m)..... 112

Figure 57. Scatter plots of the shape factor as a function of the grain size of quartz, feldspar, kaolinite and calcite grains before and after the core flooding tests on the disc cut from H1-Plug4 (depth 2505.52 m). 113

Figure 58. Box plot summarizing the distribution of the main minerals identified from the image analysis of the disc cut from sample H1-Plug4 (depth 2505.52 m). The boundary of the box closest to zero indicates the 25th percentile, and the boundary of the box farthest from zero indicates the 75th

percentile. Error bars above and below the box indicate the 90th and 10th percentiles. The black and red lines within the box indicate the median and mean of the distribution respectively. 114

Figure 59. Detail of the disc cut from sample H3-Plug1 before (top) and after (bottom) core flooding test. Q = quartz; Kao = kaolinite; K = K-feldspar. Note the presence of cracked grains in the bottom image. These are probably due to high contact stresses at surface asperities during the core flooding experiment. Also note the euhedral shape of many of the quartz grains indicative of diagenetic cementation by quartz overgrowth..... 115

Figure 60 Detail of the disc cut from sample H3-Plug1 before (top) and after (bottom) core flooding test. Width of the image is 2.5 mm. Q = quartz; Kao-ct= kaolinite coating; K = K-feldspar. Note the presence of enhanced connectivity in the bottom image mostly occurring in regions previously occupied by clays. 116

Figure 61: Detail of the disc cut from sample H3-Plug1 before (top) and after (bottom) core flooding test. Width of the image is 2.3 mm. Q = quartz; Kao-ct= kaolinite coating; K = K-feldspar. The red envelope in the top image delineates a pore throat between quartz grains. Note the presence of enhanced porosity in the bottom image mostly occurring in regions previously occupied by clays. 117

Figure 62. Mosaic of BSE images collected from the two analysed samples. 119

Figure 63. SEM images of regions of interest in disc from H4-Plug1 from well Harvey-4 (depth 1794.53 m) before (left) and after (right) flooding experiments. Salt precipitation (bright patches in the images) on the sample surface is evident in the images acquired before flooding; most of the salt appears to be removed in the images acquired after flooding test. a) and b) showing porosity enhancement by removal of pore occluding clays. c) and d) showing porosity reduction by pore occlusion. 120

Figure 64. SEM images of regions of interest in disc from H4-Plug3 from well Harvey 4 (depth 1800.47 m) before (left) and after (right) flooding experiments. a) and b) showing a tight portion of the sample with abundant pore occluding clays. No significant change can be detected in the images acquired before and after flooding. c) and d) showing a clay rich region of the samples with an aggregate of oxides (possibly Ti-oxide) in the middle of the image (bright phase). As for the previous region of interest, no significant change can be detected in the images acquired before and after flooding.. 121

Figure 65. Example of the Static equilibrium model parameters (for Harvey-1 1924m). Note the variation in Na and SO₄ used to run the model which is also reflected in Table 34..... 128

Figure 66. Calcium eluent in mg/L from the core flood experiments over volume eluted from the different rock samples or experiments (0.5 cm³ solution per minute). Long-term differences in the trends relate to different eluent chemistry (batch effect), rather than solid-phase interaction..... 130

Figure 67. Calcium eluent concentration divided by total dissolved solids (TDS) from the core flood experiments over volume eluted from the different rock samples or experiments (0.5 cm³ solution per minute)..... 131

Figure 68. Magnesium eluent in mg/L from the core flood experiments over volume eluted from the different rock samples or experiments (0.5 cm³ solution per minute). Long-term differences in the trends relate to different eluent chemistry (batch effect), rather than solid-phase interaction..... 131

Figure 69. Magnesium eluent concentration divided by total dissolved solids (TDS) from the core flood experiments over volume eluted from the different core plugs or experiments (0.5 cm³ solution per minute)..... 132

Figure 70. Potassium eluent in mg/L from the core flood experiments over volume eluted from the different rock samples or experiments (0.5 cm³ solution per minute). 133

Figure 71. Potassium eluent ratio adjusted for Total Dissolved Solids (TDS) from the core flood experiments over volume eluted from the different rock samples or experiments (0.5 cm ³ solution per minute).....	134
Figure 72. Bromide eluent in mg/L from the core flood experiments over volume eluted from the different rock samples or experiments (0.5 cm ³ solution per minute). Starting concentration was 125 mg/L (ppm).	135
Figure 73. Bromide eluent ratio adjusted for Total Dissolved Solids (TDS) from the core flood experiments over volume eluted from the different rock samples or experiments (0.5 cm ³ solution per minute). Linear regression lines have been added for each core type.	135
Figure 74. Strontium eluent in mg/L from the core flood experiments over volume eluted from the different rock samples or experiments (0.5 cm ³ solution per minute). Starting concentration was 100 mg/L (ppm).	136
Figure 75. Strontium eluent ratio adjusted for Total Dissolved Solids (TDS) from the core flood experiments over volume eluted from the different rock samples or experiments (0.5 cm ³ solution per minute).....	136
Figure 76. Copper eluent in µg/L from the core flood experiments over volume eluted from the different core plugs or experiments (0.5 cm ³ solution per minute). Starting concentration was 100,000 µg/L (ppb).....	137
Figure 77. Lead eluent in µg/L from the core flood experiments over volume eluted from the different rock samples or experiments tested (0.5 cm ³ solution per minute).	138
Figure 78. Lead eluent ratio adjusted for Total Dissolved Solids (TDS) from the core flood experiments over volume eluted from the different rock samples or experiments (0.5 cm ³ solution per minute).	139
Figure 79. Neodymium (REE) eluent in µg/L from the core flood experiments over volume eluted from the different core plugs or experiments (0.5 cm ³ solution per minute).....	140
Figure 80. Nickel eluent in µg/L from the core flood experiments over volume eluted from the different rock samples or experiments (0.5 cm ³ solution per minute).	141
Figure 81. Iron eluent in mg/L from the core flood experiments over volume eluted from the different rock samples or experiments (0.5 cm ³ solution per minute).	142
Figure 82. Probability plots of iron eluent in mg/L from the core flood experiments.	142
Figure 83. Silica eluent in µg/L from the core flood experiments over volume eluted from the different core plugs or experiments (0.5 cm ³ solution per minute).	145
Figure 84. Aluminium eluent in mg/L from the core flood experiments over volume eluted from the different core plugs or experiments (0.5 cm ³ solution per minute).	145
Figure 85 CO ₂ fugacity increasing as the reaction progresses. The black dashed line represents the approximate conditions for the core flooding experiment, with the red dashed line showing the changes related to a reduced Na, SO ₄ and Cl starting composition of the brine.	146
Figure 86 Total dissolved solids as influenced by increased CO ₂ reactant. The solid line shows the results for the standard conditions reported in Table 34 and reduced Na, SO ₄ and Cl in the dashed line. These results are for Harvey-1 1924m.....	147
Figure 87 Production of carbonic acid and loss of neutralising capacity in the rock results in reduced pH conditions as the reaction progresses.....	148
Figure 88. Major cations and anions released into solution from the injection of CO ₂ into the Harvey-1 1924m rocks. The dashed line represents the sensitivity testing of lower salinity brine.....	149

Figure 89 Minor cations and anions released into solution from the injection of CO ₂ into the Harvey-1 1924m rocks. The dashed line represents the sensitivity testing of lower salinity brine.....	150
Figure 90 Other trace cations and anions released into solution from the injection of CO ₂ into the Harvey-1 1924m rocks. The dashed line represents the sensitivity testing of lower salinity brine. ...	150
Figure 91. Reaction modelling progress for major minerals showing the destruction or weathering of paragonite (mica) and the formation of kaolinite and the precipitation of dawsonite as CO ₂ is added to the Harvey-1 1924m rock mass. Note the quartz and muscovite are only slightly changed and remain relatively stable to other mineral transformations.	151
Figure 92. Reaction modelling progress for minor minerals showing the destruction or weathering of paragonite (mica) and the formation of kaolinite and the precipitation of dawsonite as CO ₂ is added to the Harvey-1 1924m rock mass. The dashed lines show the reactions related to the reduced starting brine salinity.....	152
Figure 93. Reaction modelling progress for trace minerals showing the destruction of albite and daphnite and the formation of siderite and anhydrite as CO ₂ is added to the Harvey-1 1924m rock mass. The dashed lines show the reactions related to the reduced starting brine salinity.	152
Figure 94. Reaction modelling progress for minor minerals as CO ₂ is added to the Harvey-3 1459m rock mass. The dashed lines shows the equivalent experimental conditions used in the core flood tests. Compare to Figure 92.	153
Figure 95. Reaction modelling progress for trace minerals as CO ₂ is added to the Harvey-3 1459m rock mass. The dashed lines shows the equivalent experimental conditions used in the core flood tests. Compare to Figure 93.	154
Figure 96. Schematic of the 1 st sample assembly of Harvey-1 showing the location of the micro-CT samples.	158
Figure 97. a) X-ray transparent Hassler cell; b) micro-CT setup in scanner: the x-ray source is located on the left, the detector on the right.....	159
Figure 98. Selected axial slices through the pre-flood plug (ex-situ). The diameter of the shown circles is 3.43mm.....	159
Figure 99. Selected axial slices through the post-flood plug (ex-situ). The diameter of the shown circles is 3.43mm.....	160
Figure 100. 2D slices through the Harvey 1 (ex-situ) rock before (left) and after (right) flooding. Raw slices are shown on the top, segmented on the bottom, the mineral and void phases are indicated.	161
Figure 101. 3D visualizations of the different mineral and void phases for Harvey 1 (ex-situ), before (left) and after (right) flooding.....	162
Figure 102. The pore size distribution for Harvey 1 ex-situ before (top) and after (bottom) flooding.	164
Figure 103. Selected axial slices through the pre-flood plug fully saturated with dead brine (in-situ). The diameter of the shown circles is 3.43mm.	165
Figure 104. Selected axial slices through the plug flooded with 40 PV of live brine (in-situ). The diameter of the shown circles is 3.43mm.....	166
Figure 105. 2D slices through the Harvey 1 (in-situ) rock before (left) and after (right) flooding. Raw slices are shown on the top, segmented on the bottom, the mineral and void phases are indicated.	167
Figure 106. 3D visualizations of the different mineral and void phases for Harvey 1 (in-situ), before (left) and after (right) flooding.....	168

Figure 107a. The pore size distribution for Harvey 1 in-situ before and after flooding.	169
Figure 108. Schematic of the 2nd Harvey-4 sample assembly showing the location of the micro-CT samples.	171
Figure 109. Selected axial slices through the non-flooded Harvey-4 plug (ex-situ). The diameter of the shown circles is 3.43mm.	173
Figure 110. Selected axial slices through the Harvey 4 plug flooded with live brine (ex-situ). The diameter of the shown circles is 3.43mm.	174
Figure 111. 2D slices through the Harvey 4 (ex-situ) rock before (left) and after (right) flooding. Raw slices are shown on the top, segmented on the bottom, the mineral and void phases are indicated.	175
Figure 112. 3D visualizations of the different mineral and void phases for Harvey 4 (ex-situ), before (left) and after (right) flooding.	176
Figure 113. The pore size distribution for Harvey 4 ex-situ before (top) and after (bottom) flooding.	178
Figure 114. Selected axial slices through the Harvey-4 plug fully saturated with dead brine (in-situ). The diameter of the shown circles is 3.43mm.	179
Figure 115. Selected axial slices through the Harvey-4 plug flooded with 40 PV of live brine (in-situ). The diameter of the shown circles is 3.43mm.	180
Figure 116. 2D slices through the Harvey 4 (in-situ) rock before (left) and after (right) flooding. Raw slices are shown on the top, segmented on the bottom, the mineral and void phases are indicated.	181
Figure 117. 3D visualizations of the different mineral and void phases for Harvey 4 (in-situ), before (left) and after (right) flooding.	182
Figure 118a. The pore size distribution for Harvey 4 in-situ before and after live brine flooding.	183

List of Tables

Table 1. The depths of the core plugs and their corresponding pressures and temperatures.	6
Table 2. Formation water salinity used during the experiments.....	12
Table 3. Statistical summary of the pore segmentation from XCT images before and after flooding in the Harvey-3 plugs.....	39
Table 4. Summary of porosity and standard deviation computed from XCT mean within each plug before and after the flooding experiments on the four plugs from Harvey-4.	40
Table 5. Porosity and permeability results averaged from the three repeated measurements, along with their standard deviation (STD), at different confining pressure stages for all the plugs from Harvey-1 before and after flooding without and with salt cleaning.....	46
Table 6. Summary of extrapolated helium gas porosity and permeability from the different confining pressure stages before and after flooding without and with salt cleaning for all plugs from Harvey-1.	49
Table 7. Summary of the variations of gas porosity and permeability between different confining pressure ranges from 500 psi to 4500 psi on all the plugs before and after brine-CO ₂ flooding without and with salt cleaning for all plugs from Harvey-1.	49
Table 8. Summary of the gas porosity and permeability variations after flooding (without and with salt cleaning) for all plugs from Harvey-1 at different confining pressures. Positive porosity values correspond to a decrease in porosity after experiments while negative values correspond to an increase in porosity.....	50
Table 9. Summary of the bulk and grain density for Harvey-1 plugs computed from mass and volume measurements as well as gas porosity measurements, all before (blue cells) and after flooding (light orange cells) and after flooding with salt cleaning (dark orange cells). Note that star (*) in some volume matrix cells corresponds to helium pycnometry direct measurement while the other volume matrix cells were computed from gas porosity and bulk volume. Such direct volume matrix measurement allowed the computation of equivalent porosity.	53
Table 10. Summary of nitrogen gas porosity-permeability under increasing confining pressure before and after flooding for the two plugs from well Harvey-3. The extrapolated porosity-permeability at room conditions using a second order polynomial fit is also provided along with their stress dependency between room conditions and maximum pressure (2500 psi).	55
Table 11. Summary of nitrogen gas porosity-permeability conducted on samples from Harvey-4 under increasing confining stress before and after the flooding experiments. The extrapolated porosity-permeability at room conditions using a second order polynomial fit is also provided along with their stress dependency between room conditions and maximum pressure (3000 psi).....	56
Table 12. Summary of NMR porosity (from amplitude and T2 distribution methods) and permeability (from Coates and SDR equations) for all the plugs from Harvey-1 before and after flooding. The gas porosity and permeability results at 0 psi confining pressure are reminded (see Table 6). The best C to fit the computed NMR permeability with the gas permeability are also provided for both Coates and SDR equations. Note how the C for Coates has to be lowered to 7-8 instead of 10 to fit the gas permeability on plugs 3 and 4.....	59
Table 13. Summary of NMR porosity and permeability (from Coates equation) for all the plugs from Harvey-3 for before and after flooding. The best C to fit the computed NMR permeability with the gas permeability are also provided for Coates equation. Note how the C for Coates has to be lowered to 8 instead of 10 to fit the gas permeability on the post-flooded plugs.	62

Table 14. Summary of the water content and water-filled porosities from NMR and calculated permeabilities using Coates and SDR models before and after the flooding experiments for the plugs from well Harvey-4. C parameters are the best constant from the Coates and SDR models to match the gas permeability. T2LM is the log mean of the NMR T2 distribution used to compute permeability with the SDR model.	65
Table 15. Summary of ultrasonic velocity measurements and derived computed elastic parameters (Poisson’s ratio, Shear, bulk and Young modulus) on all the plugs from Harvey-1 before and after the flooding experiments.	68
Table 16. Workflow of electrical impedance spectroscopy measurements on each sample before and after flooding in Harvey-1. Time scan resistivity measurement at 1 kHz and EIS with confining pressure was only possible on long plugs (i.e. not possible on 2A&B and 4A&B).....	71
Table 17. Summary of electrical resistivity acquired at 1 kHz before and after flooding using 2 and 4 electrodes under 0 (and 13.8 MPa where possible) confining pressure for Harvey-1 samples. Some data were not acquired due to technical problems: dark grey cells; while data with not so good electrodes coupling are highlighted in orange cells.	72
Table 18. Summary of the electrical impedance spectroscopy between 10Hz and 100 kHz on the pre- and post-flood under room conditions using 2 electrodes system for Plug 2 of Harvey-3. The derived Archie parameters: Formation factor, M exponent and Tortuosity are also presented.	85
Table 19. Summary of the electrical impedance spectroscopy between 10Hz and 100 kHz on the pre- and post-flood plugs under room conditions using 2 electrodes system for plug segments 1A & 1B from Harvey-4 well. The derived Archie parameters: Formation factor, m exponent and Tortuosity are also presented.	87
Table 20. Summary of the electrical impedance spectroscopy between 10Hz and 100 kHz on the pre- and post-flood plugs under room conditions using 2 and 4 electrodes system for Plug 2 from Harvey-4 well. The derived Archie parameters: Formation factor, m exponent and Tortuosity are also presented.	88
Table 21. Summary of the electrical impedance spectroscopy between 10Hz and 100 kHz on the pre- and post-flood plugs under room conditions using 2 electrodes system for plug segments 3A & 3B from Harvey-4 well. The derived Archie parameters: Formation factor, m exponent and Tortuosity are also presented.	89
Table 22. Summary of the electrical impedance spectroscopy between 10Hz and 100 kHz on the pre- and post-flood plugs under room conditions using 2 and 4 electrodes system for Plug 4 from Harvey-4 well. The derived Archie parameters: Formation factor, m exponent and Tortuosity are also presented.	90
Table 23. Summary of the P- and S-wave velocities for plugs 1 and 2 of Harvey-3 before and after the flooding experiments.	93
Table 24. Summary of the P- and S-wave velocities on the four dry plugs from Harvey-4 before and after flooding experiments under room conditions.	95
Table 25. Summary of variations in pre- and post-flood petrophysical properties of the samples from Harvey-1. The orange cells mark strong change in parameters. The dark grey marks no data available. The last row in light orange integrates the overall changes within each plug.	98
Table 26. Summary of the sample characteristics and parameters measured or derived from the different experiments run on pre- and post- flood plugs from Harvey-1.....	99
Table 27. Summary of the sample characteristics and parameters measured or derived from the different experiments run on pre- and post- flood plugs from Harvey-3.....	100

Table 28. Summary of the sample characteristics and parameters measured or derived from the different experiments run on pre- and post-flood plugs from Harvey-4.....	101
Table 29. XRD mineralogy obtained on samples from the Harvey -1 well at depths adjacent to those analyzed in this study and described as the same lithofacies. Values expressed as weight %	107
Table 30. Summary of the image analysis results for the quartz and K-feldspar particles identified in the disc cut from H1-Plug2 (depth 1924.84 m). d = equivalent circular diameter; S = shape factor; S.D. = standard deviation.	109
Table 31. Summary of the image analysis results for the quartz, K-feldspar, kaolinite and calcite particles identified in the disc cut from H1-Plug4 (depth 2505.52 m) before flooding experiment. d = equivalent circular diameter; S = shape factor; S.D. = standard deviation.	111
Table 32. Summary of the image analysis results for the quartz, K-feldspar, kaolinite and calcite particles identified in the disc cut from H1-Plug4 (depth 2505.52 m) after flooding experiment. d = equivalent circular diameter; S = shape factor; S.D. = standard deviation.	111
Table 33 Mineralogy of the studied samples as obtained from X-ray diffraction analysis. Values expressed as weight %	122
Table 34. Parameters used in modelling of the Harvey-1 1924m sample. Full details for all samples are provided in Appendix A.....	127
Table 35. Experiments, samples, duplicates and missing samples (due to particle size testing).	129
Table 36. Mass balance net change in grams of major elements. Black font indicates precipitation (net loss of an element from solution) and red indicates dissolution (gain of element in solution).....	130
Table 37. Mass calculated changes after the CO ₂ passes through the core. The results assume total core volume is constant from the initial plug and uses average bulk density over the length of the plugs as a ratio of each plug length to compensate for material removed during core cutting.	137
Table 38 Composition ranges for 316L stainless steel (%) used in the core flood experiment (from http://www.azom.com/article.aspx?ArticleID=2382).	141
Table 39. Percentage of core mineral phases dissolved based on mass balance approach using the eluent chemistry. Empty cells are minerals that do not contain that element or were not measured in that core using XRD (Table 33).....	143
Table 40. Physical properties of the mineral phases identified.....	161
Table 41. Volume fractions for segmented mineral and void phase, Harvey 1 ex-situ.	163
Table 42. Volume fractions for segmented mineral and void phases, Harvey 1 in-situ.	169
Table 43. Volume fractions for segmented mineral and void phases, Harvey 4 ex-situ.	177
Table 44. Volume fractions for segmented mineral and void phase, Harvey 4 in-situ.....	183

Acknowledgement

The authors wish to acknowledge the financial assistance provided through Australian National Low Emissions Coal Research and Development (ANLEC R&D). ANLEC R&D is supported by Australian Coal Association Low Emissions Technology Limited and the Australian Government through the Clean Energy Initiative. The authors also acknowledge access to rock samples and other related data (logs, etc.) contributed by the Department of Industry and Science through the CCS Flagships Program and the Department of Mines and Petroleum-Western Australia.

The researchers also wish to acknowledge the contribution made by National Geosequestration Laboratory (NGL). Some of the analysis and measurements performed in this work were carried out using the state-of-the-art laboratory facility housed within the NGL.

We also would like to acknowledge the help from Mr Derek Winchester with the sample cutting and preparation tasks.

Executive Summary

In mid-2014, a review was conducted on some of the core analysis performed on rock material from the South West Hub Carbon Capture and Storage (CCS) Site as part of the previously completed projects. In particular, it was noted that in some of the completed research work (Projects 7-1111-0199 (Delle Piane et al., 2013), 7-1111-0200 (Stalker et al., 2013) and 3-1110-0122 (Evans et al., 2013)), a number of fluid-rock interactions had been identified. It was also noted that there were still some key uncertainties remaining about the nature of the mechanisms, the causes of the identified fluid-rock interactions and the extent to which they could impact on the future planning of the SW Hub testing. For instance, in the previous core analysis performed on the rock material from well Harvey-1 (Projects 7-1111-0199 (Delle Piane et al., 2013) and 3-1110-0122 (Evans et al., 2013)) it was noted that the permeability of the Harvey-1 samples would decrease substantially (up to 60%) after undergoing a laboratory core-flooding procedure. Such results could have significant implications for the CO₂ injectivity in the future injection wells at the SW Hub.

The three earlier mentioned projects were the first of their kinds for the SW Hub, and some of the identified fluid-rock interactions observed had not been expected. The key focus of those projects were more general and not designed to thoroughly investigate the interactions from both qualitative and quantitative perspectives. In an attempt to bridge the identified gap in knowledge and reduce the identified uncertainties to an acceptable level, a purpose-built workflow was devised based on which the current project was established. The overall objectives of this new work included:

1. the identification and characterisation of the mechanisms behind the previously observed petrophysical variations in the post-flood samples,
2. characterisation of the in-situ geochemical reactions which may occur at the SW Hub,
3. identify the extent of fines migration that occurs, and thus
4. provide an estimate of the relative contribution of geochemical reaction changes versus fines migration as contributors to changes in porosity and permeability induced by flooding.

There were a number of core and pore-scale diagnostic tools included in the project to help with achieving the above objectives. A detailed analysis of the fluid samples collected in the laboratory combined with a geochemical modelling technique was also included in the new work. A new core-flood procedure, built upon the previous work conducted (7-1111-0200 (Stalker et al., 2013)), was designed specifically for this new project. The new investigation was planned to be conducted on not only the previously available core material from well Harvey-1 but also the new material to become available from wells Harvey-3 and Harvey-4. These two wells were planned for drilling in early 2015 within the main injection/storage area of the SW Hub. It is worth noting that the focus of the new work was specifically on the Wonnerup Member of the Lesueur Formation, it being the thick and more homogenous interval that would be the primary injection/storage unit within the SW Hub site.

The workflow was designed to characterise samples both before and after core flooding in order to compare impacts on a range of samples. Overall, the pre- and post-flood petrophysical characterisations of the samples tested from the three wells revealed that the samples underwent a range of alterations to their petrophysical properties caused by the laboratory core-flood process. The results of the investigation performed on the new core samples from well Harvey-1, once again, confirmed the previously observed behaviour from these samples. That is, significant reduction in the permeability (up to 50%) of the post-flood samples while their porosity remained almost unchanged.

Similar results to the previous studies were also observed from other core analyses such as NMR (Nuclear Magnetic Resonance) spectrometry. In the previously completed work (Delle Piane et al, 2013; Evans et al, 2013), it was speculated that fines migration phenomenon was to blame for the observed petrophysical changes in the absence of sufficient evidence or sample numbers investigated. However, the special workflow of the petrophysical evaluation techniques included in this new work confirmed that, indeed, fines migration was the root cause of the alterations to the petrophysical properties of the post-flood samples from Harvey-1.

Interestingly, the response of the next batch of samples tested from well Harvey-3 to the flooding process was, to a great extent, opposite that observed from Harvey-1 samples. In other words, a considerable permeability enhancement (up to 115%) was observed in the post-flood Harvey-3 samples. Subsequently, the samples tested from well Harvey-4 in the last phase of the project yielded results falling in between those achieved from Harvey-1 and Harvey-3. In some of the post-flood Harvey-4 samples the permeability was improved, in some decreased and in others it remained almost unchanged. For the Harvey-3 samples in particular, clear evidence generated in this work indicated that while clay fines were mobilised in the samples, they were flushed out of the major flow paths within the samples resulting in enhanced pore connectivity and hence the improved permeability.

In terms of the nature of the samples collected from all three wells, while they were all from the same facies (Ai and Aii– the highest energy facies identified by Delle Piane et al, 2013), there were also some distinct differences between them. For instance, the samples from Harvey-1 were consolidated and well cemented while the samples from Harvey-3 and Harvey-4 were friable and weakly cemented, indicating diagenetic differences between the samples from different wells. What this implies is that, to a great extent, spatial variations in diagenetic alteration in the SW Hub control the characteristics of the deposited sediments such that the same facies may not respond to the CO₂ injection in the same manner throughout the study area. In fact, a single sample tested from a deep section of well Pinjarra-1 (Wonnerup Member) in another project (Project 3-1110-0122 (Evans et al., 2013)) behaved similar to Harvey-3 samples due to the fact that the cement in that samples had undergone diagenetic alteration converting to a carbonate cement which was dissolved during the core-flooding process. In practice what this means is that in the future injection wells, not all the injection intervals may behave similarly over time when subjected to CO₂ injection.

In terms of fluid-rock geochemical interactions, there were a number of observations made between various samples tested from the three wells. In general, in the analysed fluid samples an initial “first flush effect” occurs and then conditions stabilise. It is believed that a spike in the concentration of chemical species during the early period is caused by the dissolution and removal of salt residues (left from previous rock analysis e.g. NMR) from the samples by the CO₂-saturated brine rather than the acid attack by the CO₂ saturated brine. Chemical changes and impacts on the minerals present is considered to be very minor in a quantitative sense. The remanence of acid attack on minerals is observed more subtly later in the flood, particularly with respect to iron and silica. The results tend to agree with the static geochemical models that indicate greater CO₂ would be required to drive a greater geochemical change. Overall, based on the results obtained, the extent of the geochemical reactions between the CO₂-saturated brine and the rock minerals (mineral dissolution and/or precipitation) is determined to be quantitatively very low again confirming indirectly how much of the changes in permeability relate to fines migration.

Notes

The report is comprised of 7 sections. Each of the first 6 sections presents and discusses the outline, procedure and the results of a particular activity conducted during the course of development of this project. The first section also presents a discussion about the rationale behind this project and how it would contribute to the overall progress and planning of the South-West Hub CCS Project as a whole. Section 7 integrates the outcomes of all the research work whose details were presented in the first six sections. It brings all the results achieved together to present the final discussions and draw the overall conclusions. It is worth noting that in the first 6 sections, where required, cross references are made to other activities from other sections.

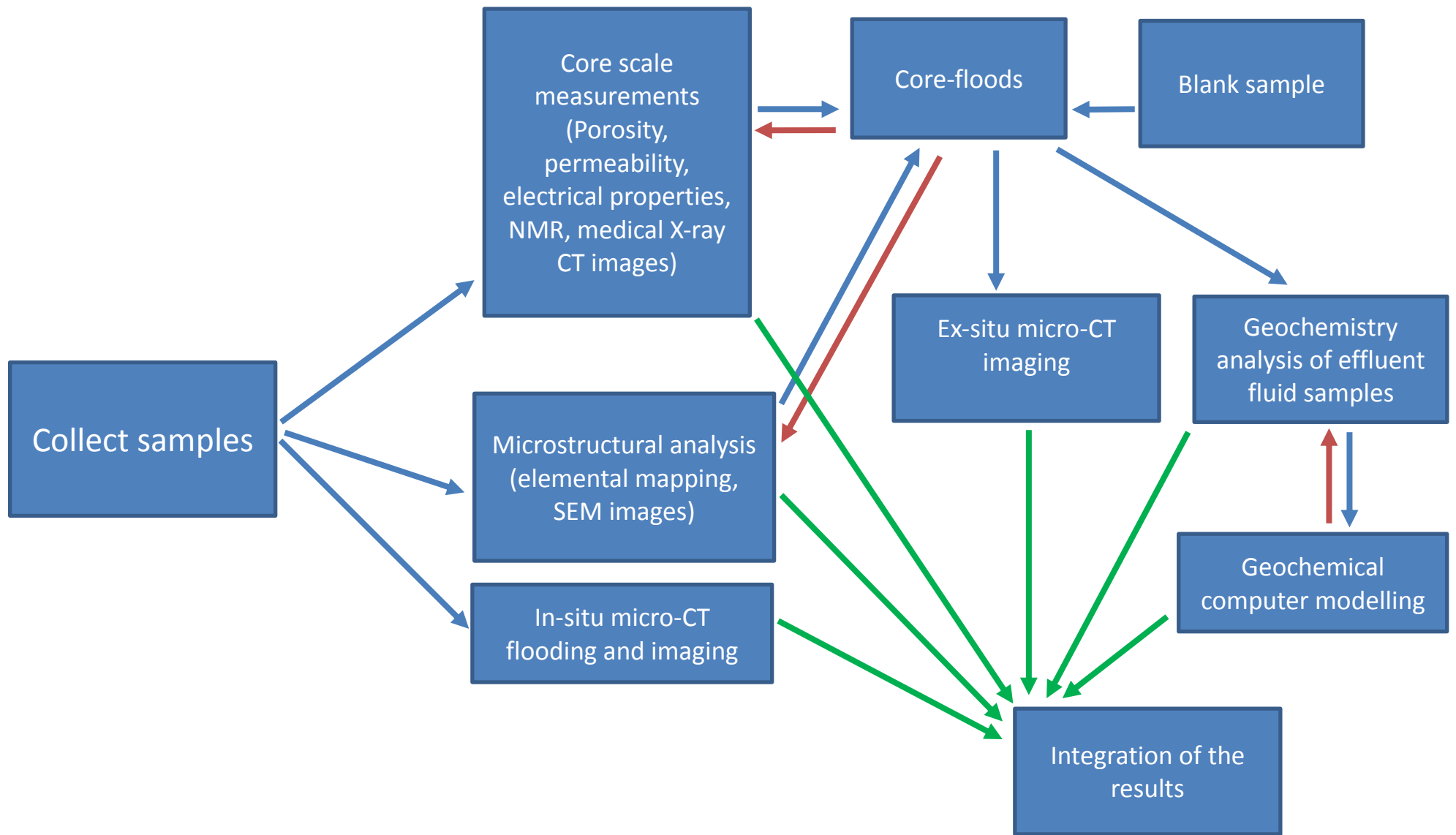
Below is a list of various sections included in this report along with the names of the researchers who contributed to the work and the preparation of the report:

- Section 1: Introduction and Sample Preparation- Dr. Lionel Esteban, Dr. Claudio Delle Piane (CSIRO) and Dr. Ali Saeedi (Curtin University).
- Section 2: Core-flood Experiments- Dr. Ali Saeedi (Curtin University).
- Section 3: Petrophysical Characterisation- Dr. Lionel Esteban (CSIRO).
- Section 4: Microstructural Evaluations- Dr. Claudio Delle Piane (CSIRO).
- Section 5: Geochemical Evaluation- Dr. Ryan Noble, Dr. David Gray and Dr. Linda Stalker (CSIRO).
- Section 6: Micro Computed Tomography (Micro-CT) Imaging- Dr. Stefan Iglauer and Dr Maxim Lebedev (Curtin University).
- Section 7: Conclusions- Dr. Ali Saeedi, Dr. Stefan Iglauer and Dr Maxim Lebedev (Curtin University), Dr. Claudio Delle Piane, Dr. Lionel Esteban, Dr. Ryan Noble, Dr. David Gray and Dr. Linda Stalker (CSIRO).

The reason behind presenting the sections covering the petrophysical and microstructural analysis of the samples after the section on the core-flood experiments is that these analyses were performed both before and after the core-floods. Comparing and discussing the pre- and post-flood analysis would be more efficient, and highlight any differences, if the two sets of data are combined and presented together under a single section.

The diagram provided on the next page presents an overview of the purpose-designed overall workflow devised for this project. This workflow has been designed to yield the maximum possible information and data based on which a conclusion can be drawn about the likely core and pore scale events occurring during the core-flood experiments resulting in change in the petrophysical properties of the post-flood samples.

Throughout this report, letter H used in the core plug IDs refers to one of the wells drilled into the SW Hub. For example, H1 refers to well Hervey-1 or H3 refers to well Harvey-3. Also, the term SW Hub refers to the South-West Hub CCS Project located in South-West of Western Australia (WA). SW Hub is one of the Federal Flagship Projects underway in Australia.



Section 1: Introduction and Sample Selection and Preparation

Contributors:

Dr. Claudio Delle Piane

Dr. Lionel Esteban

Dr. Ali Saeedi

Introduction

There are two main objectives for this section of the report. First, the rationale behind this project is explained and then in the second part the sample selection and preparation task is addressed. The first part will provide a detailed background to the project as well as an overview of the objectives pursued by this project. It will be discussed how the outcomes of this project will help to reduce the existing uncertainties surrounding the possibility of reduced injectivity in the injection wells and the in-situ geochemical reactions between the higher energy facies of the Wonnerup Member sandstone and the in-situ solute created during the CO₂ injection. The second part presents an overview of the way samples were chosen from various wells and then prepared for the subsequent laboratory work.

The Rationale behind the Project

The South West Hub Carbon Capture and Storage Project (the SW Hub) is managed by the Western Australian State Government (Department of Mines and Petroleum) with funding from the Federal Government. The project aims at reducing emissions by storing commercial quantities of CO₂ in a deep saline aquifer, the Triassic Lesueur Sandstone, located in the Southern Perth Basin of Western Australia. The Lesueur Sandstone consists of the Yalgorup and Wonnerup members (Figure 1) with the Wonnerup Member being considered the main storage unit.

Similar to any other CCS project, the storage site at the SW Hub has to be fully characterised to address a number of critical aspects such as containment security, storage capacity, monitorability and last but not least, the injectivity of the storage horizon. In order to satisfy the regulatory requirements, uncertainties associated with any of the above critical aspects have to be identified and quantified, to enable decision-making. Such information will contribute to the project plan to demonstrate that there is secure storage for commercial quantities of CO₂, that is, at least 800,000 tonnes per annum over a 30-40 year period. The primary objective of this particular research project has been to evaluate the fluid-rock interactions under in-situ conditions in the main injection interval (Wonnerup Member) at the SW Hub. The Wonnerup will also be the primary storage unit for the CCS site. The outcomes of such an evaluation will provide direct input towards reducing the uncertainties surrounding the storage capacity and injectivity at the SW Hub. Some of such uncertainties are generally known (at least from a qualitative perspective) and are common to all CCS sites such as the potential for geochemical reactions between the host rock and the injected fluids and/or in-situ created solutes. However, there are other uncertainties which may be less common but were identified to be present in the case of the SW Hub.

Before the commencement of this project, there were a number of other ANLEC R&D funded projects completed in which reservoir condition core-flood experiments were conducted for various purposes; tests range from relative permeability and residual saturation measurements to the evaluation of the geochemical reactions between the fluids and the formation rock in the SW Hub (Projects 7-1111-0199 (Delle Piane et al., 2013), 7-1111-0200 (Stalker et al., 2013) and 3-1110-0122 (Evans et al., 2013)). As part of these projects a number of rock samples from the Wonnerup recovered from wells Harvey-1 and Pinjarra-1 were examined. The data and information generated by Delle Piane et al. (2013) and Evans et al. (2013) revealed that while some petrophysical properties of the rock samples did not change appreciably, others were altered by the core-flooding procedure considerably. For instance, the porosity of the samples did not seem to be affected by the flooding procedure, but their post-flood permeability changed significantly compared to the pre-flood values. Depending on the location

and the depth from which the samples were recovered, both reduction (up to 60%) and improvement (up to 200%) in permeability values were observed. It is worth noting the permeability improvement was observed only in the sample from well Pinjarra-1. A single core-flood experiment conducted by Stalker et al. (2013) also generated some valuable information regarding the fluid-rock geochemical interactions. Based on the information generated, a number of crucial improvements were also identified to be implemented in any future geochemistry oriented core-flood experiments to better integrate with petrophysical and mineralogical assessments.

Based on the results obtained from these previous projects, the need for a more thorough investigation of injectivity was identified in 2014 to reduce the uncertainties identified in relation to the fluid-rock interactions relevant to the SW Hub. Subsequently, the current work was funded by ANLEC R&D to conduct a number of new core-flood experiments complemented by a set of purpose-designed investigations. The investigations were designed to not only pinpoint the underlying reasons behind the previously observed variations in the petrophysical properties of the post-flood samples but also characterise the in-situ geochemical reactions expected to occur at the SW Hub. The former objective was pursued using a series of experimental approaches while the plan for the latter one included a combination of both experimental and computer modelling techniques.

Sample Selection and Preparation

Ten core plugs were collected from wells Harvey-1 (four plugs), Harvey-3 (two plugs) and Harvey-4 (four plugs) to undergo the planned experimental work. The selected samples were all from the core material belonging to the Wonnerup Member. The Wonnerup can be described as medium to very coarse grained cross-bedded sandstone with significant grain size variation between beds, and is representative of high energy fluvial channel fills and barforms depositional environment. In the facies description by Delle Piane et al, 2013, the facies types sampled were classified as the Ai and Aii types which quantitatively make up the largest proportion of facies types in Harvey-1 (Delle Piane et al, 2013).

The new plugs were drilled as five pairs of “sister” samples from depths which were expected to fall within the CO₂ injection interval within the Wonnerup. In other words, depending on the available whole core material from various wells, the samples came from either 1500-1800m (Harvey-3 & 4) or 2500-2600m (Harvey-1) depths or both of these two depth ranges as they cover the top and bottom of the planned injection interval in the SW Hub. The core plugs were chosen from the most homogenous parts of the available whole core sections in an attempt to make the end results representative of the bulk of the Wonnerup Member. The sister plugs were placed one after the other to form composite cores (sample assemblies) used for the core-flood experiments (Figure 2). The reason behind using sample assemblies was to make the core flood samples long enough so they could accommodate the various types of analyses planned. Also, in the case of any change in rock properties due to flooding, the effect of flow direction could be investigated by analysing each plug on its own independently from the other samples. In order to make the planned analyses (such as SEM) possible, one of the plugs in every sample assembly was further cut into smaller segments (Figure 2). The SEM instrument accommodates thin rock samples only. In order to be able to compare the exact same part of the rock surface before and after the core-flood experiments, a thin disc was cut from one of the core plugs (Figure 2). This disc was then polished on one end face, scanned using the SEM instrument and then the pre- and post-flood images were compared for any alterations due to exposure to the

injection fluid. It is worth noting that since some of the plugs were, to some extent, friable the discs could not be polished as desired and this impacted on the quality of the SEM images acquired. This will be addressed in more details in Section 4 of this report. To summarise, in every sample assembly, one of the plugs was left intact while the other was cut into three pieces, one thin disc and two larger plug segments namely segment A and segment B.

Table 1 presents the pore pressure, confining pressure and temperature values used for the core-flood experiments. The pore pressures and temperatures were calculated using the results of the pressure and temperature survey run in well Harvey-1. The overburden pressure, on the other hand, was calculated using the widely accepted $1 \frac{psi}{ft}$ overburden pressure gradient (Tiab and Donaldson, 2004)

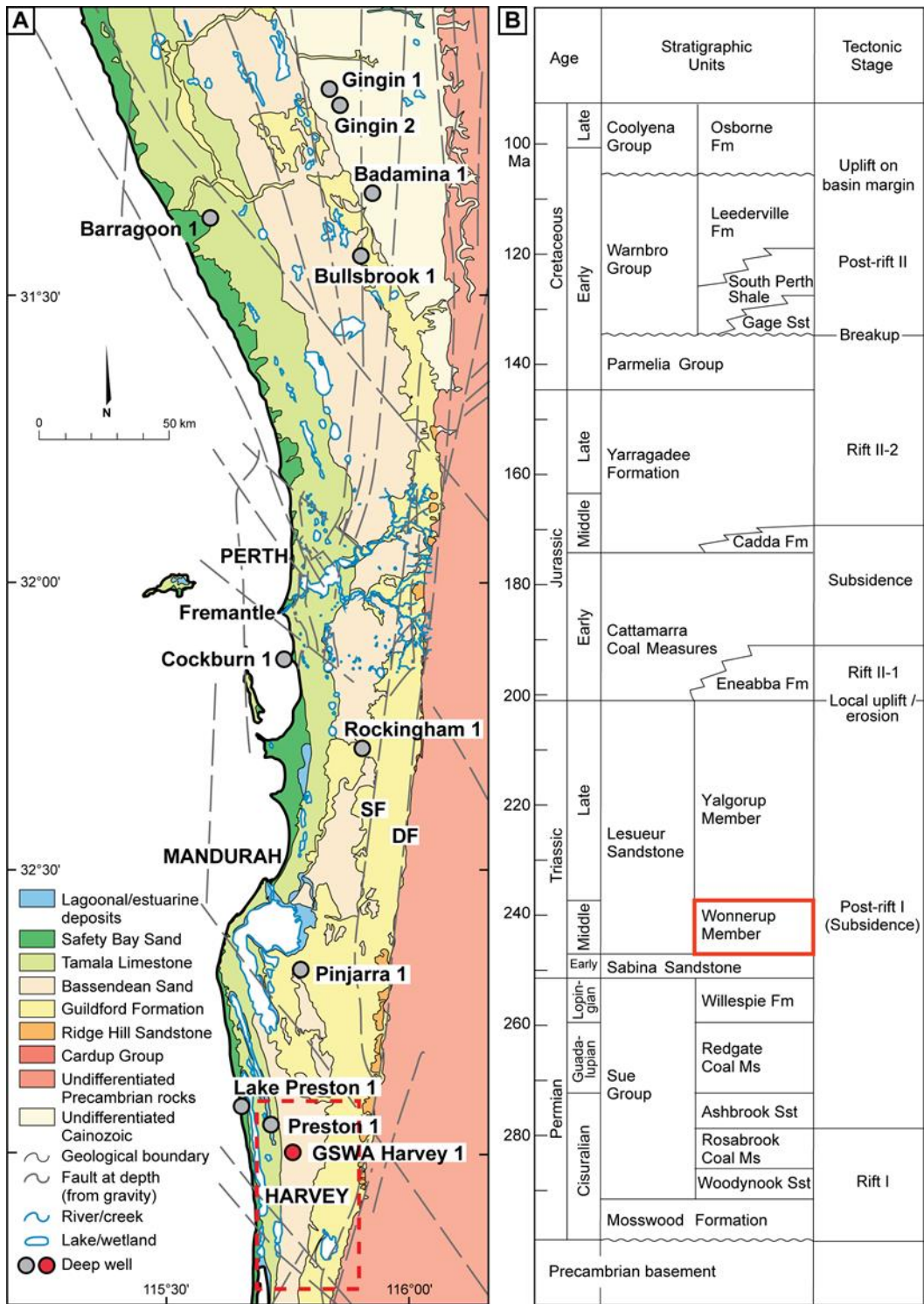


Figure 1. Surface geology of the Perth Basin, the red dashed box indicates the approximate location of the proposed South-West Hub; (B) Stratigraphy of the Central and Southern Perth Basin, the studied section is highlighted in red (modified after Olierook et al., 2014).

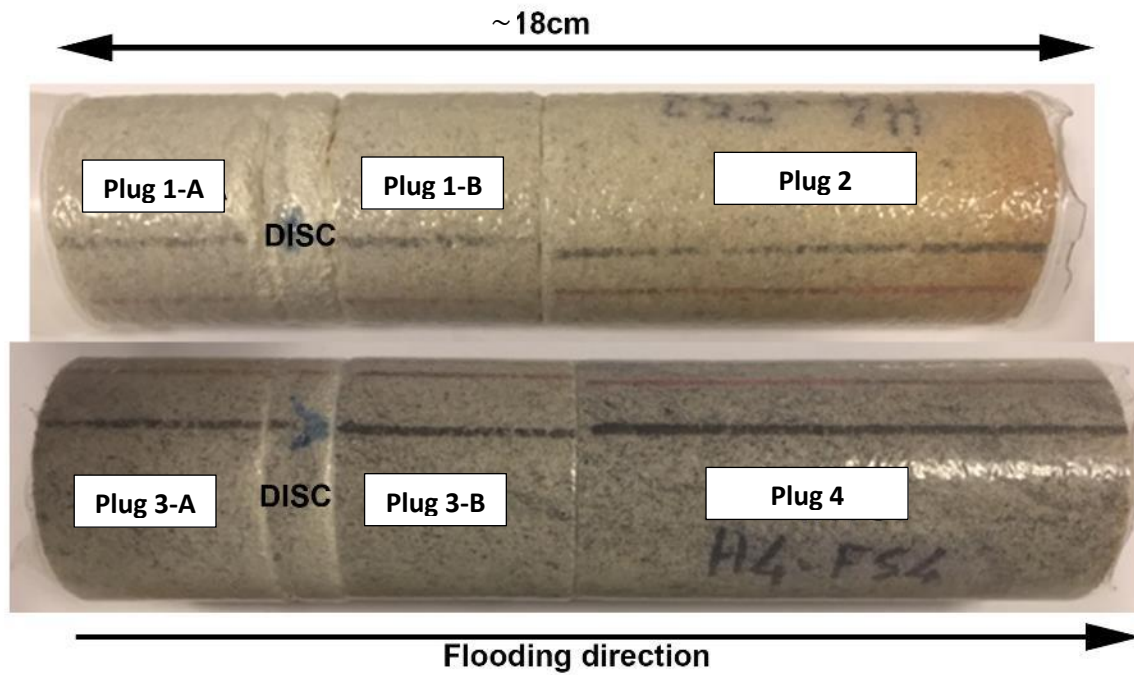


Figure 2. Examples of sample assemblies (composite cores) prepared using core-plugs from well Harvey-4.

Table 1. The depths of the core plugs and their corresponding pressures and temperatures.

Plug ID	Sample assembly ID	Depth m	Pore pressure MPa	Confining pressure MPa	T °C
H1-Plug1	H1-Assembly1	1924.73	19.28	43.54	61.0
H1-Plug2		1924.84	19.28	43.54	61.0
H1-Plug3	H1-Assembly2	2505.43	25.09	56.67	69.4
H1-Plug4		2505.52	25.09	56.68	69.4
H3-Plug1	H3-Assembly1	1459.40	14.54	32.81	54.1
H3-Plug2		1459.40	14.54	32.81	54.1
H4-Plug1	H4-Assembly1	1794.53	17.98	40.59	59.1
H4-Plug2		1794.53	17.98	40.59	59.1
H4-Plug3	H4-Assembly2	1800.42	18.04	40.73	59.2
H4-Plug4		1800.42	18.04	40.73	59.2

Section 2: Core-flood Experiments

Contributor:

Dr. Ali Saeedi

Introduction

As indicated earlier, before the commencement of this project, there were a number of other core-flood experiments conducted on samples from the Wonnerup Member. Building upon those results and experiences gained, a new, specially designed core-flood procedure was devised for this study. One main improvement over the past experiments was making the new ones more geochemically focused, and experimentally robust. This meant designing a workflow to help better quantify and understand the geochemical reactions which could occur during the experimental timeframe and how they might contribute to changes in porosity, permeability, pore size distribution, etc. In the previous tests, the core samples were left soaking in CO₂-saturated brine overnight and that impacted on the chemical behaviour of the core. The new tests, however, were designed to avoid that by using a fraction collector which collected samples continuously allowing the experiments to be run without interruption. Relatively low flowrates were also used for the new experiments to provide the injection fluid with more reaction time with the rock.

Furthermore, for every set of samples tested from each well, an additional experiment was also run, known as the “blank” experiment, where the flooding process took place in the absence of an actual rock sample. This allowed the team to evaluate the background changes in the chemistry of fluid samples caused by the contamination from the various wetted components of the core-flood rig. In addition, for comparison purposes, a single experiment was conducted on a Berea Sandstone sample sourced from the US. This sample type is relatively well characterised and commonly used in the technical community as a base case or reference sample for core-flooding experiments. The sample tested here was taken from the same sandstone block from which other samples have been drilled and tested in various other ANLEC R&D funded projects (e.g. 3-1110-0122 (Evans et al., 2013)).

Additional changes to the workflow (the composite core approach, continuous sampling, use of blanks, testing of known reference materials and replacement of stainless steel parts with hastelloy to reduce corrosion contamination) were complemented by other improvements including the definition and use of a more representative synthetic fluid salinity mix, changes to the ICPMS and OES dilution and analytical work, and use of spikes (Br and Sr) to quantify the geochemical effluent all contributed to increased accuracy and led to the provision of a more robust data package.

Experimental Setup

The core-flooding experiments were carried out using the high pressure-high temperature, three-phase steady-state core-flooding apparatus located within the Department of Petroleum Engineering at Curtin University. A schematic of the core-flooding rig is presented in Figure 3. The apparatus is capable of handling experiments with pressures up to 100 MPa (~15,000 psi) and temperatures up to 200°C. Many of the critical wetted metal parts of the apparatus are made of highly corrosion resistant metals (e.g. hastelloy, titanium or duplex and super duplex stainless steel) which make the equipment corrosion resistant even under high temperature and high salt concentrations.

All the components carrying fluids during experiments are placed inside a large constant temperature convection oven (Figure 3). The temperature inside the oven is controlled using a PID (proportional–integral–derivative) controller module which can regulate the temperature with an accuracy of ±0.5° C. The core-flooding apparatus utilises pulsation-free, positive-displacement syringe pumps (Figure 3). In the pumps, the pressure, volume and flow-rate values can be set and recorded with accuracies

of ± 35 KPa (5 psi), ± 0.05 cc and ± 0.05 cc/hr, respectively. All the pressure sensors utilised within the core-flooding rig have the same ± 35 KPa (5 psi) measurement accuracy.

The core-holder used in this research was a standard biaxial core-holder (Figure 4). Standard biaxial or hydrostatic type core-holders are defined as core-holders that have common radial and axial pressure applied to the core-sample. A specially designed spider-web-type groove pattern (Figure 4) is utilised on the end-faces of the core-holder's distribution plugs which come in contact with end-faces of the core sample. This is to make sure that the fluids, before entering or on exiting the core-sample, are evenly distributed on the whole face of the core-sample. All the core-holder out-flow fluids are passed through a dome-type back-pressure regulator (BPR) which keeps the pressure inside the sample constant and equal to reservoir in-situ pore pressure.

Over the past 10 years this instrument has been successfully used for various CO₂ geosequestration related research activities generating quality results (e.g. Saeedi, 2012; Saeedi and Rezaee, 2012; Saeedi et al., 2012; Saeedi et al., 2011).

All of the sensors and electronic interfaces of the apparatus are connected to two PCs with appropriate data logging and monitoring software installed on both. The whole system including the sensors, the PID controllers and the injection and collection pumps are monitored and controlled using these two PCs.

For the core-flood experiments, a special multilayered combination sleeve was used. This combination sleeve was necessary due to the tendency of scCO₂ to diffuse and penetrate through most flexible rubber sleeves which could cause the sleeve to lose its integrity and fail. This combination sleeve was made of three layers including one layer of heat-shrink Teflon, one layer of aluminium foil and one layer of conventional Viton sleeve. The heat-shrink Teflon had an extremely low permeability to CO₂, but, to make sure that the CO₂ would not escape to the overburden annular space, a layer of aluminium foil was also placed in between the Teflon and the Viton sleeve.

Material

Dead (deaerated) formation brine and CO₂-saturated brine were used as injection fluids during the core-flood experiment. The CO₂ gas used to saturate the brine was of at least 99.995% (vol%) purity. The synthetic formation brine was prepared in the lab using distilled water and highly soluble salts and AR grade chemicals. The formation brine salinity used is presented in Table 2. The species were added using the following compounds CaCl₂, MgSO₄.7H₂O, KBr, NaCl, NaHCO₃, SrCl₂ and CuSO₄.5H₂O. Further details on the formation brine salinity and how it was calculated can be found in Section 5 of this report.

As indicated earlier, five sample assemblies were tested, each of which included two sister plugs (Table 1). These sister plugs were from the potential injection/storage interval of the target formation in the SW Hub. The detailed petrophysical characteristics of these samples will be presented in Section 3 of this report.

Experimental Conditions

Table 1 outlines the values of the in-situ reservoir condition parameters used during the experiments.

Experimental Procedure

In order to promote chemical reactions between the rock samples and the injection fluids, the formation brine was fully saturated with CO₂ under in-situ reservoir conditions. This was achieved by using a high pressure-high temperature stirred Parr reactor in which formation water and scCO₂ were brought in contact and physically stirred under in-situ conditions until full saturation was achieved. The reactor pressure was monitored and controlled using a syringe pump to make sure full saturation was achieved for every experiment.

Below is an outline of the steps involved in carrying out the geochemically oriented core-flood experiments. This procedure has been designed based on the standard procedures and protocols available in the literature (Bennion and Bachu, 2005; Izgec et al., 2008; Perrin and Benson, 2010; Saeedi et al., 2011) as well as the lessons learned from the previously completed ANLEC R&D funded experiments.

1. A sample assembly was created using two sister plugs. A lab-grade lint-free tissue was used as the bridging material between the core segments which constituted each sample assembly (Saeedi, 2012)
2. The sample assembly was wrapped in the previously described multi-layered sleeve before being inserted into the core-holder. In order to eliminate the effect of gravity segregation within the sample while undergoing the core-flood experiment, the core-holder containing the sample assembly was placed vertically so the injection would be performed from base to the top. In order to apply overburden pressure to the sample, after loading the wrapped sample into the core-holder, the overburden fluid was pumped slowly into the annular space of the core holder using a hand pump.
3. After gradually increasing the confining pressure to the full reservoir net-effective pressure, all the inlet and outlet ports of the core-holder were capped or connected to appropriate flow-lines and pressure gauges. Then low pressure CO₂ gas was passed through the sample for at least 10 minutes. Due to its high diffusivity, CO₂ would displace and replace much of the air present in the sample's pore space. Compared to air, the CO₂ which replaced the air could be evacuated from the sample more effectively when required. Furthermore, any remaining CO₂ after the evacuation would readily dissolve in the saturating dead brine and be removed from the sample during the later in-situ saturation and subsequent brine injection.
4. After flushing the sample with CO₂, all the flow-lines and the sample inside the core-holder were vacuumed using a vacuum pump for at least 24 hours. Then the back pressure was brought to full in-situ reservoir pressure, and the air bath temperature was raised to reservoir temperature. Then the sample assembly was displaced and saturated using dead formation brine while the confining pressure was increased and then maintained equal to its in-situ reservoir value. The sample was left under reservoir conditions in contact with brine for another 24 hours to become completely saturated with the brine and to establish adsorption equilibrium.
5. In the next step the CO₂-saturated brine was injected into the core sample at constant flow-rate (0.5 mL/min) to displace the dead formation brine.

It is worth noting that H1-Assembly1 underwent two separate core-flood experiments. The first attempt to flood this sample failed half way through due to a malfunction in the fractional collector used to collect effluent fluid samples. As a result, this sample was tested in a 2nd core-flood experiment which followed the above described procedure so that a sufficient number of brine samples could be collected for subsequent geochemical analysis.

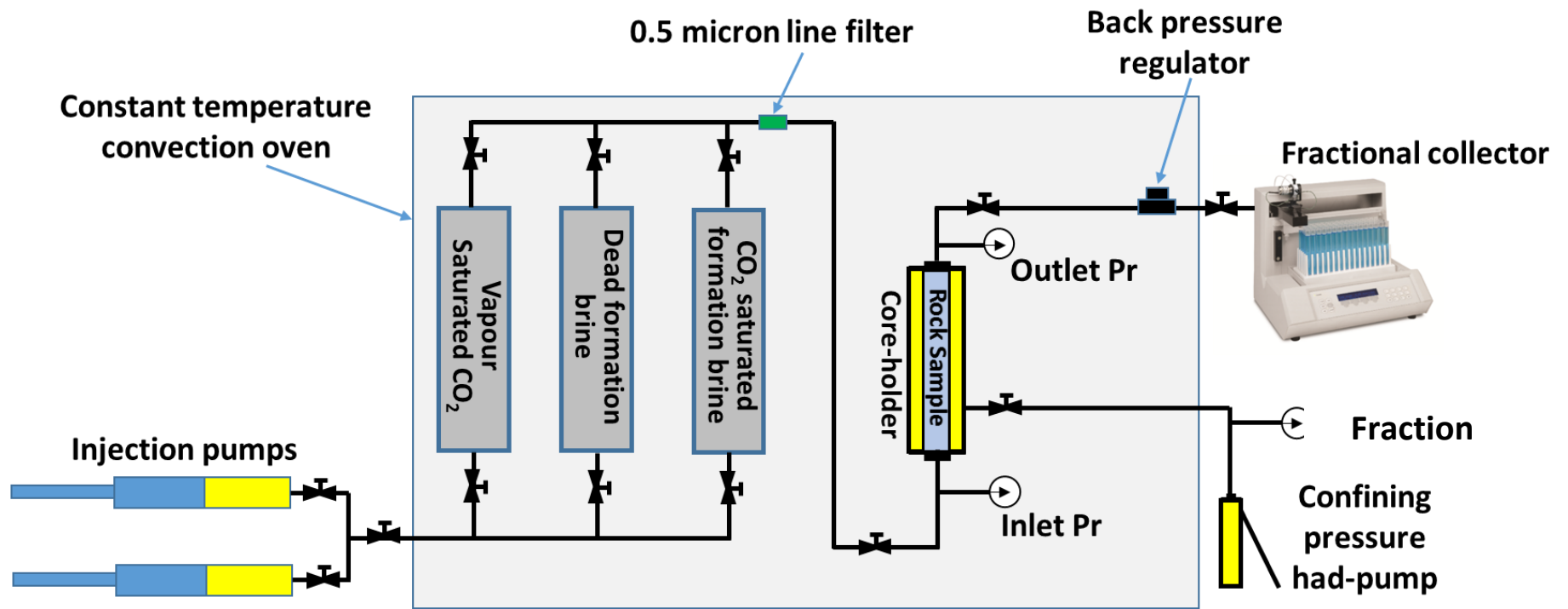


Figure 3. The schematic diagram of the core-flood apparatus

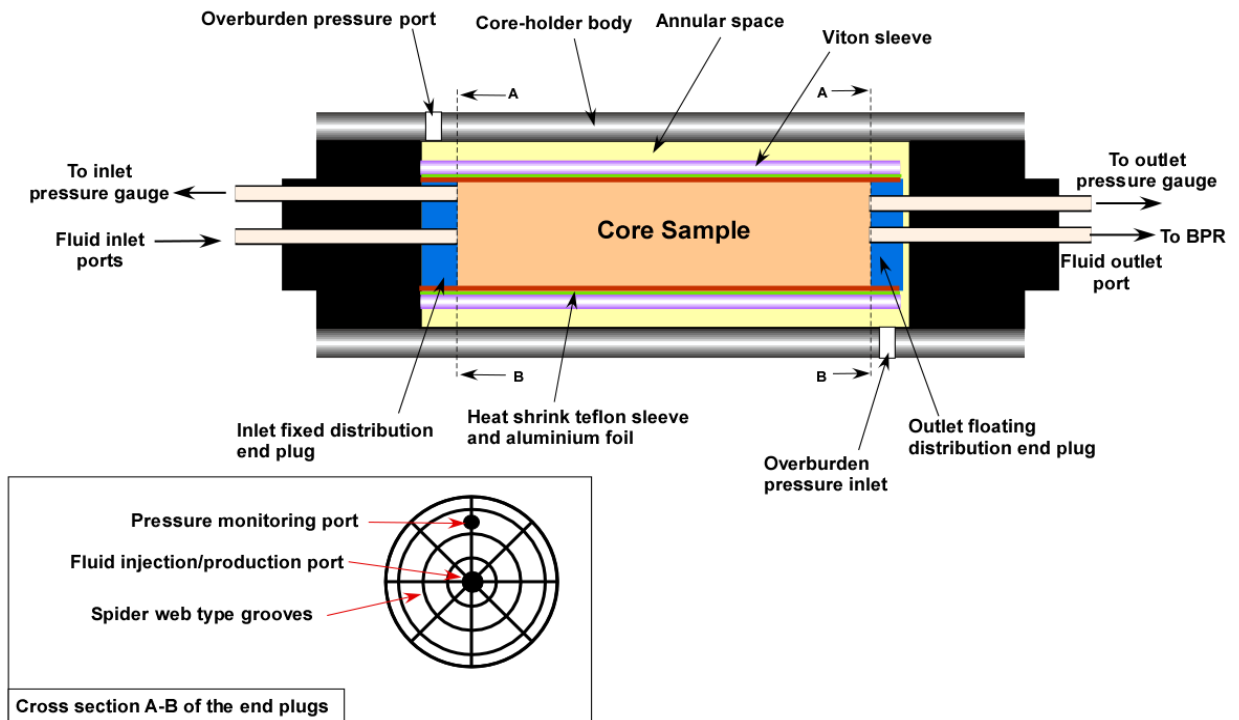


Figure 4. Schematic cross-sectional illustration of the core-holder assembly

Table 2. Formation water salinity used during the experiments

Cation/Anion	Concentration, mg/L
Ca	1200
Mg	600
K	60
Na	9647
Sr	100
Cu	100
HCO ₃	125
Br	123
Cl	17012
SO ₄	2522
Total dissolved solids (TDS)	31426

During step five of the experiments, effluent brine was collected using a fraction collector at 10 minutes' intervals in plastic tubes (5mL). These brine samples were refrigerated until they were analysed in the lab for their chemical compositions. The results of the chemical composition analysis are reported and discussed in Section 5 of this report.

As indicated earlier, a "blank" experiment was also conducted per each set of samples tested from each well. While many parts of the core-flooding rig are made of corrosion resistant metals, small quantities of the metal components were expected to dissolve in the injection brine and, therefore,

contaminate the effluent fluid samples collected. In an attempt to quantify the background contaminations, a blank core-flood test was run in which a Teflon tube was loaded into the core-holder instead of a rock sample. Subsequently, CO₂-saturated formation brine was passed through the instrument's flow lines and effluent brine was sampled as usual. The results of the blank experiment are also provided in Section 5 by way of baseline.

Observations and Results

The core-flood experiments were conducted using a flow-rate of 30 mL/hr (0.5 mL/min). For a conventional core-flood experiment conducted on samples similar to those tested here, this flow-rate is considered to be too low (Saeedi, 2012; Saeedi et al., 2012). In such an experiment where the main objective is to measure relative permeabilities and residual saturations, a low flow-rate could introduce experimental artefacts in the measured data. As indicated earlier, the experiments conducted as part of this work required a low enough flow-rate to allow the injection fluids to interact with the rock samples. In choosing this flow-rate for the current experiments, the results obtained from previous tests (Projects 7-1111-0199 (Delle Piane et al, 2013), 7-1111-0200 (Stalker et al, 2013) and 3-1110-0122 (Evans et al., 2013)) were used as a guide.

As indicated earlier, the pre- and post-flood gas permeability measurements conducted on samples from Harvey-1 and Pinjarra-1 during the previous experimental work (Projects 7-1111-0199 (Delle Piane et al, 2013), and 3-1110-0122 (Evans et al., 2013)) all revealed considerable changes in the permeabilities of the samples. However, this change in permeability could not be detected during the actual core-floods conducted previously. The main reason for not being able to detect this change in permeability was the fact that during the previous experiments, scCO₂ and brine were both injected in turn through the samples and the saturation change during the multiphase flood had a strong effect on the differential pressure measured across the samples. This effect would mask any change in differential pressure due to the actual change in the absolute permeability of the samples. In an attempt to overcome this issue and possibly monitor the evolution of sample permeability during the core-flood procedure (if it occurs), single phase formation brine only was injected through the samples. Then, the differential pressure across the samples was monitored closely for any change which would reflect the change in the absolute permeability of the samples.

Despite all the efforts and modifications to the core-flood procedure, not for all samples a significant change in the differential pressure across the sample could be detected while flooding them. The only set of differential pressure data of statistical significance was recorded for the second sample assembly of well Harvey-4 (H4-Assembly2). However, this may not be interpreted as an indication that the permeabilities of other samples did not necessarily change due to the flooding process. It is believed that due to the low flow-rate (i.e. small differential pressure) used during the experiments, any possible variation in the permeability of this sample went undetected during the experiment. As indicated earlier, the accuracy of the pressure transducers used was ± 35 KPa so any pressure variation less than 35KPa may not be detected by the pressure transducers. It is worth noting that apart from the relatively low injection flowrate, the intermediate to high permeability values of the samples tested was another contributing factor to make the differential pressure data insignificant. In fact, the main reason behind recording statistically significant pressure data for H4-Assembly2 was its low permeability (about 2 mD).

The change in differential pressure profile for H4-Assembly2 is presented in Figure 5. As can be seen, this figure reveals a degree of reduction in the sample permeability over time as evident from the continuous increase in the differential pressure measured across the sample. It is worth noting that while this data indicate the evolution of sample permeability as the fluid injection proceeds, it is not possible to determine quantitatively how much the permeability has decreased. That is because the differential pressure profile never stabilises and from the onset of fluid injection to the end of the experiment the rock permeability keeps evolving.

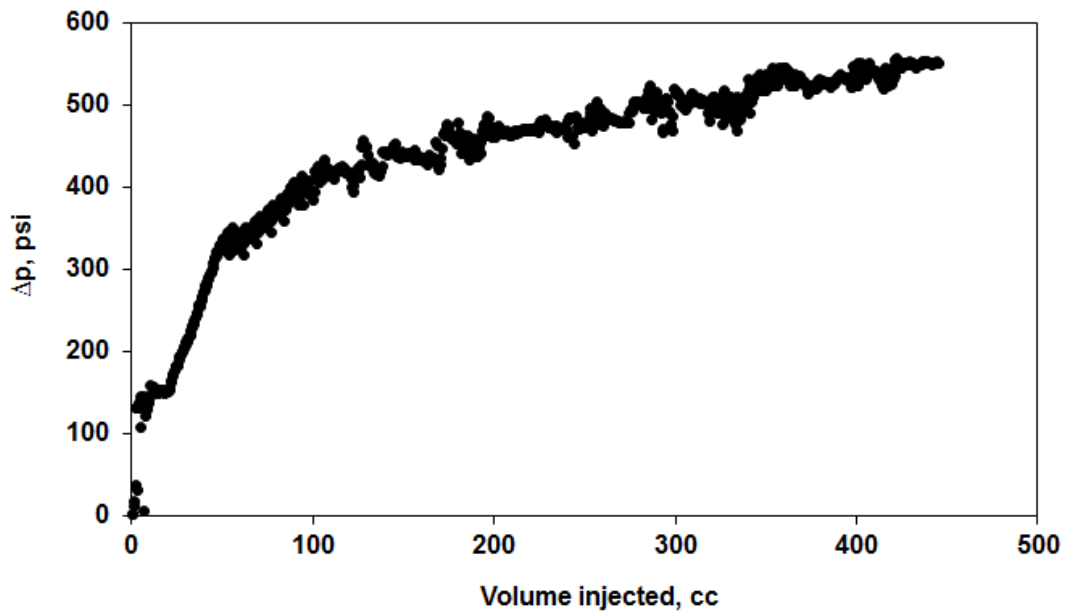


Figure 5. Differential pressure evolution for the second sample assembly (plugs 3 and 4) of Harvey-4

A sample of the less reliable differential pressure data recorded for the 2nd sample assembly belonging to well Harvey-1 is presented in Figure 6. As can be seen, the values of the differential pressures recorded for this sample are about 11 KPa on average which is well below the measurement accuracy of 35 KPa. Therefore, any variation in this data set has no statistical significance and may not be indicative of a change in the sample properties during the flooding.

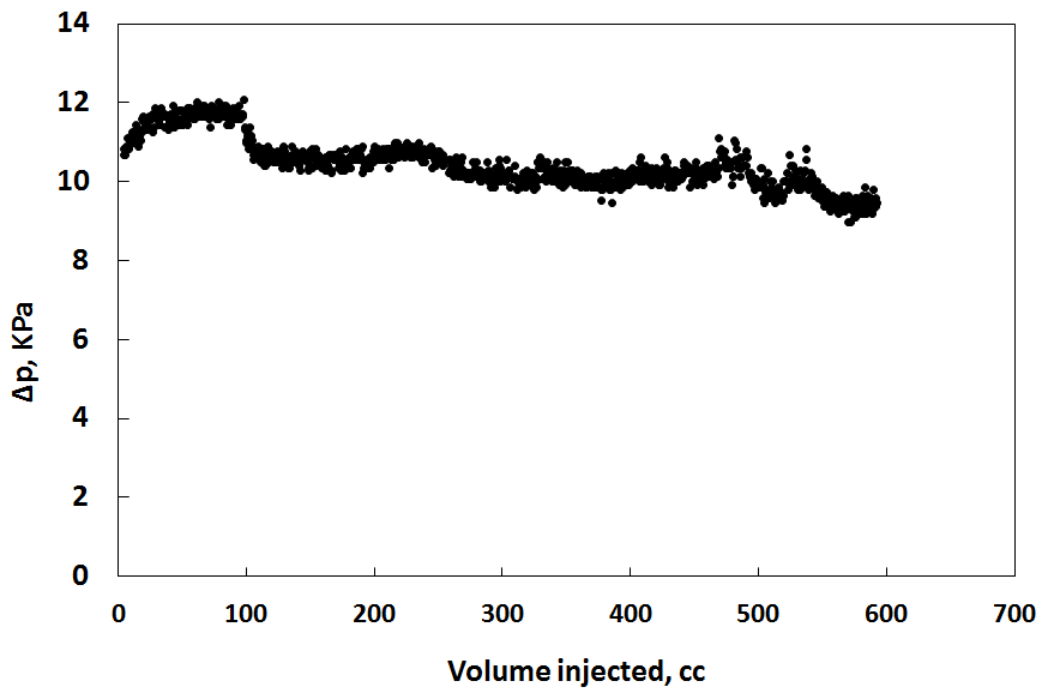


Figure 6. Calculated differential pressure across the second sample assembly (plugs 3 and 4) of Harvey-1

Summary and Conclusion

A new specially designed core-flood procedure was implemented in this new work. The new procedure was built upon the experiences gained from the previously completed studies. Low injection flowrate and uninterrupted fluid sampling made the new tests well suited for geochemical investigation. However, as a downside of using such a low flowrate, only for one sample from well Harvey-4 statistically significant differential pressure data could be recorded. Such data could be very helpful as an early indicator of formation damage (i.e. fines migration) within the samples tested.

Also, as part of the new procedure, in every phase of the project, a so-called “blank” experiment was conducted to help with quantitatively evaluating the background contamination of the fluid samples collected during the flooding caused by the slight corrosion of the metal components of the core-flood rig.

Section 3: Petrophysical Characterisation

Contributor:

Dr. Lionel Esteban

Introduction

This section of the report covers the laboratory-based techniques used to evaluate the pre- and post-flood petrophysical properties of the rock samples tested in this work. Overall, this section is divided into two parts. In the first part, the experimental techniques and procedures used to conduct the laboratory measurements are all described in details with, where necessary, specific references made to particular measurements conducted per each of the Harvey wells (Harvey-1, 3 and 4). In the second part, the experimental results achieved for the different groups of samples from the Harvey wells are presented and discussed in details.

Principles and Methodologies

X-ray Medical CT Imaging

X-ray CT (X-ray Computed Tomography) or XCT is a radiological imaging system first developed by Hounsfield (1973). The non-destructive technique uses X-rays to create a three-dimensional data set of a sample by stacking contiguous cross-sectional two-dimensional images. The principles of imaging have been extensively described elsewhere (e.g. Wellington and Vinegar 1987) and will not be repeated here. In brief, CT-scan imagery corresponds to a 2-D or 3-D linear X-ray attenuation pixel matrix, where the attenuation is a function of the density and atomic number of the material being analysed.

In geo-materials studies, the applications of CT scanning include viewing full-diameter plug sections to determine orientation relative to bedding, presence of fractures and nodules. The same acquisition is repeated with the same plug orientation after core-flooding samples to compare with the initial state and detect potential changes in the pore sizes, distribution, structure, mineral surfaces and perhaps pore throat clogging and fine particle accumulations. Additionally, the CT systems can be used for quality assessment and evaluate the integrity of the samples and sub-samples prior to specialized core testing. This technique is generally suitable for visualization from the metre to millimetre scale.

The three-dimensional data of the core plugs tested at CSIRO was acquired using a Siemens SOMATOM definition AS with 64 slices from the National Geosequestration Laboratory (NGL). An energy beam of 140kV/500mAs with a helical acquisition type was applied to acquire transversal images every 0.4 mm (in z axis) and ~ 0.1 mm in x and y axes. Osirix software Ltd was used to process the X-ray images and provide 2D orthogonal views along the core axis. The CT mean value of each transversal XCT image was computed, removing 1 cm material from the sample's edge to avoid possible beam-hardening artefacts. An example of area to compute a CT mean from a transversal XCT image is given in Figure 7. Computing such a CT mean for each transversal image provides a CT profile along the core axis that can then be converted into bulk density and porosity using the results of the petrophysical measurements (i.e. gas porosity measurements) performed on the plugs as a "density-porosity calibration" for CT mean value. In Harvey-3 plugs only, an attempt to extract the macro-pores (i.e. pore sizes \geq to the medical XCT resolution) was used by basic segmentation where values below 1165 CT units are considered as pores. A 3D volume of these segmented pores was run with Osirix software to visualize any special pore distributions inside each plug. Image-J software was then used on these segmented images to fit ellipses in each pore and run statistics module to extract the macro-porosity, mean pore size, circularity of the pores, and number of pores/cm³.

The resolved pores from medical XCT ($> 100 \mu\text{m}$) are pore sizes which contain movable fluid available for reservoir production. However, based on some pore throat distributions from MICP (Delle Piane et al., 2014; and this report), most of the pore throat sizes are around $10 \mu\text{m}$ (i.e. below the medical XCT resolution), which are mostly related to capillary pore network. Note that MICP data are indicative of the pore throat sizes rather than the pore body sizes; one would think that pore body should be bigger than pore throat sizes. These meso-pore sizes are still related to movable water to some extent. In other words, the segmentation of the pores from medical XCT are not exactly representative of the whole sample pore network but it is a quick and easy to use indicator of the reservoir producibility and fluid transport potential.

Nitrogen Gas Porosity-Permeability

After trimming the initial top and bottom end of each plug to achieve the correct geometry, the plugs were oven dried under vacuum at 105°C for 72 hours and then tested using an automated nitrogen permeameter-porosimeter (AP-608 by Coretest Inc.). Such measurements were repeated on the dry plugs (or sub-plugs) after undergoing the flooding experiments. The post-flood samples were oven dried under vacuum at 105°C for 72 hours before undergoing the nitrogen gas porosity-permeability measurements.

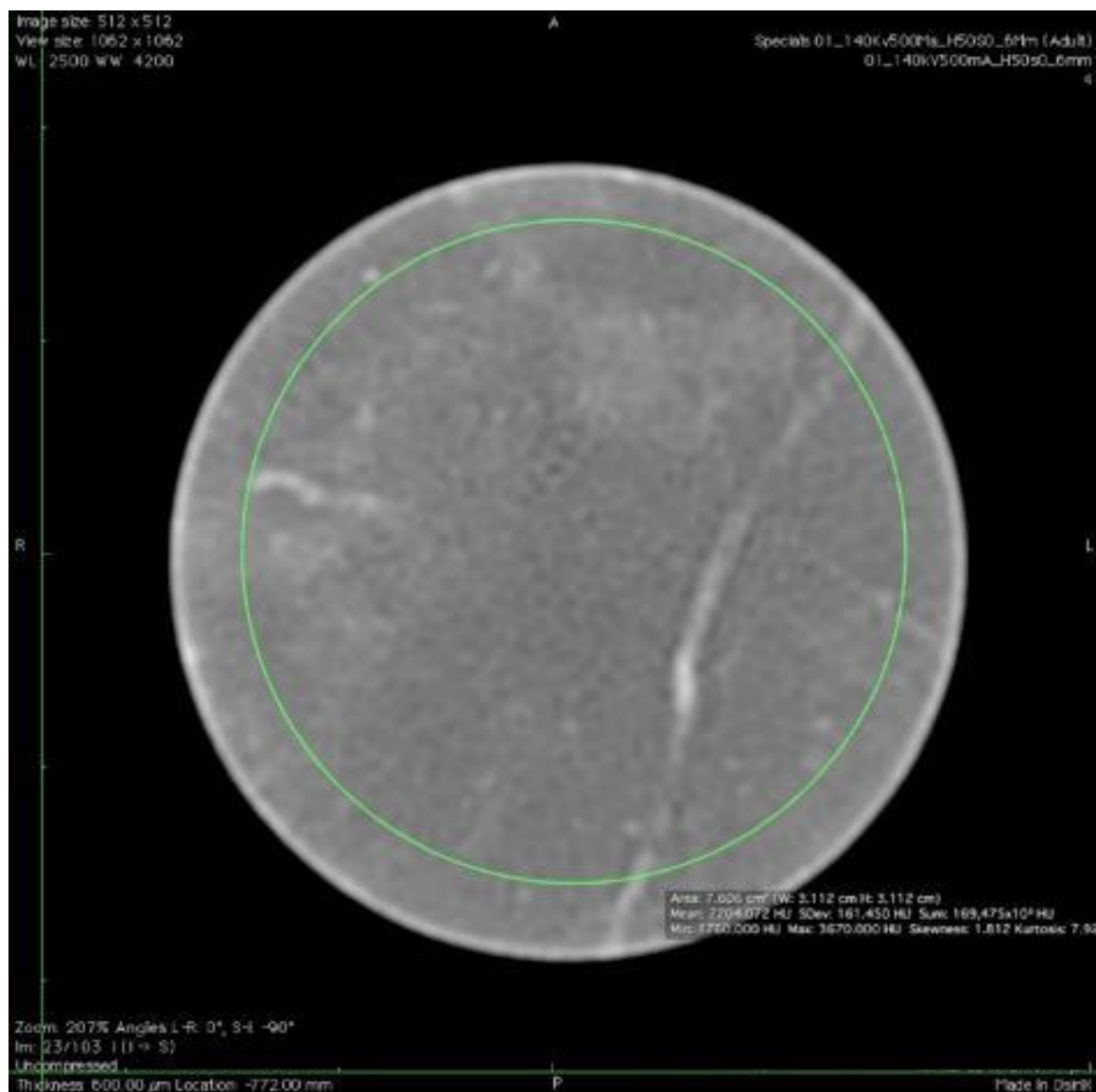


Figure 7. Example of a XCT transversal image from a plug with the green circle representing the area where the CT mean is computed.

For Harvey-1 plugs only, the residual salts inside the pores and around the samples which had accumulated after drying (the samples were brine-saturated before this stage) were tentatively removed by immersing the samples in hot tap water at 60°C under vacuum. The salinity of the water, or more precisely, the electrical conductivity of the tap water was monitored with an Orion conductivimeter. The hot tap water was regularly changed until the conductivimeter measured the same as the initial fresh tap water conductivity (i.e. no more salts had dissolved from the samples in the water) for an extended period of time (> 6 hours) upon which the sample was considered to be free from salt residue. After the salt cleaning process, the samples were oven dried under vacuum one last time for 72 hours before repeating the nitrogen porosity-permeability measurements. It is worth noting that the objective of the salt cleaning process was to ensure that salt would not clog the pore throats or change pore size distribution, which would affect the porosity-permeability measurements. A comparison between the data and information generated for the samples that had been cleaned, compared with untreated samples indicated little or no differences between porosity-permeability values. Therefore, the above described salt cleaning process was not repeated on Harvey-3 and Harvey-4 plugs. It is also worth noting that in the absence of clay types susceptible to fresh water (e.g.

smectite), no damage to the samples (i.e. clay swelling) was expected to occur with the exposure of the samples to tap water.

In a standard nitrogen gas porosity-permeability test a sample is loaded into the core holder and flooded with inert nitrogen gas. Nitrogen expansion is monitored and the pore volume or the porosity of the rock sample is calculated following Boyle's law:

$$V_1 = \frac{P_2 \cdot V_2}{P_1} \quad \text{Eq. 1}$$

Where V_1 is the volume of nitrogen permeating the rock sample; P_2 and V_2 are the pressure and the calibrated volume of nitrogen before being released into the sample, and P_1 is the pressure of gas after sample infiltration.

Permeability was measured using the unsteady state pulse decay method (Jones, 1972) which involves recording the differential pressure across a core plug when the inlet of the plug is connected to a gas tank, initially with a given pressure. The technique has been widely used in core analysis and returns the equivalent liquid permeability, which can then be readily used to estimate water flow behaviour under the assumption of no interaction between fluid phase and solid rock frame.

Following the estimated pressure applied under in-situ conditions at the plug recovery depths (Table 1), the porosity and permeability of each of the core plugs were measured under the following confining pressures:

Samples H1-Plug1 and H1-Plug2: 3.4, 13.8 and 24.1 MPa.

Samples H1-Plug3 and H1-Plug4: 3.4, 13.8, 24.1 and 31 MPa.

Samples H3-Plug1 and H3-Plug2: 3.4, 6.9, 13.8 and 17.2 MPa.

Samples H4-Plug1, H4-Plug2, H4-Plug3 and H4-Plug4: 3.4, 6.9, 10.3, 13.8 and 20.7 MPa

Three measurements were taken at each pressure to assess the statistical error of the analysis.

Bulk and Grain Density

The geometric shape of the plugs allows the accurate measurement of their dimensions with a calliper. The plug volume can therefore be computed and the dry bulk density can be determined from the dry mass (or brine-saturated mass for the wet bulk density) conditions as:

$$\rho_{\text{bulk}} = \text{Mass}_{\text{sample dry or brine saturated}} / \text{Bulk Volume}_{\text{sample}} \quad \text{Eq. 2}$$

with ρ_{bulk} in g/cm^3 , mass in g and volume in cm^3 .

Following the drying process under vacuum at 105°C , the sample is cooled down under vacuum and then immediately weighed and its pore volume accurately measured with a helium gas displacement pycnometer. An Accupyc II 1340 from Micromeritics was used for sample volume measurement where the volume of the helium gas invading the connected pores of the dry sample is precisely measured with an accuracy of 0.001 cm^3 to yield the grain matrix volume. The grain density (in g/cm^3) is then simply computed as:

$$\rho_{\text{grain}} = \text{Mass}_{\text{dry sample}} / \text{Volume}_{\text{grain matrix}}$$

Eq. 3

with ρ_{grain} in g/cm^3 , mass in g and volume in cm^3 .

The grain and bulk density can then be used to compute the total porosity assuming that: (i) helium gas or brine was able to invade all the pores of each plug. The porosity can then be computed as:

$$\phi = \frac{(r_{\text{grain}} - r_{\text{bulk}})}{(r_{\text{grain}} - r_{\text{fluid}})} \times 100$$

Eq. 4

where ϕ is the porosity in percent, densities (ρ) are all in g/cm^3 and ρ_{fluid} is 0 for air and $1.03 \text{ g}/\text{cm}^3$ for the brine.

It is worth noting that ideally, the grain density measurement using the helium pycnometer should be more accurate when conducted on the powdered dry sample as no isolated pores exist after grinding the sample. But such a test is destructive and could not be performed on the samples tested in this work. Furthermore, the amount of isolated pores is expected to be very small for the relatively clean sandstone samples tested here.

The measurements were conducted on all the plugs before and after flooding experiments (and repeated after the salt cleaning process on dry samples for Harvey-1 plugs). It is also worth noting that only the volumes of the short plug segments post-flood (A&B; Figure 2) were measured with the Accupyc. The other plugs were too long to fit into the Accupyc chamber. For the long plugs, the grain matrix volume was back calculated knowing the pore volumes from nitrogen gas porosity measurements.

Nuclear Magnetic Resonance

Nuclear magnetic resonance (NMR) relaxation time measurements can provide critical information about the physico-chemical properties of fluids in porous materials from both wireline logging and laboratory tools (Grunewald and Knight, 2011; Walbrecker et al., 2011). Applications of NMR in petroleum well logging over the past several decades have demonstrated robust links between measured relaxation times and important formation properties, including pore size distribution and permeability (Clennell et al., 2006; Coates et al., 1991; Josh et al., 2012). During NMR measurement, proton nuclei are first aligned according to the direction of an applied magnetic field B_0 , and then perturbed from their equilibrium state by a pulse characterized by the proton resonance frequency. In an NMR test the magnetization and transverse relaxation time (T_2) of hydrogen nuclei contained in the pore fluid is measured. Different pore sizes in fluid saturated rocks will produce characteristic T_2 distributions as the amplitude of transverse magnetization is proportional to the number of hydrogen nuclei. As a consequence, the observed T_2 distribution of a saturated core sample represents the pore size distribution of the rock (assuming a simple pore geometry-planar pore-types).

Low field NMR measurements have been done on all the plugs using a Maran-Ultra spectrometer at 2 MHz (Oxford Instruments Ltd.) to investigate water content, its relation with pore size and mobility as well as deriving permeability from empirical equations. Before NMR measurements, the dry samples were brine saturated under vacuum for 24-48 hours followed by 7 MPa hydrostatic pressure brine injection using dedicated cells connected to a Teledyne syringe pump. The injection was stopped when

the pump did not inject anymore brine volume over a period of 4 to 6 hours. The period of time necessary for such saturation was usually about 1 to 2 week(s). The difference in mass between the dry and brine-saturated plugs was used to calculate the equivalent water-saturated porosity (so-called Water Imbibition Porosity or WIP) and was then compared to the nitrogen gas porosity results to check for full saturation (i.e. both methods should return the same values, ideally). A saturated sample was then wrapped in cling film to avoid water evaporation, placed in a plastic vial and tested in the NMR spectrometer using the Carr–Purcell–Meiboom–Gill (CPMG) pulse sequence. This spin-echo method measures the water content and so the equivalent water-filled porosity. The NMR porosity can be calculated from the total NMR amplitude calibrated against the NMR amplitude of a known brine volume (“NMR porosity by amplitude”). The NMR porosity can also be calculated by integration of the T_2 distribution curve computed by Laplace inversion (“NMR porosity by inversion”). The equivalent pore body size distribution is obtained using the distribution of transverse magnetic relaxation time (T_2) similarly to pore throat size distribution acquired from the mercury porosimetry method. The principle and details of this analysis are described elsewhere (Jorand et al., 2011; Kleinberg et al., 2003a; Kleinberg et al., 2003b); The experimental protocol used here ensures a resolution of pore body size > 10 nm from the T_2 values as indicated by Dunn et al. (2002).

Finally, NMR acquisition does not provide a direct measurement of permeability, an estimate can however be calculated from the T_2 distribution spectrum using a permeability model based on a combination of empirical and theoretical relationships. The permeability was deduced herein by following the free fluid model of Coates, a variation of the Timur equation, in which the irreducible water saturation S_{wirr} has been replaced by the Bulk Volume of Immobile fluid (BVI) and the Free Fluid Index (FFI) representing the volumes of immobile (clay bound water and capillary bound water; or strongly and weakly bound water) and movable water respectively (Timur, 1968; Coates et al., 1991; Coates et al., 1998):

$$k_{Coates} = \left[\left(\frac{\phi}{C} \right)^2 \left(\frac{FFI}{BVI} \right) \right]^2 \quad \text{Eq. 5}$$

Where ϕ is the total porosity (%), and C is a constant normally used to adjust the NMR logs. C is initially set at 10 following the literature data on sandstones (Jorand, 2011) but the appropriate C can be back computed knowing the permeability from the gas method by using Eq. 5. This new more appropriate C parameter can then be used on NMR logs to accurately compute permeability using Coates model across the reservoir. Note that NMR permeability modelling would be more appropriate to fit with brine permeability measurements. However, NMR was measured under no confining stress while brine permeability was acquired under pressure. We know from stress dependency of gas porosity-permeability experiments (see section 3 – gas porosity-permeability and density results) that Harvey samples are quite sensitive and permeability can be extrapolated to no confining pressure. Therefore, to be more consistent with the room conditions, we preferred to fit NMR permeability modelling with gas permeability dataset. It is also worth to note that gas permeability was Klinkenberg corrected which should give similar permeability to brine permeability. Eq. 5 implies the knowledge of the T_2 cut-off, which separates the capillary and clay-bound water (BVI), residing in small pores and clay layers, from the movable water (FFI) residing in large pores and susceptible to flow during well production. Based on the literature, the classical T_2 cut-off is set at 33 ms (milliseconds) for sandstone reservoirs (Coates et al., 1998). This NMR cut-off was successfully used in sandstone reservoirs of the

Gulf of Mexico (Hurlimann et al., 2003; Daigle and Dugan, 2009) though it can be severely affected by lithology variations, fluid chemistry, pore geometry, and occurrence of paramagnetic and/or ferromagnetic minerals (smectite and magnetite for instance). C factor can be accurately defined and constrained by facies if permeability values from standard methods such as nitrogen injection are used conjointly with NMR.

In any case, the free fluid model is a matrix model that will under-estimate the permeability in fractured formations or under stress regimes. They assume that a good correlation exists between porosity, pore-body and pore-throat size, and pore connectivity. This assumption is generally valid in clastic sequences (sand/shaly-sand).

Electrical Resistivity Spectroscopy

Low frequency electrical resistivity

Electrical resistivity consists of recording the strength of a solid material or fluid to oppose the flow of an electric current. Such a property is dependent on the electrical charges available in the tested material and most of all their mobility through the material. A high resistivity indicates that (i) little charge is available to flow such as in a dry porous rock or in a very fresh (no ions available) water saturated rock, or (ii) the available charge cannot easily migrate from point A to B within a material. This is the case in a tight, water saturated porous rock where most of the pores are not well connected to let the charge migrate from one pore to another within a conductive pore fluid. Under an alternate current (AC), the resistivity becomes *complex* and is expressed by an amplitude and phase angle that defines the impedance. In this study, Electrical Impedance Spectroscopy (EIS) was used to perform the monitoring. This technique is based on recording the current through a pair of electrodes when a sinusoidal potential propagates within a material where the applied potential is:

$$E = \Delta E \sin \omega t \quad \text{Eq. 6}$$

where ΔE is the amplitude of the AC signal, ω the frequency of the AC signal and t is the duration of the acquisition.

The current through the electrode corresponds to:

$$i = \Delta i \sin (\omega t + \phi) \quad \text{Eq. 7}$$

where Δi is the amplitude of the current and ϕ is the phase angle.

The impedance can then be simplified as:

$$|Z| = \sqrt{(Z')^2 + (Z'')^2} \quad \text{Eq. 8}$$

Where Z is for impedance (in ohm.m), Z' and Z'' are the real and imaginary components of the impedance, respectively. The real component (i.e. in-phase, energy loss) corresponds to the ohmic conduction. The imaginary component (out of phase, energy storage) represents the polarization.

The phase angle (in - degree) of the impedance is described as:

$$\phi = \arctan[(Z''/Z') \cdot 180^\circ/\pi] \quad \text{Eq. 9}$$

The resistivity of the sample is defined as:

$$R = Z \cdot (A/L) \quad \text{Eq. 10}$$

with A/L as the geometric constant of the plug with L being the length and A the cross-sectional area of the plug.

The impedance being dependent on the temperature and brine resistivity, it is therefore crucial to record the temperature within the tested material.

The thermal correction of the equivalent resistivity at 25 °C ($R_{25^\circ\text{C}}$) is a linear variation for relatively low temperature range (< 100°C) and can be simplified for rocks as (Arps's formula, 1953):

$$R_{25^\circ\text{C}} = R_T \cdot (T+21.5)/(25+21.5) \quad \text{Eq. 11}$$

where R_T is the measured resistivity (ohm.m) at the temperature of T (°C).

Using Archie's law (1942), for "clean" porous rocks fully saturated with a fluid, several parameters can be extracted:

$$F = R_o/R_w = \phi^{-m} \quad \text{Eq. 12}$$

where, F is the formation factor that normalizes the resistivity of the sample from the resistivity contribution of the saturating brine; R_o and R_w are the resistivity of the fluid saturated sample and the resistivity of the fluid respectively; ϕ is the fractional porosity of the sample and m is the Archie cementation exponent (unitless and >1).

Usually m increases when the pore connectivity becomes more complex for the electrical current to easily flow. The concept of tortuosity (τ , unitless; see Clennell, 1997 for more details) can underline this aspect and can be defined as:

$$\tau = F \cdot \phi \quad \text{Eq. 13}$$

Electrical Impedance Spectroscopy

In two electrode configuration (capacitor principle), two flat silver electrodes are put in contact on opposite parallel faces of the plug. Both electrodes inject a voltage and measure the current. Because the sample-electrodes system is not under stress or in a confined environment, the electrode coupling is not optimum and trapped air bubbles can develop at the top of the plug during experiments as the water flows by gravity at the bottom of this very permeable and porous plug. In lab electrical measurements, bubbles of air often occur despite all the care applied in the experimental preparation, and this can significantly affect the electrical reading. In a 4-electrode configuration, additional silver pins between the two previous electrodes, surround the plug to measure the current while the other two electrodes measure a voltage only (Garrouch and Sharma 1992). The four electrode spacing is 25 mm.

Both 2- and 4-electrode systems have their own advantages and disadvantages: the 2-electrode system tends to over-estimate the impedance because of potential high contact resistance at the sample-electrode interface and because of the electrode polarization (ionic charge accumulation from the pore fluid at the electrodes; Johnson and Cole 1951) occurring particularly toward very low frequency (< 10 Hz). A proper sample-electrode coupling and working at relatively high frequency should limit these artefacts on the impedance measurement. With a 4-electrode system in highly

conductive saturated rocks, the electrodes are free from polarization effects. However poor ring contact can generate high resistance, leading to potential over-estimation of electrical impedance. A combination of 2- and 4-electrode methods, when possible, is always preferable to check if unexpected artefacts occur as a means of quality control.

The electrodes were used in a potentiostat condition where a voltage of 100 mV is applied and the current measured. An Autolab electrochemical spectroscopy apparatus from Ecochemie Ltd. was used as an AC-impedance bridge (Bona et al., 2008) to perform electrical impedance spectroscopy at low frequency range (< 1 MHz). The electrical impedance and phase spectrum (real and imaginary part of the impedance (Kahraman and Alber, 2006) were recorded along 31 logarithmically distributed points between 10 Hz and 10 kHz. Frequency dependency of the electrical impedance response of H3-Plug2 was recorded during the experiment under 2- and 4-electrode configurations.

The impedance measurements were then used to compute the Archie formation factor (F), Archie m exponent and the tortuosity. The Archie formation factor (F) requires knowledge of the brine resistivity, which is directly related to the brine salinity and was recorded with a portable Orion conductivity Ltd meter 4-contacts system, calibrated against standard solutions and temperature corrected at 25°C. The brine conductivity used in this experiment was 48.44 mS/cm, which corresponds to a resistivity of about 0.2 ohm.m.

For the plugs from wells Harvey-3 and Harvey-4, benchtop electrical resistivity measurements were performed on the short plugs with 2 electrodes and for the long plugs with both 2 and 4 electrodes when possible.

One main purpose of this exercise is to provide reliable parameters as much as possible close from the in-situ reservoir conditions to compute Archie's saturation from electrical resistivity logs and predict evolution of the Archie's pore connectivity during CO₂ injection. Therefore, extracting the initial resistivity and m Archie's exponent is crucial. Knowing the evolution of these parameters after the flooding experiments should also help and guide modellers when using the electrical logs to monitor reservoir tortuosity and pore structure evolution during CO₂ storage over time.

Ultrasonic Velocities

Elastic wave velocities correspond to the speed of a mechanical vibration (equivalent to seismic wave) travelling through a continuum material (i.e. gas, liquid or solid). This elastic wave does not induce mechanical damage or deformation to the material, and is often described by two types of waves through materials: (i) Primary wave (P-wave or V_p) that corresponds to highest velocity and the first to be recorded by wave detectors. It is defined as a pressure wave due to an alternating compressions-extensions mechanism; (ii) secondary wave (S-wave or V_s) describes the shear or transverse wave mechanism through solid materials and arrives after the P-wave. Its motion is normal to the direction of the wave propagation and can only propagate through solid materials. These two elastic waves can help to compute several parameters such as Poisson's ratio, bulk, shear and Young's moduli defined as:

Poisson's ratio (dimensionless) defines the change of an elastic material's volume when submitted to an uniaxial compression. It usually expands or contracts in the transverse directions to the direction of compression depending on the material's properties:

$$v = (V_P^2 - 2V_S^2) / (2V_P^2 - V_S^2) \quad \text{Eq. 14}$$

Bulk modulus (or modulus of incompressibility) defines the resistance to uniform compression:

$$K = \rho \cdot (V_P^2 - (4/3) \cdot (V_S^2)) / 10^9 \quad \text{Eq. 15}$$

with K in GPa, ρ (bulk density) in kg/m³, V_P and V_S in m/s. V_P is usually around 6000 m/s in limestone and decreases as pores and/or mechanical damage increases.

Shear modulus (or modulus of rigidity) measures the resistance of a material to shear stress:

$$\mu \text{ or } G = \rho \cdot V_S^2 / 10^9 \quad \text{Eq. 16}$$

where μ or G is in GPa.

Young's modulus describes the resistance of a material to uniaxial stress:

$$E = 2\rho \cdot V_S^2 \cdot (1 + v) / 10^9 \quad \text{Eq. 17}$$

where E is in GPa.

These two rock physical properties (V_P and V_S) are commonly used in rock characterization as they are determined using non-destructive methods (Archie, 1942; Barbera et al., 2012; Christaras, 2003; Kahraman and Alber, 2006; Martinez-Martinez et al., 2011; Shevnin et al., 2007). Electrical resistivity and ultrasonic wave velocities depend on petrophysical parameters of the rock such as grain size, porosity, pore connectivity, pore-fluid saturation, pressure and temperature (Winkler, 1997; Kahraman and Alber, 2006; Shevnin et al., 2007). Some published works started to use DC electrical resistivity to detect cracks and salt precipitation in some concrete structures (Chouteau and Beaulieu, 2002; Lataste et al., 2003). The elastic properties are notable for evaluating the changes in rock stiffness and grain contacts/cracks and/or discontinuities (Guéguen and Palciauskas, 1992), which should be an excellent tool for comparing the plugs before and after flooding experiments.

Simultaneous Electrical and Acoustic Acquisition

Temperature monitoring

Temperature monitoring was used during all the experiments to correct the resistivity for any variation in the temperatures in the rig. The temperature of the samples was measured via a temperature differential probe, with an accuracy of ± 0.1 °C (manufacture accuracy), fixed against the electro-acoustic rig body. The temperature was recorded every 60 seconds to coincide with electrical impedance spectroscopy measurements.

Electrical impedance spectroscopy (EIS) and time scan

Frequency dependency of the electrical impedance response of the plugs was recorded during experiments under 2- and 4-electrode configuration as well as continuous electrical impedance over time at 1 kHz (similar to electrical logging tool frequency) using 2- or 4-electrode contact mode.

In the 2-electrode configuration (capacitor principle), two flat silver electrodes are put in contact on opposite parallel faces of the plug. Both electrodes apply a voltage and measure the current. All the system and core plug are quickly vacuumed and then flushed with brine to enhance sample-electrode coupling and remove any trapped air bubble. In the laboratory electrical measurements, bubbles of

air often occur despite all the care taken with the experimental setting. This would affect the electrical readings considerably. In 4-electrode configuration, two additional silver radial rings between the two previous electrodes surround the plug to measure the current while the other two electrodes measure a voltage only (Garrouch and Sharma 1992). A small pore pressure (P_p) of 10-20 psi is applied by the pump, while a higher radial confining pressure is applied (10 to 2000 psi).

The electrodes were used in a potentiostat condition where a voltage of 100 mV is applied and the current measured as explained earlier. The Autolab electrochemical spectroscopy apparatus from Ecochemie Ltd. was used as an AC-impedance bridge to perform: (i) electrical impedance spectroscopy at low frequency range (< 1 MHz) and (ii) impedance scan at 1 kHz (time scan) recorded every 60 seconds, over the duration of the experiment, applying increasing stages of confining pressure up to a maximum of 2000 psi. The electrical impedance and phase spectrum (real and imaginary part of the impedance) were recorded along 21 logarithmically distributed points between 10 Hz and 10 kHz.

Ultrasonic P- and S-wave velocities

Elastic properties from ultrasonic velocity measurements in rocks were recorded following the pulse transmission technique (Birch, 1960). This was conducted using two transducers, integrating two piezoelectric crystals each, within the silver platen used for EIS acquisition: one crystal able to generate/receive P-waves and the second one able to generate/receive S-waves. These transducers were applied against the end-plug surface in opposite directions (axial direction measurement). The method consists of measuring the travel time of an elastic pulse through a plug of known path length between the two opposite transducers. The nominal excitation frequency was set at 0.5 MHz for P- and S- waves. The ultrasonic propagation system consists of a pulser-receiver and a digital oscilloscope recording the signals which are then transferred to a computer. Arrival times were manually picked from the digitized waveforms, each trace consisting of 5000 points over a time range of 1×10^{-4} seconds. The uncertainty in the determination of the P-wave velocity is about 2 % ($\pm 0.1 \mu\text{s}$), up to 10 % ($\pm 0.2 \mu\text{s}$) for the S-wave velocity when its arrival is not obscured by the precursory P-waves (Sarout and Gueguen 2008). Ultrasonic velocities were acquired at each confining pressure stage from 0 to 2000 psi after the electrical resistivity stabilized.

Mercury Porosimetry

For evaluation of pore size distribution of the samples tested, in a previous study (Delle Piane et al., 2013) quarter inch offcuts of the core plugs from Harvey-1 only were provided to Geotechnical Services by GSWA for mercury injection capillary pressure measurements. The samples were tested in a Micrometrics Autopore IV porosimeter by injecting mercury at increasing capillary pressure steps up to a maximum pressure of 413 MPa.

Measurement Results

Medical CT images

Figures 8 to 16 summarize the XCT images obtained under dry conditions for the pre- and post-flood plugs from the three Harvey wells investigated.

The blue/red images in Harvey-1 images are just a special colour table (Stern CLUT) applied on the grey scale images to enhance weak or low density areas (red colours) or pores/voids (black colours). The bedding is quite visible along the core axis for the H1-Plug1 and H1-Plug2 while the same bedding orientation is less obvious in H1-Plug3 and H1-Plug4 despite an attempt made to enhance the contrast of the images. The H1-Plugs3 and H1-Plug4 are also clearly denser than the other two plugs from this well: more dark blue colours. A much higher contrast/brightness window was necessary on these denser plugs to highlight their internal structures. However, after post-processing the \pm dense elements of the plugs in 3D, the bedding is then visible with a bedding oriented along the core axis on all the plugs (Figure 10), though the bedding is quite inclined in Plug 1. The comparison before and after flooding of the exact same view and orientation of the plugs shows some subtle variations for plugs 1 and 2 while no variations are visible in plugs 3 and 4. The initial big pores that were slightly filled by fine particles (dark greyish colours) are then fully black and washed-out after flooding experiment. Such wash-out is particularly obvious in plug 2 (plug segments A&B).

For the Harvey-3 samples, no strong visual differences could be observed between the two sets of images (Figures 10 and 11). It is worth noting that there is less contrast in the images from the post-flood plugs as these plugs were scanned under saturated conditions while the pre-flood plugs were scanned in dry condition. The visual representation of pores in 3D is also presented in "red colour" in Figures 10 and 11 after the segmentation method. The bedding planes can be easily observed which are slightly inclined along the plug axis as some layers have much less pores than others. Possible changes to the pores after flooding are not obvious at this image resolution.

For the Harvey-4 samples, in general, it is obvious that plugs 3 and 4 are much tighter than plugs 1 and 2: the open porosity is not visible in the transversal and longitudinal XCT images, and the reconstructed 3D volumes of the pores barely detect any pores with a size $> 100 \mu\text{m}$. No strong visual differences could be seen between the before and after flooding images at this image resolution.

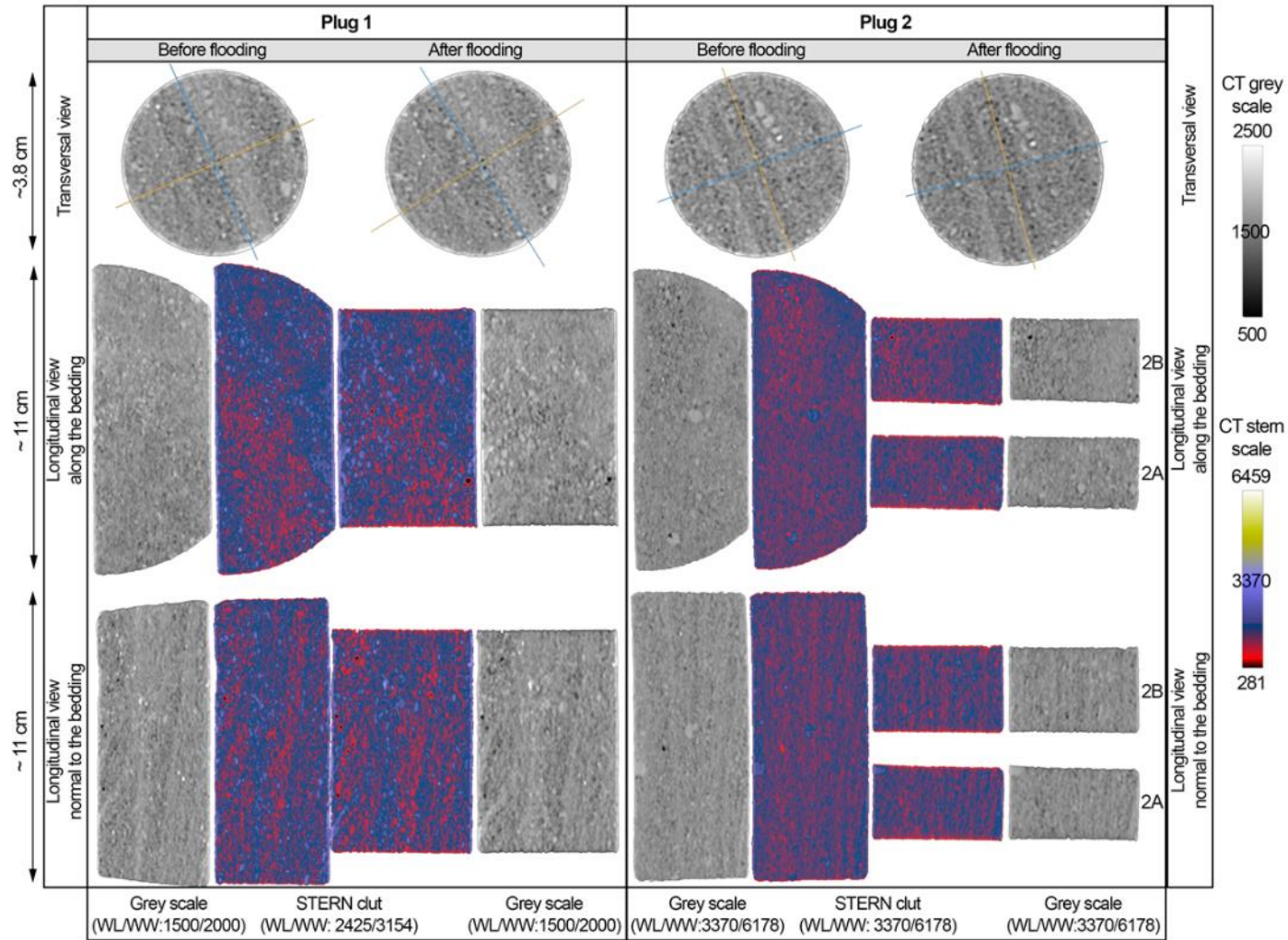


Figure 8. Visual display of the medical CT images before and after flooding (salt cleaned) under dry conditions for the Harvey-1 plugs 1 and 2. The top images represent a transversal image of the plug in its middle part; the middle images are longitudinal XY plane and the bottom images are longitudinal YZ plan along the core axis. The grey and stern CLUTS along with their corresponding CT scale are presented.

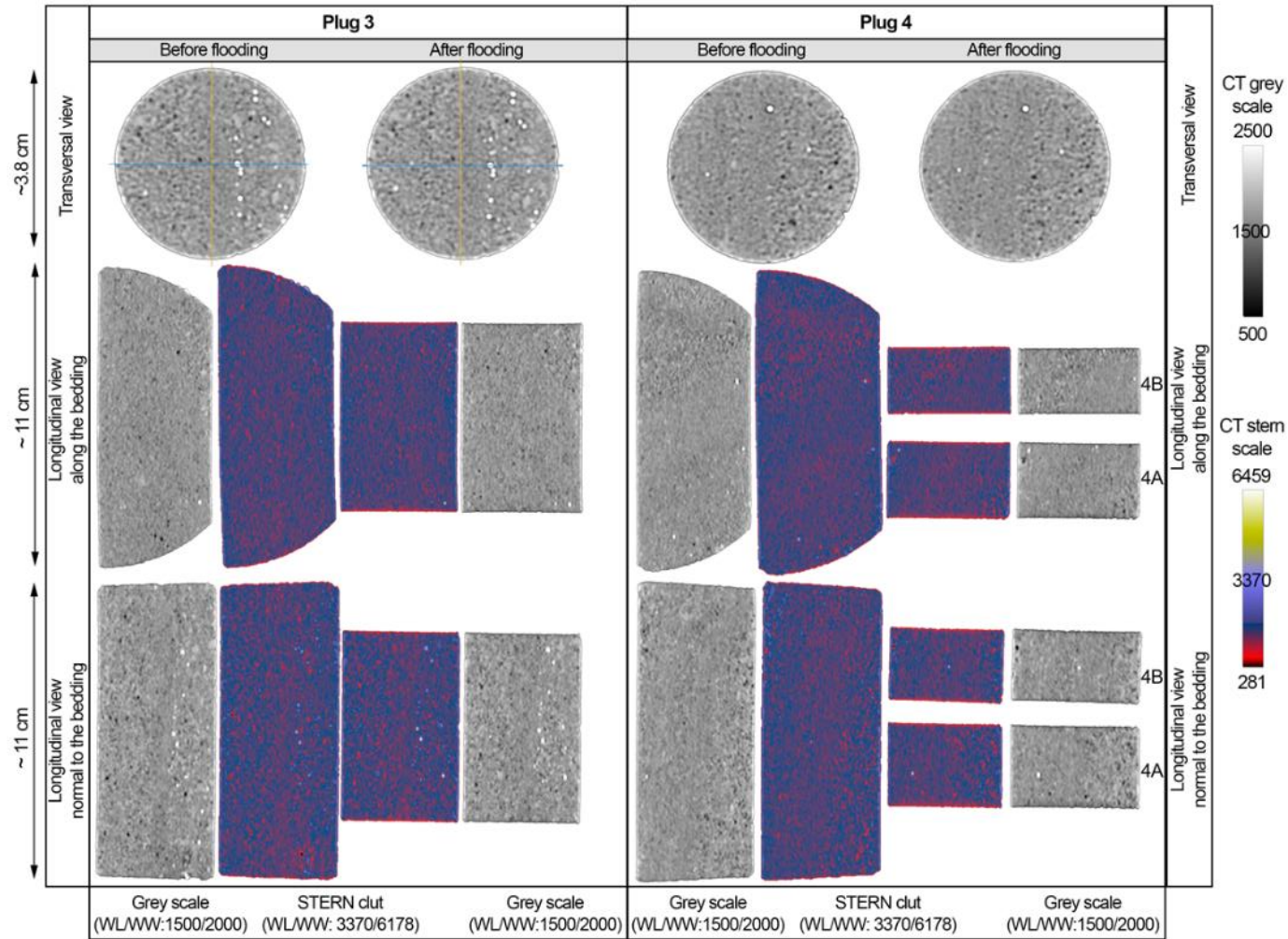


Figure 9. Visual display of the medical CT images before and after flooding (salt cleaned) under dry conditions for the Harvey-1 plugs 3 and 4. The top images represent a transversal image of the plug in its middle part; the middle images are longitudinal XY plan and the bottom images are longitudinal YZ plan along the core axis. The grey and stern CLUTS along with their corresponding CT scale are presented.

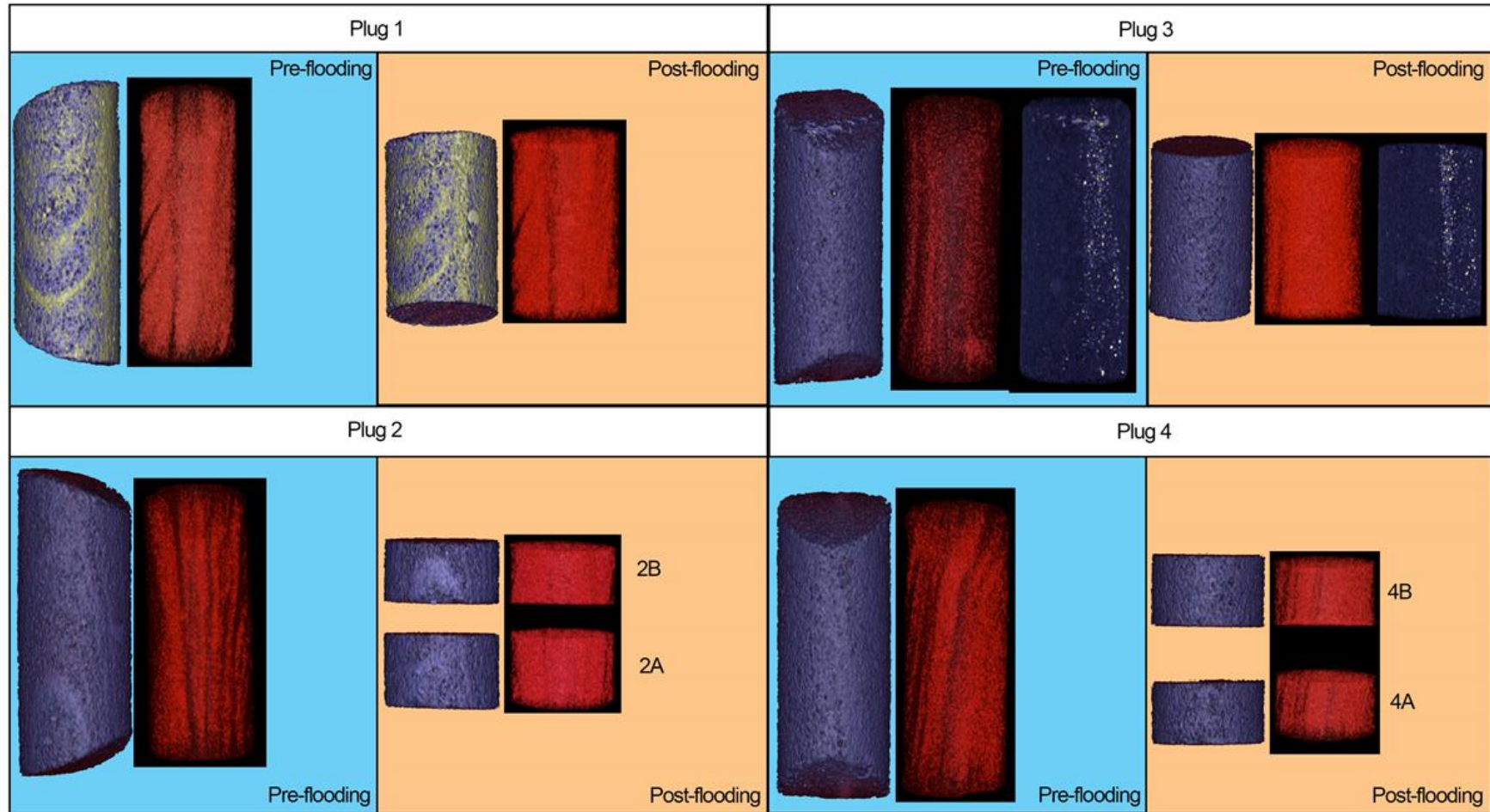


Figure 10. 3D snapshot views from medical x-ray CT image processing on all the plugs from Harvey-1 before (blue background) and after flooding (orange background). The left images represent a surface rendering of the full plug using a STERN CLUT to highlight the bedding and visible macro-pores. The red images are 3D view of low density materials with CT < 1400; therefore, anything black in such images represent denser layers. A third type of 3D image was added in Plug 3 as a flat layer full of pyrite along the core axis was detected. The white/yellow dots represent pyrite visually enhanced by using a stern CLUT. Note how the bedding is oriented in all the plugs: along the core axis. Plug 1 also integrates a specific layer with inclined bedding.

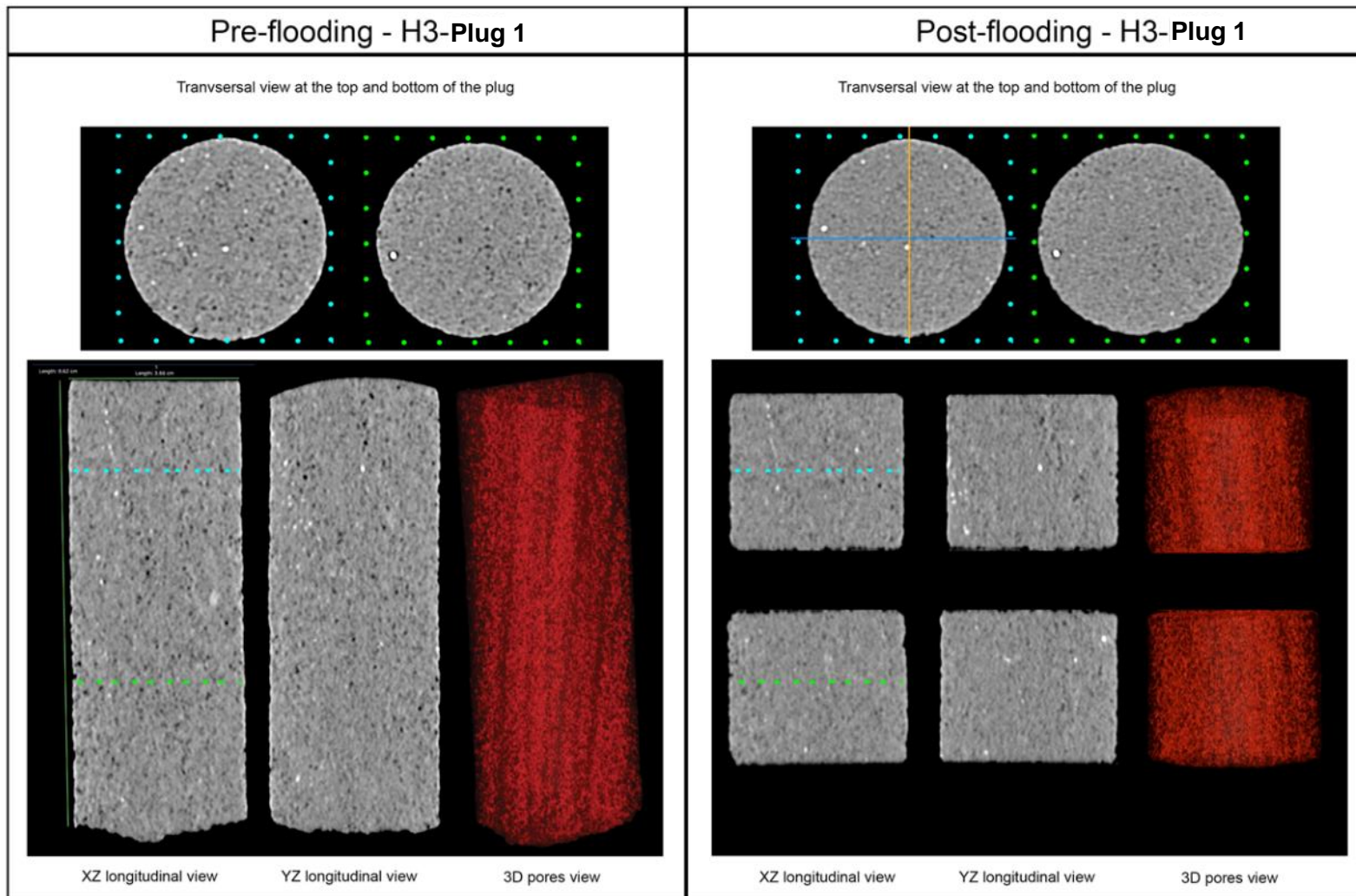


Figure 11. Transversal and longitudinal medical X-ray CT images for pre- and post-flood Harvey-3 plug 1. The visual representation of the pores in 3D after segmentation for the whole plug is also presented with pores coloured in red.

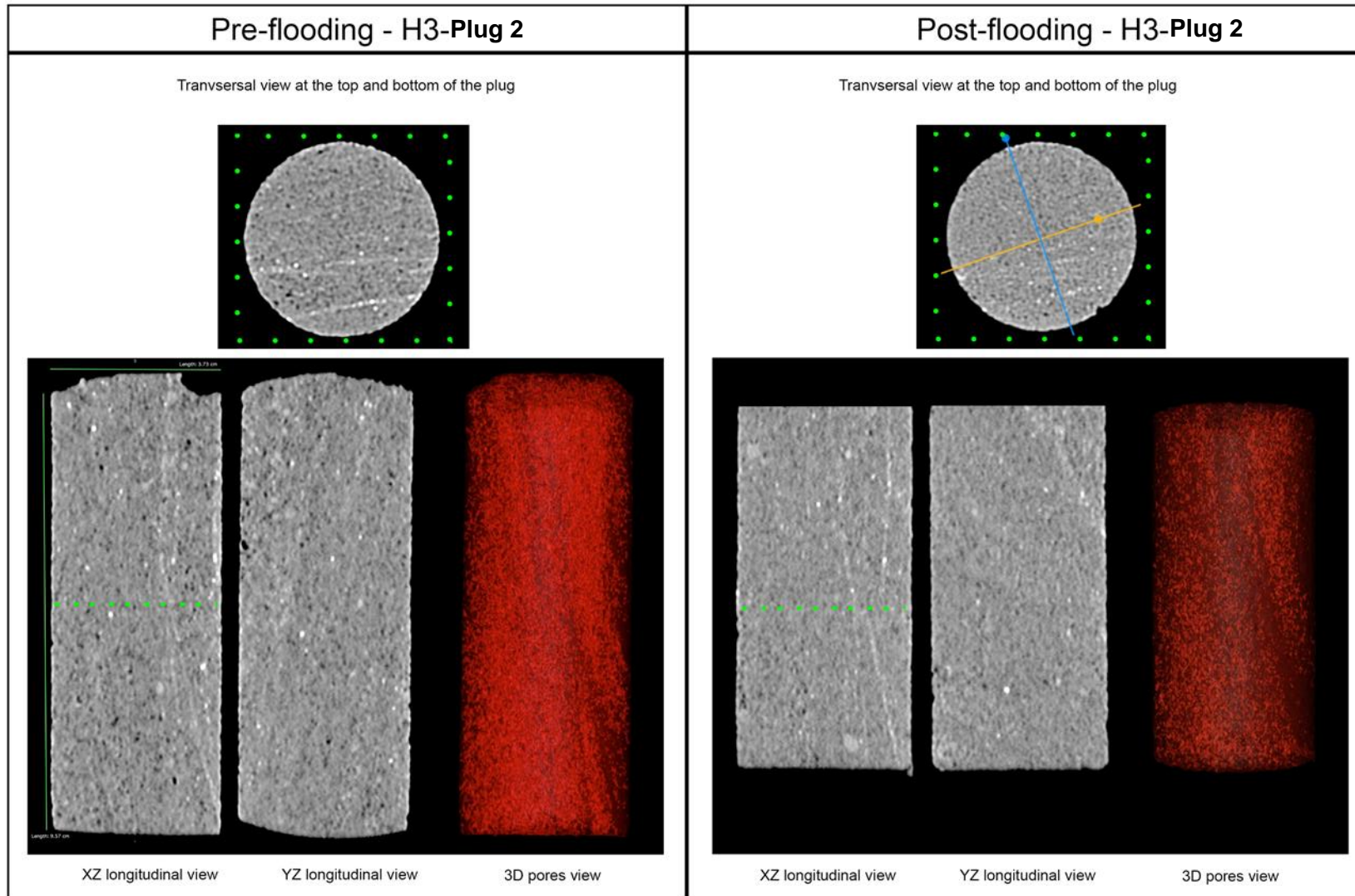


Figure 12. Transversal and longitudinal medical X-ray CT images for pre- and post-flood Harvey-3 plug 2. The visual representation of the pores in 3D after segmentation for the whole plug is also presented with pores coloured in red.

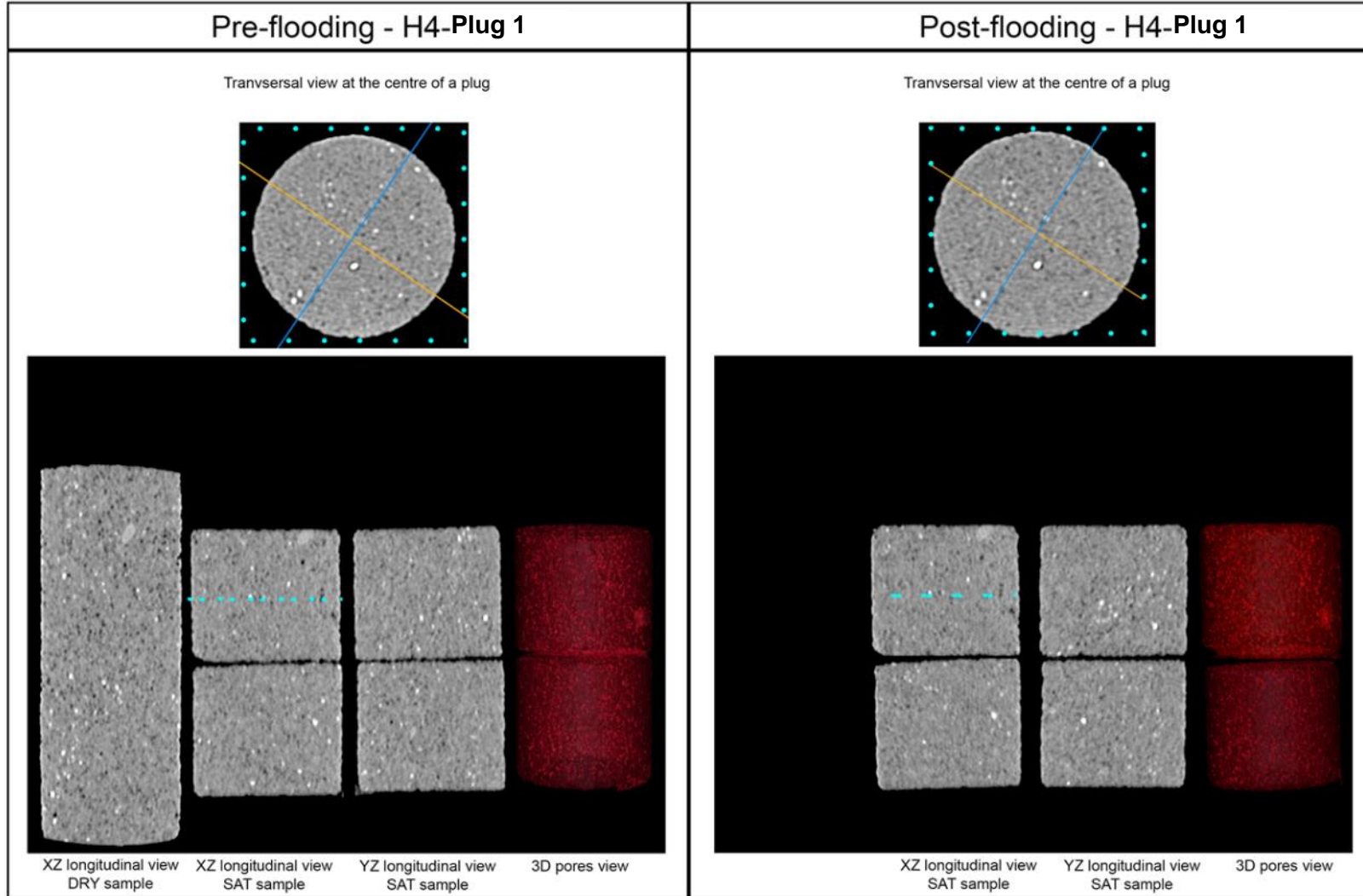


Figure 13. Transversal and longitudinal medical X-ray CT images on pre- and post-flood Harvey 4 plug 1. The visual representation of the pores in 3D after segmentation for the whole plug is also presented with pores shown in red.

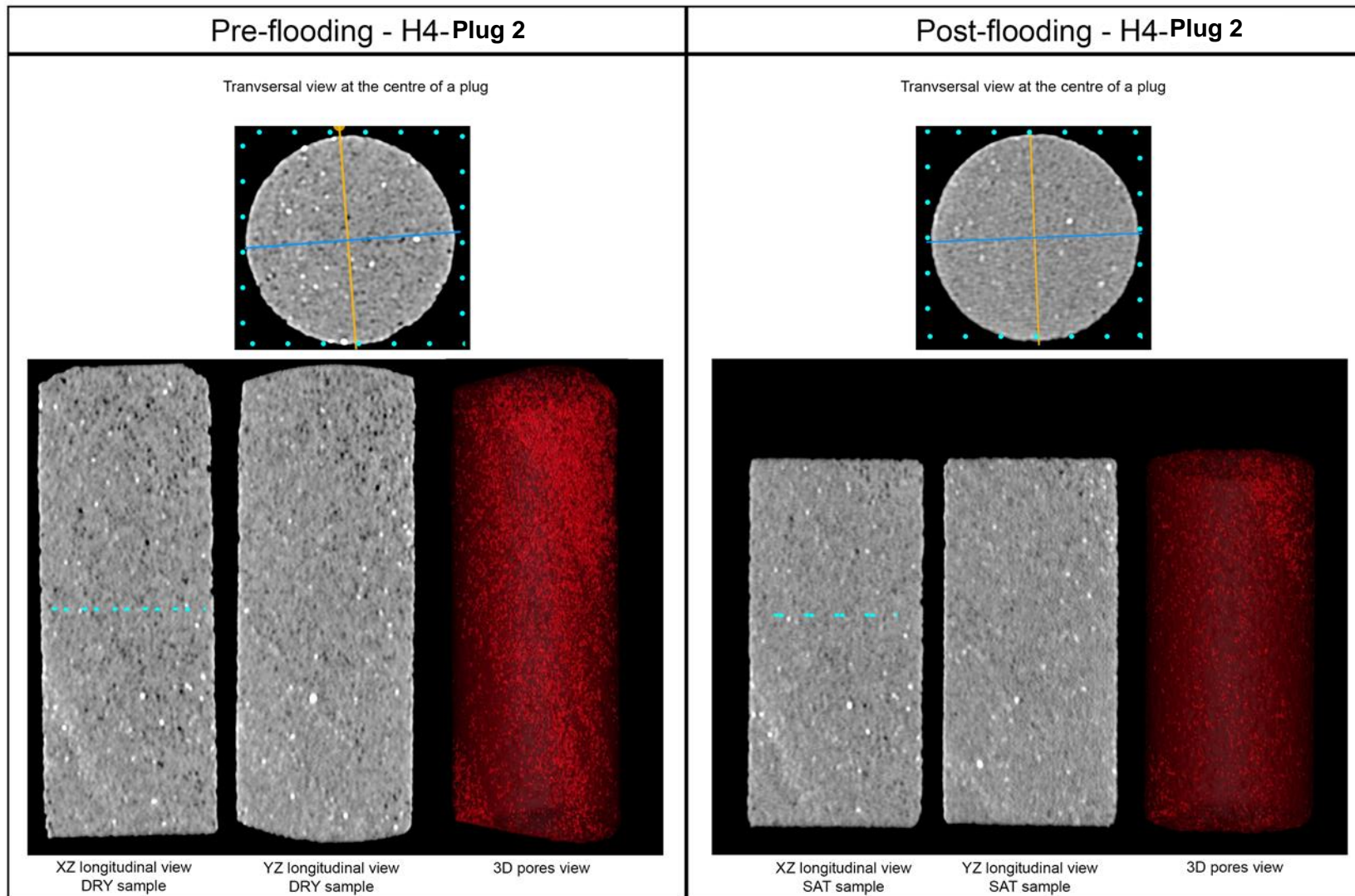


Figure 14. Transversal and longitudinal medical X-ray CT images for pre- and post-flood Harvey-4 plug 2. The visual representation of the pores in 3D after segmentation for the whole plug is also presented with pores coloured in red.

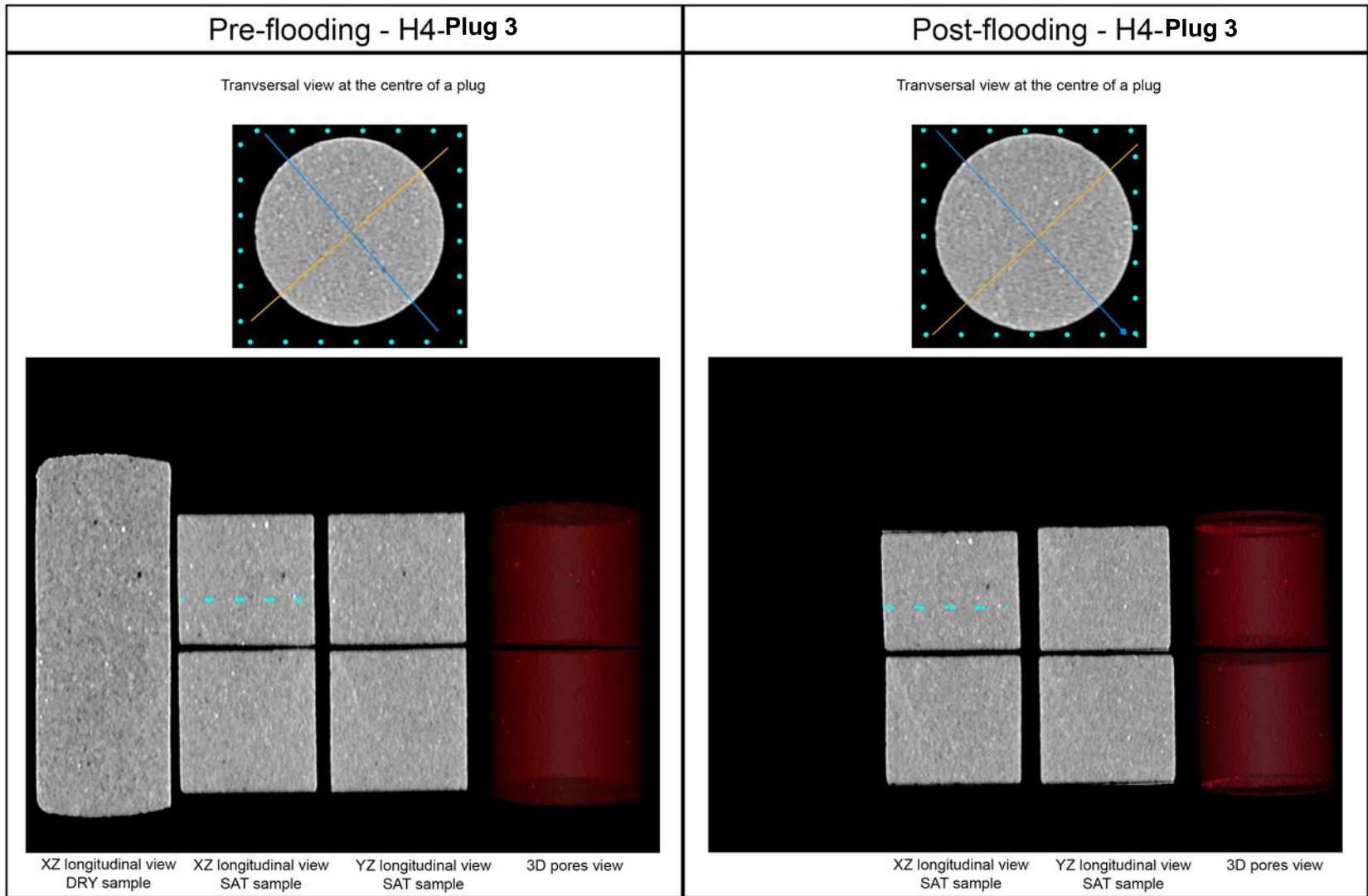


Figure 15. Transversal and longitudinal medical X-ray CT images for pre- and post-flood Harvey-4 plug 3. The visual representation of the pores in 3D after segmentation for the whole plug is also presented with pores coloured in red.

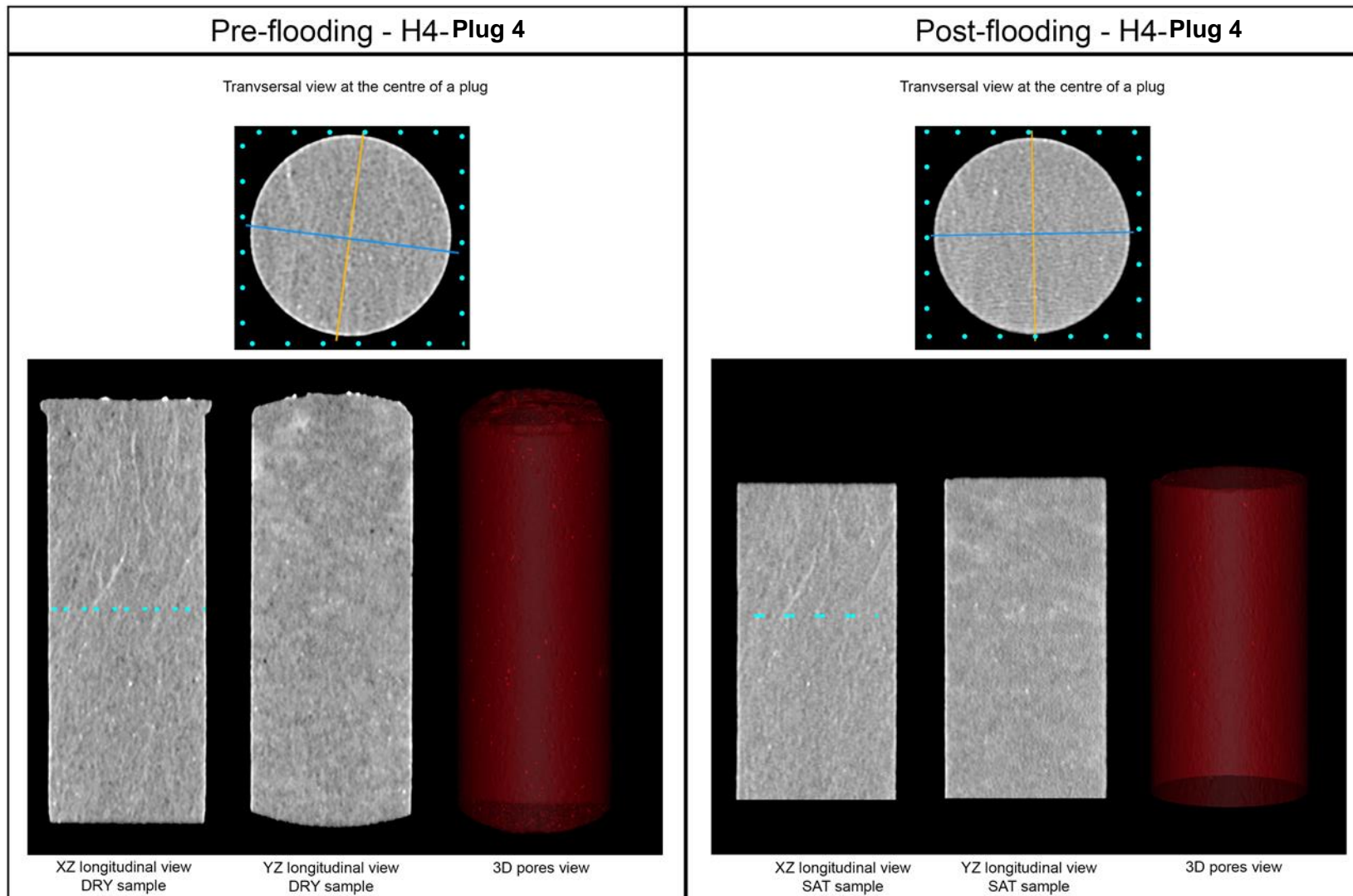


Figure 16. Transversal and longitudinal medical X-ray CT images for pre- and post-flood Harvey-4 plug 4. The visual representation of the pores in 3D after segmentation for the whole plug is also presented with pores coloured in red.

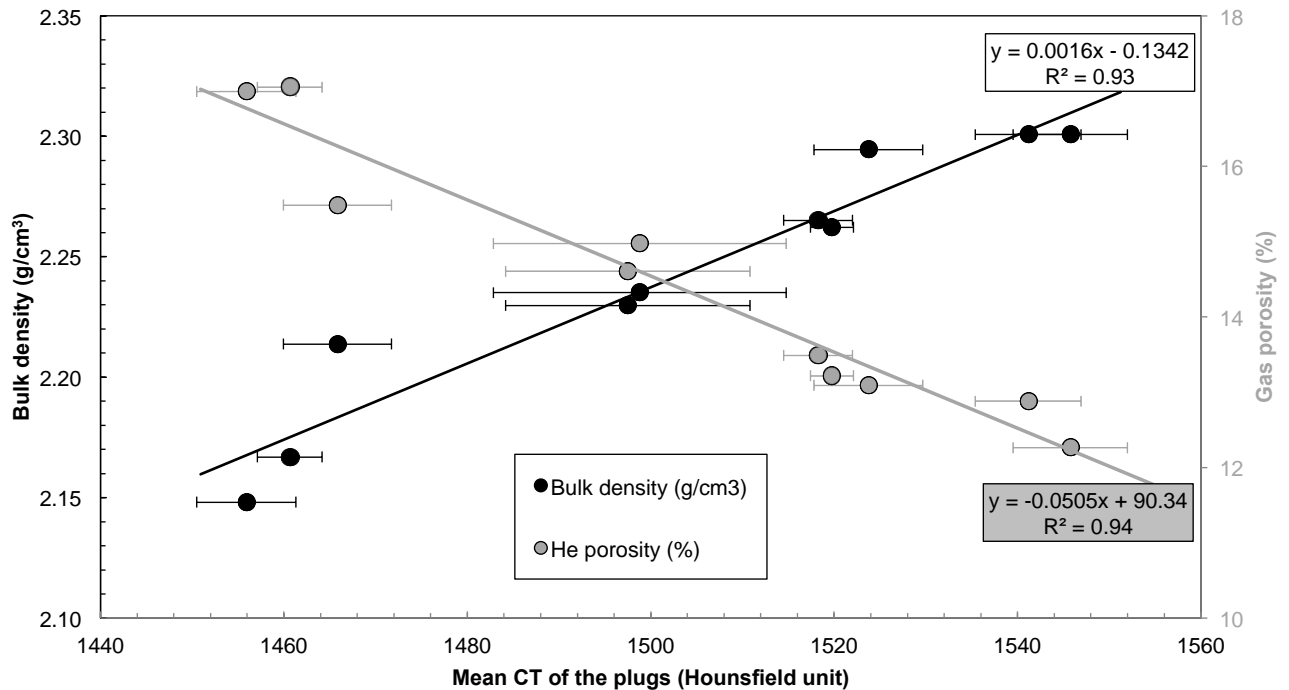


Figure 17. X-ray CT calibration for bulk density and porosity using the mean CT computed from all the transversal XCT images (with their standard deviation error bars), the dry bulk density from Harvey-1 plugs and the helium gas porosity extrapolated at 0 psi confining pressure. The data fitting can be used to convert the CT profile along the core axis into bulk density and porosity profile.

Using the bulk density and gas porosity measured on the plugs and the average from the mean CT calculated on each transversal XCT image, a calibration can be proposed to convert any CT values into bulk density or porosity similar to the following equations derived for Harvey-1 samples:

- (1) Bulk density = $(0.0016 \times \text{CT}) - 0.1342$
- (2) Porosity = $(-0.0505 \times \text{CT}) + 90.34$

It is worth noting that that porosity can be derived from two approaches:

- (1) Direct calibration of the CT values to other laboratory measurements of porosity conducted on the tested samples, similar to what has been achieved in the 2nd equation just above.
- (2) Calibration of the CT values to bulk density values obtained from other laboratory measurements conducted on the tested samples, similar to what has been achieved in the 1st equation above for Harvey-1 samples. Then, an assumption on grain density must be applied to compute total porosity using Eq. 4. The commonly used sandstone grain density of 2.65 g/cc is a good assumption for the Harvey samples.

Using these calibration equations, the mean CT profiles along each core axis can be converted into bulk density profile and porosity profile. For Harvey-1, plugs 2, 3 and 4 show a quite remarkable constant CT value along the core axis while plug 1 shows two distinct parts of contrasting but constant CT values (Figure 18). After the flooding experiment, plug 1 (bottom part where the highest CT values are recorded) and the plug segment 2A in particular (in contact with the flooding inlet) show decrease in CT values: more pores and/or less dense materials. The H1-Plugs 3 and 4 do not show particular

change after flooding, though plug segment 4A shows slightly lower CT values than its initial state before flooding (Figure 18).

With regards to the sample from Harvey-3, the XCT processing was slightly deepened to extract the mean pore size with more statistics around using pore segmentation on top of the profiles of density-porosity analysis. On both H3-Plugs 5 and 6, the porosity profiles follow the same pattern before and after the flooding experiment (Figure 19). However, the post-flood profiles are shifted toward higher values with the exception of the post-flood plug segment 1A where the CT mean approach was used and shows lower values than its pre-flood condition. Knowing the porosity from the gas method, it looks like the segmentation approach also gives close results to the real measured independent porosity (see upcoming part of the report). It is worth noting that the CT mean approach for porosity profile employs direct porosity measurement conducted on a core plug (calibration on page 38). Therefore, such profile is highly averaged and less sensitive to local variations. While the porosity profile from pore segmentation is very sensitive the local variations but only see part of the porosity with pore sizes > 100 μm .

Assuming that the segmentation method is reliable, the "macro-porosity" can then be statistically analysed to offer a better insight into the pores themselves (Table 3). For instance, the amount of pores per cubic centimetre has increased for all post-flood samples. All tested plugs from Harvey-3 start with similar amounts of pores at around 500 pores/cm³. This has increased to around 580 pores/cm³ in the post-flood samples. This aspect is therefore reflected in the porosity shifting from around 18-19 % to 21 %. However, the mean pore body size remains the same between the pre- and post-flood samples at around 0.5 mm and are slightly elongated along the core axis direction with a circularity of about 0.8 (the value 1 being perfectly circular and 0 completely elongated and flattened).

Table 3. Statistical summary of the pore segmentation from XCT images before and after flooding in the Harvey-3 plugs.

Sample	Status Flooding experiment	Amount of pores/cm ³	Total pores area (mm ²)	Average pore body size (mm)	Macro-porosity (%)	Pore circularity
H3-Plug1	Pre-flood	499	110 ± 7.7	0.49 ± 0.04	18.28 ± 1.3	0.82 ± 0.01
H3-Plug1A	Post-flood	571	128 ± 5.4	0.50 ± 0.04	21.10 ± 0.9	0.80 ± 0.01
H3-Plug1B	Post-flood	584	127 ± 5	0.49 ± 0.03	20.88 ± 0.8	0.80 ± 0.01
H3-Plug2	Pre-flood	493	117 ± 9.8	0.62 ± 0.05	19.02 ± 1.6	0.81 ± 0.02
H3-Plug2	Post-flood	583	130 ± 10.3	0.50 ± 0.06	20.95 ± 1.6	0.79 ± 0.02

With regards to the samples tested from well Harvey-4, the computed porosity profiles along the core axis using CT mean and calibrated against the gas porosity are presented in Figure 20. In all the tested plugs before and after flooding, the profile is quite similar along the core axis and follows the same small variations. The standard deviation of such computed porosity is << 1% (Table 4). H4-Plug 2 presents a slight progressive change in the porosity profile along its core axis. Despite small porosity changes, most of the post-flood plugs show slightly higher porosity than before flooding. Only plug segment H4-Plug1B has a lower post-flood value and porosity of plug segment H4-Plug3B is quasi-unchanged.

Table 4. Summary of porosity and standard deviation computed from XCT mean within each plug before and after the flooding experiments on the four plugs from Harvey-4.

Harvey-4	Plugs	1A	1B	2	3A	3B	4
Before flooding	Porosity (%)	20.4	19.6	19.6	16.9	16.9	15.4
	Standard deviation (%)	0.07	0.31	0.31	0.04	0.05	0.06
After flooding	Porosity (%)	21.5	19.5	20.8	17.6	17.1	15.3
	Standard deviation (%)	0.05	0.04	0.18	0.03	0.05	0.05

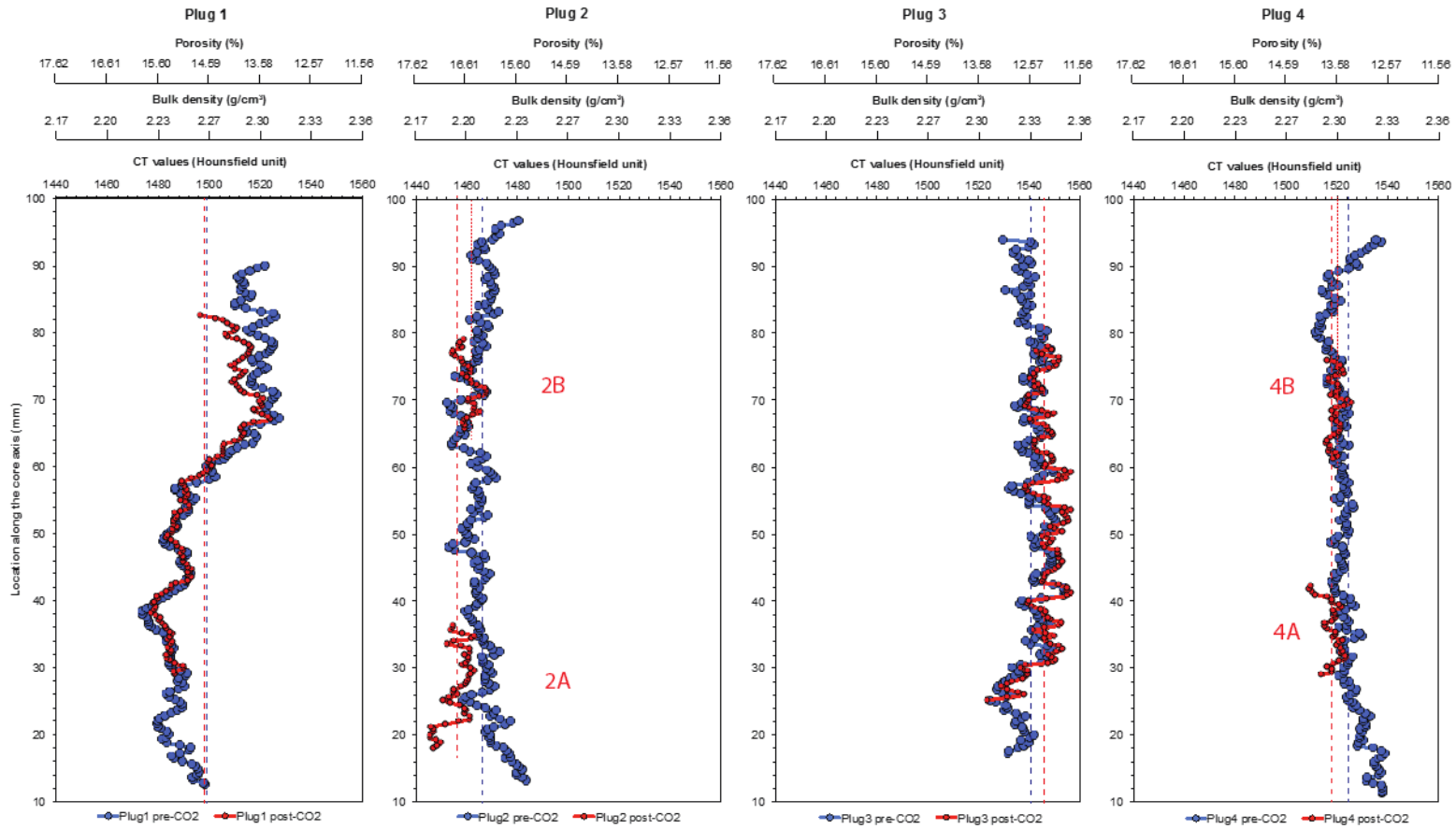


Figure 18. X-ray CT profile along the cores axis for each plug from Harvey-1 before (blue curves) and after flooding (salt cleaned) under dry condition (red curves). The XCT scale was converted into bulk density and porosity using the calibration equations from Figure 17. The blue and red dashed vertical lines mark the mean CT value for each plug before and after flooding, respectively. The red dashed and red dotted vertical lines differentiate plug segments A and B mean CT, respectively. The injection direction is from the bottom to the top of the graph.

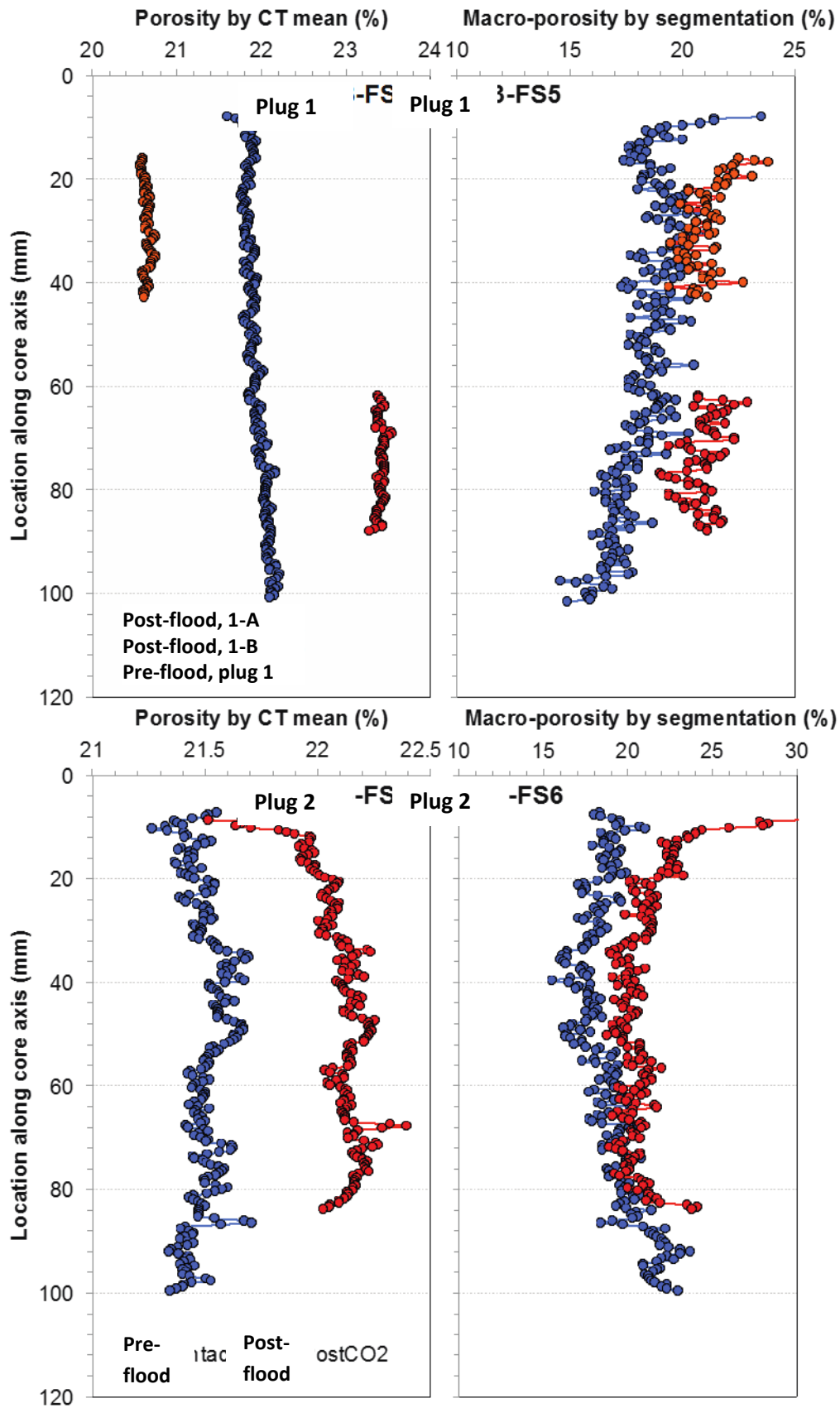


Figure 19. Computed porosity profiles derived from the mean XCT and pore segmentation methods on the XCT images before (blue colors) and after flooding experiment (red & orange colors) on plugs from Harvey-3.

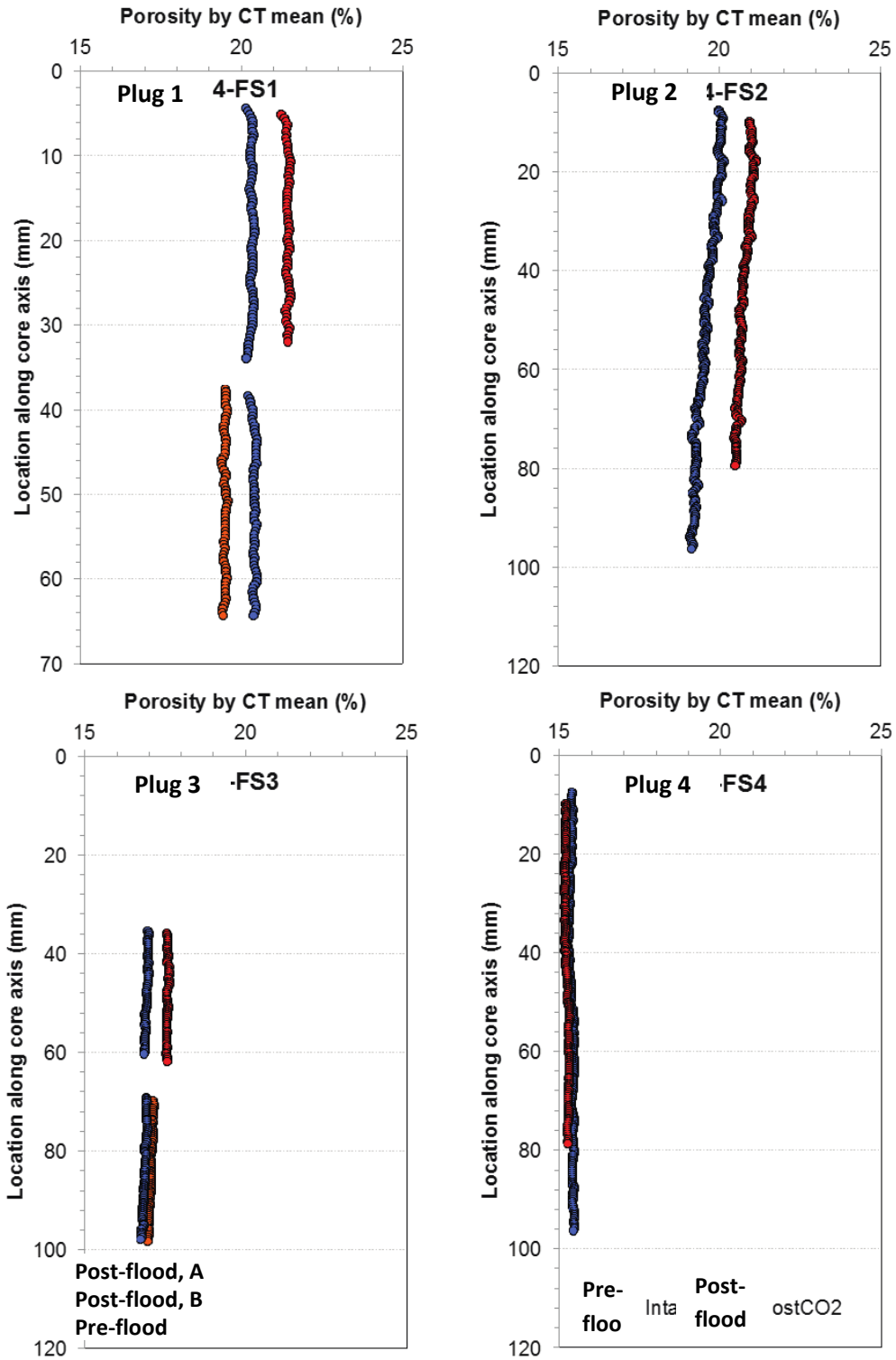


Figure 20. Computed porosity profiles derived from the mean CT within each transversal XCT image before (blue colors) and after (red & orange colors) flooding for all four plugs from Harvey-4.

Gas porosity-permeability and density results

As may be expected and similar to other previously completed work, besides the pore-scale images generated using SEM (will be presented and discussed in Section 4), the comparison of the pre- and

post-flood gas porosity and permeability data are the most revealing when it comes to evaluating the effect of the flooding process on the petrophysical properties of the rock samples tested.

Harvey-1

For the samples tested from Harvey-1, figures 21 and 22 and Table 5 present the results of the porosity and permeability measurements under three or four confining pressures (3.4; 13.8; 24.1 MPa; and up to 31 MPa for plugs 3 and 4) before and after flooding and also after removing the salt from the pore volume of the plugs. The general porosity is higher for plugs 1 and 2 compared with plugs 3 and 4. Using a 2^d order polynomial curve fit, the porosity and permeability can be extrapolated to zero confining pressure with an excellent accuracy (Correlation coefficient: $R^2 > 95$) (Table 6). A porosity of 15 % for plugs 1 and 2 and 12.5% for plugs 3 and 4 are found at zero confining pressure. Using the same technique to extrapolate to zero confining pressure, the permeability is found to be about 95 mD for plugs 3 and 4 while a difference is recorded between plug 1 (40.6 mD) and the plug segments 2A&B (79.1 mD). After flooding, all the samples recorded lower permeability: about half of their original values. The porosity is also slightly lower for all plugs with the exception of plug segments 2A&B now with higher values at 16.5%. It is worth noting that, as can also be seen from Table 5, for the majority of the samples that the salt cleaning process seems to have little effect on the results of the measurements.

Figure 23 presents a comparison of the porosity and permeability stress dependency, at a range of different pressures, between the plugs tested, before and after the flooding. The effect of removing salts on such measurements is also added to this plot (triangle symbols). Most of the samples record similar values, which would support that crystal salts do not affect the transport properties of the plugs. Only plug segments 2A&B, and perhaps 4B, show a clear increase in stress sensitivity for porosity after flooding (Figure 23a). Removing the salts may have slightly enhanced such differences in plug segments 2A&B. The permeability stress sensitivity remains similar before and after flooding with or without salt cleaning (Figure 23b).

For each confining pressure from 0 (extrapolated) to 31 MPa (maximum), the variation in porosity and permeability was computed for each plug between their initial state and after flooding, with and without salts in their pore network. The results are presented as histograms in Figure 24. As can be seen in Figure 24a, the porosity variation slightly increases with stress from about 1 to 10 maximum (Table 7); with positive values when the variation in porosity decreased after flooding and negative values when the variation in porosity increased. The highest variations are recorded in plug segments 2A&B and the lowest values in plug segments 4A&B of the Harvey-1 sample. However, as mentioned in the description of Figure 23, the relative porosity drastically changes with stress in plug segments 2A&B and 4A, even more so after the salt cleaning process. Only plugs 2 and 4 show negative values: that is an increase in porosity after flooding experiments while plugs 1 and 3 record a similar decrease in porosity after flooding.

From the permeability point of view (Figure 24b), the decrease after flooding is about 20-40%, except in plug segment 2A that shows a decrease of 55%. The stress does not affect such permeabilities. After salt cleaning, the variations are slightly lower for all samples, particularly for plug segments 2B and 4A while only plug 3 shows a higher variation after salt cleaning.

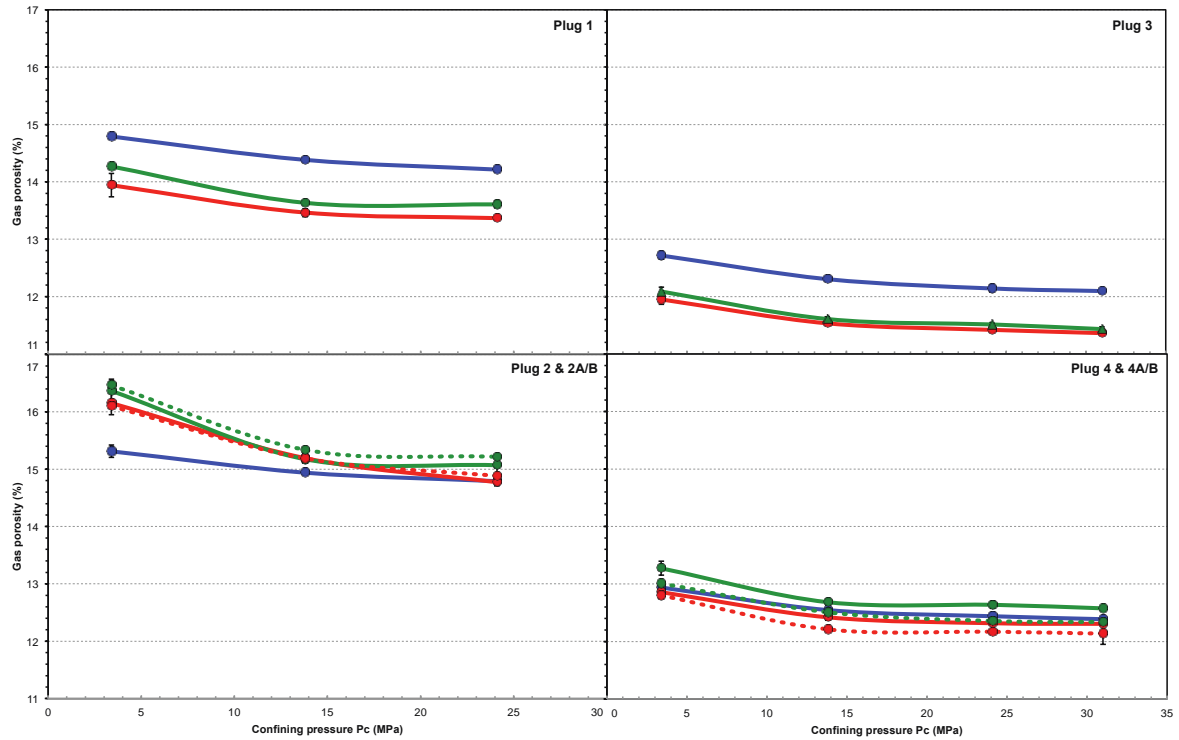


Figure 21. Evolution of the gas porosity at different confining pressures before (blue curves) and after flooding without salt cleaned (red curves) and with salt cleaned (green curves) in Harvey-1 plugs. The dashed curves correspond to the plug segments B (i.e. 2B and 4B) while the plain curves are full plugs (i.e. 1 and 3) and plug segments A (i.e. 2A and 4A). Note how the salt cleaning tends to slightly increase the porosity: the green curves are always above the red curves. Some plugs are marked by a decrease in porosity after flooding: plugs 1 and 3 (full plugs) while the other plugs record an increase after flooding.

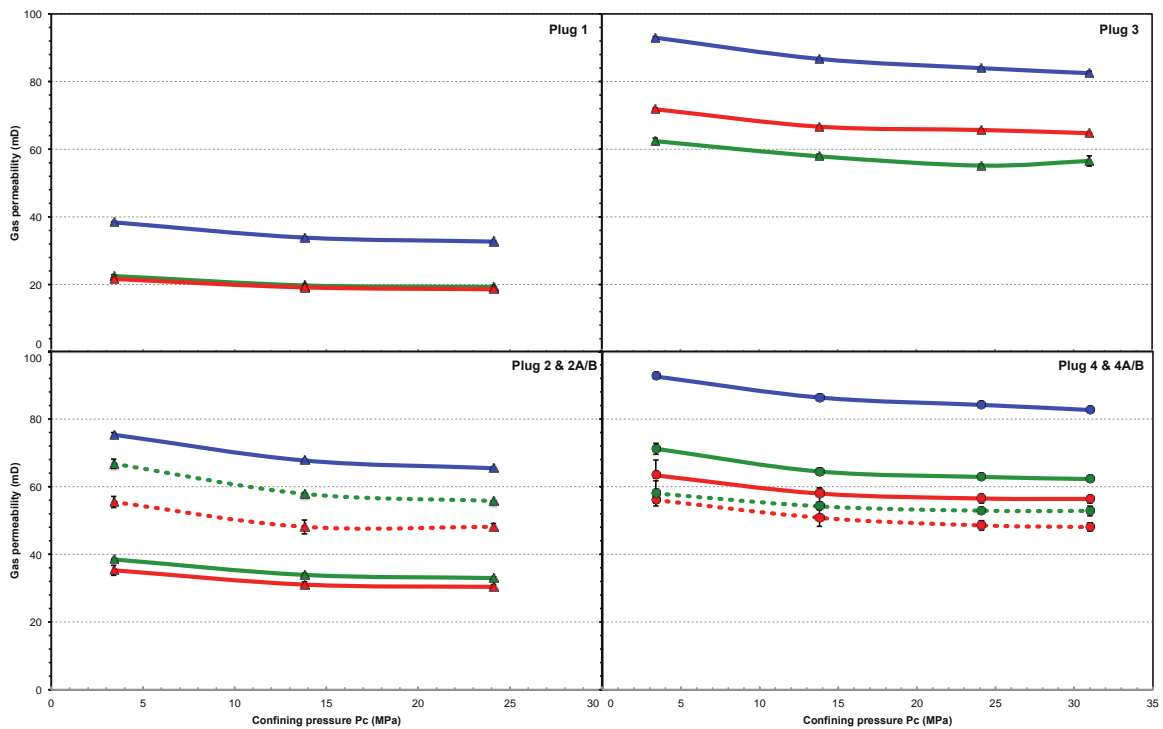


Figure 22. Evolution of the gas permeability at different confining pressures before (blue curves) and after flooding without salt cleaned (red curves) and with salt cleaned (green curves) in Harvey-1 plugs. The dashed curves correspond to the plug segments B (i.e. 2B and 4B) while the solid curves are full plugs (i.e. 1 and 3) and plug segments A (i.e. 2A and 4A). Note how the salt cleaning tends to slightly increase the permeability but for plug 3, the green curves are always above the red curves. All the samples record a decrease in permeability after flooding.

Table 5. Porosity and permeability results averaged from the three repeated measurements, along with their standard deviation (STD), at different confining pressure stages for all the plugs from Harvey-1 before and after flooding without and with salt cleaning.

Plug/Segment #	P _{conf} (psi)	P _{conf} (MPa)	Before flooding				After flooding				After flooding and salt cleaned			
			Porosity (%)	STD porosity (%)	Permeability (mD)	STD permeability (%)	Porosity (%)	STD porosity (%)	Permeability (mD)	STD permeability (%)	Porosity (%)	STD porosity (%)	Permeability (mD)	STD permeability (%)
1	500	3.4	14.8	0.04	38.4	0.04	13.9	0.20	21.7	0.14	14.3	0.02	22.6	0.36
	2000	13.8	14.4	0.02	33.9	0.10	13.5	0.07	19.2	0.26	13.6	0.03	19.7	0.25
	3500	24.1	14.2	0.04	32.7	0.12	13.4	0.02	18.6	0.10	13.6	0.06	19.3	0.23
2 or 2A	500	3.4	15.3	0.11	75.4	0.63	16.2	0.04	35.3	1.50	16.4	0.20	38.5	0.14
	2000	13.8	14.9	0.02	67.7	0.12	15.2	0.23	31.0	0.86	15.2	0.06	33.9	0.47
	3500	24.1	14.8	0.04	65.5	0.12	14.8	0.13	30.4	0.69	15.1	0.04	33.0	0.34
2B	500	3.4	15.3	0.11	75.4	0.63	16.1	0.03	55.5	1.64	16.5	0.07	66.8	1.37
	2000	13.8	14.9	0.02	67.7	0.12	15.2	0.08	48.1	2.04	15.3	0.04	57.9	0.19
	3500	24.1	14.8	0.04	65.5	0.12	14.9	0.18	48.1	0.98	15.2	0.02	55.8	0.03
3	500	3.4	12.7	0.06	93.0	0.32	12.0	0.09	71.8	0.31	12.1	0.08	62.4	0.95
	2000	13.8	12.3	0.03	86.7	0.12	11.5	0.01	66.7	0.14	11.6	0.04	57.9	0.62
	3500	24.1	12.1	0.06	84.0	0.19	11.4	0.01	65.7	0.05	11.5	0.03	55.2	0.45
	4500	31	12.1	0.02	82.5	0.60	11.4	0.01	64.7	0.06	11.4	0.04	56.6	1.52
4 or 4A	500	3.4	12.9	0.07	92.5	0.50	12.9	0.12	63.4	4.51	13.3	0.12	71.2	1.64
	2000	13.8	12.5	0.03	86.3	0.23	12.4	0.05	58.0	1.68	12.7	0.05	64.5	0.85
	3500	24.1	12.4	0.04	84.2	0.16	12.3	0.03	56.5	0.29	12.6	0.06	62.9	0.19
	4500	31	12.4	0.01	82.7	0.41	12.3	0.02	56.3	0.51	12.6	0.04	62.2	0.19
4B	500	3.4	12.9	0.07	92.5	0.50	12.8	0.05	56.1	0.86	13.0	0.04	58.0	3.73
	2000	13.8	12.5	0.03	86.3	0.23	12.2	0.03	50.8	2.52	12.5	0.06	54.2	1.05
	3500	24.1	12.4	0.04	84.2	0.16	12.2	0.04	48.5	1.37	12.4	0.15	52.9	0.31
	4500	31	12.4	0.01	82.7	0.41	12.1	0.19	48.1	1.22	12.3	0.04	52.8	1.44

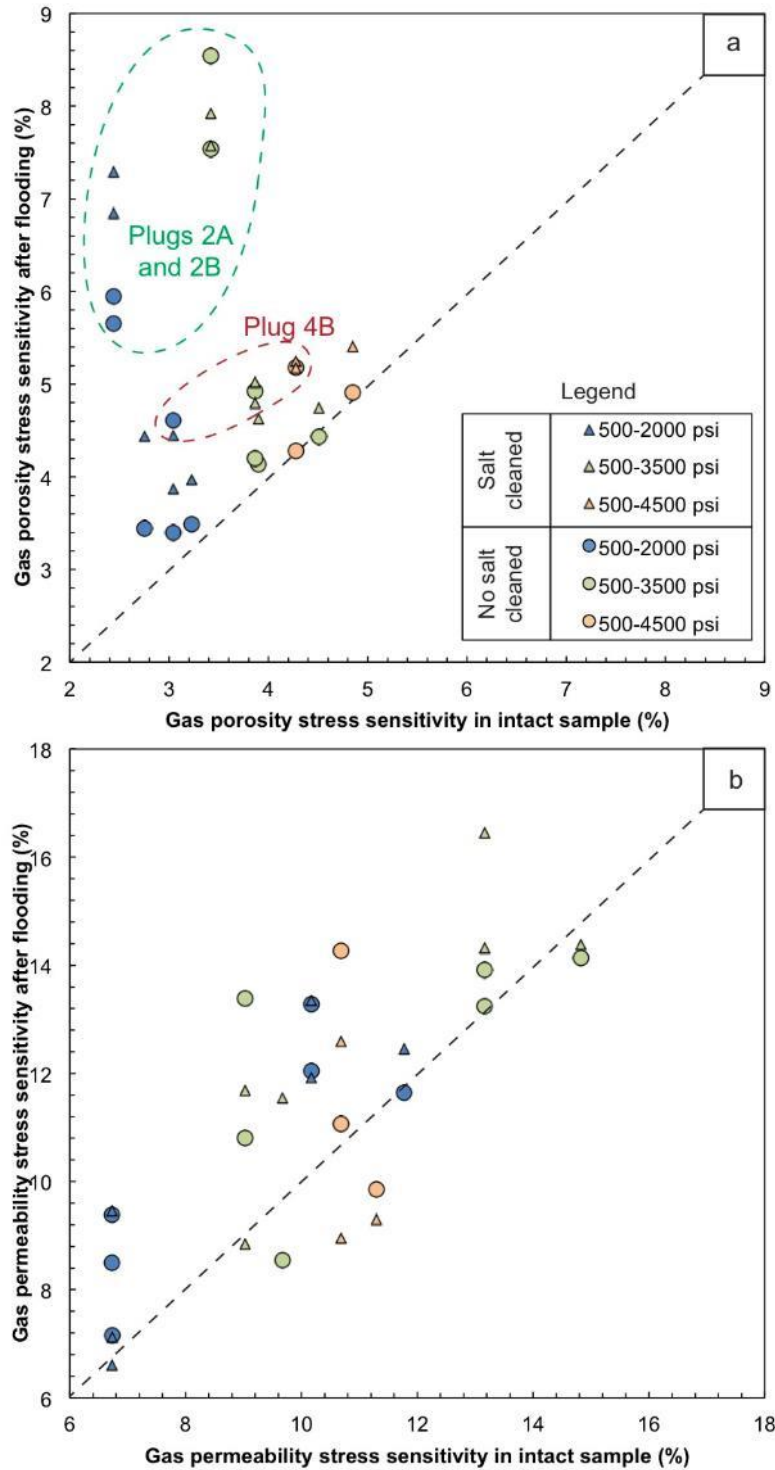


Figure 23. Comparison of gas porosity (a) and gas permeability (b) variations at each confining pressure stage between the initial state (before flooding experiments) and after the flooding experiments for Harvey-1 samples. The label colours correspond to the confining pressure range: blue for a pressure up to 2000 psi, green up to 3500 psi and orange up to 4500 psi for only plugs 3 and 4. The circle symbols are the comparison between initial state and after flooding experiments while the triangle symbols compare the initial state with the post flooding after removing the residual salts from the pores. Note how the porosity of plug segments 2A/B and 4B are much more stress sensitive after flooding experiments (dashed areas). The plug segment 4A marks such sensitivity only after salt cleaning. The black dashed curves define “unchanged” porosity or permeability between the initial and post flooding.



Figure 24. Variations of gas porosity (a) and gas permeability (b) between the initial state and post-flooding without salt cleaning (red bars) and after salt cleaning (green bars) at each confining pressure for all the plugs from well Harvey-1.

Table 6. Summary of extrapolated helium gas porosity and permeability from the different confining pressure stages before and after flooding without and with salt cleaning for all plugs from Harvey-1.

Plug #	Extrapolated gas porosity at 0 psi (%)		
	Before flooding	After flooding	After flooding and salt cleaned
Plug 1	15.0	14.2	14.6
Plug 2A	15.5	16.6	17.0
Plug 2B	15.5	16.5	17.1
Plug 3	12.9	12.1	12.3
Plug 4A	13.1	13.0	13.5
Plug 4B	13.1	13.0	13.2
Plug #	Extrapolated gas permeability at 0 psi (mD)		
	Before flooding	After flooding	After flooding and salt cleaned
Plug 1	40.6	22.9	24.0
Plug 2A	79.1	37.5	40.8
Plug 2B	79.1	59.5	71.2
Plug 3	95.3	73.7	64.8
Plug 4A	94.8	65.6	73.8
Plug 4B	94.8	58.2	59.6

Table 7. Summary of the variations of gas porosity and permeability between different confining pressure ranges from 500 psi to 4500 psi on all the plugs before and after brine-CO₂ flooding without and with salt cleaning for all plugs from Harvey-1.

Plug	Pressure stress differential (psi)	Before flooding		After flooding		After flooding and salt cleaned	
		Porosity stress sensitivity (%)	Permeability stress sensitivity (%)	Porosity stress sensitivity (%)	Permeability stress sensitivity (%)	Porosity stress sensitivity (%)	Permeability stress sensitivity (%)
1	500-2000	2.7	11.8	3.4	11.6	4.4	12.5
	500-3500	3.9	14.8	4.1	14.1	4.6	14.4
2 or 2A	500-2000	2.4	10.2	5.9	12.0	7.3	11.9
	500-3500	3.4	13.2	8.5	13.9	7.9	14.3
2B	500-2000	2.4	10.2	5.7	13.3	6.8	13.3
	500-3500	3.4	13.2	7.5	13.2	7.6	16.5
3	500-2000	3.2	6.7	3.5	7.2	4.0	7.1
	500-3500	4.5	9.7	4.4	8.5	4.7	11.5
	500-4500	4.9	11.3	4.9	9.9	5.4	9.3
4 or 4A	500-2000	3.0	6.7	3.4	8.5	4.4	9.5
	500-3500	3.9	9.0	4.2	10.8	4.8	11.7
	500-4500	4.3	10.7	4.3	11.1	5.2	12.6
4B	500-2000	3.0	6.7	4.6	9.4	3.9	6.6
	500-3500	3.9	9.0	4.9	13.4	5.0	8.8
	500-4500	4.3	10.7	5.2	14.3	5.2	8.9

Table 8. Summary of the gas porosity and permeability variations after flooding (without and with salt cleaning) for all plugs from Harvey-1 at different confining pressures. Positive porosity values correspond to a decrease in porosity after experiments while negative values correspond to an increase in porosity.

Plug	Confining pressure (psi)	Porosity variation after flooding (%)	Porosity variation after flooding & Salt cleaned (%)	Permeability variation after flooding (%)	Permeability variation after flooding & Salt cleaned (%)
1	0	5.3	2.5	43.5	40.9
	500	5.7	3.5	43.6	41.3
	2000	6.4	5.2	43.5	41.7
	3500	6.0	4.3	43.1	41.0
2A	0	-7.1	-9.8	52.6	48.4
	500	-5.5	-6.9	53.2	48.9
	2000	-1.7	-1.6	54.2	49.9
	3500	0.1	-1.9	53.6	49.6
2B	0	-6.7	-10.1	24.8	10.0
	500	-5.1	-7.5	26.4	11.4
	2000	-1.7	-2.7	29.0	14.5
	3500	-0.6	-2.9	26.5	14.8
3	0	6.0	4.8	22.7	32.0
	500	6.0	4.9	22.7	32.9
	2000	6.3	5.7	23.1	33.2
	3500	5.9	5.2	21.8	34.3
	4500	6.1	5.5	21.5	31.4
4A	0	0.4	-3.0	30.8	22.1
	500	0.6	-2.6	31.5	23.0
	2000	1.0	-1.1	32.8	25.3
	3500	1.0	-1.6	32.9	25.3
	4500	0.6	-1.5	31.8	24.7
4B	0	0.5	-1.0	38.6	37.1
	500	1.1	-0.5	39.4	37.3
	2000	2.7	0.3	41.2	37.2
	3500	2.2	0.7	42.3	37.2
	4500	2.0	0.4	41.9	36.1

Three samples from well Harvey-1 had undergone mercury porosimetry and pore throat size distribution measurement (Figure 25). The results of the measurements show that the Harvey-1 samples all have fairly similar pore throat size distributions. The slight differences in their characteristics may be related to the type of facies they come from. Plugs 1 and 4 come from facies Ai (see Timms et al., 2009) while Plug 3 comes from another facies Aii representing a more fine grained sand.

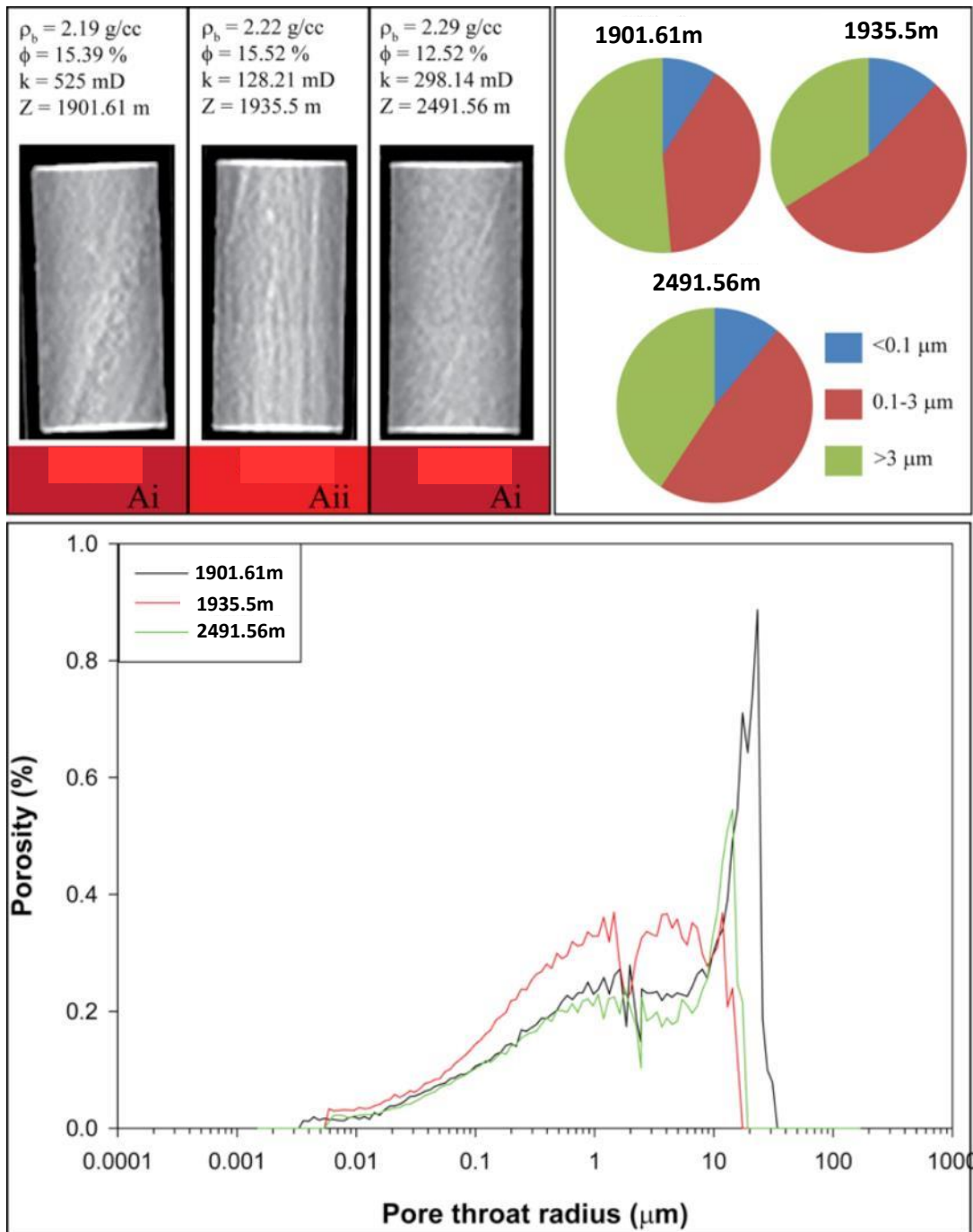


Figure 25. X-ray CT images and mercury injection results of three previous samples from Harvey-1. Top left: Medical XCT image from the 3 tested plugs along with their bulk density, gas porosity and permeability and depth. Top right: pie charts representing the relative percentage of pore space subdivided in three pore throat size classes from mercury injection porosimetry data. Bottom: pore size distribution as measured by mercury injection porosimetry on offcuts of the three samples.

Table 9 and Figure 26 present the detailed results of bulk and grain density measurements as well as the water-saturation efficiency. The recorded grain density, before and after flooding, is about $2.64 \pm 0.02 \text{ g/cm}^3$ with the lowest densities recorded in plugs 1 & 2 and the highest densities in plugs 3 & 4. Comparisons of the porosity measured from the gas method and water mass before and after imbibition (WIP) give exactly the same results (Figure 17) on the intact samples (before flooding). The water-saturation is therefore quite well done with respect to the nitrogen gas porosity: Saturation > 98%. After flooding, the WIP porosity gives similar results to the gas method but some lower values on plug segments 4A&B and particularly for plug segments 2A&B, leading to a water-saturation down to 92% in the worst case. Such inefficiency to fully re-saturate the samples with water may point to possible effects of clay particles. They may have been displaced and lodged in critical pore and/or pore throats during flooding (fines migration) making those pores less accessible to water. Mineral dissolution mechanisms alone may not cause such issues and would rather facilitate similar results between gas and water saturation methods by enhancing pore connectivity.

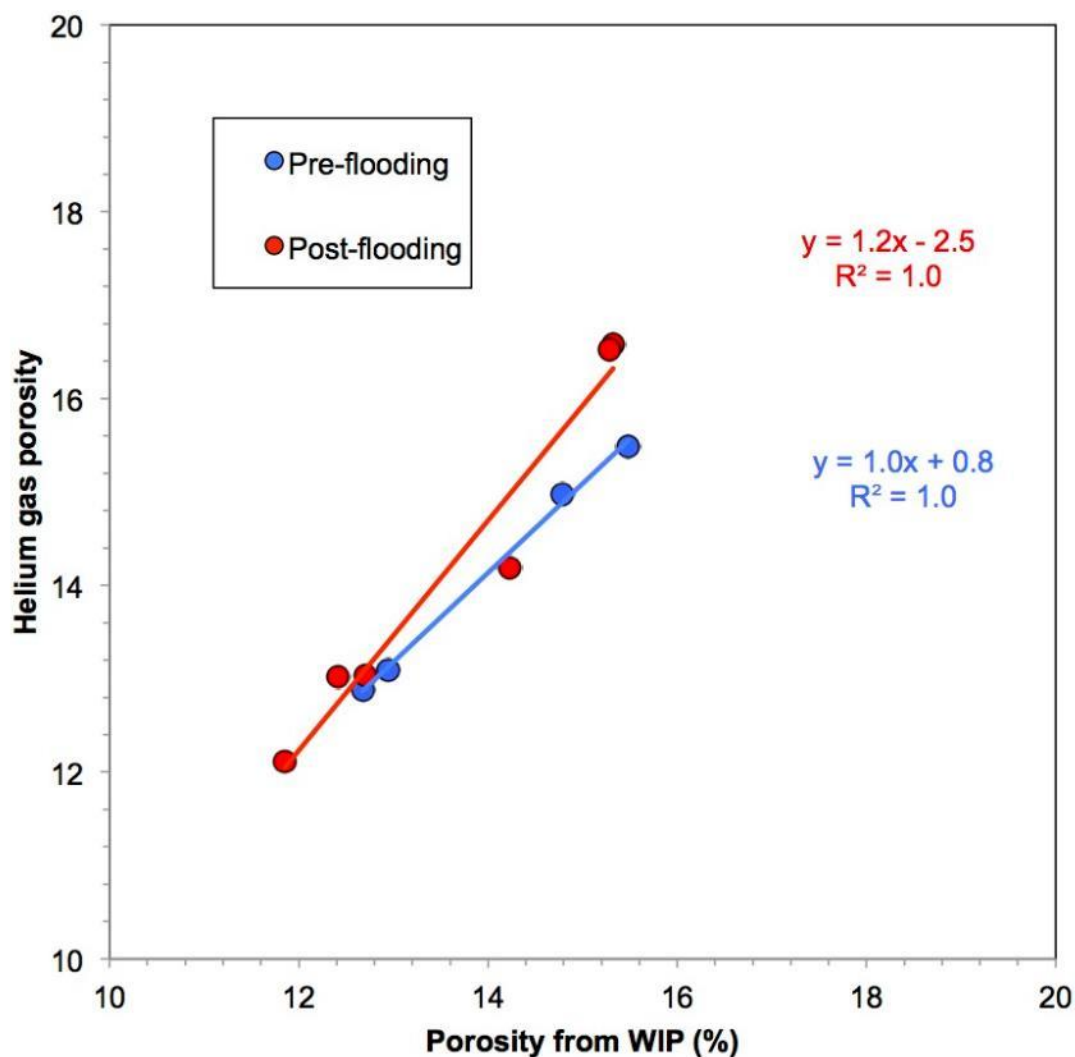


Figure 26. Validation of proper water saturation of the plugs from Harvey-1 in the pre- and post-flood stages by comparing the helium gas porosity (extrapolated to 0 psi) with water imbibition mass porosity method (WIP). Note however that water saturation is slightly less effective on the post-flood plugs (red symbols) than the pre-flood plugs (blue symbols).

Table 9. Summary of the bulk and grain density for Harvey-1 plugs computed from mass and volume measurements as well as gas porosity measurements, all before (blue cells) and after flooding (light orange cells) and after flooding with salt cleaning (dark orange cells). Note that star (*) in some volume matrix cells corresponds to helium pycnometry direct measurement while the other volume matrix cells were computed from gas porosity and bulk volume. Such direct volume matrix measurement allowed the computation of equivalent porosity.

Before flooding (at 0 psi)								
Plugs	Mass dry (g)	Mass saturated (g)	Dry bulk density (g/cm ³)	Porosity gas (%)	Volume matrix (cm ³)	Water saturation (%)	Grain density (g/cm ³)	Porosity computation by density* (%)
1	158.73	169.23	2.24	15.0	60.38	99	2.63	
2	168.90	180.71	2.21	15.5	64.48	100	2.62	
3	168.27	177.53	2.30	12.9	63.67	98	2.64	
4	163.785	173.026	2.29	13.09	62.04	99	2.64	
After flooding (at 0 psi)								
Plugs	Mass dry (g)	Mass saturated (g)	Dry bulk density (g/cm ³)	Porosity gas (%)	Volume matrix (cm ³)	Water saturation (%)	Grain density (g/cm ³)	Porosity computation by density* (%)
1	158.69	168.793	2.23	14.2	60.94	100	2.60	
2A	54.985	58.877	2.16	16.6	20.91*	92	2.63*	17.7
2B	64.892	69.458	2.17	16.5	24.62*	92	2.64*	17.6
3	168.545	177.206	2.31	12.1	64.23	98	2.62	
4A	65.13	68.762	2.28	13.0	24.68*	97	2.64*	13.7
4B	56.792	59.902	2.27	13.0	21.59*	95	2.63*	13.8
After flooding and salt cleaning (at 0 psi)								
Plugs	Mass dry (g)	Mass saturated (g)	Dry bulk density (g/cm ³)	Porosity gas (%)	Volume matrix (cm ³)	Water saturation (%)	Grain density (g/cm ³)	Porosity computation by density* (%)
1	158.338		2.23	14.6	60.64		2.61	
2A	54.831		2.16	17.0	20.80*		2.64*	18.11
2B	64.739		2.17	17.1	24.31*		2.66*	18.61
3	168.27		2.30	12.3	64.12		2.62	
4A	65.009		2.27	13.5	24.64*		2.64*	13.79
4B	56.681		2.26	13.2	21.46*		2.64*	14.31

Harvey-3

Table 10 and Figure 27 summarize the results of the gas porosity and permeability conducted on the samples from well Harvey-3 before and after the flooding experiments under various overburden pressures. In general, the porosity on the pre-flood plugs is around 21 % in both samples after extrapolation of the data to room conditions using a second order polynomial fit. But the permeability, again extrapolated to room conditions, is quite different between the two plugs with a value of 138 mD for Plug 1 and 94 mD for Plug 2. The first striking observation from these results is the difference

between the pre- and post-flood permeabilities of the plugs. Permeabilities of both plugs show significant increase compared to their pre-flood values while change to their porosity is minor. The second observation is the decrease in the stress sensitivity of the permeability in both plugs after undergoing the flooding process while the porosity stress sensitivity remains unchanged.

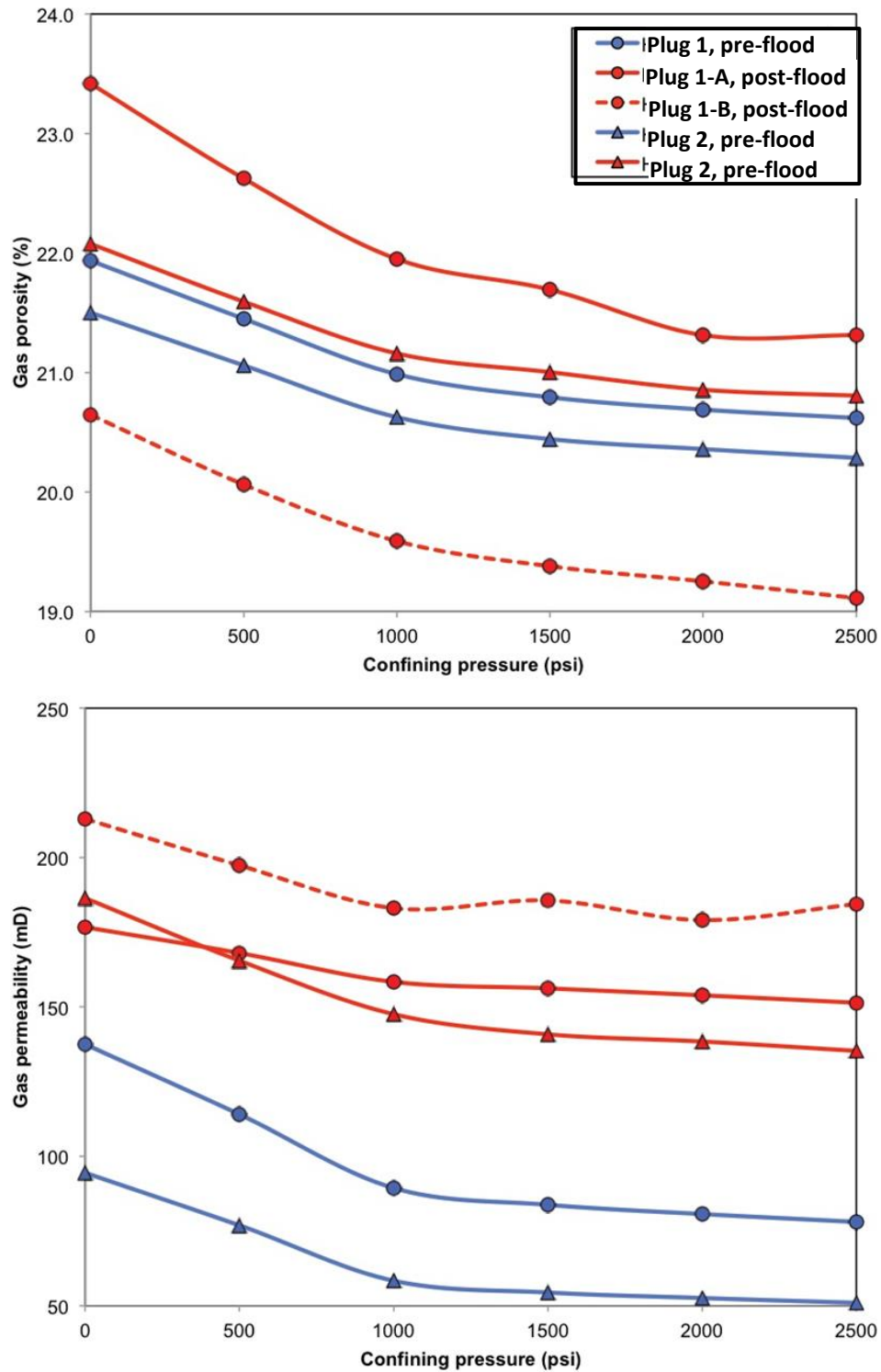


Figure 27. Nitrogen gas porosity (top graph) and permeability (bottom graph) measured for Harvey-3 plugs under various overburden pressures with the extrapolation of the porosity-permeability from 500 psi to 0 psi (room conditions). The blue curves represent the pre-flood plugs and the red curves the post-flood plugs.

Table 10. Summary of nitrogen gas porosity-permeability under increasing confining pressure before and after flooding for the two plugs from well Harvey-3. The extrapolated porosity-permeability at room conditions using a second order polynomial fit is also provided along with their stress dependency between room conditions and maximum pressure (2500 psi).

Confining pressure (psi)	Plug 1, pre-flood		Plug 1-A, post-flood		Plug 1-B, post-flood		Plug 2, pre-flood		Plug 2, post-flood	
	Porosity (%)	Perm. (mD)	Porosity (%)	Perm. (mD)	Porosity (%)	Perm. (mD)	Porosity (%)	Perm. (mD)	Porosity (%)	Perm. (mD)
0 (Extrapolated)	21.9	138	23.4	177	20.6	213	21.5	94	22.1	186
500	21.5	114	22.6	168	20.1	197	21.1	77	21.6	165
1000	21.0	89	22.0	158	19.6	183	20.6	58	21.2	148
1500	20.8	84	21.7	156	19.4	186	20.4	54	21.0	141
2000	20.7	81	21.3	154	19.3	179	20.4	53	20.9	138
2500	20.6	78	21.3	151	19.1	184	20.3	51	20.8	135
Stress dependency (%)	6.0	43.2	9.0	14.3	7.4	13.4	5.7	46.0	5.8	27.4

Harvey-4

Table 11 and Figure 28 summarize the results of the gas porosity and permeability measurements conducted on the pre- and post-flood plugs from well Harvey-4 under various overburden pressures. In general, the porosity of the pre-flood plugs is around 21 % for plugs 1 and 2 and slightly less at around 17% for plugs 3 and 4. These data are extrapolated values to room conditions using a second order polynomial fit. All samples have a low stress dependency of porosity at around 6% between no stress and 3000 psi. The permeability, also extrapolated to room conditions, is quite different between these two sets of samples: plugs 1 and 2 range between 70 and 100 mD while plugs 3 and 4 are both around 3 mD. The stress dependency of permeability is higher ranging between 25 and 50%.

After flooding experiments, the porosity of all samples were quasi-unchanged as well as the stress dependency of the porosity. However, the permeabilities seem to have remained quasi-unchanged in Plug 1 and improved in Plug 2, but slightly decreased in plugs 3 and 4. The permeabilities also exhibit less stress dependency than in most of the post-flood samples. It is worth noting that the observed pre- and post-flood differences in terms of the sample permeabilities, are more subtle compared to the previously tested samples from Harvey-1 and 3 wells.

Table 11. Summary of nitrogen gas porosity-permeability conducted on samples from Harvey-4 under increasing confining stress before and after the flooding experiments. The extrapolated porosity-permeability at room conditions using a second order polynomial fit is also provided along with their stress dependency between room conditions and maximum pressure (3000 psi).

	Plug 1- pre-flood		Plug 1A post-flood		Plug 1B post- flood		Plug 2 pre- flood		Plug 2 post- flood	
Confining pressure (psi)	Average Porosity (%)	Average Permeability (mD)								
Extrapolated to nil	20.4	98	21.4	69	21.6	71	19.6	72	20.8	80
500	19.9	82	20.7	65	21.0	67	19.3	63	20.4	74
1000	19.4	61	20.5	60	20.4	61	18.9	52	20.0	66
1500	19.2	57	19.9	60	20.2	60	18.7	48	19.8	65
2000	19.1	53	19.8	59	20.0	59	18.7	47	19.7	63
3000	18.9	51	19.6	58	19.7	58	18.5	45	19.6	62
Stress dependency (%)	7.1	47.9	8.7	16.0	8.6	18.6	5.7	37.7	5.5	22.9
	Plug 3 pre-flood		Plug 3A post-flood		Plug 3B post-flood		Plug 4 pre-flood		Plug 4 post-flood	
Confining pressure (psi)	Average Porosity (%)	Average Perm (mD)	Average Porosity (%)	Average Permeability (mD)	Average Porosity (%)	Average Permeability (mD)	Average Porosity (%)	Average Permeability (mD)	Average Porosity (%)	Average Permeability (mD)
Extrapolated to nil	16.8	3.6	17.1	2.7	17.6	3.4	15.4	2.7	15.3	2.1
500	16.6	3.3	16.7	2.5	17.3	3.3	15.1	2.4	15.0	1.9
1000	16.3	3.0	16.4	2.3	17.0	3.0	14.8	2.1	14.7	1.7
1500	16.2	2.9	16.3	2.2	16.9	2.9	14.7	1.9	14.5	1.6
2000	16.1	2.8	16.2	2.1	16.8	2.8	14.6	1.9	14.5	1.5
3000	16.0	2.7	16.1	2.1	16.7	2.7	14.5	1.7	14.3	1.4
Stress dependency (%)	4.7	25.0	5.7	22.9	5.1	19.2	6.2	35.0	6.2	33.1

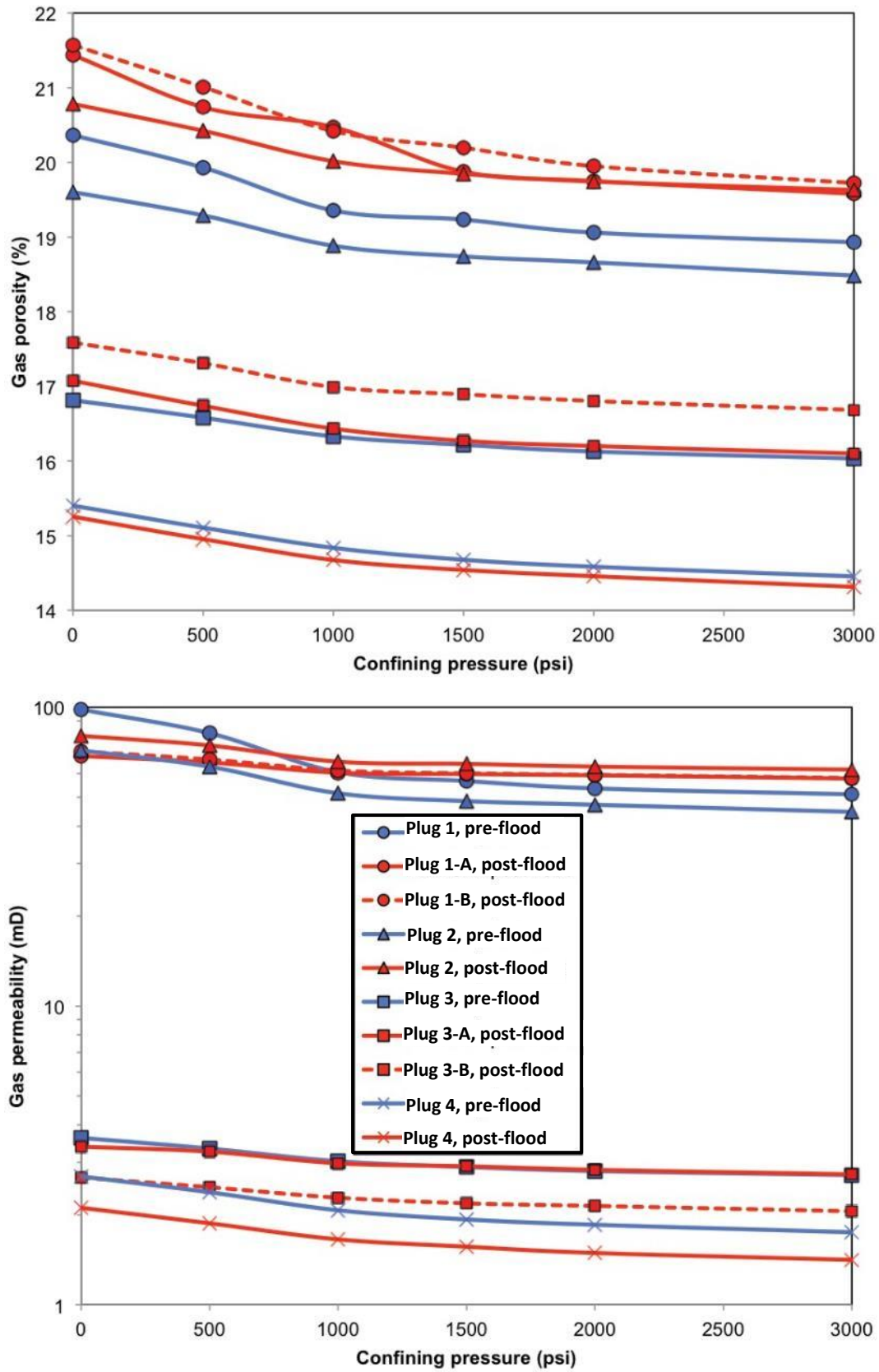


Figure 28. Nitrogen gas porosity (top graph) and permeability (bottom graph) measured on Harvey-4 samples under various overburden pressures with the extrapolation of the porosity-permeability from 500 psi to 0 psi (room conditions). The blue curves represent the pre-flood plugs and the red curves the post-flood plugs.

Nuclear Magnetic Resonance Spectrometry

Harvey-1

For the samples tested from well Harvey-1, before flooding, both NMR porosity methods (amplitude and T₂ distribution) give exactly the same results as the gas porosities measured for the same samples (Figure 29 and Table 12). After flooding, as might be expected based on the discussions presented earlier, water saturation was not as efficient as before flooding in plug segments 2A&B, leading to an under-estimation of the porosity compared to the gas porosity results.

The T₂ distribution on pre-flood samples, reflecting the pore size distribution, is quite different between plugs 1 & 2 and 3 & 4 (Figure 30a). Three populations can be detected in plugs 3 and 4:

- Short T₂ (T_{2s}): centred around 0.3 ms, typically related to clay-bound water.
- Intermediate T₂ (T_{2i}): centred around 30 ms, related to capillary-bound water; movable but at the cost of strong differential pressure.
- Long T₂ (T_{2l}): centred around 400 ms, related to easily movable water.

In plugs 1 and 2, only 2 populations are detected with the same previously mentioned T_{2s} while T_{2i} and T_{2l} seem to be combined into one single population. It is possible that pore size distribution is well distributed to the point that the NMR machine cannot decouple capillary from movable water as clearly as in plugs 3 and 4.

After flooding (Figure 30b), all the plugs show the same three populations detected on intact plugs 3 and 4, with plug segment 4B recording the biggest pore sizes (Longest T_{2l}). This aspect is better displayed in Figure 31 where the T₂ distribution is compared before and after flooding for each plug on its own:

- (i) The first observation is a clear decrease in the general magnitude of the T₂ distribution after flooding.
- (ii) The second observation is that bigger pores, longer T₂, appear after flooding only in plugs 1 and 2 (segments A&B) that have similar structure from XCT analysis.
- (iii) The third and last observation is that short T₂, related to clay-bound water, became more intense in plugs 2 (segments A&B) and 4 (segments A&B).

The above observations may be explained by the impact of clays clogging the pores/pore-throats. Indeed, gas porosity measurements do not show drastic differences between the pre- and post-flood values while water porosity measurements reveal differences between the two sets of data. It could be speculated that clays that were present in pores of the pre-flood plugs became dislodged during the flooding and migrated downstream of the plugs. Therefore, the water may gain access to bigger pores while water can surround more “free” dislodged surface of ± agglomerated clays, generating higher CBW (clay bound water) signal.

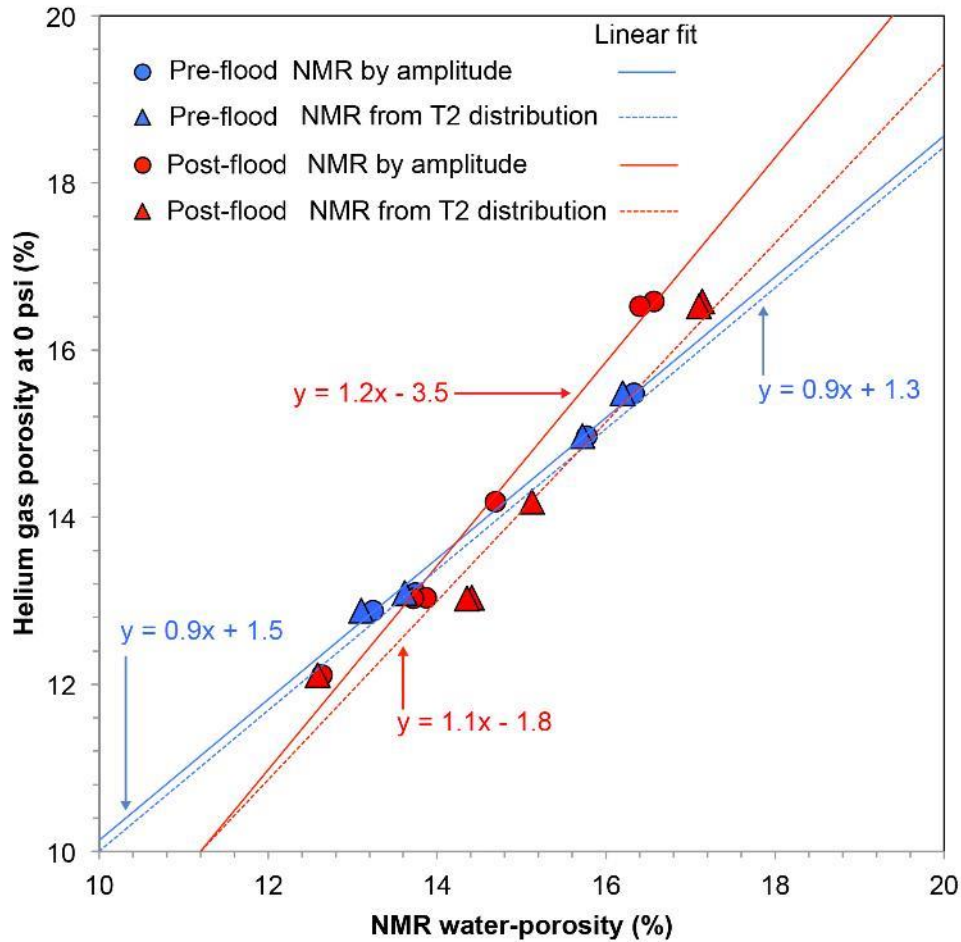


Figure 29. Helium gas porosity (at 0 psi confining pressure) versus NMR water-porosity computed from amplitude (circles) and T2 distribution (triangles) methods, on all the plugs from Harvey-1 before (blue colours) and after (red colours) flooding. Note how the linear fit of the pre-flooded plugs (red linear curves) are similar on both NMR methods and very close to 1:1 ratio with gas porosity.

Table 12. Summary of NMR porosity (from amplitude and T2 distribution methods) and permeability (from Coates and SDR equations) for all the plugs from Harvey-1 before and after flooding. The gas porosity and permeability results at 0 psi confining pressure are reminded (see Table 6). The best C to fit the computed NMR permeability with the gas permeability are also provided for both Coates and SDR equations. Note how the C for Coates has to be lowered to 7-8 instead of 10 to fit the gas permeability on plugs 3 and 4.

Plug ID	NMR Porosity from amplitude (%)	NMR porosity from T2 distribution (%)	Porosity from mass evaluation (%)	T2lm (ms)	NMR permeability Coates (mD)	NMR permeability SDR (mD)	Gas porosity (%)	Gas permeability (mD)	Best C for NMR Coates	Best C for NMR SDR
Before flooding										
1	15.8	15.7	14.8	54	36	72	15.0	41	10	12
2	16.3	16.2	15.5	60	52	99	15.5	79	9	11
3	13.2	13.1	12.7	99	33	116	12.9	95	8	11
4	13.7	13.6	12.9	94	36	123	13.1	95	8	11
After flooding										
1	14.7	15.1	14.2	66	26	92	14.2	23	10	14
2A	16.6	17.1	15.3	42	31	61	16.6	37	10	11
2B	16.4	17.1	15.3	13	35	77	16.5	59	9	11
3	12.6	12.6	11.9	93	24	87	12.1	74	8	10
4A	13.9	14.4	12.7	54	19	50	13.0	66	7	9
4B	13.7	14.4	12.4	55	17	51	13.0	58	7	10

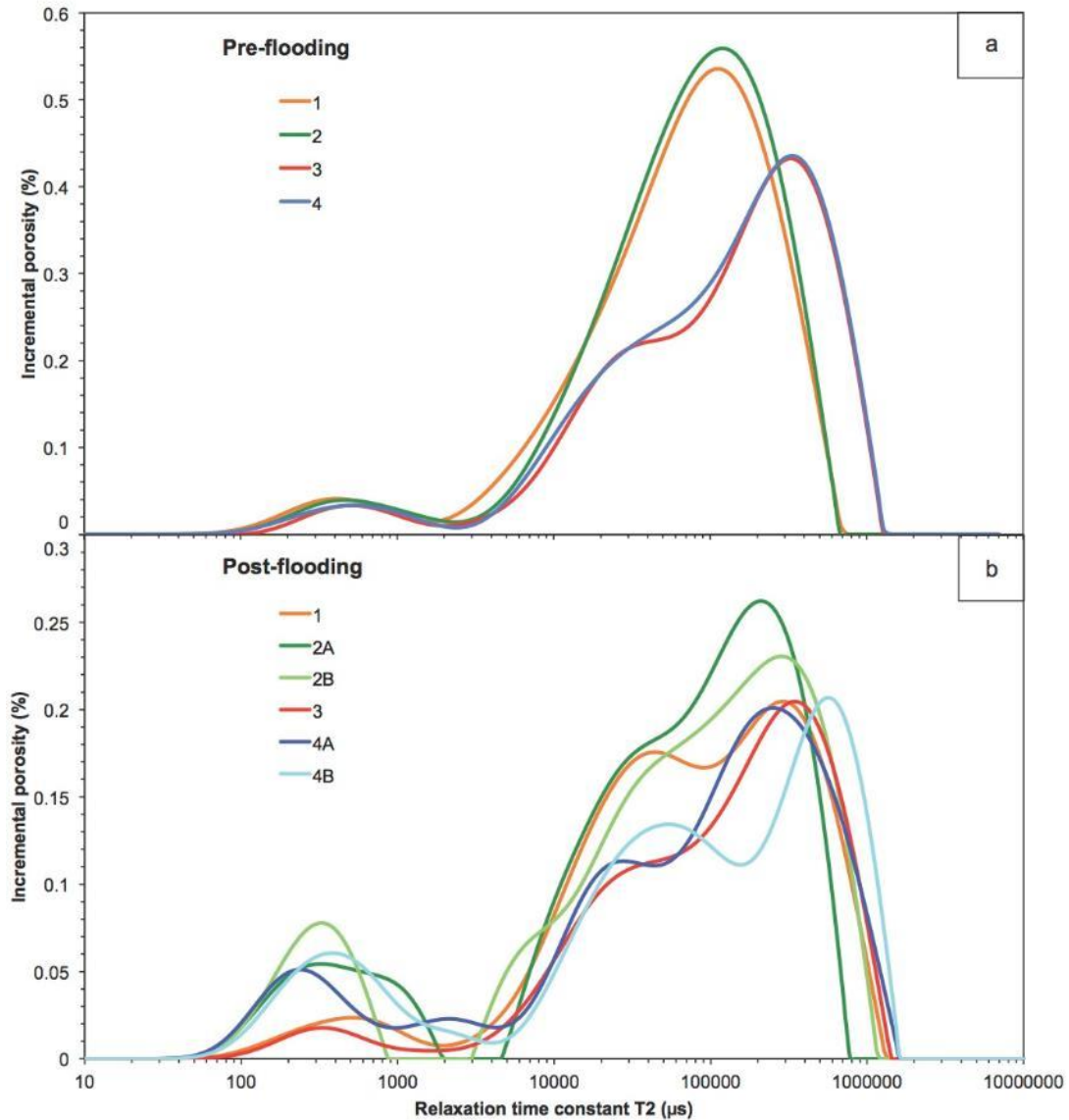


Figure 30. NMR T2 distribution from CPMG sequence on the Harvey-1 plugs before (a) and after (b) flooding. The volume of water measured by NMR was normalised to the sample volume assuming a water density of 1 g/cm³ to convert the y axis into incremental porosity. The integration of all the T2 distribution will give the total water porosity of the plug. Note how the plugs 1 and 2 are different from the plugs 3 and 4 before flooding.

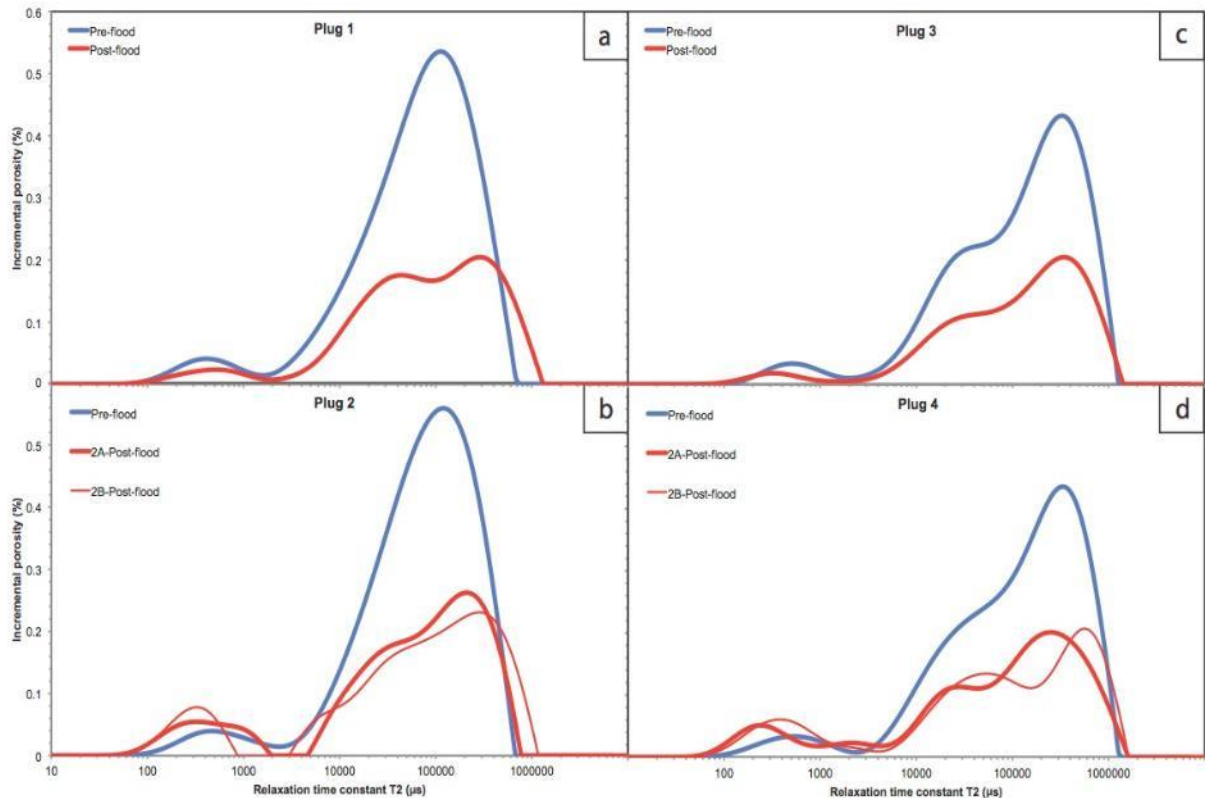


Figure 31. Comparison of NMR T2 distribution from CPMG sequence before and after flooding for each plug from Harvey-1. The volume of water measured by NMR was normalised to the sample volume assuming a water density of 1 g/cm³ to convert the y axis into incremental porosity. The integration of all the T2 distribution will give the total water porosity of the plug.

The computed NMR permeability using parameters extracted from the literature and the empirical equations for sandstones, give reasonable matches with gas permeability before and after flooding (Table 12). The similar decrease in permeability after flooding, as previously observed from the gas method, are also revealed by the NMR data. Using gas permeability as a reference, the C factor from Coates equation can be computed (Table 12). If the C factor is indeed around 10 as suggested from the literature, a need for slightly lower C values is needed for plugs 3 and 4 in order to match the gas permeability, before and after flooding. Lower C underlines simpler pore geometry, which is corroborated with better gas permeability results. A simpler geometry would mean more tubular-type pores which are well connected and/or less clays clogging the pores related to the sand grain matrix.

Harvey-3

The water-filled porosity measured for the samples from well Harvey-3 using NMR technique is summarised in Table 13 along with the NMR derived permeability data calculated using the Coates and SDR models. The water-filled porosity records similar values to the gas porosity measurements. The water imbibition porosity derived from mass intake of the plugs also records similar values to those calculated from NMR data. The NMR pore distribution (Figure 32) shows a bimodal distribution for both pre-flood samples with a dominant population with long T2 time around 80 ms corresponding to big pore sizes while a small population exists at short T2 time around 1 ms related to capillary pore sizes (i.e. few μm). After the flooding experiments, the dominant population is subdivided into two sub-populations with one population similar to the previous pre-flood population while the 2nd population extends toward much longer T2 time (i.e. bigger pores). The short T2 component seems to

also shift toward even shorter T2 time composed of a mixture of smaller capillary pore sizes and possibly clay bound water, or an increase of the grain surface roughness. This may be interpreted a “cleaning” process of the fine particles from some pore throats and pore walls allowing water to access smaller pores and invading bigger pores more efficiently.

The changes in the pre- and post-flood permeability data calculated from the NMR data (Table 13) show opposite behaviour when compared with the changes observed in gas permeabilities (Table 10). The NMR measurements on the pre-flood samples record similar permeabilities to the gas permeabilities (around 150 mD in plug 1 and 95 mD in plug 2). However, NMR derived permeabilities for the post-flood samples show significant decrease while the porosity changes are minor. One possible explanation is a change in the surface relaxivity of the minerals. Assuming the mineralogy to remain unchanged, the surface texture may have changed leading to change in the NMR surface relaxivity. This aspect is reflected in the C parameters from Coates model. Assuming the gas permeability as the most reliable measurement, the C parameter from Coates equation was back-computed to obtain an NMR permeability equal to gas permeability. The C parameters, usually around 10 in sandstones, shifted to 8 in all the post-flood samples meaning increase in the mineral surface roughness. More specifically, parameter C can impact on the NMR logs analysis if the classical C = 10 is used to compute the permeability on post-CO₂ flooded reservoirs. In the light of the results achieved here, using C= 10 is appropriate in Harvey-3 to compute permeability quite accurately. However, if NMR log is recorded on CO₂ injected units, it may be needed to change the C parameter to 8 to take into account the change of surface roughness of the minerals induced by CO₂ interactions. The C=8 is calculated for the flooding conditions applied in this work. Further NMR C parameter analysis should be carried out with different flooding conditions to evaluate the evolution of this parameter with the duration of CO₂ interaction experimental conditions. Decrease in C values in the post-flood samples was also observed in some of the plugs tested from Harvey-1 (Table 12).

Table 13. Summary of NMR porosity and permeability (from Coates equation) for all the plugs from Harvey-3 for before and after flooding. The best C to fit the computed NMR permeability with the gas permeability are also provided for Coates equation. Note how the C for Coates has to be lowered to 8 instead of 10 to fit the gas permeability on the post-flooded plugs.

Sample	Depth (m)	Status	NMR water amount (wt%)	NMR water-filled porosity (%)	Water imbibition porosity (WIP; %)	Computed NMR permeability (Coates model; mD)	Best C Coates model parameter
Plug 1	1459.40	Pre-flood	9.48	21.2	21.3	156.19	10.3
Plug 1-A	1459.40	Post-flood	10.31	22.4	21.6	97.88	8.6
Plug 1-B	1459.40	Post-flood	10.29	22.5	22.3	101.93	8.3
Plug 2	1459.46	Pre-flood	9.22	20.9	20.9	96.47	10.1
Plug 2	1459.46	Post-flood	9.42	21.1	21.0	73.64	8.0

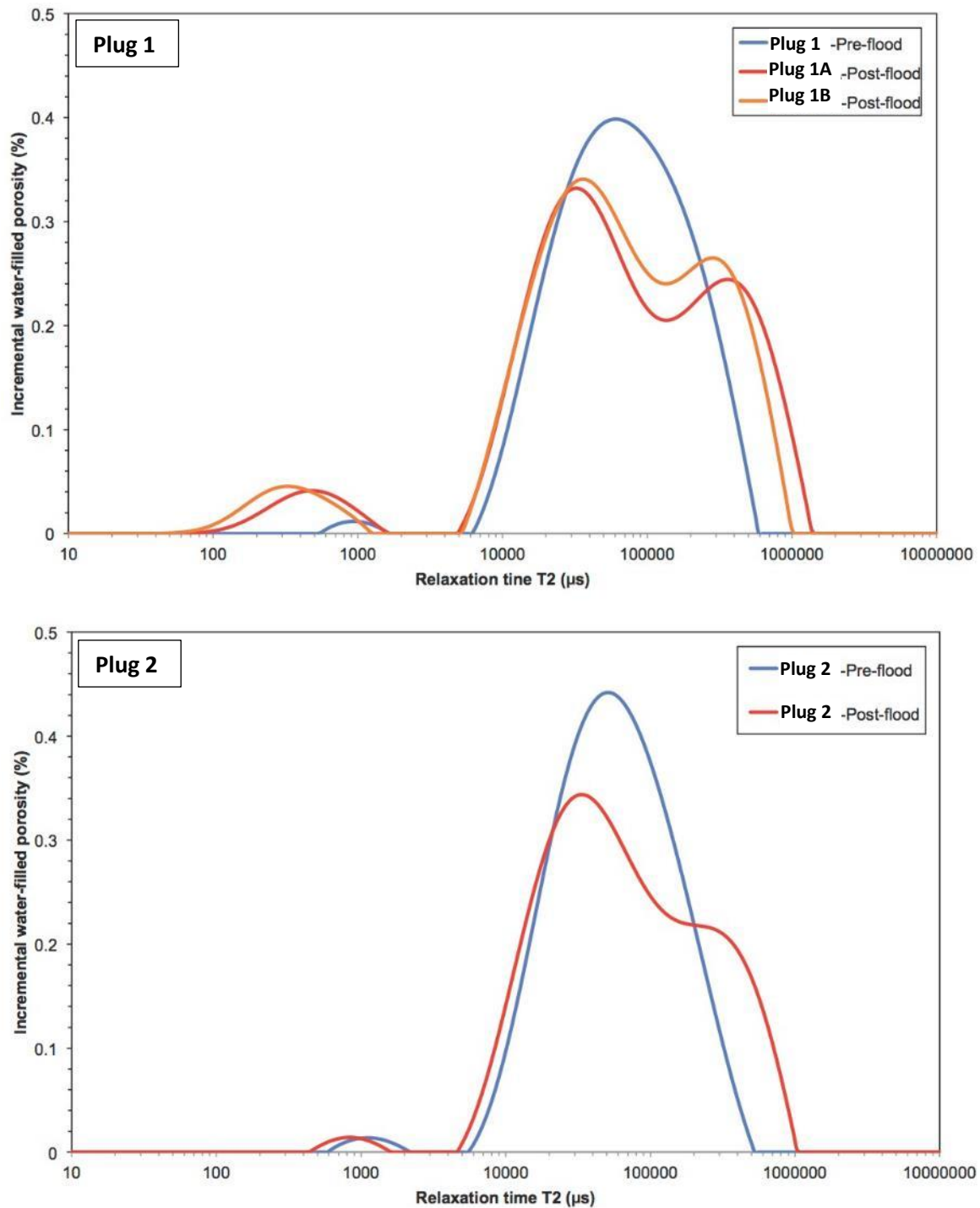


Figure 32. NMR T2 distribution for the pre-flood (blue curves) and post-flood (red/orange curves) plugs from Harvey-3.

Harvey-4

The water-filled porosity measured from NMR on core plugs from well Harvey-4 is summarised in Table 14 along with the permeability computations using the Coates and SDR models. The water-filled porosity records similar values to those of gas porosity measurements with initial values around 20 % and 17% for the first (plugs 1 and 2) and second (plugs 3 and 4) sample assemblies, respectively, with quasi-unchanged porosities in the post-flood samples.

The water imbibition porosity derived from mass intake of the plugs records similar values to the NMR porosities and validates the quality NMR data acquisitions. The NMR pore distribution (Figure 33) shows a classical bimodal distribution for the pre-flood samples with:

- (i) a dominant population with long T2 time around 80 ms in plugs 1 and 2 and slightly less at 50 ms in plugs 3 and 4, corresponding to big pore sizes and,
- (ii) a small population exists at short T2 time around 1 ms related to small pore sizes (i.e. few μm).

After the flooding experiments, the dominant population is subdivided into two sub-population, with one population similar to the previous pre-flood plug population while the 2nd population extends toward much longer T2 time (i.e. bigger pores). The short T2 component seems to also shift toward even shorter T2 time composed of a mixture of smaller capillary pore sizes and possibly clay bound water, or an increase of the grain surface roughness.

In the post-flood plugs, the NMR permeabilities also show variations compared with their pre-flood values. These changes are not always consistent with the observations made from the gas permeability measurements. For the changes observed in the NMR derived data, apart from potential changes to the pore channels, one explanation is possible changes in the surface relaxivity of the minerals. As also discussed for the samples from Harvey-3, even if the overall mineral chemistry is assumed to remain unchanged, the surface texture could have changed leading to change in the NMR surface relaxivity. This aspect is reflected in the C parameters calculated from NMR models. Assuming the gas permeability as the most reliable measurements, the C parameter from Coates equation was back-computed to reach an NMR permeability equal to gas permeability. The newly computed C parameter is around 10 for plugs 1 and 2 while it is shifted to 12-14 in tighter plugs of 3 and 4. The C parameter from SDR model is higher but records the same trend with higher C values in the tight samples (plugs 3 and 4) at around 17 and lower for plugs 1 and 2 at around 12.

Table 14. Summary of the water content and water-filled porosities from NMR and calculated permeabilities using Coates and SDR models before and after the flooding experiments for the plugs from well Harvey-4. C parameters are the best constant from the Coates and SDR models to match the gas permeability. T2LM is the log mean of the NMR T2 distribution used to compute permeability with the SDR model.

Sample	Status	NMR water amount (wt%)	NMR water-filled porosity (%)	Water imbibition porosity (WIP; %)	Computed NMR permeability (Coates model; mD)	Best C Coates model parameter	T2LM (ms)	Computed NMR permeability (SDR model; mD)	Best C SDR model parameter
Plug 1	Pre-flood	8.65	19.6	19.3	119.90	10.5	58	172.10	11.5
Plug 1A	Post- flood	9.65	21.1	20.3	83.76	10.3	46	181.93	12.5
Plug 1B	Post- flood	9.55	21.0	20.6	106.63	11.0	55	241.18	13.5
Plug 2	Pre- flood	8.71	19.8	19.0	103.69	11	54	156.74	12.2
Plug 2	Post- flood	8.73	19.7	20.5	88.78	10.3	65	243.75	13.2
Plug 3	Pre- flood	6.96	16.4	17.0	9.03	12.6	33	27.72	16.63
Plug 3A	Post- flood	7.51	17.7	16.7	10.84	14.2	23	24.49	17.41
Plug 3B	Post- flood	7.84	18.3	17.4	15.42	14.6	26	34.92	17.92
Plug 4	Pre- flood	6.43	15.4	15.3	3.62	10.8	24	11.31	14.32
Plug 4	Post- flood	6.31	15.0	15.6	4.55	12.1	27	15.19	16.38

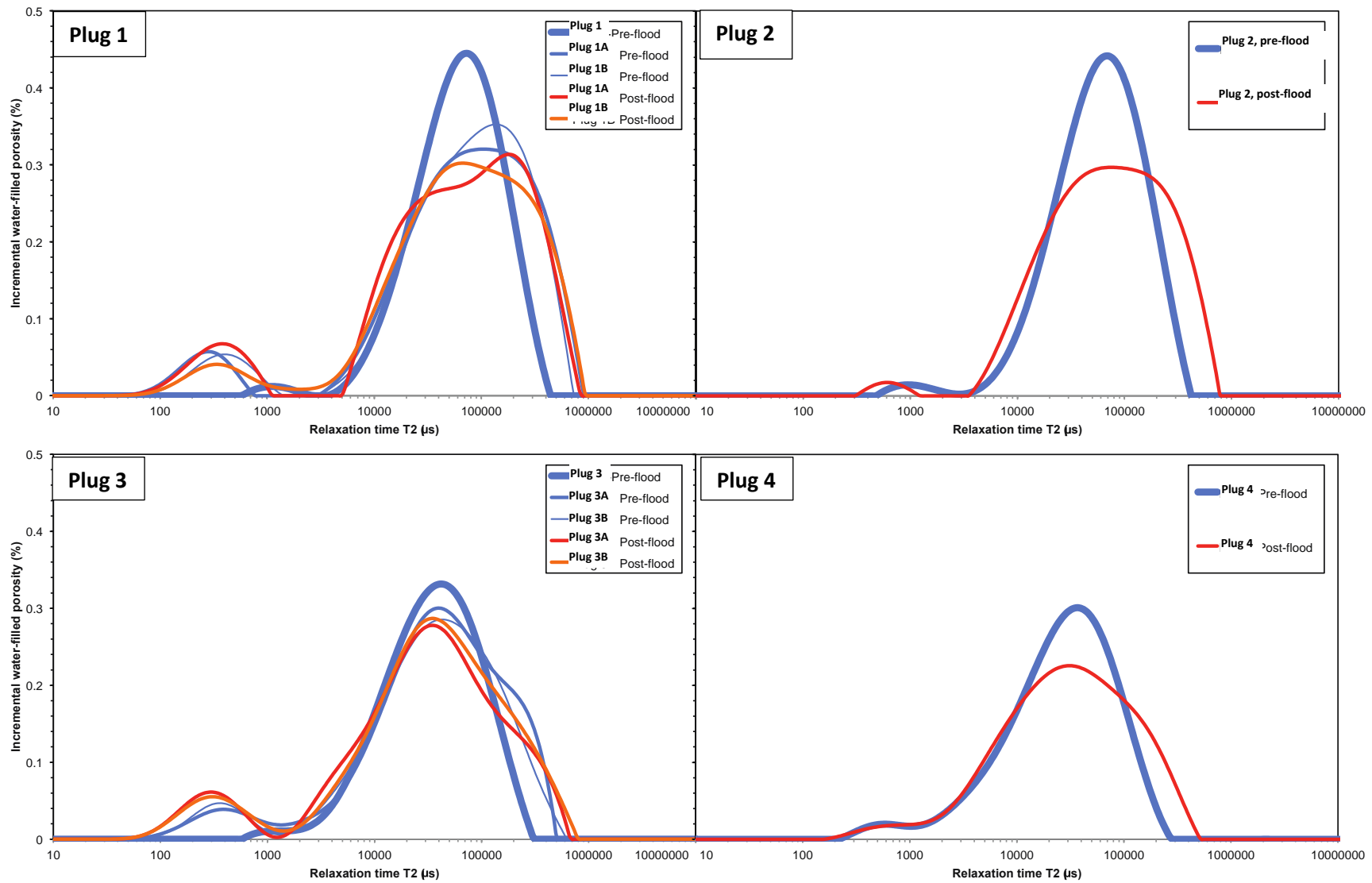


Figure 33. NMR T2 pore distribution for the pre- (blue curves) and post-flood (red/orange curves) plugs from well Harvey-4.

Simultaneous Electrical and Acoustic Measurement under Confining Pressure-Harvey-1 Samples

Ultrasonic velocity measurement

The ultrasonic velocities (VP and VS) along with the computed shear, bulk and Young modulus are summarised in Table 15 for each confining pressure stage applied on the brine-saturated plugs before and after flooding experiments. Unfortunately, in many cases, the records of the S-waves are unavoidably poor leading to a poor accuracy on VS determination. The Vs data are still presented in this report, but extreme care must be taken when using them.

From previous ultrasonic velocities measurements done on fresh Harvey-1 samples (Delle Piane et al., 2013), VP and VS were recorded around 5000 m/s. The measured P- and S-wave velocities under no confining stress are much lower on these new plugs at around 2200-2300 m/s for VP and 1500-1700 m/s for VS. It is worth noting that the pre-flood plugs 1 and 2 have lower P- and S-wave velocities than that of pre-flood plugs 3 and 4. This observation confirms the previous conclusion from the XCT imaging and density results that plugs 3 and 4 are mechanically stronger (i.e. denser). However, after flooding the measurements conducted on plugs 1 and 3 record the same VP and VS around 2750 and 2050 m/s respectively under 2000 psi confining stress (no post-flood measurement was done on plugs 2 and 4 as they were cut into smaller segments making them unsuitable for the measurements). The post flood velocities are slightly higher than those measured for the initial pre-flood samples under the same stress condition. However, the differences are within the accuracy of the measurements, so the changes before and after flooding are not statistically significant. The computed modulus also do not show clear changes after flooding (Figure 34): the pre- and post-flood results are very similar. On the other hand, the shear modulus (blue circles in Figure 34) seems to record higher values on post-flood plugs 1 and 3. Also the bulk modulus (red squares in Figure 34) for plug 1 only records lower values for the post-flood sample.

The stress sensitivity of the measured parameters is presented in Figure 34a&b and Figure 35 with progressive increase of the VP-VS values (and so the computed modulus) with increase in the confining pressure. The VP-VS seems to reach a plateau around 2000 psi confining pressure with no more increase in the values for Plug 3 (Figure 34c). It is not the case for Vs recorded on Plug 1 (Figure 34a) but this could be possibly due to the poor quality of the Vs recording, particularly under low confining pressures (< 1000 psi). A comparison between the Vp-Vs values recorded under the lowest stress (0 psi) and highest stress (2000 psi) is presented in the form of a histograms in Figure 35 with their differences (in %) depicted in Figure 35c. as can be seen, the differences are about 20% of the pre-flood samples for plugs 1 and 2 and less than 10% in plugs 3 and 4. Overall, the flooding experiments tend to decrease the effect of stress on VP (Proper recording of VS at low stress could not be performed so a comparison between low and high overburden stresses could be presented here).

Table 15. Summary of ultrasonic velocity measurements and derived computed elastic parameters (Poisson's ratio, Shear, bulk and Young modulus) on all the plugs from Harvey-1 before and after the flooding experiments.

	P _{conf} (psi)	P- velocity (m/s)	S- velocity (m/s)	Poisson's ratio	Young's modulus (GPa)	Shear modulus (GPa)	Bulk modulus (GPa)
Plug1 Pre-flood	20	2255	1446	0.150	11.5	5.0	5.5
	200						
	500	2517	1468	0.242	12.8	5.1	8.3
	1000	2650	1520	0.255	13.8	5.5	9.4
	1500	2693	1705	0.165	16.2	6.9	8.0
	2000	2765	1928	0.027	18.2	8.9	6.4
Plug1 Post-flood	0.1						
	200	2422					
	500	2570					
	1000	2683	1928	-0.034	17.1	8.8	5.3
	1500	2743	2041	-0.120	17.4	9.9	4.7
	2000	2787	2083	-0.132	17.9	10.3	4.7
Plug2 Pre-flood	0.1	2221	1498	0.082	11.5	5.3	4.6
	100	2575	1932	-0.144	15.1	8.8	3.9
	1500	2624	1976	-0.156	15.6	9.2	4.0
	2000	2636	2027	-0.223	15.1	9.7	3.5
Plug2 Post-flood							
Plug3 Pre-flood	0.1	2316	1688	-0.067	12.9	6.9	3.8
	200						
	500	2385	1749	-0.082	13.6	7.4	3.9
	1000	2512	1773	0.004	15.3	7.6	5.1
	1500	2615	1801	0.049	16.5	7.9	6.1
	2000	2630	1828	0.032	16.8	8.1	6.0
Plug3 Post-flood	0.1	2385					
	200	2403	1767	-0.089	13.8	7.6	3.9
	500	2520	1868	-0.110	15.1	8.5	4.1
	1000	2631	2006	-0.194	15.7	9.8	3.8
	1500	2659	2042	-0.218	15.8	10.1	3.7
	2000	2711	2048	-0.165	17.0	10.2	4.3
Plug4 Pre-flood	0.1	2432	1579	0.135	13.7	6.0	6.3
	100	2496	1584	0.163	14.1	6.1	7.0
	500	2575	1651	0.151	15.2	6.6	7.3
	1000	2666	1651	0.189	15.7	6.6	8.4
	1500	2681	1651	0.195	15.8	6.6	8.6
	2000	2697	1687	0.178	16.3	6.9	8.4
Plug4 Post-flood							

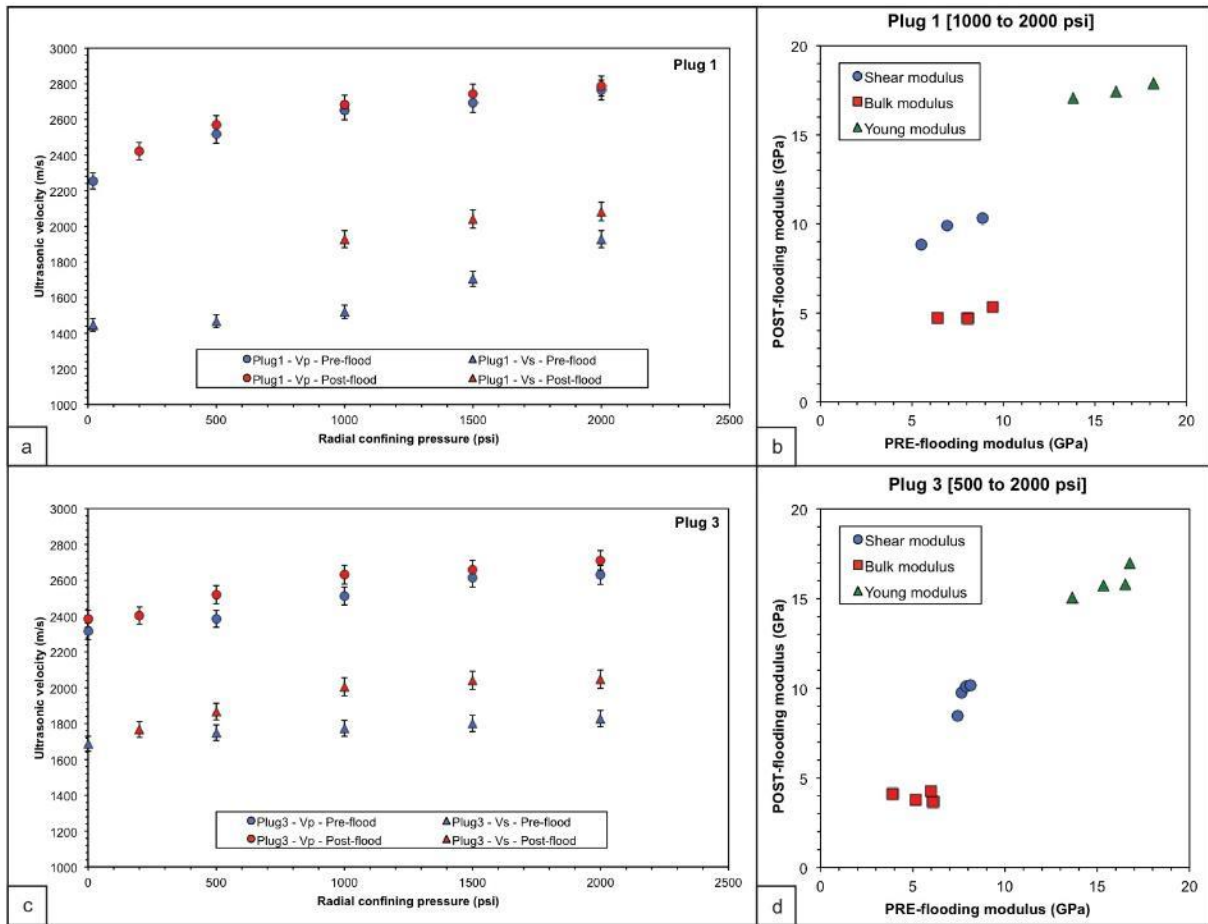


Figure 34. Ultrasonic P- and S-wave measurements on plugs from well Harvey-1 before and after flooding experiments. (a) and (c) correspond to velocities on plugs 1 and 3 respectively before (blue) and after (red) flooding. P-wave velocities are represented by circle symbols while the triangle symbols define the S-wave velocities. The elastic parameters derived from P- and S-wave velocities before flooding are compared with the post-flooding for the plug 1 (b) and plug 3 (d) with red symbols for the bulk modulus, blue symbols for the shear modulus and triangle symbols for the Young modulus.

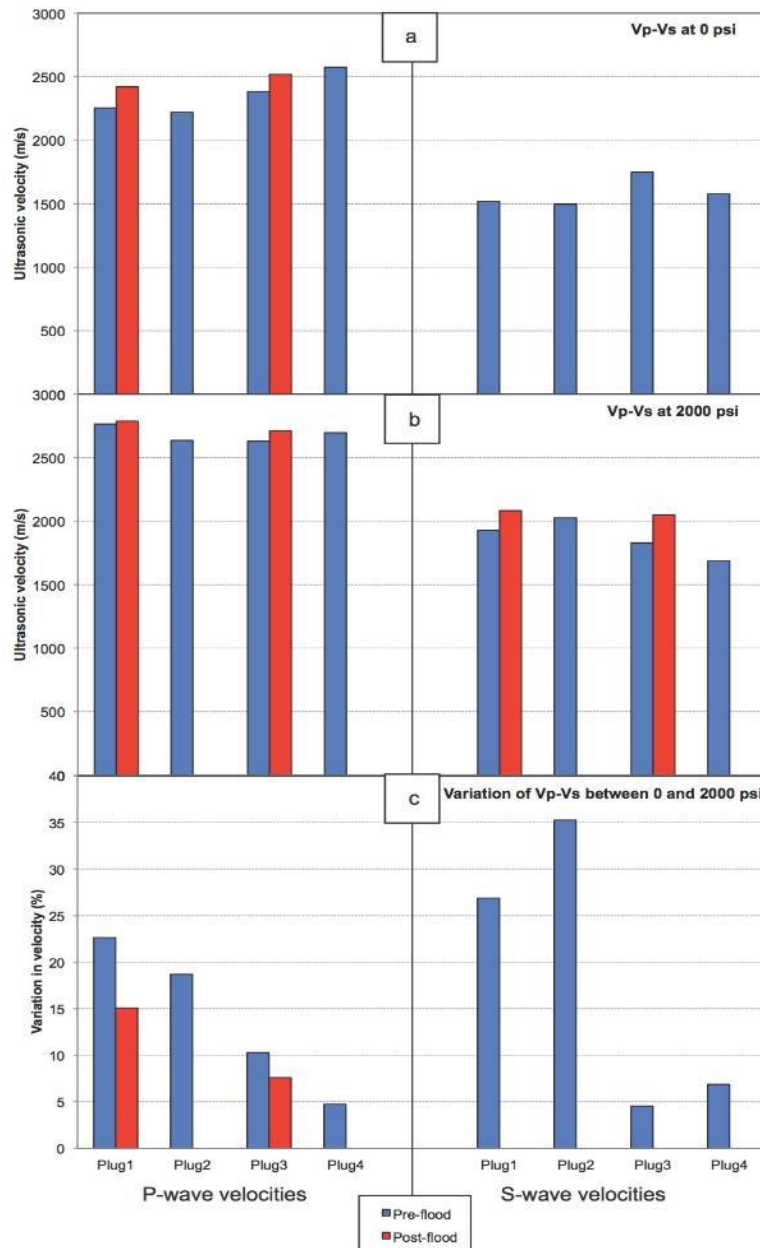


Figure 35. Histograms of P- and S-wave velocities before (blue bars) and after (red bars) flooding for plugs from Harvey-1. (a) velocities at no confining pressure; (b) velocities at 2000 psi confining pressure and (c) Difference (in %) between the velocities recorded at 0 and 2000 psi. Note that the poor S-wave velocities recording at 0 psi confining pressure for the post-flooding experiments did not allow the computation of such variation between 0 and 2000 psi (i.e. no red bars for the post-flooded plugs on histogram (c)).

Electrical resistivity measurement

Electrical resistivity was recorded using both 2- and 4-electrode configurations (where possible) under confining pressure, on the plugs from Harvey-1 before and after flooding. Table 16 summarizes the type of measurements done for each plug from 0 to 13.8 MPa radial confining pressure. The post-flood plug segments H1-2A&B and -4A&B were too short for the electrical rig with confining pressure capability and therefore, measurements without confining stress were possible only. The resistivity results at 1 kHz along with the corresponding computed parameters from Archie's law (Formation factor F, Archie m exponent and Archie tortuosity) are summarized in Table 17. This specific frequency represents the same frequency used in logging tools allowing direct calibration if need be. The resistivity of pre-flood Plug 1 records the highest value at 360 ohm.m while the recorded data for

other plugs are around 100 ohm.m. It is worth noting that the measurements made under the 2- and 4-electrode modes are similar (i.e. good quality measurements) only for Plug 1. The results of the 4-electrode configuration on the other plugs may not be accurate with the recorded resistivity around 3 ohm.m. Poor coupling between the ring and sample could explain unsatisfactory measurement. This type of error is common with such measurements. The effect of confining pressure on resistivity is relatively strong for plugs 2 and 4 with 20-30 % decrease in resistivity under 13.8 MPa pressure compared with that recorded at 0 pressure.

The resistivity evolution with the electrical frequency is presented in Figure 36 and Figure 37 for the pre- and post-flood samples as well as the effect of confining pressure (0 and 13.8MPa). At a given pressure, the resistivity is quite constant at the range of frequencies tested in these experiments, though some polarization effects tend to increase the resistivity towards the low frequency at 10 Hz. At higher stress, the resistivity behaviour is similar over the range of frequencies but only shifted towards higher values for most of the samples. This polarization effect seems to appear prematurely in plug 1 under higher stress at around 1000 Hz using 2 electrodes while issues with electrodes resonance is possible on plug 2 at high stress using the 4 electrodes where high resistivities are recorded toward high frequency (> 200 Hz).

The Archie m exponent is around 3 for all the plugs with the exception of Plug 1 at 3.9 indicating a very complex tortuosity of the pores: tortuosity at 255 for plug 1 when the other samples recorded much lower values around 45-70. As expected, the stress tends to help to "reconnect" some pores to improve the pore connectivity and so decrease the tortuosity complexity.

After flooding, the resistivities decrease moderately for Plug 1 and drastically for Plug 2, while Plug 3 seems to record higher values (Table 17). The frequency behaviour of the resistivity on the post-flood plugs is similar to their pre-flood state (Figure 36 and Figure 37). Less polarization effects is also observed toward low frequencies on the post-flood samples. The Archie parameters record lower values than those measured during the pre-flood tests (Table 17). The Archie m exponent is now about 3 for plugs 1 and 3 and 2.4 in Plug 2. The stress effect on these post-flood samples is less pronounced. The stress tends to increase the resistivity with the exception of Plug 2, similar to its pre-flood state with lower resistivities.

Table 16. Workflow of electrical impedance spectroscopy measurements on each sample before and after flooding in Harvey-1. Time scan resistivity measurement at 1 kHz and EIS with confining pressure was only possible on long plugs (i.e. not possible on 2A&B and 4A&B).

Sample	BEFORE flooding		AFTER flooding	
	0 MPa	13.8 MPa	0 MPa	13.8 MPa
1	2 and 4 electrodes Time scan at 2 electrodes	x	2 and 4 electrodes Time scan at 2 electrodes	2 and 4 electrodes
2	2 and 4 electrodes Time scan at 4 electrodes	2 and 4 electrodes	x	x
2A	x	x	2 and 4 electrodes	x
2B	x	x	2 and 4 electrodes	x
3	2 and 4 electrodes Time scan at 4 electrodes	2 and 4 electrodes	2 and 4 electrodes Time scan at 2 electrodes	2 and 4 electrodes
4	2 and 4 electrodes Time scan at 4 electrodes	2 and 4 electrodes	x	x
4A	x	x	2 electrodes	x
4B	x	x	2 electrodes	x

Table 17. Summary of electrical resistivity acquired at 1 kHz before and after flooding using 2 and 4 electrodes under 0 (and 13.8 MPa where possible) confining pressure for Harvey-1 samples. Some data were not acquired due to technical problems: dark grey cells; while data with not so good electrodes coupling are highlighted in orange cells.

Plug ID	Electrodes mode - P _{conf} (MPa)	Pre-flood				Electrodes mode - P _c (MPa)	Post-flood			
		Sample resistivity at 25°C	Archie Formation Factor	Archie m exponent	Archie tortuosity		Sample resistivity at 25°C	Archie Formation Factor	Archie m exponent	Archie tortuosity
1	2 - 0	359	1706	3.9	255	2 - 0	89	458	3.1	65
						2 - 6.9	150	788	3.4	110
						2 - 13.8	153	766	3.3	103
	4 - 0	367	1745	3.9	258	4 - 0	64	328	3.0	47
						4 - 6.9	143	753	3.4	105
					4 - 13.8	144	726	3.3	98	
2	2 - 0	62	289	3.0	45	2-A - 0	14	73	2.4	12
	2 - 13.8	43	196	2.8	29	2-B - 0	11	59	2.3	10
	4 - 0	3	15	1.5	2	4-A - 0	13	66	2.3	11
	4 - 13.8	36	167	2.7	25	4-B - 0	10	51	2.2	8
3	2 - 0	75	343	2.8	44	2 - 0	149	778	3.2	94
	2 - 13.8	1000	4612	4.0	567	2 - 13.8	821	4029	3.8	465
	4 - 0	3	13	1.2	2	4 - 0	50	262	2.6	32
	4 - 13.8	2	11	1.1	1	4 - 13.8	20	100	2.1	12
4	2 - 0	112	514	3.1	67					
	2 - 13.8	81	371	2.8	46					
	4 - 0					4-A - 0	10	51	1.9	7
	4 - 13.8	3	15	1.3	2	4-B - 0	12	61	2.0	8

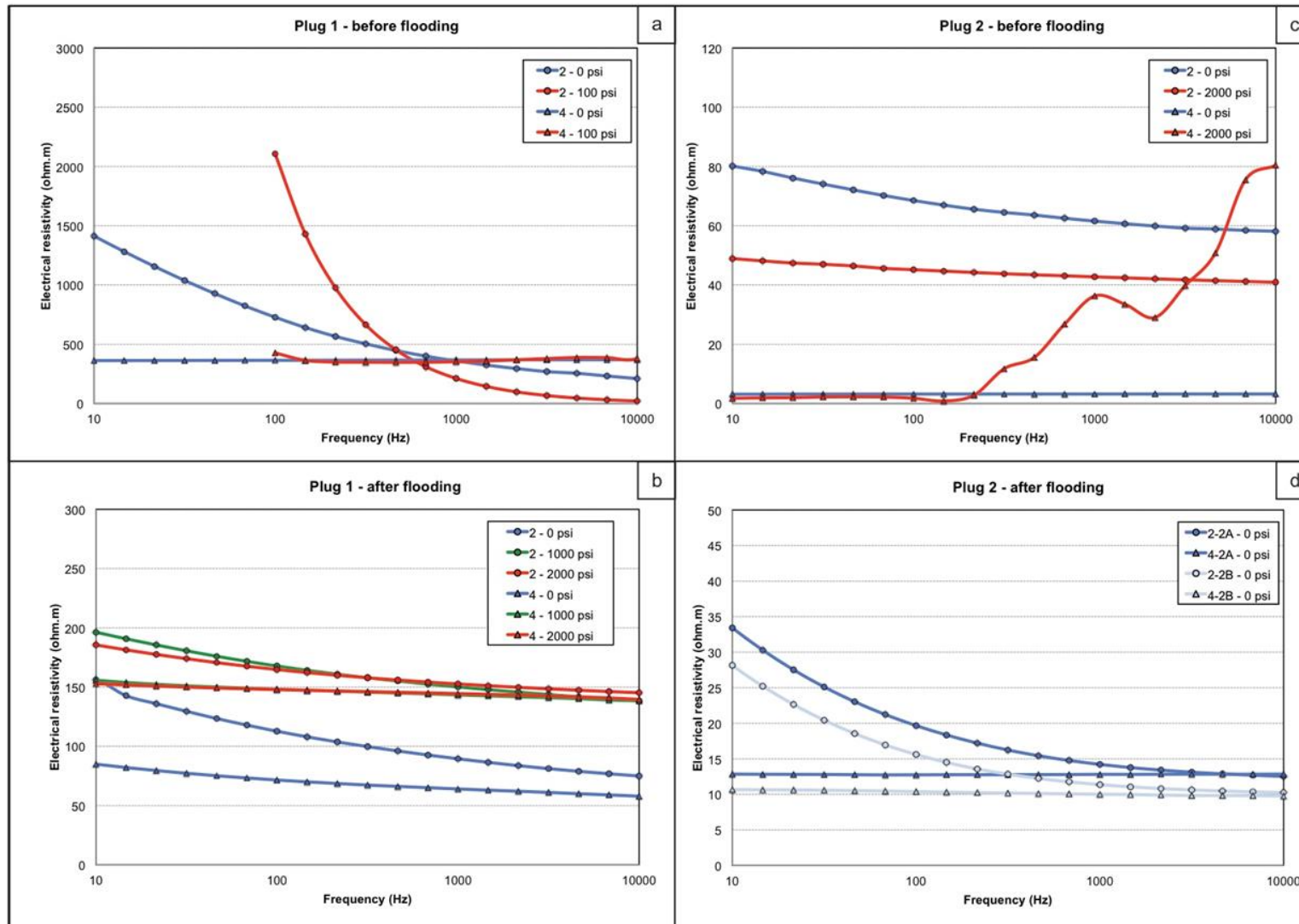


Figure 36. EIS spectrum from 10 Hz to 10 kHz before and after flooding under various confining pressures for samples from Harvey-1: Plug 1 before (a) and after (b) flooding; and Plug 2 before (c) and after (d) flooding. The circle symbols represent the 2 electrodes mode and the triangles are the 4 electrodes mode. The blue curves represent 0 psi confining pressure, the red are for 2000 psi (or 100 psi) and the green curves are recorded at 1000 psi.

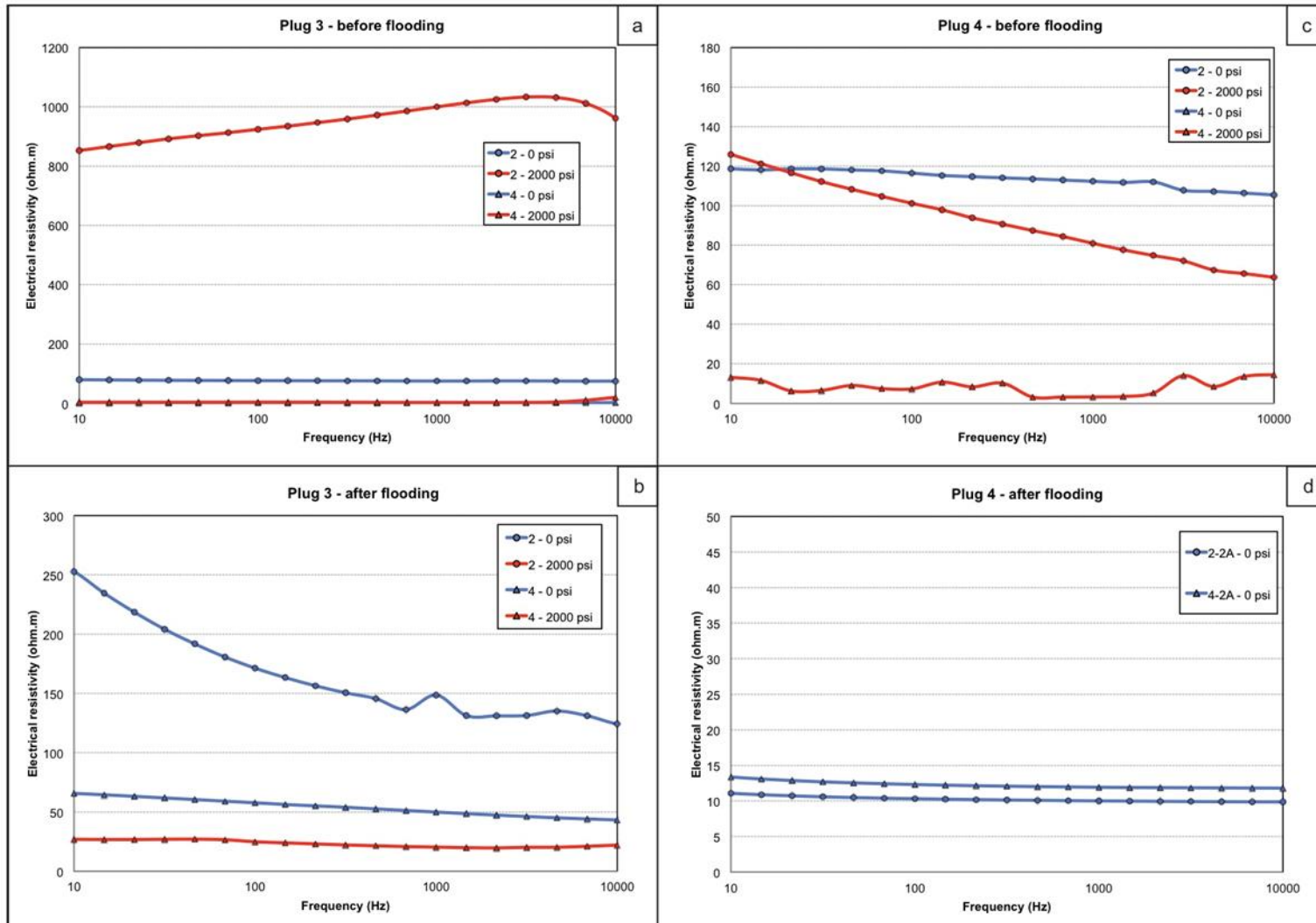


Figure 37. EIS spectrum from 10 Hz to 10 kHz before and after flooding under various confining pressures for samples from Harvey-1: Plug 3 before (a) and after (b) flooding; and Plug 4 before (c) and after (d) flooding. The circle symbols represent the 2 electrodes mode and the triangles are the 4 electrodes mode. The blue curves represent 0 psi confining pressure, the red are for 2000 psi (or 100 psi) and the green curves are recorded at 1000 psi.

The resistivity evolutions with time and stress along with the temperature log of the measurements for the experiments conducted on Harvey-1 samples are presented in Figure 38 to Figure 43 for both before and after flood samples. The post-flood results for plugs 2 and 4 are not provided as, for the flooding experiments, they were each cut into smaller plug segments and the length of each segment was not long enough for the resistivity measurement apparatus.

Plug 1 was tested before and after the flooding experiments using a 2-electrode configuration (Figure 38 and Figure 39). After applying a small confining stress, the electrode coupling is immediately enhanced and therefore the resistivity drops more or less depending on the quality of the coupling. Indeed, the coarse grained nature of these samples is not optimum for the silver flat electrodes to establish perfect contact with the sample surface. However, after applying reasonable stress (> 0.1 MPa), the electrodes seem to stabilize indicating good contact with the sample. The resistivity needs about 5000 seconds to reach a stabilised plateau at a given stress when the pre-flood sample is tested, while the stabilization is quasi-instantaneous on the same plug in its post-flood state. However, a higher stress (about 7 MPa) is required to enhance the electrode coupling with the sample compared to the pre-flood sample.

Plugs 2 and 4 were tested only in their pre-flood state using a 4-electrode configuration (Figure 40 and Figure 43). On plug 2, the resistivity coupling seems of good quality even at no confining pressure (i.e. stable response over time) with quasi-instantaneous electrical response when the pressure changes. When a pressure of 6.9 MPa is applied, the electrical signal starts to become unstable with strong variations. Beyond 10 MPa, a linear moving window using 10 points had to be used to smooth out such variations (green curve – Figure 40). Under these new higher confining pressures, longer time is necessary to reach electrical stabilization. For instance, when 10.3 MPa and 13.8 MPa are applied, the resistivity only stabilizes after waiting for around 1000 seconds (or around 20 minutes at least). More interestingly, the resistivity decreases at different stages of pressures from 0 to 6.9 MPa and then starts to increase with pressures higher than that. It may be speculated that pore connectivity is improved under low pressure before a decrease in pore size and/or pore connectivity under higher pressure leading to increase in the resistivity. Given the very low resistivity under low pressure, it is also possible that a poor coupling between the sample and electrodes may have affected the resistivity reading at low pressure. The coupling seems to be reasonable only from 7 MPa confining stress.

For Plug 4 (Figure 43), the resistivity is extremely unstable from 0 to the highest confining pressures, much more than the previously tested Plug 2. Using a linear moving average window with 10 points, the signal is improved but still noisy. It looks like that the resistivity responds slowly to each new pressure taking more than 1000 seconds: the signal stabilizes with time. As expected, the resistivity increases with the confining pressure, except for around 6.9 MPa. It is possible that sample coupling with electrodes was not perfect or that the brine saturating the sample was released at the sample interface with the electrodes at this pressure, decreasing the general resistivity. In Plug 4, it is important to note that resistivity went from values around 100 ohm.m at low pressure to one order higher under pressures > 10 MPa. The pore connectivity seems to be particularly sensitive to pressure.

Finally, Plug 3 was measured before and after flooding using 4- and 2-electrode configurations respectively (Figure 41 and Figure 42). Before flooding, the general resistivity of the sample at low pressure is around 300 ohm.m and doubles after 7 MPa confining stress. The time required for measurement to stabilise is quite long: ~ 1000 to 2000 seconds. But when 10 MPa confining stress is

applied, the resistivity progressively decreases with time and never stabilises. At this pressure, the sample-electrodes coupling should be excellent and such a drift in measurements cannot be explained. After flooding, such drift in resistivity is only visible after applying 6.9 MPa where the resistivity suddenly drops; but then increases again after waiting for a very long period of time (~ 5000 seconds) and then keep increasing under higher pressures. The sample always records higher resistivity at each increasing confining pressure with similar resistivities at very low pressure and slightly higher for 3.4 and 6.9 MPa at around 800 ohm.m. The post-flood sample still needs 1000 to 2000 seconds to stabilize at every new confining pressure. At high pressure (> 10 MPa), the resistivity is around 900 ohm.m.

As a general learning point from Harvey-1 electrical analysis, if electrical logs measured in a well is to be processed, these data would suggest using an Archie $m = 3$ to compute the saturation and directly derive porosity. Such processing could result in an independent porosity log besides Density, Neutron-density or NMR. It appears that Plug 1 is an exception with Archie $m = 3.9$ precluding more complex pore geometry: diagenetic processes and/or clays interactions. It is worth noting that among the plugs tested from Harvey-1 this plug has a much lower permeability (38 mD compared with around 80 mD for other plugs). In general, the “tightness” of the rocks interferes with their electrical properties due to their poorer pore connectivity. Therefore, Archie m must be increased to assess more properly the saturation/porosity. The stress effect (reservoir in-situ conditions) would tend to decrease the pore geometry complexity: close micro-cracks.

On the post flooded samples, the Archie m is reduced to 2.4, close to “clean” standard sandstones, though plug 1 still records high $m = 3$. The flooding seems to have improved the pore connectivity. Therefore, tracking the resistivity decrease intensity using $m = 2.4$ would help to monitor the intensity of reservoir alteration and back compute porosity evolution. However, the stress tends to hide such effects, as the alteration caused by flooding in these rock samples is very small. But the major learning is that electrical measurements seem to be very sensitive to any change in pore connectivity and porosity making this tool a good candidate for monitoring pore network changes with time during CO₂ injection/storage.

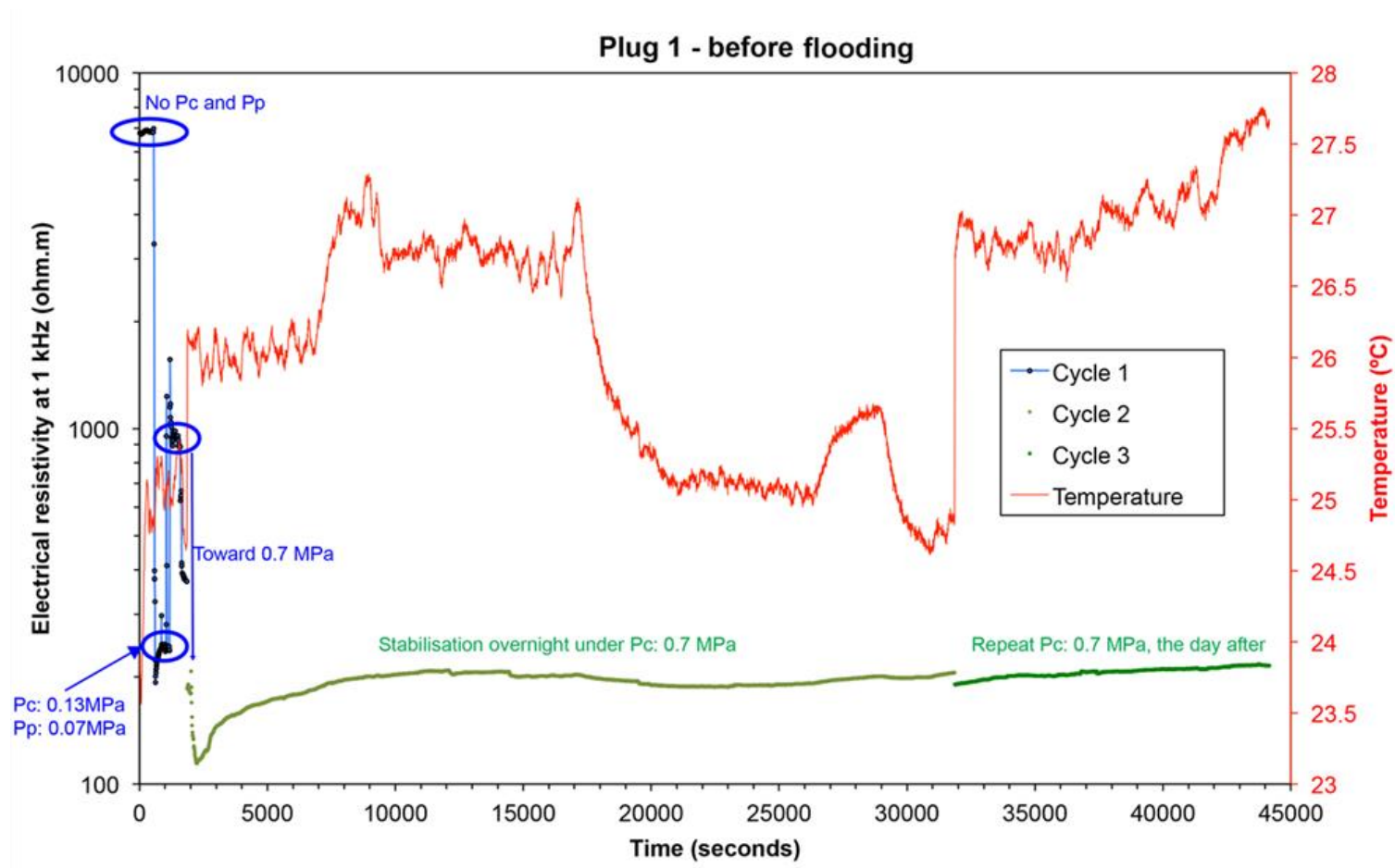


Figure 38. Electrical resistivity at 1 kHz with time recorded with 2 electrodes under progressive increase of confining pressure stages of plug 1 of Harvey-1 before flooding. The red curves represent the temperature monitoring with time while the other curves are successive recording of resistivity with time.

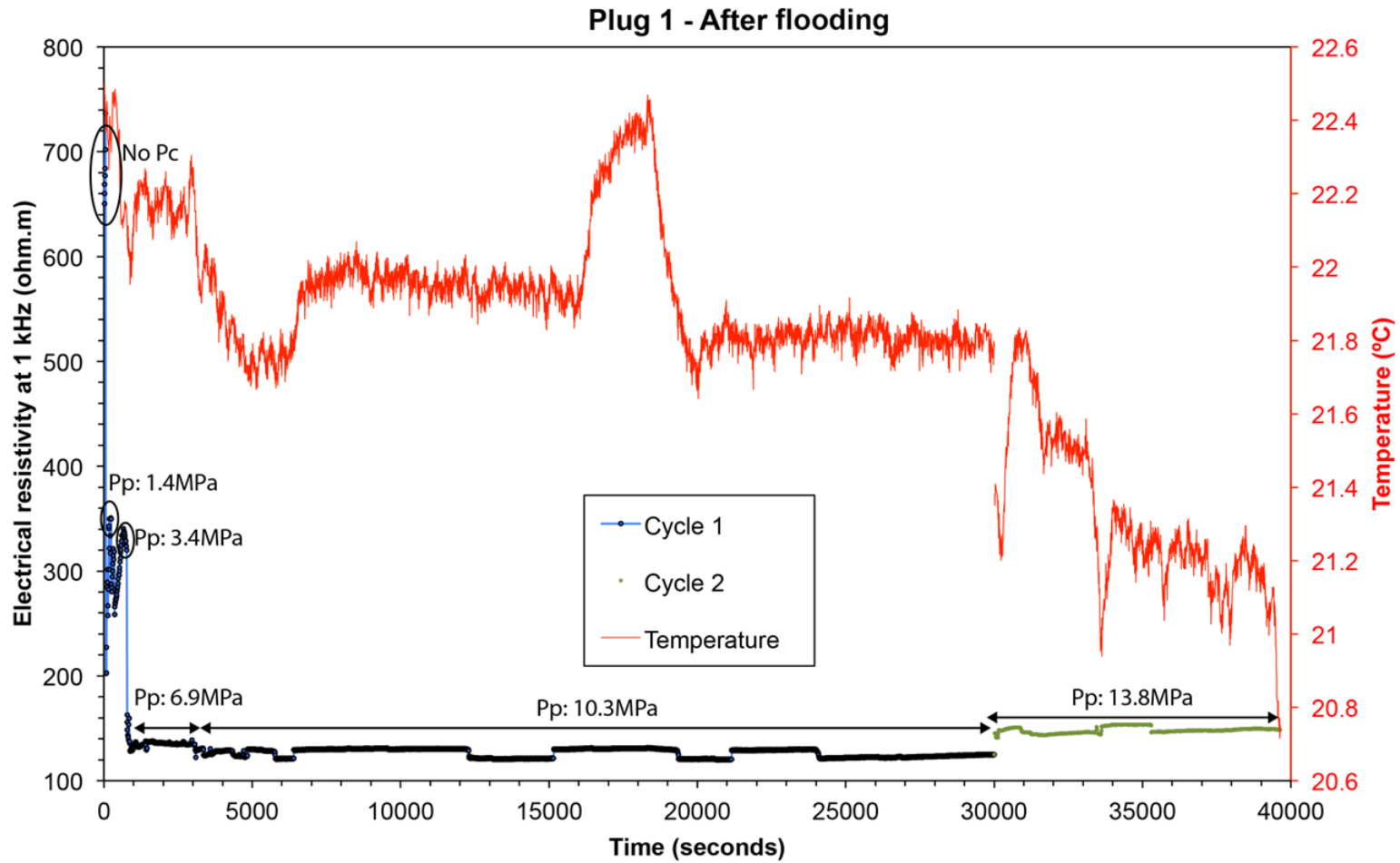


Figure 39. Electrical resistivity at 1 kHz with time recorded with 2 electrodes under progressive increase of confining pressure stages of plug 1 of Harvey-1 after flooding. The red curves represent the temperature monitoring with time while the other curves are successive recording of resistivity with time.

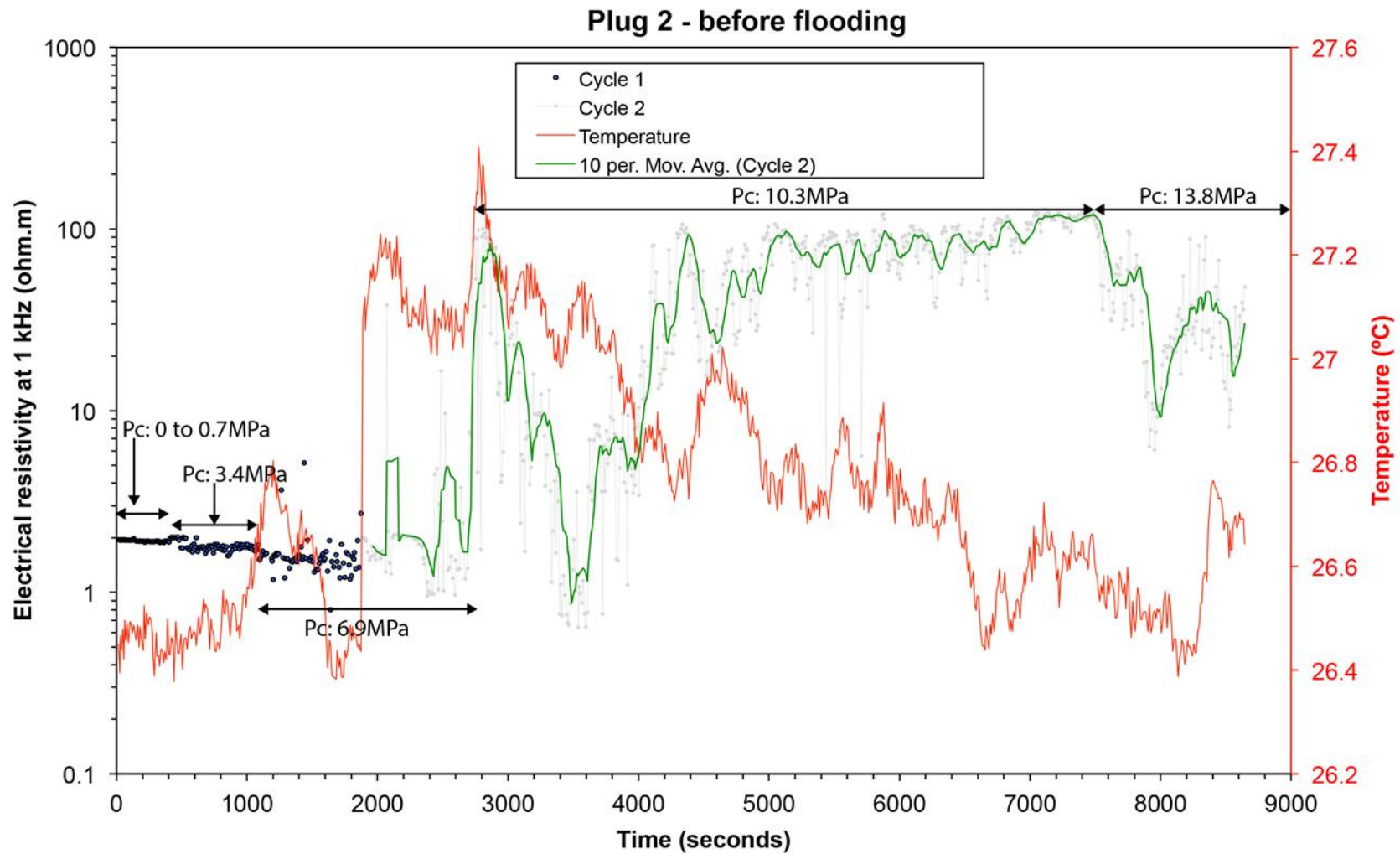


Figure 40. Electrical resistivity at 1 kHz with time recorded with 4 electrodes under progressive increase of confining pressure stages of plug 2 of Harvey-1 before flooding. The red curves represent the temperature monitoring with time while the other curves are successive recording of resistivity with time.

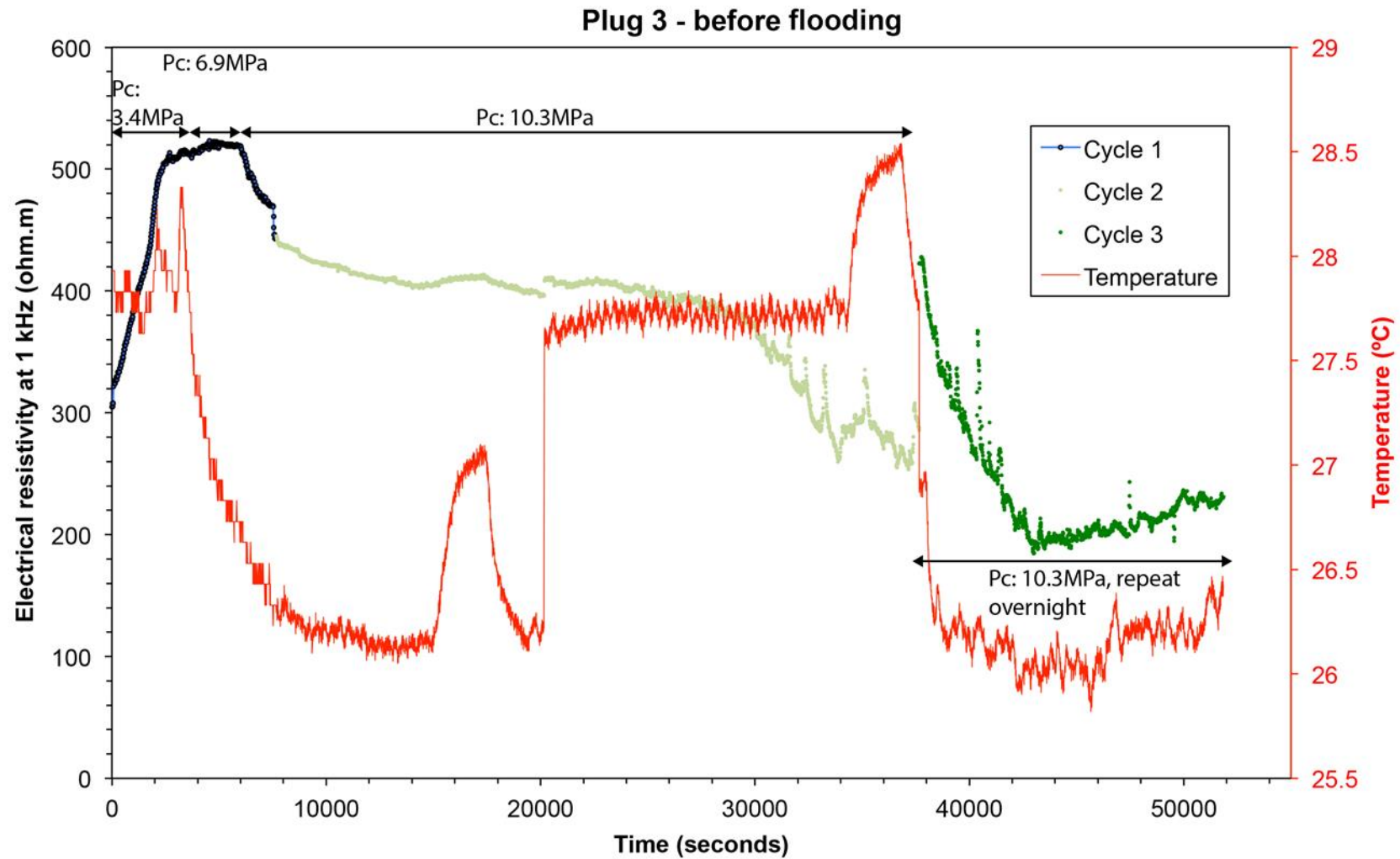


Figure 41. Electrical resistivity at 1 kHz with time recorded with 4 electrodes under progressive increase of confining pressure stages of plug 3 of Harvey-1 before flooding. The red curves represent the temperature monitoring with time while the other curves are successive recording of resistivity with time.

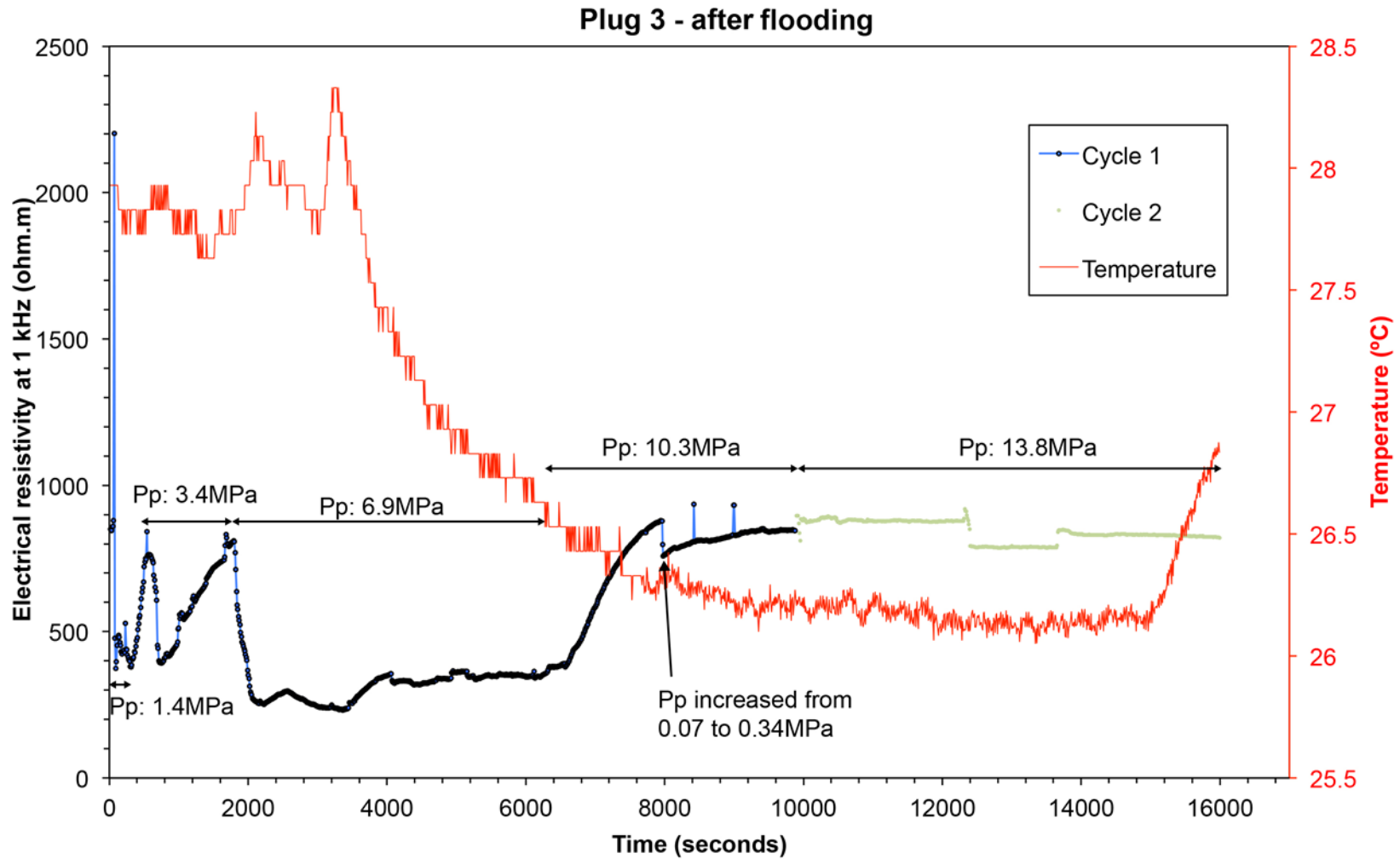


Figure 42. Electrical resistivity at 1 kHz with time recorded with 2 electrodes under progressive increase of confining pressure stages of plug 3 of Harvey-1 after flooding. The red curves represent the temperature monitoring with time while the other curves are successive recording of resistivity with time.

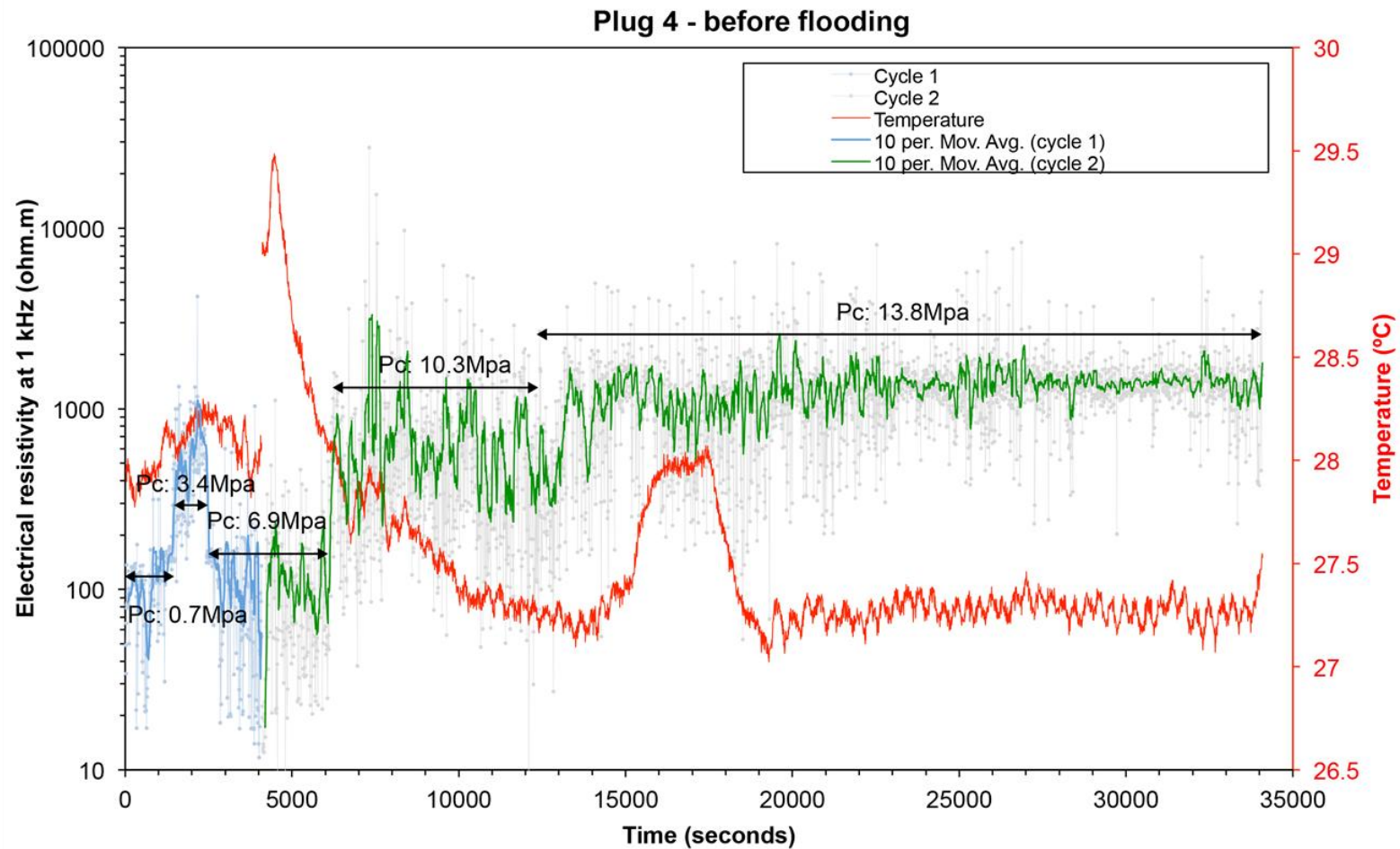


Figure 43. Electrical resistivity at 1 kHz with time recorded with 4 electrodes under progressive increase of confining pressure stages of plug 4 of Harvey-1 before flooding. The red curves represent the temperature monitoring with time while the other curves are successive recording of resistivity with time.

Electrical Resistivity Results- Harvey-3 and 4

For the Harvey-3 samples, the electrical resistivity spectrum was measured on Plug 2 (H3-Plug2) before and after the core-flood experiment at room condition. Because of the lack of pressure applied on the sample and the relatively high permeability of the plug, the water from the pores at the top of the plug tended to move towards the bottom of the plug under gravity, with plug placed vertically, leading to extra water at the interface between sample and electrode at the bottom of the plug. This phenomenon led to the generation of a strong polarisation (Figure 44) that permeates toward low frequency (1 kHz) while it is usually occurring at the higher frequencies (> 10 kHz). Therefore, only the range between 10 and 100 Hz is free of polarisation and records proper resistivity (Figure 44). Both 2 and 4 electrodes systems record similar values around 3 ohm.m (Table 18). The derived Archie's parameters show also similar values with a formation factor at 16 and an m Archie exponent close to a clean sandstone: 1.8. The tortuosity remains very low at 3.5.

For the Harvey-4 samples, the Electrical resistivity spectrum was measured on pre- and post-flood samples under room conditions using 2 electrodes for the short plug segments of A and B in plugs 1 and 3 and with 4 electrodes for the long plugs (2 and 4). Because no confining pressure was applied on the samples the pores at the top of the plugs tend to quickly become empty during the measurements while the pores at the bottom become over-filled leading to extra water at the interface between the samples and bottom electrodes. This phenomenon led to the generation of a strong polarization (Figure 45 and Figure 46) that permeated toward low frequency (100 Hz), something that usually occurs at the higher frequencies (> 10 kHz). Therefore, only the range between 10 and 100 Hz is free of polarization and records proper resistivity (Figure 45 and Figure 46). The 2 (and 4) electrodes systems record similar values around 5-6 ohm.m at 100 Hz (Table 19 to Table 22). After the flooding experiments, this resistivity remains unchanged on the permeable samples (plugs 1 and 2) while slightly increases (about 1 ohm.m) from its original value on the tight samples (plugs 3 and 4). The derived Archie's parameters show also similar trends among the sample collections with Archie m parameter around 1.8 (which is similar to previously recorded samples from Harvey-1 and -3) which increases to 2.1 after flooding. The Archie formation factor is around 25 for the pre-flood samples and remains quasi-unchanged in plugs 1, 2 and 4 while it doubles in the short 3A and 3B plugs.

For some of the samples from Harvey-3 and -4, the low recorded resistivities is reflective of the relatively moderate to high porosity and permeability of these samples and the fact that these samples were weakly cemented (compared with Harvey-1 samples). This masks any difference between the pre- and post-flood states of the samples in terms of their electrical resistivities.

In comparison to Harvey-1 samples, the samples from Harvey-3 and Harvey-4 are behaving as clean sandstones with Archie $m = 1.8$ and stress tends to hide changes with m quasi-similar at $m = 2.1$ close to the observed values for Harvey-1. Combining all measurements for all three Harvey wells, a pattern seems to appear for Archie m : after flooding, Archie m tends to decrease if the permeability is below 50 mD; above such permeability limit, m remains the same or slightly increase to $m = 2$ (clean sandstone behaviour). The effect of change in stress on the post-flood Harvey-1 samples seems to be somewhat opposite that achieved for the post-flood Harvey-3/Harvey-4 samples:

- In Harvey-1 samples: when $k < 50$ mD, stress sensitivity of porosity-permeability-electrical parameters remains unchanged after flooding. When $k > 50$ mD, stress sensitivity of all the above parameters increases.

- In Harvey-3/Harvey-4 samples: when $k < 50$ mD, stress sensitivity of porosity-permeability-electrical parameters remains unchanged after flooding. When $k > 50$ mD, stress sensitivity of all the above parameters decreases.

Different cementation/diagenetic processes could explain the above observed opposite trends on when $k > 50$ mD.

Table 18. Summary of the electrical impedance spectroscopy between 10Hz and 100 kHz on the pre- and post-flood under room conditions using 2 electrodes system for Plug 2 of Harvey-3. The derived Archie parameters: Formation factor, M exponent and Tortuosity are also presented.

PRE-FLOOD							PRE-FLOOD						
2 electrodes - no confining stress							4 electrodes - no confining stress						
Frequency	Impedance	Phase	Sample resistivity at 25°C	Archie Formation Factor	Archie m exponent	Archie tortuosity	Z	Phase	Sample resistivity at 25°C	Archie Formation Factor	Archie m exponent	Archie tortuosity	
Hz	(ohm)	(°)	(ohm.m)	[]	[]	[]	(ohm)	(°)	(ohm.m)	[]	[]	[]	
100000	100000.9	0.2	1348.7	6905.1	5.8	1484.6	100000.0	0.1	3558.3	18217.8	6.4	3916.8	
73565	73566.0	0.3	992.2	5079.8	5.6	1092.1	73565.1	0.1	2617.7	13401.9	6.2	2881.4	
54117	54118.3	0.4	729.9	3736.9	5.4	803.4	54117.1	0.1	1925.7	9858.9	6.0	2119.7	
39811	39812.5	0.5	537.0	2749.1	5.2	591.1	39811.1	0.1	1416.6	7252.7	5.8	1559.3	
29286	29287.8	0.6	395.0	2022.3	5.0	434.8	29286.1	0.2	1042.1	5335.3	5.6	1147.1	
21544	21546.1	0.7	290.6	1487.8	4.8	319.9	21544.2	0.2	766.6	3924.9	5.4	843.8	
15849	15851.6	0.8	213.8	1094.6	4.6	235.3	15849.2	0.3	564.0	2887.4	5.2	620.8	
11659	11662.2	0.9	157.3	805.3	4.4	173.1	11659.3	0.4	414.9	2124.1	5.0	456.7	
8576.9	8580.9	1.1	115.7	592.5	4.2	127.4	8577.3	0.5	305.2	1562.6	4.8	336.0	
6309.6	6314.7	1.2	85.2	436.0	4.0	93.7	6310.2	0.6	224.5	1149.6	4.6	247.2	
4641.5	4648.2	1.3	62.7	321.0	3.8	69.0	4642.2	0.8	165.2	845.7	4.4	181.8	
3414.6	3423.4	1.3	46.2	236.4	3.6	50.8	3415.6	0.9	121.5	622.2	4.2	133.8	
2511.9	2523.5	1.4	34.0	174.2	3.4	37.5	2513.3	1.1	89.4	457.9	4.0	98.4	
1847.8	1863.3	1.4	25.1	128.7	3.2	27.7	1849.7	1.2	65.8	337.0	3.8	72.4	
1359.4	1380.1	1.5	18.6	95.3	3.0	20.5	1361.9	1.3	48.5	248.1	3.6	53.3	
1000	1027.8	1.5	13.9	71.0	2.8	15.3	1003.4	1.4	35.7	182.8	3.4	39.3	
735.64	772.9	1.5	10.4	53.4	2.6	11.5	740.3	1.4	26.3	134.9	3.2	29.0	
541.16	590.8	1.5	8.0	40.8	2.4	8.8	547.4	1.5	19.5	99.7	3.0	21.4	
398.11	463.5	1.5	6.3	32.0	2.3	6.9	406.5	1.5	14.5	74.1	2.8	15.9	
292.87	377.5	1.5	5.1	26.1	2.1	5.6	304.2	1.5	10.8	55.4	2.6	11.9	
215.44	322.0	1.6	4.3	22.2	2.0	4.8	230.6	1.5	8.2	42.0	2.4	9.0	
158.49	288.3	1.6	3.9	19.9	1.9	4.3	178.5	1.5	6.4	32.5	2.3	7.0	
116.59	269.2	1.6	3.6	18.6	1.9	4.0	142.6	1.5	5.1	26.0	2.1	5.6	
85.769	259.6	1.6	3.5	17.9	1.9	3.9	118.7	1.6	4.2	21.6	2.0	4.6	
63.095	255.8	1.6	3.5	17.7	1.9	3.8	103.5	1.6	3.7	18.8	1.9	4.1	
46.416	255.7	1.6	3.4	17.7	1.9	3.8	94.2	1.6	3.4	17.2	1.8	3.7	
34.146	258.0	1.6	3.5	17.8	1.9	3.8	88.7	1.6	3.2	16.2	1.8	3.5	
25.119	262.1	1.6	3.5	18.1	1.9	3.9	85.6	1.6	3.0	15.6	1.8	3.4	
18.479	268.0	1.6	3.6	18.5	1.9	4.0	83.8	1.6	3.0	15.3	1.8	3.3	
13.594	275.6	1.6	3.7	19.0	1.9	4.1	82.8	1.6	2.9	15.1	1.8	3.2	
10	285.0	1.6	3.8	19.7	1.9	4.2	82.1	1.6	2.9	15.0	1.8	3.2	
Mean	265.4	1.6	3.6	18.3	1.9	3.9	98.0	1.6	3.5	17.9	1.9	3.8	
STDEV	10.0	0.0	0.1	0.7	0.0	0.1	20.6	0.0	0.7	3.8	0.1	0.8	

POST-FLOOD							POST-FLOOD						
2 electrodes - no confining stress							4 electrodes - no confining stress						
Frequency	Impedance	Phase	Sample resistivity at 25°C	Archie Formation Factor	Archie m exponent	Archie tortuosity	Z	Phase	Sample resistivity at 25°C	Archie Formation Factor	Archie m exponent	Archie tortuosity	
Hz	(ohm)	(°)	(ohm.m)	[]	[]	[]	(ohm)	(°)	(ohm.m)	[]	[]	[]	
100000	100000.3	0.1	1373.2	6905.1	5.9	1526.0	100000.0	0.0	3623.0	18217.8	6.5	4026.1	
73565	73565.3	0.2	1010.2	5079.7	5.7	1122.6	73565.0	0.1	2665.3	13401.9	6.3	2961.8	
54117	54117.5	0.2	743.2	3736.8	5.4	825.8	54117.1	0.1	1960.7	9858.9	6.1	2178.8	
39811	39811.6	0.3	546.7	2749.0	5.2	607.5	39811.1	0.1	1442.4	7252.7	5.9	1602.8	
29286	29286.9	0.4	402.2	2022.3	5.0	446.9	29286.1	0.2	1061.0	5335.3	5.7	1179.1	
21544	21545.2	0.5	295.9	1487.7	4.8	328.8	21544.2	0.2	780.6	3924.9	5.5	867.4	
15849	15850.6	0.7	217.7	1094.5	4.6	241.9	15849.2	0.3	574.2	2887.4	5.3	638.1	
11659	11661.2	0.8	160.1	805.2	4.4	178.0	11659.3	0.4	422.4	2124.1	5.1	469.4	
8576.9	8579.9	1.0	117.8	592.4	4.2	130.9	8577.3	0.5	310.8	1562.6	4.9	345.3	
6309.6	6313.7	1.1	86.7	436.0	4.0	96.3	6310.1	0.6	228.6	1149.6	4.7	254.1	
4641.5	4647.0	1.2	63.8	320.9	3.8	70.9	4642.2	0.8	168.2	845.7	4.5	186.9	
3414.6	3422.1	1.3	47.0	236.3	3.6	52.2	3415.6	0.9	123.7	622.2	4.3	137.5	
2511.9	2522.1	1.4	34.6	174.2	3.4	38.5	2513.2	1.1	91.1	457.9	4.1	101.2	
1847.8	1861.7	1.4	25.6	128.5	3.2	28.4	1849.6	1.2	67.0	337.0	3.9	74.5	
1359.4	1378.2	1.5	18.9	95.2	3.0	21.0	1361.8	1.3	49.3	248.1	3.7	54.8	
1000	1025.5	1.5	14.1	70.8	2.8	15.6	1003.3	1.4	36.4	182.8	3.5	40.4	
735.64	769.9	1.5	10.6	53.2	2.6	11.7	740.1	1.4	26.8	134.8	3.2	29.8	
541.16	587.0	1.5	8.1	40.5	2.5	9.0	547.2	1.5	19.8	99.7	3.0	22.0	
398.11	458.6	1.5	6.3	31.7	2.3	7.0	406.3	1.5	14.7	74.0	2.9	16.4	
292.87	371.1	1.5	5.1	25.6	2.1	5.7	303.9	1.5	11.0	55.4	2.7	12.2	
215.44	313.8	1.6	4.3	21.7	2.0	4.8	230.1	1.5	8.3	41.9	2.5	9.3	
158.49	278.2	1.6	3.8	19.2	2.0	4.2	177.9	1.5	6.4	32.4	2.3	7.2	
116.59	257.0	1.6	3.5	17.7	1.9	3.9	141.7	1.5	5.1	25.8	2.2	5.7	
85.769	245.1	1.6	3.4	16.9	1.9	3.7	117.5	1.6	4.3	21.4	2.0	4.7	
63.095	238.9	1.6	3.3	16.5	1.9	3.6	101.9	1.6	3.7	18.6	1.9	4.1	
46.416	235.9	1.6	3.2	16.3	1.8	3.6	92.2	1.6	3.3	16.8	1.9	3.7	
34.146	235.0	1.6	3.2	16.2	1.8	3.6	86.3	1.6	3.1	15.7	1.8	3.5	
25.119	235.5	1.6	3.2	16.3	1.8	3.6	82.6	1.6	3.0	15.1	1.8	3.3	
18.479	237.0	1.6	3.3	16.4	1.9	3.6	80.3	1.6	2.9	14.6	1.8	3.2	
13.594	239.5	1.6	3.3	16.5	1.9	3.7	78.6	1.6	2.8	14.3	1.8	3.2	
10	243.1	1.6	3.3	16.8	1.9	3.7	77.2	1.6	2.8	14.1	1.8	3.1	
Mean	240.8	1.6	3.3	16.6	1.9	3.7	95.4	1.6	3.5	17.4	1.9	3.8	
STDEV	7.0	0.0	0.1	0.5	0.0	0.1	21.7	0.0	0.8	4.0	0.1	0.9	

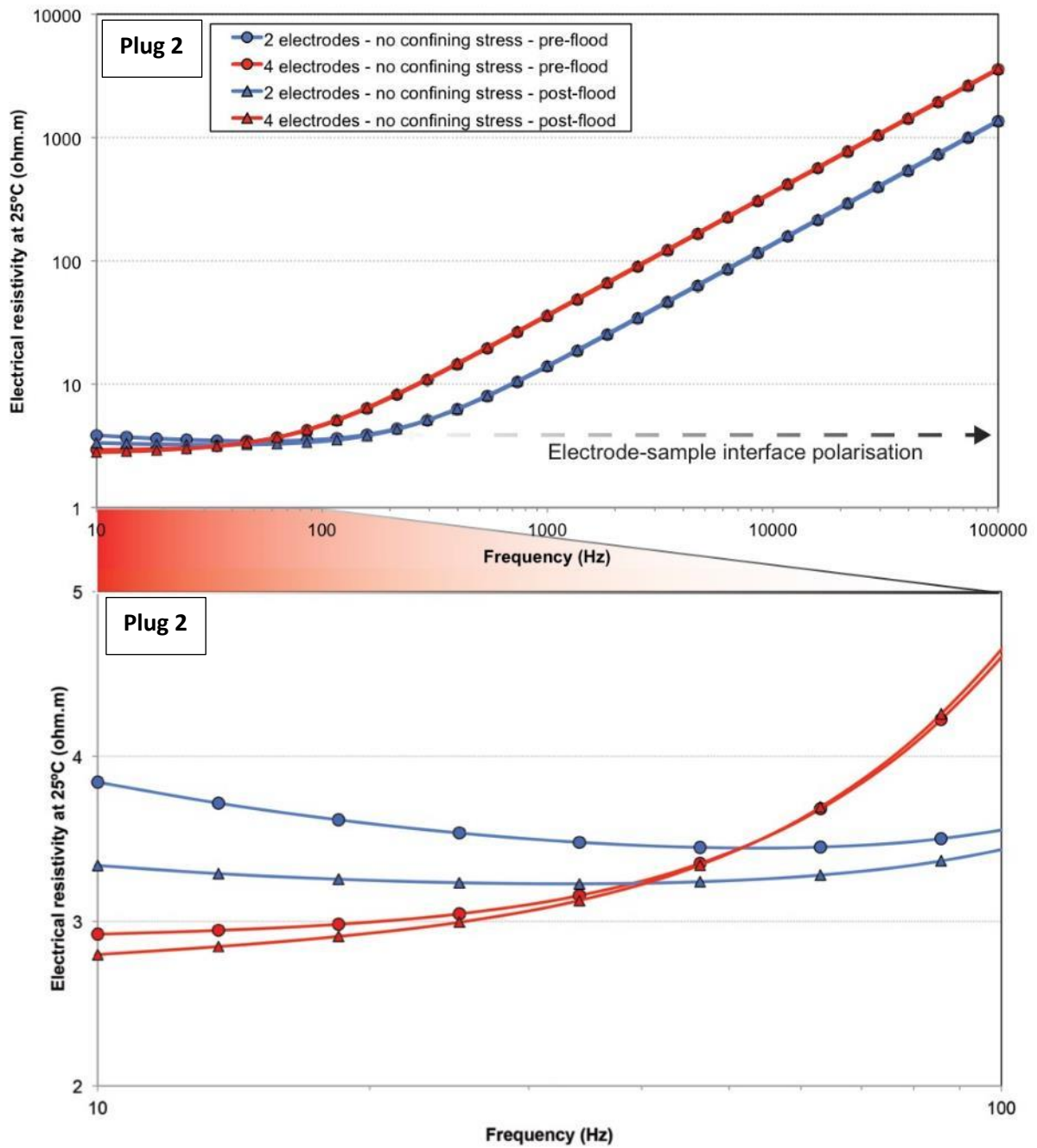


Figure 44. Electrical Impedance spectroscopy of saturated plug 2 of Harvey-3 before (blue curves) and after flooding (red curves) between 10 and 10 kHz (top graph). Note the strong polarization from 100 Hz to 100 kHz: high values with a linear trend. The bottom plot shows a magnification of the top graph only between 10 and 100 Hz free of polarization effect.

Table 19. Summary of the electrical impedance spectroscopy between 10Hz and 100 kHz on the pre- and post-flood plugs under room conditions using 2 electrodes system for plug segments 1A & 1B from Harvey-4 well. The derived Archie parameters: Formation factor, m exponent and Tortuosity are also presented.

PRE-FLOOD													
H4FS1A - 2 electrodes - no confining stress							H4FS1B - 2 electrodes - no confining stress						
Frequency	Impedance	Phase	Sample resistivity at 25°C	Archie Formation Factor	Archie m exponent	Archie tortuosity	Frequency	Impedance	Phase	Sample resistivity at 25°C	Archie Formation Factor	Archie m exponent	Archie tortuosity
Hz	(ohm)	(°)	(ohm.m)	[]	[]	[]	Hz	(ohm)	(°)	(ohm.m)	[]	[]	[]
100000	100000.0	0.0	3200.3	16303.3	6.1	3325.9	100000	100000.0	0.0	3200.3	16303.3	6.1	3325.9
73565	73565.0	0.1	2354.3	11993.5	5.9	2446.7	73565	73565.0	0.1	2354.3	11993.5	5.9	2446.7
54117	54117.1	0.1	1731.9	8822.9	5.7	1799.9	54117	54117.1	0.1	1731.9	8822.9	5.7	1799.9
39811	39811.1	0.1	1274.1	6490.5	5.5	1324.1	39811	39811.1	0.1	1274.1	6490.5	5.5	1324.1
29286	29286.1	0.2	937.2	4774.6	5.3	974.0	29286	29286.1	0.2	937.2	4774.6	5.3	974.0
21544	21544.2	0.2	689.5	3512.4	5.1	716.5	21544	21544.2	0.2	689.5	3512.4	5.1	716.5
15849	15849.2	0.3	507.2	2583.9	4.9	527.1	15849	15849.2	0.3	507.2	2583.9	4.9	527.1
11659	11659.3	0.4	373.1	1900.9	4.7	387.8	11659	11659.3	0.4	373.1	1900.9	4.7	387.8
8576.9	8577.3	0.5	274.5	1398.4	4.6	285.3	8576.9	8577.3	0.5	274.5	1398.4	4.6	285.3
6309.6	6310.2	0.7	201.9	1028.8	4.4	209.9	6309.6	6310.2	0.7	201.9	1028.8	4.4	209.9
4641.5	4642.3	0.8	148.6	756.8	4.2	154.4	4641.5	4642.3	0.8	148.6	756.8	4.2	154.4
3414.6	3415.6	1.0	109.3	556.9	4.0	113.6	3414.6	3415.6	1.0	109.3	556.9	4.0	113.6
2511.9	2513.3	1.1	80.4	409.8	3.8	83.6	2511.9	2513.3	1.1	80.4	409.8	3.8	83.6
1847.8	1849.7	1.2	59.2	301.6	3.6	61.5	1847.8	1849.7	1.2	59.2	301.6	3.6	61.5
1359.4	1362.0	1.3	43.6	222.1	3.4	45.3	1359.4	1362.0	1.3	43.6	222.0	3.4	45.3
1000	1003.6	1.4	32.1	163.6	3.2	33.4	1000	1003.5	1.4	32.1	163.6	3.2	33.4
735.64	740.6	1.4	23.7	120.7	3.0	24.6	735.64	740.4	1.4	23.7	120.7	3.0	24.6
541.16	547.9	1.5	17.5	89.3	2.8	18.2	541.16	547.7	1.5	17.5	89.3	2.8	18.2
398.11	407.3	1.5	13.0	66.4	2.6	13.5	398.11	407.0	1.5	13.0	66.4	2.6	13.5
292.87	305.3	1.5	9.8	49.8	2.5	10.2	292.87	305.0	1.5	9.8	49.7	2.5	10.1
215.44	232.2	1.5	7.4	37.9	2.3	7.7	215.44	231.8	1.5	7.4	37.8	2.3	7.7
158.49	180.9	1.5	5.8	29.5	2.1	6.0	158.49	180.4	1.5	5.8	29.4	2.1	6.0
116.59	145.9	1.5	4.7	23.8	2.0	4.9	116.59	145.3	1.5	4.7	23.7	2.0	4.8
85.769	123.2	1.6	3.9	20.1	1.9	4.1	85.769	122.6	1.6	3.9	20.0	1.9	4.1
63.095	109.4	1.6	3.5	17.8	1.8	3.6	63.095	108.7	1.6	3.5	17.7	1.8	3.6
46.416	101.6	1.6	3.3	16.6	1.8	3.4	46.416	100.9	1.6	3.2	16.5	1.8	3.4
34.146	97.8	1.6	3.1	15.9	1.7	3.3	34.146	97.2	1.6	3.1	15.8	1.7	3.2
25.119	96.6	1.6	3.1	15.7	1.7	3.2	25.119	96.0	1.6	3.1	15.6	1.7	3.2
18.479	97.0	1.6	3.1	15.8	1.7	3.2	18.479	96.5	1.6	3.1	15.7	1.7	3.2
13.594	98.7	1.6	3.2	16.1	1.7	3.3	13.594	98.2	1.6	3.1	16.0	1.7	3.3
10	101.3	1.6	3.2	16.5	1.8	3.4	10	100.9	1.6	3.2	16.4	1.8	3.4
Mean	107.9	1.6	3.5	17.6	1.8	3.6	Mean	107.4	1.6	3.4	17.5	1.8	3.6
STDEV	16.6	0.0	0.5	2.7	0.1	0.6	STDEV	16.6	0.0	0.5	2.7	0.1	0.6

POST-FLOOD													
H4FS1A - 2 electrodes - no confining stress							H4FS1B - 2 electrodes - no confining stress						
Frequency	Impedance	Phase	Sample resistivity at 25°C	Archie Formation Factor	Archie m exponent	Archie tortuosity	Frequency	Impedance	Phase	Sample resistivity at 25°C	Archie Formation Factor	Archie m exponent	Archie tortuosity
Hz	(ohm)	(°)	(ohm.m)	[]	[]	[]	Hz	(ohm)	(°)	(ohm.m)	[]	[]	[]
100000	100000.0	0.0	3285.7	16303.3	6.3	3488.9	100000	100000.0	0.0	3285.7	16303.3	5.9	3179.1
73565	73565.0	0.1	2417.1	11993.5	6.1	2566.6	73565	73565.0	0.1	2417.1	11993.5	5.7	2338.7
54117	54117.1	0.1	1778.1	8822.9	5.9	1888.1	54117	54117.1	0.1	1778.1	8822.9	5.6	1720.5
39811	39811.1	0.1	1308.1	6490.5	5.7	1389.0	39811	39811.1	0.1	1308.1	6490.5	5.4	1265.7
29286	29286.1	0.2	962.3	4774.6	5.5	1021.8	29286	29286.1	0.2	962.3	4774.6	5.2	931.0
21544	21544.2	0.2	707.9	3512.4	5.3	751.7	21544	21544.2	0.2	707.9	3512.4	5.0	684.9
15849	15849.3	0.3	520.8	2584.0	5.1	553.0	15849	15849.2	0.3	520.8	2584.0	4.8	503.9
11659	11659.4	0.4	383.1	1900.9	4.9	406.8	11659	11659.3	0.4	383.1	1900.9	4.6	370.7
8576.9	8577.4	0.6	281.8	1398.4	4.7	299.3	8576.9	8577.4	0.5	281.8	1398.4	4.4	272.7
6309.6	6310.3	0.7	207.3	1028.8	4.5	220.2	6309.6	6310.3	0.7	207.3	1028.8	4.2	200.6
4641.5	4642.5	0.9	152.5	756.9	4.3	162.0	4641.5	4642.5	0.9	152.5	756.9	4.1	147.6
3414.6	3416.1	1.0	112.2	556.9	4.1	119.2	3414.6	3416.0	1.0	112.2	556.9	3.9	108.6
2511.9	2514.0	1.2	82.6	409.9	3.9	87.7	2511.9	2513.9	1.2	82.6	409.9	3.7	79.9
1847.8	1850.7	1.3	60.8	301.7	3.7	64.6	1847.8	1850.7	1.3	60.8	301.7	3.5	58.8
1359.4	1363.5	1.4	44.8	222.3	3.5	47.6	1359.4	1363.5	1.4	44.8	222.3	3.3	43.3
1000	1005.8	1.4	33.0	164.0	3.3	35.1	1000	1005.9	1.4	33.1	164.0	3.1	32.0
735.64	743.8	1.5	24.4	121.3	3.1	26.0	735.64	744.0	1.5	24.4	121.3	2.9	23.7
541.16	552.6	1.5	18.2	90.1	2.9	19.3	541.16	552.9	1.5	18.2	90.1	2.8	17.6
398.11	414.1	1.5	13.6	67.5	2.7	14.4	398.11	414.6	1.5	13.6	67.6	2.6	13.2
292.87	315.1	1.5	10.4	51.4	2.6	11.0	292.87	315.8	1.5	10.4	51.5	2.4	10.0
215.44	246.0	1.5	8.1	40.1	2.4	8.6	215.44	246.9	1.5	8.1	40.3	2.3	7.8
158.49	199.6	1.5	6.6	32.5	2.3	7.0	158.49	200.7	1.5	6.6	32.7	2.1	6.4
116.59	170.5	1.6	5.6	27.8	2.2	5.9	116.59	171.6	1.6	5.6	28.0	2.0	5.5
85.769	154.0	1.6	5.1	25.1	2.1	5.4	85.769	154.8	1.6	5.1	25.2	2.0	4.9
63.095	146.2	1.6	4.8	23.8	2.1	5.1	63.095	146.3	1.6	4.8	23.9	1.9	4.7
46.416	144.3	1.6	4.7	23.5	2.0	5.0	46.416	143.2	1.6	4.7	23.3	1.9	4.6
34.146	146.3	1.6	4.8	23.9	2.1	5.1	34.146	143.4	1.6	4.7	23.4	1.9	4.6
25.119	151.0	1.6	5.0	24.6	2.1	5.3	25.119	145.9	1.6	4.8	23.8	1.9	4.6
18.479	158.1	1.6	5.2	25.8	2.1	5.5	18.479	149.8	1.6	4.9	24.4	2.0	4.8
13.594	167.2	1.6	5.5	27.3	2.1	5.8	13.594	154.8	1.6	5.1	25.2	2.0	4.9
10	178.2	1.6	5.9	29.1	2.2	6.2	10	161.0	1.6	5.3	26.2	2.0	5.1
Mean	157.3	1.6	5.2	25.6	2.1	5.5	Mean	152.3	1.6	5.0	24.8	2.0	4.8
STDEV	12.1	0.0	0.4	2.0	0.0	0.4	STDEV	9.4	0.0	0.3	1.5	0.0	0.3

Table 20. Summary of the electrical impedance spectroscopy between 10Hz and 100 kHz on the pre- and post-flood plugs under room conditions using 2 and 4 electrodes system for Plug 2 from Harvey-4 well. The derived Archie parameters: Formation factor, m exponent and Tortuosity are also presented.

PRE-FLOOD												
H4FS2 - 2 electrodes - no confining stress							H4FS2 - 4 electrodes - no confining stress					
Frequency	Impedance	Phase	Sample resistivity at 25°C	Archie Formation Factor	Archie m exponent	Archie tortuosity	Z	Phase	Sample resistivity at 25°C	Archie Formation Factor	Archie m exponent	Archie tortuosity
Hz	(ohm)	(°)	(ohm.m)	[]	[]	[]	(ohm)	(°)	(ohm.m)	[]	[]	[]
100000	100000.7	0.2	1345.9	6856.6	5.4	1343.9	100000.0	0.0	3585.6	18265.9	6.0	3580.1
73565	73565.9	0.3	990.1	5044.1	5.2	988.6	73565.0	0.0	2637.7	13437.3	5.8	2633.7
54117	54118.1	0.3	728.4	3710.6	5.0	727.3	54117.5	-0.2	1940.4	9885.0	5.6	1937.5
39811	39812.3	0.4	535.8	2729.8	4.9	535.0	39812.0	-0.4	1427.5	7272.0	5.5	1425.3
29286	29287.6	0.5	394.2	2008.1	4.7	393.6	29287.2	-0.5	1050.1	5349.6	5.3	1048.5
21544	21546.0	0.7	290.0	1477.3	4.5	289.6	21545.7	-0.6	772.5	3935.5	5.1	771.4
15849	15851.4	0.8	213.3	1086.9	4.3	213.0	15851.7	-0.8	568.4	2895.5	4.9	567.5
11659	11662.0	0.9	157.0	799.6	4.1	156.7	11662.9	-1.0	418.2	2130.3	4.7	417.5
8576.9	8580.8	1.0	115.5	588.3	3.9	115.3	8582.1	-1.1	307.7	1567.6	4.5	307.2
6309.6	6314.6	1.2	85.0	433.0	3.7	84.9	6316.1	-1.2	226.5	1153.7	4.3	226.1
4641.5	4648.0	1.3	62.6	318.7	3.5	62.5	4651.0	-1.3	166.8	849.5	4.1	166.5
3414.6	3423.2	1.3	46.1	234.7	3.3	46.0	3427.4	-1.4	122.9	626.1	4.0	122.7
2511.9	2523.3	1.4	34.0	173.0	3.2	33.9	2529.1	-1.4	90.7	462.0	3.8	90.5
1847.8	1863.1	1.4	25.1	127.7	3.0	25.0	1873.6	-1.5	67.2	342.2	3.6	67.1
1359.4	1380.0	1.5	18.6	94.6	2.8	18.5	1393.2	-1.5	50.0	254.5	3.4	49.9
1000	1027.7	1.5	13.8	70.5	2.6	13.8	1043.3	-1.5	37.4	190.6	3.2	37.4
735.64	772.8	1.5	10.4	53.0	2.4	10.4	800.6	-1.5	28.7	146.2	3.1	28.7
541.16	590.8	1.5	8.0	40.5	2.3	7.9	621.6	-1.5	22.3	113.5	2.9	22.3
398.11	463.7	1.5	6.2	31.8	2.1	6.2	503.7	-1.5	18.1	92.0	2.8	18.0
292.87	377.9	1.5	5.1	25.9	2.0	5.1	431.9	-1.6	15.5	78.9	2.7	15.5
215.44	322.6	1.6	4.3	22.1	1.9	4.3	386.6	-1.6	13.9	70.6	2.6	13.8
158.49	289.2	1.6	3.9	19.8	1.8	3.9	364.9	-1.6	13.1	66.7	2.6	13.1
116.59	270.4	1.6	3.6	18.5	1.8	3.6	344.5	-1.6	12.4	62.9	2.5	12.3
85.769	261.0	1.6	3.5	17.9	1.8	3.5	389.4	-1.6	14.0	71.1	2.6	13.9
63.095	257.3	1.6	3.5	17.6	1.8	3.5	326.0	-1.6	11.7	59.5	2.5	11.7
46.416	257.1	1.6	3.5	17.6	1.8	3.5	480.9	-1.6	17.2	87.8	2.7	17.2
34.146	259.1	1.6	3.5	17.8	1.8	3.5	347.4	-1.6	12.5	63.5	2.5	12.4
25.119	262.9	1.6	3.5	18.0	1.8	3.5	349.4	-1.6	12.5	63.8	2.6	12.5
18.479	268.3	1.6	3.6	18.4	1.8	3.6	1288.6	-1.6	46.2	235.4	3.4	46.1
13.594	275.0	1.6	3.7	18.9	1.8	3.7	293.9	-1.6	10.5	53.7	2.4	10.5
10	283.3	1.6	3.8	19.4	1.8	3.8	522.2	-1.6	18.7	95.4	2.8	18.7
Mean	266.0	1.6	3.6	18.2	1.8	3.6	482.5	-1.6	17.3	88.1	2.7	17.3
STDEV	9.0	0.0	0.1	0.6	0.0	0.1	311.3	0.0	11.2	56.9	0.3	11.1

POST-FLOOD												
H4FS2 - 2 electrodes - no confining stress							H4FS2 - 4 electrodes - no confining stress					
Frequency	Impedance	Phase	Sample resistivity at 25°C	Archie Formation Factor	Archie m exponent	Archie tortuosity	Z	Phase	Sample resistivity at 25°C	Archie Formation Factor	Archie m exponent	Archie tortuosity
Hz	(ohm)	(°)	(ohm.m)	[]	[]	[]	(ohm)	(°)	(ohm.m)	[]	[]	[]
100000	100000.6	0.2	1388.5	6889.3	5.6	1433.0	100000.1	0.1	3681.3	18265.9	6.2	3799.3
73565	73565.8	0.3	1021.4	5068.2	5.4	1054.2	73565.2	0.1	2708.1	13437.3	6.1	2795.0
54117	54118.0	0.3	751.4	3728.4	5.2	775.5	54117.2	0.2	1992.2	9885.0	5.9	2056.1
39811	39812.4	0.4	552.8	2742.8	5.0	570.5	39811.3	0.2	1465.6	7271.9	5.7	1512.6
29286	29287.9	0.6	406.6	2017.7	4.8	419.7	29286.5	0.3	1078.1	5349.6	5.5	1112.7
21544	21546.5	0.7	299.2	1484.4	4.7	308.8	21544.6	0.4	793.1	3935.3	5.3	818.5
15849	15852.4	0.9	220.1	1092.1	4.5	227.2	15849.8	0.5	583.5	2895.1	5.1	602.2
11659	11663.6	1.0	161.9	803.5	4.3	167.1	11660.2	0.7	429.2	2129.8	4.9	443.0
8576.9	8583.0	1.1	119.2	591.3	4.1	123.0	8578.5	0.8	315.8	1566.9	4.7	325.9
6309.6	6317.8	1.2	87.7	435.3	3.9	90.5	6311.7	1.0	232.4	1152.9	4.5	239.8
4641.5	4652.4	1.3	64.6	320.5	3.7	66.7	4644.4	1.1	171.0	848.3	4.3	176.5
3414.6	3429.0	1.4	47.6	236.2	3.5	49.1	3418.5	1.2	125.8	624.4	4.1	129.9
2511.9	2530.8	1.4	35.1	174.4	3.3	36.3	2517.3	1.3	92.7	459.8	3.9	95.6
1847.8	1872.3	1.5	26.0	129.0	3.1	26.8	1855.1	1.4	68.3	338.8	3.7	70.5
1359.4	1391.0	1.5	19.3	95.8	2.9	19.9	1369.3	1.4	50.4	250.1	3.5	52.0
1000	1040.5	1.5	14.4	71.7	2.7	14.9	1013.4	1.5	37.3	185.1	3.3	38.5
735.64	787.1	1.5	10.9	54.2	2.5	11.3	753.8	1.5	27.7	137.7	3.1	28.6
541.16	606.0	1.5	8.4	41.8	2.4	8.7	565.6	1.5	20.8	103.3	3.0	21.5
398.11	479.0	1.5	6.7	33.0	2.2	6.9	430.8	1.5	15.9	78.7	2.8	16.4
292.87	392.2	1.6	5.4	27.0	2.1	5.6	336.1	1.5	12.4	61.4	2.6	12.8
215.44	334.9	1.6	4.6	23.1	2.0	4.8	271.4	1.5	10.0	49.6	2.5	10.3
158.49	298.6	1.6	4.1	20.6	1.9	4.3	228.9	1.6	8.4	41.8	2.4	8.7
116.59	276.7	1.6	3.8	19.1	1.9	4.0	202.3	1.6	7.4	37.0	2.3	7.7
85.769	264.1	1.6	3.7	18.2	1.8	3.8	186.5	1.6	6.9	34.1	2.2	7.1
63.095	257.5	1.6	3.6	17.7	1.8	3.7	177.5	1.6	6.5	32.4	2.2	6.7
46.416	254.8	1.6	3.5	17.6	1.8	3.7	172.7	1.6	6.4	31.5	2.2	6.6
34.146	254.6	1.6	3.5	17.5	1.8	3.6	170.3	1.6	6.3	31.1	2.2	6.5
25.119	256.4	1.6	3.6	17.7	1.8	3.7	169.4	1.6	6.2	30.9	2.2	6.4
18.479	259.9	1.6	3.6	17.9	1.8	3.7	169.3	1.6	6.2	30.9	2.2	6.4
13.594	265.1	1.6	3.7	18.3	1.8	3.8	169.9	1.6	6.3	31.0	2.2	6.5
10	272.2	1.6	3.8	18.8	1.9	3.9	171.0	1.6	6.3	31.2	2.2	6.5
Mean	262.4	1.6	3.6	18.1	1.8	3.8	176.6	1.6	6.5	32.3	2.2	6.7
STDEV	7.9	0.0	0.1	0.5	0.0	0.1	11.2	0.0	0.4	2.0	0.0	0.4

Table 21. Summary of the electrical impedance spectroscopy between 10Hz and 100 kHz on the pre- and post-flood plugs under room conditions using 2 electrodes system for plug segments 3A & 3B from Harvey-4 well. The derived Archie parameters: Formation factor, m exponent and Tortuosity are also presented.

PRE-FLOOD						
H4FS3A - 2 electrodes - no confining stress						
Frequency	Impedance	Phase	Sample resistivity at 25°C	Archie Formation Factor	Archie m exponent	Archie tortuosity
Hz	(ohm)	(°)	(ohm.m)	[]	[]	[]
100000	100000.1	0.1	3195.8	16511.6	5.4	2774.0
73565	73565.1	0.1	2351.0	12146.8	5.3	2040.7
54117	54117.2	0.1	1729.5	8935.6	5.1	1501.2
39811	39811.2	0.2	1272.3	6573.5	4.9	1104.3
29286	29286.3	0.3	935.9	4835.6	4.8	812.4
21544	21544.4	0.4	688.5	3557.3	4.6	597.6
15849	15849.6	0.5	506.5	2617.0	4.4	439.7
11659	11659.8	0.6	372.6	1925.2	4.2	323.4
8576.9	8578.0	0.8	274.1	1416.4	4.1	238.0
6309.6	6311.2	0.9	201.7	1042.1	3.9	175.1
4641.5	4643.6	1.0	148.4	766.7	3.7	128.8
3414.6	3417.5	1.2	109.2	564.3	3.6	94.8
2511.9	2515.8	1.3	80.4	415.4	3.4	69.8
1847.8	1853.2	1.3	59.2	306.0	3.2	51.4
1359.4	1366.7	1.4	43.7	225.7	3.0	37.9
1000	1010.0	1.4	32.3	166.8	2.9	28.0
735.64	749.3	1.5	23.9	123.7	2.7	20.8
541.16	559.7	1.5	17.9	92.4	2.5	15.5
398.11	423.2	1.5	13.5	69.9	2.4	11.7
292.87	326.4	1.5	10.4	53.9	2.2	9.1
215.44	259.4	1.5	8.3	42.8	2.1	7.2
158.49	214.9	1.6	6.9	35.5	2.0	6.0
116.59	186.7	1.6	6.0	30.8	1.9	5.2
85.769	169.8	1.6	5.4	28.0	1.9	4.7
63.095	160.4	1.6	5.1	26.5	1.8	4.4
46.416	155.7	1.6	5.0	25.7	1.8	4.3
34.146	153.8	1.6	4.9	25.4	1.8	4.3
25.119	153.7	1.6	4.9	25.4	1.8	4.3
18.479	155.0	1.6	5.0	25.6	1.8	4.3
13.594	157.3	1.6	5.0	26.0	1.8	4.4
10	160.4	1.6	5.1	26.5	1.8	4.4
Mean	161.4	1.6	5.2	26.7	1.8	4.5
STDEV	10.7	0.0	0.3	1.8	0.0	0.3

PRE-FLOOD						
H4FS3B - 2 electrodes - no confining stress						
Frequency	Impedance	Phase	Sample resistivity at 25°C	Archie Formation Factor	Archie m exponent	Archie tortuosity
Hz	(ohm)	(°)	(ohm.m)	[]	[]	[]
100000	100000.1	0.1	2978.7	15390.0	5.4	2585.5
73565	73565.1	0.1	2191.3	11321.6	5.2	1902.0
54117	54117.1	0.1	1612.0	8328.6	5.1	1399.2
39811	39811.2	0.2	1185.8	6126.9	4.9	1029.3
29286	29286.2	0.2	872.3	4507.1	4.7	757.2
21544	21544.3	0.3	641.7	3315.7	4.5	557.0
15849	15849.5	0.4	472.1	2439.2	4.4	409.8
11659	11659.6	0.5	347.3	1794.4	4.2	301.5
8576.9	8577.8	0.7	255.5	1320.1	4.0	221.8
6309.6	6310.8	0.8	188.0	971.2	3.9	163.2
4641.5	4643.1	1.0	138.3	714.6	3.7	120.0
3414.6	3416.8	1.1	101.8	525.8	3.5	88.3
2511.9	2514.9	1.2	74.9	387.0	3.3	65.0
1847.8	1851.9	1.3	55.2	285.0	3.2	47.9
1359.4	1364.9	1.4	40.7	210.1	3.0	35.3
1000	1007.5	1.4	30.0	155.1	2.8	26.0
735.64	745.9	1.5	22.2	114.8	2.7	19.3
541.16	555.1	1.5	16.5	85.4	2.5	14.4
398.11	416.9	1.5	12.4	64.2	2.3	10.8
292.87	318.1	1.5	9.5	49.0	2.2	8.2
215.44	248.8	1.5	7.4	38.3	2.0	6.4
158.49	201.9	1.5	6.0	31.1	1.9	5.2
116.59	171.4	1.6	5.1	26.4	1.8	4.4
85.769	152.7	1.6	4.5	23.5	1.8	3.9
63.095	142.0	1.6	4.2	21.9	1.7	3.7
46.416	136.4	1.6	4.1	21.0	1.7	3.5
34.146	134.0	1.6	4.0	20.6	1.7	3.5
25.119	133.7	1.6	4.0	20.6	1.7	3.5
18.479	134.6	1.6	4.0	20.7	1.7	3.5
13.594	136.7	1.6	4.1	21.0	1.7	3.5
10	139.7	1.6	4.2	21.5	1.7	3.6
Mean	142.4	1.6	4.2	21.9	1.7	3.7
STDEV	12.4	0.0	0.4	1.9	0.0	0.3

POST-FLOOD						
H4FS3A - 2 electrodes - no confining stress						
Frequency	Impedance	Phase	Sample resistivity at 25°C	Archie Formation Factor	Archie m exponent	Archie tortuosity
Hz	(ohm)	(°)	(ohm.m)	[]	[]	[]
100000	100000.2	0.1	3083.5	15266.3	5.5	2610.5
73565	73565.2	0.1	2268.4	11230.7	5.3	1920.4
54117	54117.3	0.2	1668.7	8261.7	5.1	1412.8
39811	39811.4	0.3	1227.6	6077.7	4.9	1039.3
29286	29286.6	0.4	903.1	4471.0	4.8	764.5
21544	21544.9	0.5	664.3	3289.1	4.6	562.4
15849	15850.2	0.6	488.7	2419.7	4.4	413.8
11659	11660.7	0.8	359.6	1780.2	4.2	304.4
8576.9	8579.2	0.9	264.5	1309.7	4.1	224.0
6309.6	6312.8	1.1	194.7	963.7	3.9	164.8
4641.5	4646.0	1.2	143.3	709.3	3.7	121.3
3414.6	3420.9	1.3	105.5	522.2	3.5	89.3
2511.9	2520.8	1.4	77.7	384.8	3.4	65.8
1847.8	1860.2	1.4	57.4	284.0	3.2	48.6
1359.4	1376.8	1.5	42.5	210.2	3.0	35.9
1000	1024.4	1.5	31.6	156.4	2.9	26.7
735.64	769.5	1.5	23.7	117.5	2.7	20.1
541.16	587.7	1.5	18.1	89.7	2.5	15.3
398.11	461.1	1.5	14.2	70.4	2.4	12.0
292.87	376.4	1.5	11.6	57.5	2.3	9.8
215.44	322.7	1.6	10.0	49.3	2.2	8.4
158.49	291.7	1.6	9.0	44.5	2.1	7.6
116.59	275.5	1.6	8.5	42.1	2.1	7.2
85.769	268.4	1.6	8.3	41.0	2.1	7.0
63.095	267.0	1.6	8.2	40.8	2.1	7.0
46.416	269.1	1.6	8.3	41.1	2.1	7.0
34.146	273.5	1.6	8.4	41.8	2.1	7.1
25.119	279.6	1.6	8.6	42.7	2.1	7.3
18.479	287.0	1.6	8.8	43.8	2.1	7.5
13.594	295.6	1.6	9.1	45.1	2.2	7.7
10	305.7	1.6	9.4	46.7	2.2	8.0
Mean	280.2	1.6	8.6	42.8	2.1	7.3
STDEV	13.4	0.0	0.4	2.0	0.0	0.3

POST-FLOOD						
H4FS3B - 2 electrodes - no confining stress						
Frequency	Impedance	Phase	Sample resistivity at 25°C	Archie Formation Factor	Archie m exponent	Archie tortuosity
Hz	(ohm)	(°)	(ohm.m)	[]	[]	[]
100000	100000.1	0.1	3337.8	16561.7	5.6	2914.9
73565	73565.2	0.1	2455.4	12183.6	5.4	2144.3
54117	54117.3	0.2	1806.3	8962.7	5.2	1577.4
39811	39811.4	0.2	1328.8	6593.4	5.1	1160.4
29286	29286.5	0.3	977.5	4850.3	4.9	853.7
21544	21544.7	0.4	719.1	3568.2	4.7	628.0
15849	15849.9	0.6	529.0	2625.0	4.5	462.0
11659	11660.3	0.7	389.2	1931.1	4.4	339.9
8576.9	8578.7	0.9	286.3	1420.8	4.2	250.1
6309.6	6312.1	1.0	210.7	1045.4	4.0	184.0
4641.5	4645.0	1.1	155.0	769.3	3.8	135.4
3414.6	3419.5	1.3	114.1	566.3	3.6	99.7
2511.9	2518.8	1.3	84.1	417.1	3.5	73.4
1847.8	1857.4	1.4	62.0	307.6	3.3	54.1
1359.4	1372.9	1.4	45.8	227.4	3.1	40.0
1000	1018.9	1.5	34.0	168.7	3.0	29.7
735.64	762.0	1.5	25.4	126.2	2.8	22.2
541.16	577.6	1.5	19.3	95.7	2.6	16.8
398.11	447.9	1.5	14.9	74.2	2.5	13.1
292.87	359.6	1.5	12.0	59.6	2.4	10.5
215.44	302.4	1.6	10.1	50.1	2.3	8.8
158.49	267.8	1.6	8.9	44.4	2.2	7.8
116.59	248.9	1.6	8.3	41.2	2.1	7.3
85.769	240.2	1.6	8.0	39.8	2.1	7.0
63.095	237.7	1.6	7.9	39.4	2.1	6.9
46.416	239.1	1.6	8.0	39.6	2.1	7.0
34.146	243.0	1.6	8.1	40.2	2.1	7.1
25.119	248.7	1.6	8.3	41.2	2.1	7.2
18.479	255.9	1.6	8.5	42.4	2.2	7.5
13.594	264.1	1.6	8.8	43.7	2.2	7.7
10	273.6	1.6	9.1	45.3	2.2	8.0
Mean	250.1	1.6	8.3	41.4	2.1	7.3
STDEV	12.3	0.0	0.4	2.0	0.0	0.4

Table 22. Summary of the electrical impedance spectroscopy between 10Hz and 100 kHz on the pre- and post-flood plugs under room conditions using 2 and 4 electrodes system for Plug 4 from Harvey-4 well. The derived Archie parameters: Formation factor, m exponent and Tortuosity are also presented.

PRE-FLOOD												
H4FS4 - 2 electrodes - no confining stress					H4FS4 - 4 electrodes - no confining stress							
Frequency	Impedance	Phase	Sample resistivity at 25°C	Archie Formation Factor	Archie m exponent	Archie tortuosity	Z	Phase	Sample resistivity at 25°C	Archie Formation Factor	Archie m exponent	Archie tortuosity
Hz	(ohm)	(°)	(ohm.m)	[]	[]	[]	(ohm)	(°)	(ohm.m)	[]	[]	[]
100000	100001.5	0.3	1337.8	6850.8	4.7	1055.0	100001.2	0.3	3708.9	18314.3	5.2	2820.4
73565	73566.9	0.4	984.2	5039.8	4.6	776.1	73566.4	0.3	2728.5	13473.0	5.1	2074.8
54117	54119.4	0.5	724.0	3707.5	4.4	571.0	54118.8	0.4	2007.2	9911.4	4.9	1526.3
39811	39813.9	0.6	532.6	2727.5	4.2	420.0	39813.3	0.5	1476.6	7291.4	4.8	1122.9
29286	29289.6	0.7	391.8	2006.5	4.1	309.0	29288.8	0.7	1086.3	5364.0	4.6	826.1
21544	21548.4	0.9	288.3	1476.2	3.9	227.3	21547.6	0.8	799.2	3946.2	4.4	607.7
15849	15854.5	1.0	212.1	1086.1	3.7	167.3	15853.6	0.9	588.0	2903.4	4.3	447.1
11659	11666.0	1.1	156.1	799.2	3.6	123.1	11664.9	1.1	432.6	2136.3	4.1	329.0
8576.9	8585.8	1.2	114.9	588.2	3.4	90.6	8584.6	1.2	318.4	1572.2	3.9	242.1
6309.6	6321.1	1.3	84.6	433.0	3.2	66.7	6319.7	1.3	234.4	1157.4	3.8	178.2
4641.5	4656.6	1.4	62.3	319.0	3.1	49.1	4654.9	1.3	172.6	852.5	3.6	131.3
3414.6	3434.5	1.4	45.9	235.3	2.9	36.2	3432.4	1.4	127.3	628.6	3.4	96.8
2511.9	2538.3	1.5	34.0	173.9	2.8	26.8	2535.6	1.4	94.0	464.4	3.3	71.5
1847.8	1882.9	1.5	25.2	129.0	2.6	19.9	1879.4	1.5	69.7	344.2	3.1	53.0
1359.4	1406.2	1.5	18.8	96.3	2.4	14.8	1401.7	1.5	52.0	256.7	3.0	39.5
1000	1062.1	1.5	14.2	72.8	2.3	11.2	1056.3	1.5	39.2	193.4	2.8	29.8
735.64	817.5	1.5	10.9	56.0	2.2	8.6	810.0	1.5	30.0	148.4	2.7	22.8
541.16	647.4	1.5	8.7	44.4	2.0	6.8	638.2	1.5	23.7	116.9	2.5	18.0
398.11	533.0	1.6	7.1	36.5	1.9	5.6	521.9	1.6	19.4	95.6	2.4	14.7
292.87	459.2	1.6	6.1	31.5	1.8	4.8	446.4	1.6	16.6	81.8	2.4	12.6
215.44	413.4	1.6	5.5	28.3	1.8	4.4	399.5	1.6	14.8	73.2	2.3	11.3
158.49	386.4	1.6	5.2	26.5	1.8	4.1	371.4	1.6	13.8	68.0	2.3	10.5
116.59	370.9	1.6	5.0	25.4	1.7	3.9	355.2	1.6	13.2	65.0	2.2	10.0
85.769	362.2	1.6	4.8	24.8	1.7	3.8	346.3	1.6	12.8	63.4	2.2	9.8
63.095	357.5	1.6	4.8	24.5	1.7	3.8	341.3	1.6	12.7	62.5	2.2	9.6
46.416	355.0	1.6	4.7	24.3	1.7	3.7	336.6	1.6	12.5	61.6	2.2	9.5
34.146	353.8	1.6	4.7	24.2	1.7	3.7	337.6	1.6	12.5	61.8	2.2	9.5
25.119	353.6	1.6	4.7	24.2	1.7	3.7	337.8	1.6	12.5	61.9	2.2	9.5
18.479	354.1	1.6	4.7	24.3	1.7	3.7	338.1	1.6	12.5	61.9	2.2	9.5
13.594	355.0	1.6	4.7	24.3	1.7	3.7	338.9	1.6	12.6	62.1	2.2	9.6
10	356.5	1.6	4.8	24.4	1.7	3.8	340.6	1.6	12.6	62.4	2.2	9.6
Mean	357.6	1.6	4.8	24.5	1.7	3.8	341.4	1.6	12.7	62.5	2.2	9.6
STDEV	5.7	0.0	0.1	0.4	0.0	0.1	5.9	0.0	0.2	1.1	0.0	0.2

POST-FLOOD												
H4FS4 - 2 electrodes - no confining stress					H4FS4 - 4 electrodes - no confining stress							
Frequency	Impedance	Phase	Sample resistivity at 25°C	Archie Formation Factor	Archie m exponent	Archie tortuosity	Z	Phase	Sample resistivity at 25°C	Archie Formation Factor	Archie m exponent	Archie tortuosity
Hz	(ohm)	(°)	(ohm.m)	[]	[]	[]	(ohm)	(°)	(ohm.m)	[]	[]	[]
100000	1000000.1	0.0	13997.8	68549.2	5.9	10488.0	1000000.0	0.0	37397.3	183140.7	6.5	28020.5
73565	681290.1	0.0	9536.5	46701.9	5.7	7145.4	681290.0	0.0	25478.4	124771.9	6.3	19090.1
54117	464160.1	0.0	6497.2	31817.8	5.5	4868.1	464160.0	0.0	17358.3	85006.6	6.0	13006.0
39811	316230.2	0.1	4426.5	21677.3	5.3	3316.6	316230.0	0.0	11826.2	57914.6	5.8	8860.9
29286	215440.3	0.1	3015.7	14768.3	5.1	2259.5	215440.0	0.0	8056.9	39455.8	5.6	6036.7
21544	146780.4	0.1	2054.6	10061.7	4.9	1539.4	146780.1	0.1	5489.2	26881.4	5.4	4112.9
15849	100000.6	0.2	1399.8	6855.0	4.7	1048.8	100000.1	0.1	3739.7	18314.1	5.2	2802.1
11659	68129.9	0.3	953.7	4670.3	4.5	714.5	68129.1	0.1	2547.8	12477.2	5.0	1909.0
8576.9	46417.3	0.4	649.7	3181.9	4.3	486.8	46416.2	0.2	1735.8	8500.7	4.8	1300.6
6309.6	31625.0	0.6	442.7	2167.9	4.1	331.7	31623.3	0.2	1182.6	5791.5	4.6	886.1
4641.5	21546.9	0.8	301.6	1477.0	3.9	226.0	21544.4	0.3	805.7	3945.7	4.4	603.7
3414.6	14682.3	0.9	205.5	1006.5	3.7	154.0	14678.6	0.5	548.9	2688.3	4.2	411.3
2511.9	10006.3	1.1	140.1	685.9	3.5	104.9	10000.9	0.7	374.0	1831.6	4.0	280.2
1847.8	6822.2	1.2	95.5	467.7	3.3	71.6	6814.2	0.8	254.8	1248.0	3.8	190.9
1359.4	4655.2	1.3	65.2	319.1	3.1	48.8	4643.5	1.0	173.7	850.4	3.6	130.1
1000	3182.4	1.4	44.5	218.1	2.9	33.4	3165.2	1.2	118.4	579.7	3.4	88.7
735.64	2183.8	1.5	30.6	149.7	2.7	22.9	2158.6	1.3	80.7	395.3	3.2	60.5
541.16	1510.8	1.5	21.1	103.6	2.5	15.8	1474.0	1.4	55.1	270.0	3.0	41.3
398.11	1062.2	1.5	14.9	72.8	2.3	11.1	1009.1	1.4	37.7	184.8	2.8	28.3
292.87	769.9	1.5	10.8	52.8	2.1	8.1	694.6	1.5	26.0	127.2	2.6	19.5
215.44	586.8	1.5	8.2	40.2	2.0	6.2	483.5	1.5	18.1	88.6	2.4	13.5
158.49	478.9	1.6	6.7	32.8	1.9	5.0	344.0	1.5	12.9	63.0	2.2	9.6
116.59	419.8	1.6	5.9	28.8	1.8	4.4	254.4	1.5	9.5	46.6	2.0	7.1
85.769	389.7	1.6	5.5	26.7	1.7	4.1	199.6	1.6	7.5	36.5	1.9	5.6
63.095	375.5	1.6	5.3	25.7	1.7	3.9	168.0	1.6	6.3	30.8	1.8	4.7
46.416	369.4	1.6	5.2	25.3	1.7	3.9	150.9	1.6	5.6	27.6	1.8	4.2
34.146	367.4	1.6	5.1	25.2	1.7	3.9	142.0	1.6	5.3	26.0	1.7	4.0
25.119	367.7	1.6	5.1	25.2	1.7	3.9	137.4	1.6	5.1	25.2	1.7	3.8
18.479	369.5	1.6	5.2	25.3	1.7	3.9	134.8	1.6	5.0	24.7	1.7	3.8
13.594	372.5	1.6	5.2	25.5	1.7	3.9	133.2	1.6	5.0	24.4	1.7	3.7
10	376.9	1.6	5.3	25.8	1.7	4.0	132.0	1.6	4.9	24.2	1.7	3.7
Mean	378.7	1.6	5.3	26.0	1.7	4.0	161.4	1.6	6.0	29.6	1.8	4.5
STDEV	16.9	0.0	0.2	1.2	0.0	0.2	41.2	0.0	1.5	7.5	0.1	1.2

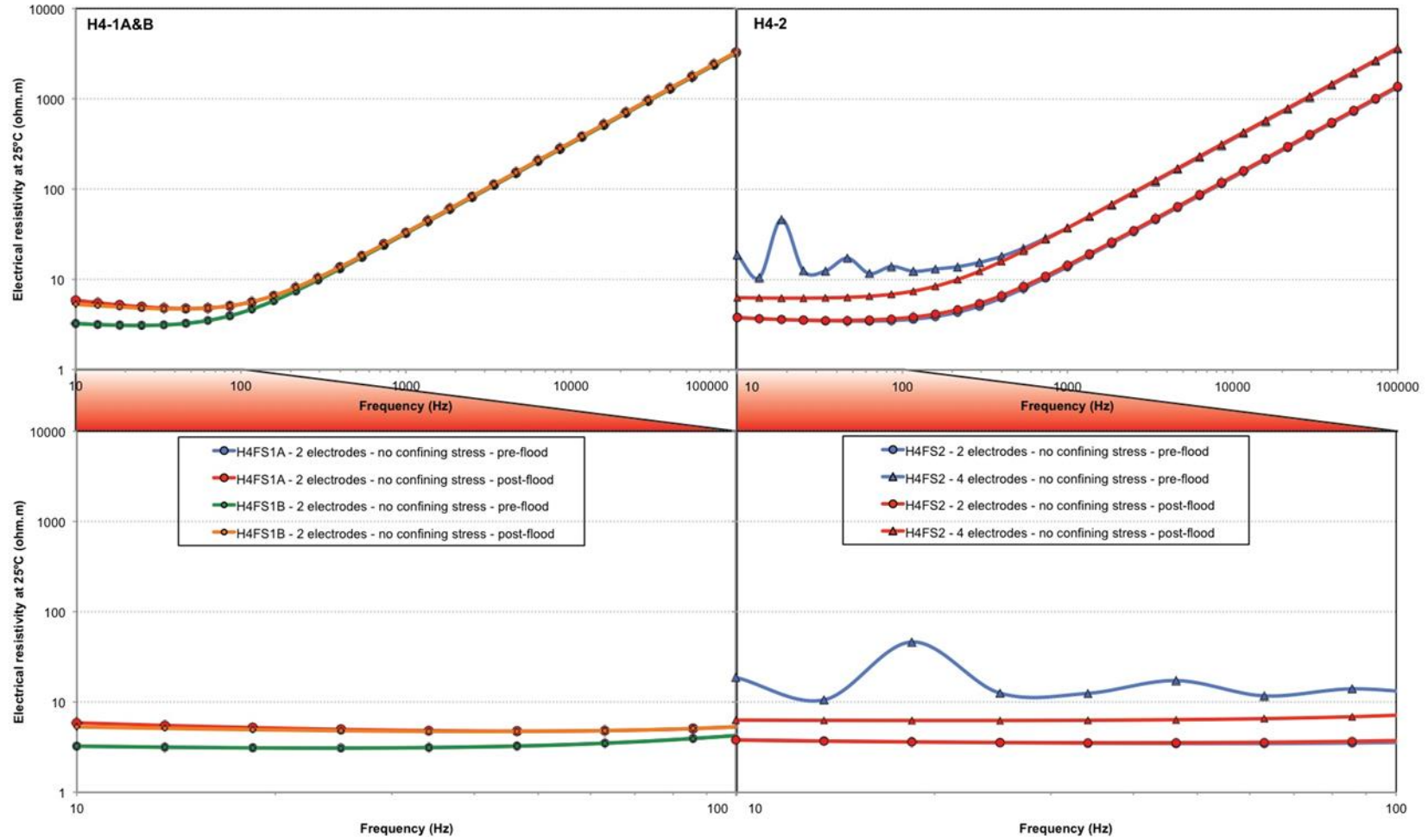


Figure 45. Electrical Impedance spectroscopy of saturated plugs 1 and 2 before (blue curves) and after flooding experiment (red/orange curves) between 10 and 10 kHz (top graph). Note the strong polarization from 100 Hz to 100 kHz: high values with a linear trend. The bottom plot shows a magnification of the top graph only between 10 and 100 Hz free of polarization effect.

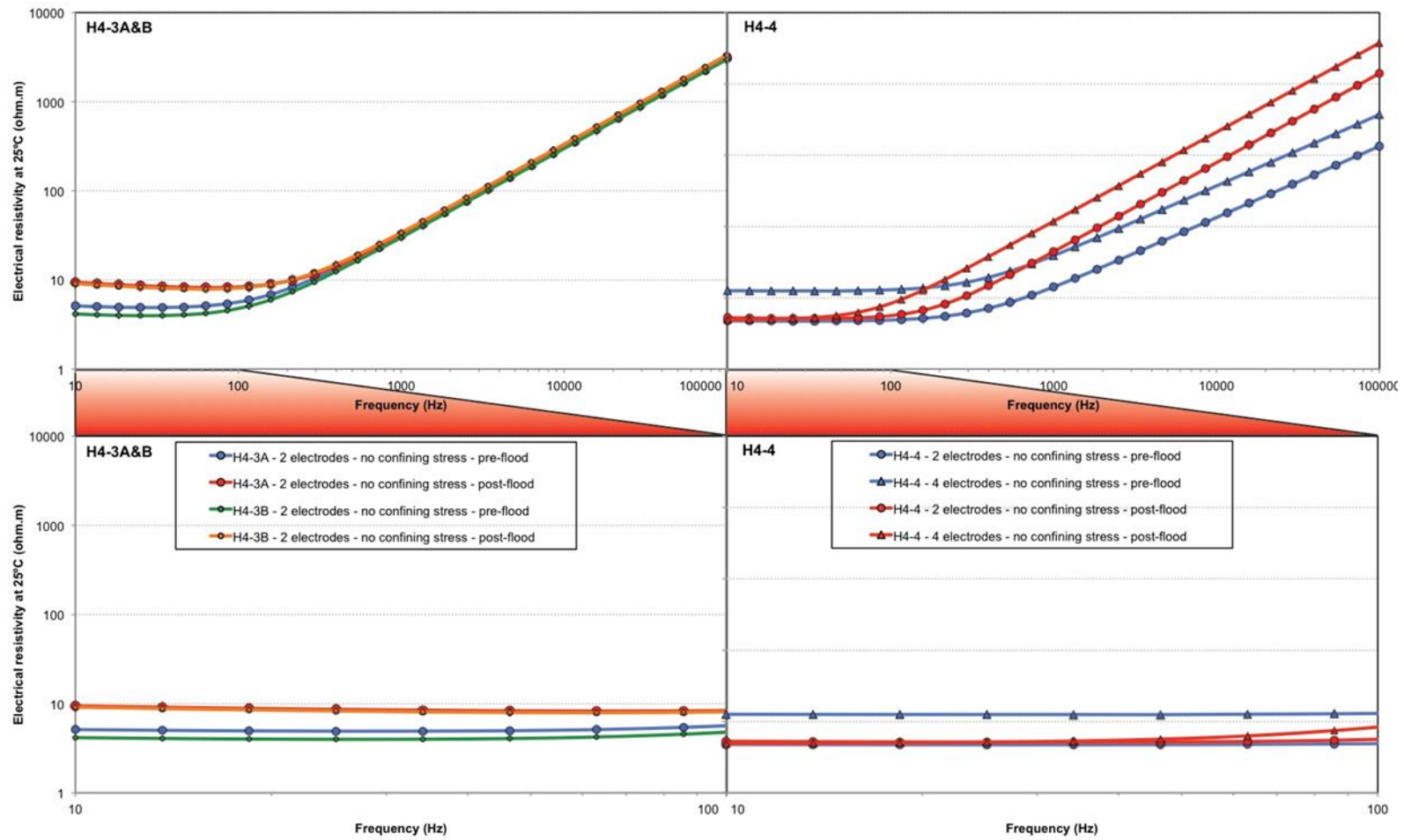


Figure 46. Electrical Impedance spectroscopy of saturated plugs 3 and 4 before (blue curves) and after flooding experiment (red/orange curves) between 10 and 10 kHz (top graph). Note the strong polarization from 100 Hz to 100 kHz: high values with a linear trend. The bottom plot shows a magnification of the top graph only between 10 and 100 Hz free of polarization effect.

Benchtop Ultrasonic Results

Harvey-3

For Harvey-3 samples, the ultrasonic P- and S-wave velocities were measured on dry plugs before and after the flooding experiments to evaluate potential changes in the stiffness of the rock. The velocities are summarized in Table 23 and the waveforms are presented in Figure 47. The P velocities on the pre-flood samples are similar for both samples around 2000 m/s which is also similar to those measured for samples from well Harvey-1 while older reports suggested much higher velocities around 4000 m/s. The P- and S-velocities tend to decrease slightly in the post-flood samples to around 1700-1800 m/s and 1200-700 m/s, respectively.

Table 23. Summary of the P- and S-wave velocities for plugs 1 and 2 of Harvey-3 before and after the flooding experiments.

	Plug1	Plug1A	Plug1B	Plug2	Plug2	Plug2	Plug2	Plug1	Plug1A	Plug1B
Status	Vp pre-flood	Vp post-flood	Vp post-flood	Vp pre-flood	Vp post-flood	Vs pre-flood	Vs post-flood	Vs pre-flood	Vs post-flood	Vs post-flood
Flying time (s)	3.90E-05	1.84E-05	1.83E-05	3.78E-05	4.60E-05	5.84E-05	6.56E-05	5.40E-05	4.88E-05	4.88E-05
Length (m)	7.94E-02	3.45E-02	3.27E-02	7.92E-02	7.92E-02	7.92E-02	7.92E-02	7.94E-02	3.45E-02	3.27E-02
Velocities (m/s)	2036	1875	1784	2094	1721	1355	1207	1470	707	669

Harvey-4

For the Harvey-4 samples, the ultrasonic P- and S-wave velocities were measured on dry plugs before and after the flooding experiments to evaluate potential changes in the stiffness of the rock samples. The velocities are summarised in Table 24. The P velocities for pre-flood samples are around 2000 m/s in plugs 1 and 2 and around 2200 m/s in the tighter plugs 3 and 4 which is also similar to the results from Harvey-1 and Harvey-3 samples. The P velocities tend to slightly decrease after flooding to around 1500 m/s in plugs 1 and 2 while it remains quasi-unchanged in plugs 3 and 4. The S velocities are much more complicated to process as the signal to noise is not optimum on dry samples. Assuming a rough picking of S-waves, their velocities before flooding is around 1200 m/s on plugs 1 and 2 and increasing to 1400-1600 m/s in plugs 3 and 4. Such velocities significantly decrease after flooding in plugs 1 and 2 to $\pm 900-1000$ m/s while it still remains unchanged in plugs 3 and 4.

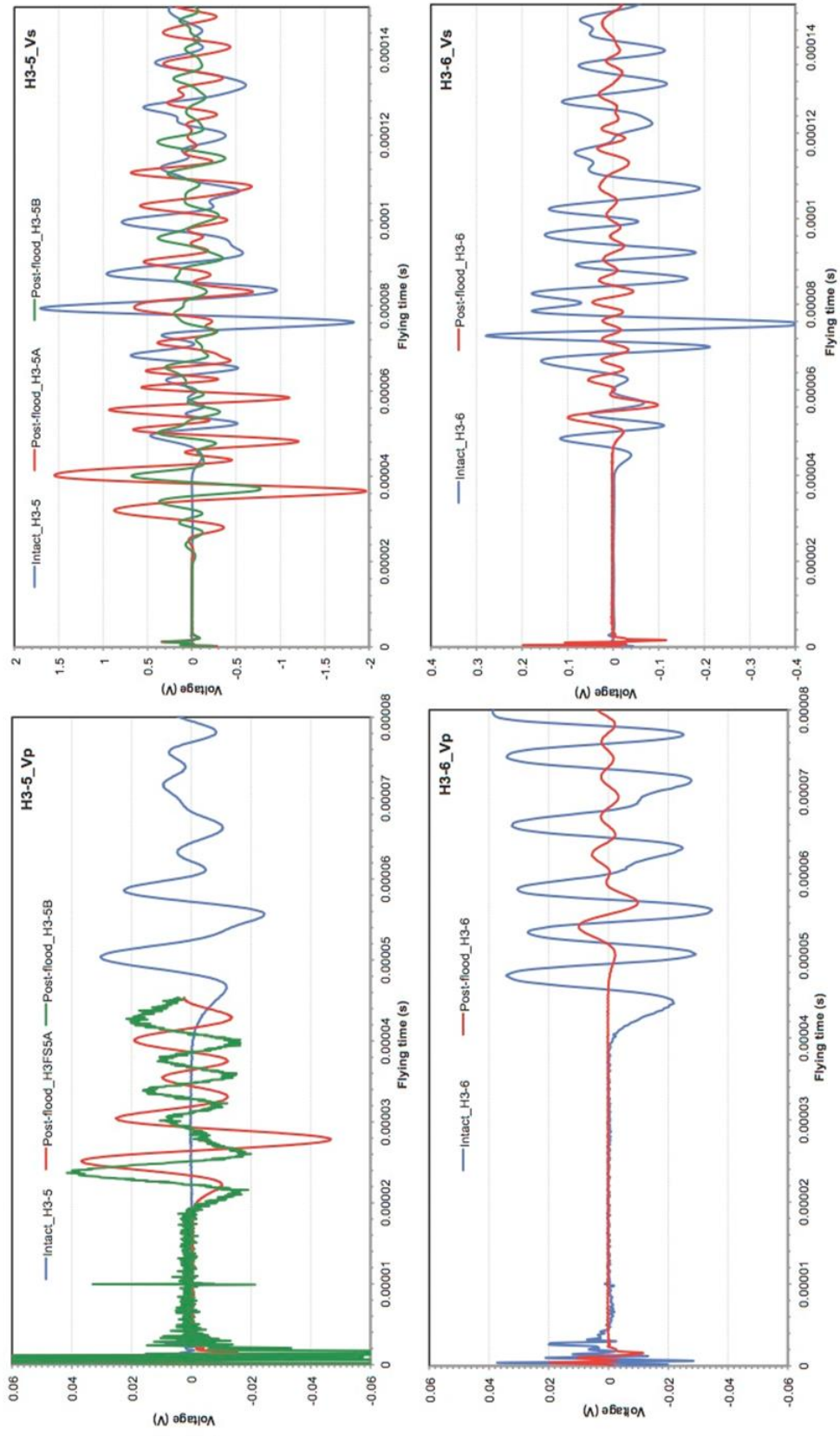


Figure 47. Ultrasonic P- and S-wave forms on pre- (blue curves) and post-flood (red/green curves) plugs 1 and 2 of Harvey-3.

Table 24. Summary of the P- and S-wave velocities on the four dry plugs from Harvey-4 before and after flooding experiments under room conditions.

	Plug1 pre-flood	Plug1A post-flood	Plug1B post-flood	Plug2 pre-flood	Plug2 post-flood	Plug3 pre-flood	Plug3A post-flood	Plug3B post-flood	Plug4 pre-flood	Plug4 post-flood
Status	Vp	Vp	Vp	Vp	Vp	Vp	Vp	Vp	Vp	Vp
Flying time (s)	4.20E-05	2.16E-05	2.28E-05	3.93E-05	5.12E-05	3.55E-05	1.66E-05	1.50E-05	3.50E-05	3.78E-05
Length (m)	0.0794	0.0337	0.0337	0.07992	0.07975	0.07995	0.0358	0.033	0.0802	0.08015
Velocities (m/s)	1890	1560	1478	2034	1558	2252	2157	2200	2291	2120

	Plug1 pre-flood	Plug1A post-flood	Plug1B post-flood	Plug2 pre-flood	Plug2 post-flood	Plug3 pre-flood	Plug3A post-flood	Plug3B post-flood	Plug4 pre-flood	Plug4 post-flood
Status	Vs	Vs	Vs	Vs	Vs	Vs	Vs	Vs	Vs	Vs
Flying time (s)	6.76E-05	3.88E-05	4.50E-05	6.32E-05	7.28E-05	5.46E-05	2.58E-05	2.30E-05	5.02E-05	5.18E-05
Length (m)	0.0794	0.0337	0.0337	0.07992	0.07975	0.07995	0.0358	0.033	0.0802	0.08015
Velocities (m/s)	1175	869	749	1265	1095	1464	1388	1435	1598	1547

Summary and Conclusions

Presented here are the final conclusions which could be drawn from the results presented in this section of the report. The conclusions have been arranged according to the different petrophysical techniques used in the characterising the pre- and post-flood samples.

X-ray CT imaging: Based on the x-ray CT number profiles plotted for various samples in their pre- and post-flood states, it seems that, at least for some of the samples, the axial location of a plug in each sample assembly during the flooding (i.e. being close to the inlet or outlet of the flood) or in other words the flood direction, plays a role when it comes to the changes that the samples may undergo during the flooding process. The plugs placed at the inlet end of an assembly are always the most affected by flooding with systematically recording lower CT values compared to their pre-flood state. It is worth noting that, such variation is also detectable in the plugs placed at the outlet end of an assembly but the intensity of the changes is much less. Due to the limitation imposed by the resolution of the images generated, a solid conclusion cannot be drawn as what causes the change in the CT number profiles. However, since the changes were much more pronounced at the inlet side of the sample assemblies, one possible explanation could be that some of the material (very likely clay particles) residing in the pores initially were flushed out and pushed towards the downstream of the samples. This explanation finds support in the experimental results obtained in other tasks whose results are provided in subsequent sections of this report (Sections 4 and 5).

Porosity measurements: In general, the flooding did not affect the gas porosity considerably. But further scrutiny of the results may reveal that the flooding affected the porosity of the samples (at least some of them) in two ways according to the axial location of the plugs in the sample assemblies. The porosity of the plugs placed at the outlet end of the assemblies was either slightly decreased or remained unchanged after flooding while the plugs in contact with the inlet end recorded a small

increase in porosity as well as becoming much more stress sensitive. Furthermore, in the samples from Harvey-1, the gas porosity versus the water-filled porosity record the same values in the pre-flood samples while after flooding the water-filled porosity shows lower values than that measured using gas. The lower water-filled porosity is most likely due to the inefficient saturation of the post-flood plugs by water. Such inefficiency to fully re-saturate the post-flood samples may point to the effect of the clay particles on the pore connectivity in the post-flood plugs impeding the water access to some pores. In other words, clay particles may have been displaced and lodged in critical pores and/or pore throats due to the flooding process (i.e. fines migration). It is believed that mineral dissolution mechanisms did not play a role here otherwise they would have counteracted the fines migration phenomenon, bringing the results of the gas and water methods closer. Again, the possible explanations provided here find support in the experimental results obtained in other tasks whose results are provided in subsequent sections of this report (Sections 4 and 5). Figure 48a is a cross plot comparing the pre- and post-flood porosity values for all the samples tested from all three wells. As can be seen, the trend is almost a linear one with a slope close to unity.

Permeability measurements: As can be seen from Figure 48b, a trend line following a power law is used to model the relationship between pre- and post-flood permeabilities of the samples from all three wells. In other words, opposite behaviours in the sample permeabilities were observed from one well to another when the pre- and post-flood data are compared. For instance, the gas permeability shows a systematic decrease in the post-flood Harvey-1 samples while the complete opposite is observed in the samples from Harvey-3 and then the Harvey-4 samples sit in between with some samples showing increase in post-flood permeability, some decrease and others no change at all. The permeability of the samples is not particularly stress sensitive before or after flooding. The changes observed in the post-flood samples permeabilities finds strong support in the data and information generated in Section 4 of this report. The likely reason behind observing opposite behaviours in the samples coming from different wells is believed to have roots in the diagenetic features of the samples, something which will be discussed in more details in the upcoming sections of this report.

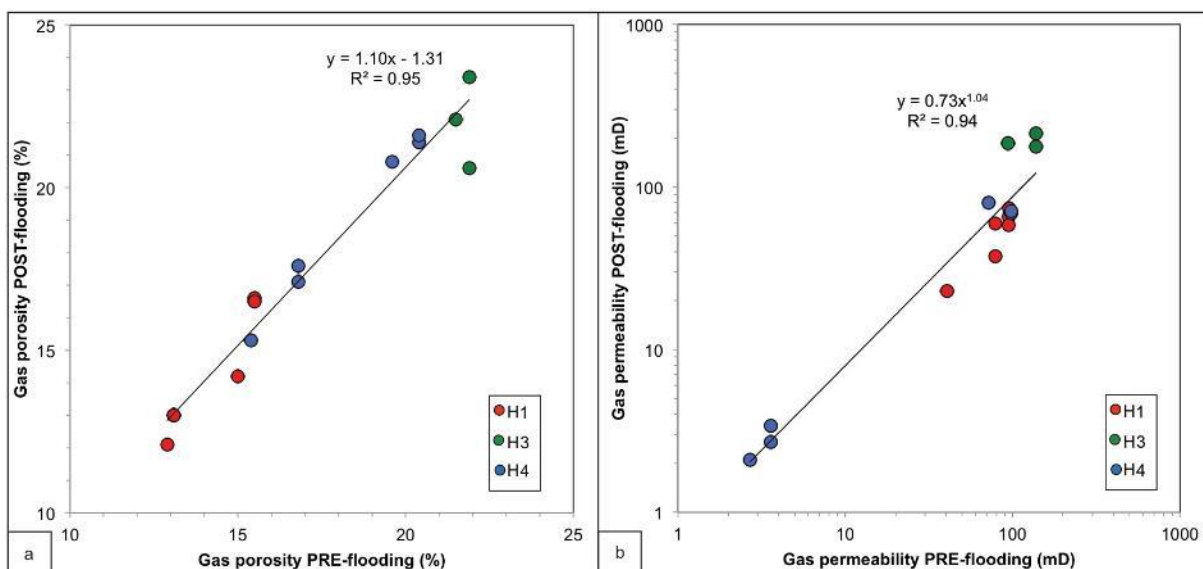


Figure 48. Comparison of gas porosity and permeability before and after flooding for all the tested three Harvey wells.

NMR spectrometry: A similar observation made about the ability of water to access all the pores after flooding when the water-filled and gas porosities were compared, can be made again about the NMR porosities. In general, at least for some of the samples, the T2 distributions show that after flooding the big pores are more accessible and detected clay bound water is increased, especially for the plugs close to the injection point in the sample assemblies. Once again, it might be speculated that the clay particles clogging the pores in the pre-flood plugs were dislodged during the flooding and migrated downstream. Therefore, the water has access to bigger pores and can surround more “free” dislodged surface of \pm agglomerated clays, favouring higher clay bound water.

Another interesting observation made about the NMR derived information for some of the samples was that the changes in the pre- and post-flood permeability data calculated from the NMR measurements showed opposite behaviour when compared with the changes observed in gas permeabilities. In the samples from Harvey-3, the NMR measurements on the pre-flood samples recorded similar permeabilities to the gas permeabilities. However, the NMR derived permeabilities for the post-flood samples showed significant decrease while the porosity changes were minor. The only explanation for this behaviour is a change in the surface relaxivity of the minerals. Assuming the mineralogy to remain unchanged, the surface texture should have changed leading to change in the NMR surface relaxivity. This aspect is reflected in the C parameters from Coates model. Assuming the gas permeability as the most reliable measurement, the C parameter from Coates equation can be back-computed to reach an NMR permeability equal to gas permeability. The C parameters, usually around 10 in sandstones, shifted to 8 in all the post-flood samples from Harvey-3 meaning increase in the mineral surface roughness. More specifically, parameter C can impact on the NMR logs analysis if the classical $C = 10$ is used to compute the permeability on post-CO₂ flooded reservoirs. In the light of the results achieved here, using $C = 10$ is appropriate in Harvey-3 to compute permeability quite accurately. However, if NMR log is recorded on CO₂ injected units, it may be needed to change the C parameter to 8 to take into account the change of surface roughness of the minerals induced by CO₂-brine-rock interactions. The $C=8$ is calculated for the flooding conditions applied in this work. Further analysis should be carried out with different flooding conditions to evaluate the evolution of this parameter with the duration of CO₂-brine-rock interaction as well as other experimental conditions.

Ultrasonic benchtop velocities: The flooding does not seem to have a significant effect on the ultrasonic velocities recorded for all the samples. Although, the flooding experiments seem to decrease the stress sensitivity of the samples, at least for V_p, but only by a few percent. It is believed that these results could be the effect of being very close to a full saturation (95 to 98% brine saturation) on the P- and S-wave velocities. Indeed, when approaching the full saturation, the ultrasonic velocities can change drastically (Mavko and Nolen-Hoeksema, 1994; Lebedev et al., 2009). Such effect is even more pronounced when samples are under the influence of hydrostatic pressure (Wuff and Burkhardt, 1997; Mayr and Bukhardt, 2006). It should be noted that the VP-VS of the post-flood plugs increase for Harvey-1 samples while they decrease quite significantly for samples from Harvey-3 and Harvey-4. Such behaviour is similar to the gas permeability behaviour outlined earlier.

Electrical resistivity: The laboratory resistivity measurement under brine-saturated system and confining stress is a challenging task that requires extreme care when interpreting the results as many issues can arise such as poor electrode-sample coupling, electrode polarization at low frequency, electrode resonance at high frequencies, trapped air bubble(s) at the sample-electrode interface, etc. However, considering the reasonable quality of the measurements, some general conclusions can be

drown. The comparison between the pre- and post-flood resistivity data can be presented in two ways: (i) the resistivity decreases on the plugs close to the inlet side of the sample assemblies; (ii) the resistivity increases or remains unchanged on the plugs away from the samples inlet. Such behaviour may support the dislodgment of fines from the plugs at the inlet side and their transport and re-deposition in the downstream plugs toward the outlet of flood. The overburden stress tends to increase the resistivity of the plugs but becomes less efficient on the post-flooded samples. The overburden stress makes the electrode polarization effect less common, usually visible at low frequencies (< 100 Hz), and particularly for the post-flood samples. Archie m exponent is usually around 3 which remains unchanged after flooding for the plugs away from the injection inlet while it decreases to around 2.5 in the plugs placed close to the inlet.

The following tables provide a comparison between the petrophysical properties of the samples in their pre- and post-flood states. Where applicable, the symbols “+”, “-” and “0” represent an increase, decrease or no change respectively in the post-flood properties compared to their pre-flood values.

Table 25. Summary of variations in pre- and post-flood petrophysical properties of the samples from Harvey-1. The orange cells mark strong change in parameters. The dark grey marks no data available. The last row in light orange integrates the overall changes within each plug.

Methods	Initial porosity high/ initial permeability low			Initial porosity low/ initial permeability good		
	Plug1	Plug2A	plug2B	Plug3	Plug4A	Plug4B
XCT	+	++	+	0	+	0
XCT - bedding contrast	Good	Good	Good	Poor	Poor	Poor
Nitrogen porosity	-	+	+	-	+	0
Nitrogen permeability	--	---	--	-	-	--
Stress sensitivity porosity	0	+++	++	0	+	0
Stress sensitivity permeability	0	0	0	0	0	0
Bulk density	-	--	--	-	0	0
Water saturation effectiveness	+	--	--	+	-	-
NMR porosity	-	++	+	-	+	0
NMR best C parameter for model permeability	0	0	0	-	--	--
Ultrasonic Vp	+			+		
Ultrasonic Vs	+			+		
Stress sensitivity on Vp	++			+		
Electrical resistivity	-	--	--	+	+	+
Archie m exponent	0	--	--	0		
Stress sensitivity of the resistivity	+			+		
Equilibration time for resistivity	Quick			Long		
Intensity of changes after flooding	+	+++	++	0	+	0

Table 26. Summary of the sample characteristics and parameters measured or derived from the different experiments run on pre- and post- flood plugs from Harvey-1.

	H1-Plug1 pre-flood	H1-Plug1 post-flood	H1-Plug2 pre-flood	H1-Plug2A post-flood	H1-Plug2B post-flood
Length (cm)	6.1	6.1	6.52	2.165	2.546
Diameter (cm)	3.85	3.85	3.86	3.865	3.865
Volume (cm ³)	71.0	71.0	76.3	25.4	29.9
Mass dry (g)	158.7	158.7	168.9	55.0	64.9
Gas porosity at room conditions (%)	15.0	14.2	15.5	16.6	16.5
Gas permeability at room conditions (md)	41	23	79	37	59
Mass saturated (g)	169.2	168.8	180.7	58.9	69.5
Brine Saturation (%)	99	100.3	100	92.4	92.5
Bulk dry density (g/cm ³)	2.24	2.23	2.21	2.16	2.17
Water imbibition porosity (%)	14.8	14.2	15.5	15.3	15.3
NMR water content (wt%)	6.6	6.2	6.9	7.1	7.1
NMR water-filled porosity (%)	15.8	14.7	16.3	16.6	16.4
NMR permeability computed (mD)	36	26	52	31	35
Best C NMR parameter for Coates model	10	10	9	10	9
Ultrasonic P-waves dry condition (m/s)	2255	2683	2221		
Ultrasonic S-waves dry condition (m/s)	1446	1928	1498		
Electrical resistivity at 1 kHz - no confining stress (ohm.m)	359	89	62	14	11
Archie Formation factor	1706	458	289	73	59
Archie m exponent	3.9	3.1	3.0	2.4	2.3

	H1-Plug3 pre-flood	H1-Plug3 post-flood	H1- Plug4 pre-flood	H1- Plug4A post-flood	H1- Plug4B post-flood
Length (cm)	6.245	6.245	6.1	2.436	2.135
Diameter (cm)	3.86	3.86	3.86	3.865	3.865
Volume (cm ³)	73.1	73.1	71.4	28.6	25.0
Mass dry (g)	168.3	168.5	163.8	65.1	56.8
Gas porosity at room conditions (%)	12.9	12.1	13.1	13.0	13.0
Gas permeability at room conditions (md)	95	74	95	66	58
Mass saturated (g)	177.5	177.2	173.0	68.8	59.9
Brine Saturation (%)	98	97.9	99	97.5	95.3
Bulk dry density (g/cm ³)	2.30	2.31	2.29	2.28	2.27
Water imbibition porosity (%)	12.7	11.9	12.9	12.7	12.4
NMR water content (wt%)	5.4	5.2	5.7	5.8	5.7
NMR water-filled porosity (%)	13.2	12.6	13.7	13.9	13.7
NMR permeability computed (mD)	33	24	36	19	17
Best C NMR parameter for Coates model	8	8	8	7	7
Ultrasonic P-waves dry condition (m/s)	2316	2403	2432		
Ultrasonic S-waves dry condition (m/s)	1688	1767	1579		
Electrical resistivity at 1 kHz - no confining stress (ohm.m)	75	149	3	10	12
Archie Formation factor	343	778	514	51	61
Archie m exponent	2.8	3.2	3.1	1.9	2.0

Table 27. Summary of the sample characteristics and parameters measured or derived from the different experiments run on pre- and post- flood plugs from Harvey-3.

	H3- Plug1 pre-flood	H3- Plug1A post-flood	H3- Plug1B post-flood	H3- Plug2 pre-flood	H3- Plug2 post-flood
Length (cm)	7.94	3.45	3.265	7.915	7.915
Diameter (cm)	3.8	3.8	3.8	3.79	3.79
Volume (cm ³)	90.0	39.1	37.0	89.3	89.3
Mass dry (g)	181.9	76.7	72.9	183.5	181.6
Gas porosity at room conditions (%)	21.9	23.4	20.6	21.5	22.1
Gas permeability at room conditions (md)	138	177	213	94	186
Mass saturated (g)	201.1	85.1	81.2	202.1	200.4
Brine Saturation (%)	100	95	111	100	98
Bulk dry density (g/cm ³)	2.02	1.96	1.97	2.05	2.03
Bulk wet density (g/cm ³)	2.23	2.18	2.19	2.26	2.24
Water imbibition porosity (%)	21.3	21.6	22.3	20.9	21.9
NMR water-filled porosity (%)	21.2	22.4	22.5	20.9	20.6
NMR water content (wt%)	9.5	10.3	10.3	9.2	9.2
NMR permeability computed (mD)	156	98	102	96	74
Best C NMR parameter for Coates model	10.3	8.6	8.3	10.1	8.0
Ultrasonic P-waves dry condition (m/s)	2036	1875	1784	2094	1721
Ultrasonic S-waves dry condition (m/s)	1470	707	669	1355	1207
Porosity computed by XCT segmentation (%)	18.3	12.2	12.8	19.0	9.4
Mean pore size from XCT segmentation (mm)	0.49	0.30	0.33	0.53	0.26

Table 28. Summary of the sample characteristics and parameters measured or derived from the different experiments run on pre- and post-flood plugs from Harvey-4.

	H4-Plug1 pre-flood	H4-Plug1A pre-flood	H4-Plug1B pre-flood	H4-Plug1A post-flood	H4-Plug1B post-flood	H4-Plug2 pre-flood	H4-Plug2 post-flood
Length (cm)	7.94	3.37	3.37	3.37	3.37	7.992	7.975
Diameter (cm)	3.79	3.8	3.8	3.8	3.8	3.795	3.79
Volume (cm ³)	89.6	38.2	38.2	38.2	38.2	90.4	90.0
Mass dry (g)	185.4			75.8	76.0	188.1	185.1
Gas porosity at room conditions (%)	20.366			21.4	19.5	19.604	20.783
Gas permeability at room conditions (md)	98.179			74	73	71.683	80.175
Mass saturated (g)	202.6	84.7	84.6	83.5	83.9	205.2	203.5
Brine Saturation (%)	97			98	108	100	101
Bulk dry density (g/cm ³)	2.07			1.98	1.99	2.08	2.06
Bulk wet density (g/cm ³)	2.26	2.22	2.21	2.19	2.20	2.27	2.26
Water imbibition porosity (%)	19.3			20.3	20.6	19.0	20.5
NMR water content (wt%)	8.7			9.6	9.6	8.7	8.7
NMR water-filled porosity (%)	19.6			21.1	21.0	19.8	19.7
NMR permeability computed (mD)	120			84	107	104	89
Best C NMR parameter for Coates model	10.5			10.3	11.0	11.0	10.3
Ultrasonic P-waves dry condition (m/s)	1890			1560	1478	2034	1558
Ultrasonic S-waves dry condition (m/s)	1175			869	749	1265	1095
Electrical resistivity at 100 Hz - no confining stress (ohm.m)		5	6	6	6	4	4
Archie Formation factor		24	29	28	28	19	19
Archie m exponent		2.0	2.1	2.2	2.0	1.8	1.9

	H4-Plug3 pre-flood	H4-Plug3A pre-CO ₂	H4-Plug3B pre-flood	H4-Plug3A post-flood	H4-Plug3B post-flood	H4-Plug4 pre-Flood	H4-Plug4 post-flood
Length (cm)	7.995	3.305	3.57	3.58	3.3	8.02	8.015
Diameter (cm)	3.8	3.79	3.795	3.79	3.79	3.8	3.8
Volume (cm ³)	90.7	37.3	40.4	40.4	37.2	91.0	90.9
Mass dry (g)	198.4			88.2	80.3	203.2	202.2
Gas porosity at room conditions (%)	16.816			17.1	17.6	15.401	15.252
Gas permeability at room conditions (md)	3.6218			3	3	2.6915	2.1117
Mass saturated (g)	213.8	87.2	95.3	95.0	86.8	217.1	216.4
Brine Saturation (%)	104			101	102	102	105
Bulk dry density (g/cm ³)	2.19			2.18	2.16	2.23	2.22
Bulk wet density (g/cm ³)	2.36	2.34	2.36	2.35	2.33	2.39	2.38
Water imbibition porosity (%)	17.0			16.7	17.4	15.3	15.6
NMR water content (wt%)	7.0			7.5	7.8	6.4	6.3
NMR water-filled porosity (%)	16.4			17.7	18.3	15.4	15.0
NMR permeability computed (mD)	9			11	15	4	5
Best C NMR parameter for Coates model	12.6			14.2	14.6	10.8	12.1
Ultrasonic P-waves dry condition (m/s)	2252			2157	2200	2291	2120
Ultrasonic S-waves dry condition (m/s)	1464			1388	1435	1598	1547
Electrical resistivity at 100 Hz - no confining stress (ohm.m)		6	5	8	8	5	6
Archie Formation factor		31	26	42	41	25	29
Archie m exponent		1.9	1.8	2.1	2.1	1.7	1.8

Section 4: Microstructural Evaluations

Contributor

Dr. Claudio Delle Piane

Introduction

This section of the report is concerned with the chemical, mineralogical and microstructural evaluation of the samples tested. In order to track possible modifications in the microstructural arrangement of the samples (e.g. mineral dissolution and/or precipitation; grain dislodgement) a novel microstructural workflow was developed to allow quantitative analysis to be repeated on the same specimens before and after the flooding experiments. The information generated in the previous studies (Projects 7-1111-0199 (Delle Piane et al, 2013), 7-1111-0200 (Stalker et al, 2013) and 3-1110-0122 (Evans et al., 2013)) pointed to possible pore scale events occurring during the flooding process as the cause of the observed changes in the petrophysical properties of the samples tested. The above workflow was designed in a way that it would help to pinpoint and better understand such pore scale alterations if they indeed occur.

Methodology

A Philips XL 40 scanning electron microscope (SEM) was used to visualize the microstructure and acquire elemental maps from the surface of the samples. Images were collected in back scattered electron (BSE) mode: the bit depth of the images expressed in grey levels is related to the atomic number (Z) of the material such that minerals characterized by low Z appear dark and minerals with high Z are bright. Electron bombardment of the sample surface also produces X-rays that are captured via an energy dispersive detector allowing the elemental mapping of desired elements on the sample surface. For this study, maps of the following elements were collected: Al; Ca; Fe; K; Mg; Na; S; Si with the purpose of monitoring eventual element mobilization during the core flooding tests. The choice of elements was based on the mineralogy of the samples known from previous studies on the Harvey-1 cores (e.g. Delle Piane et al. 2013; Olierook et al. 2014).

Large areas were mapped at high resolution by collecting a matrix of images each having a size of 1500 by 1294 pixels with pixel size of 3.17 microns (Figure 49). The single images were then stitched together in one file using the algorithm developed by Preibisch et al., (2009) in the freeware image analysis package Fiji (Schindelin et al., 2012).

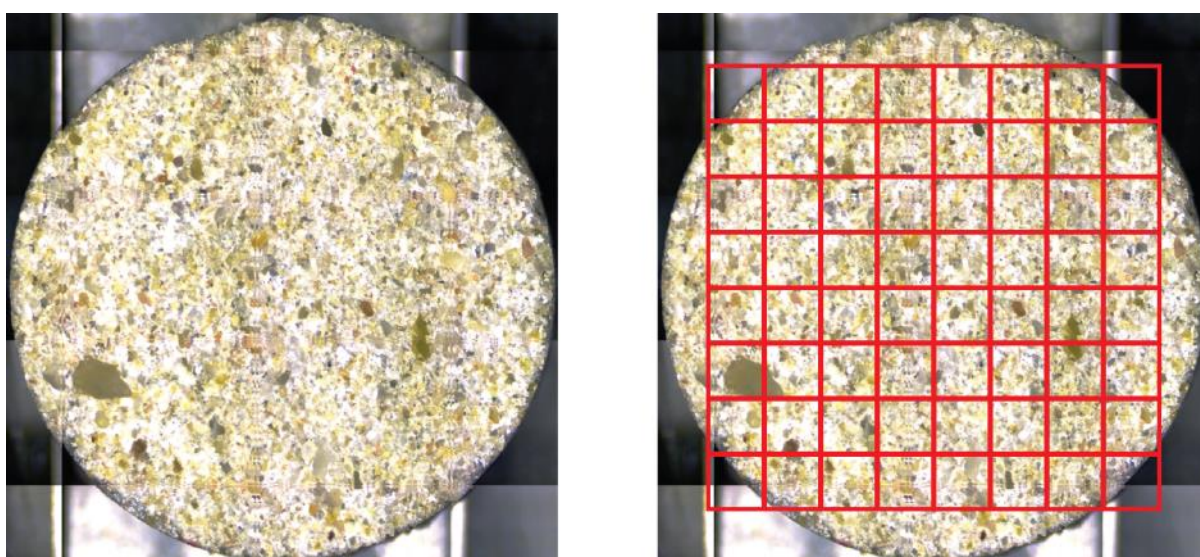


Figure 49 Left: Reflected light image of a polished surface of a disc belonging to H1-Plug4, diameter of the circular surface is 38 mm. Right: overlay showing the grid of images acquired with the SEM.

During acquisition, operating conditions of SEM imaging and elemental mapping were as follows: 30 KV acceleration voltage; 28.7 mm working distance; 50 X magnification; the energy dispersive detector was set to acquire X-rays with energy up to 20 KeV at a maximum rate of 130 Kcps.

The same sample area was imaged again after flooding experiments; for quantitative analysis the two images need to be registered, this was done by identifying a set of corresponding points of interest in the two images via the Scale Invariant Feature Transform (SIFT; Lowe, 2004) and subsequently applying geometric translation and rotation to the images to match the position of the points of interest.

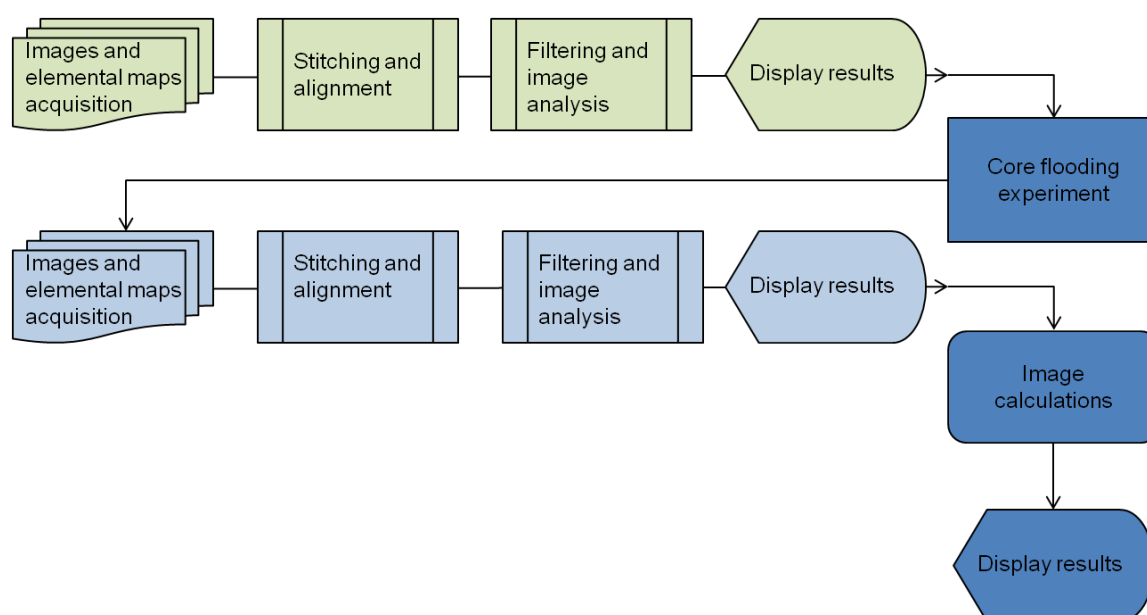


Figure 50 Flow chart illustrating the acquisition, treatment and analysis steps performed on the SEM mosaics acquired on the Wonnerup samples.

The main steps of the image acquisition and treatment are summarized as a flow chart in Figure 50 the last step is a quantitative image analysis used to:

- Evaluate mineral abundance in the samples;
- Determine grain size and shape of particular minerals of interest;
- Assess microstructural modifications in the identified mineral species as a consequence of the experimental flooding procedure.

Examples of the large area BSE image and elemental maps are given in Figure 51; elemental maps were used as single files and as layers in multi-channel analysis to trace element mobility and mineralogical variations before and after flooding, respectively. For example K-feldspar (KAlSi_3O_8) was visualized by adding the Si, Al, and K elemental maps, while Kaolinite ($\text{Al}_2(\text{Si}_2\text{O}_5)(\text{OH})_4$) was highlighted by adding the Si and Al elemental maps and subtracting the K one.

Quantitative image analysis was conducted on the stitched mosaic using the ImageJ freeware (<http://rsbweb.nih.gov/ij/>); the original images were converted to 8 bits and de-noised using a Gaussian blur filter; the contrast was then improved by normalizing the grey level values of the images.

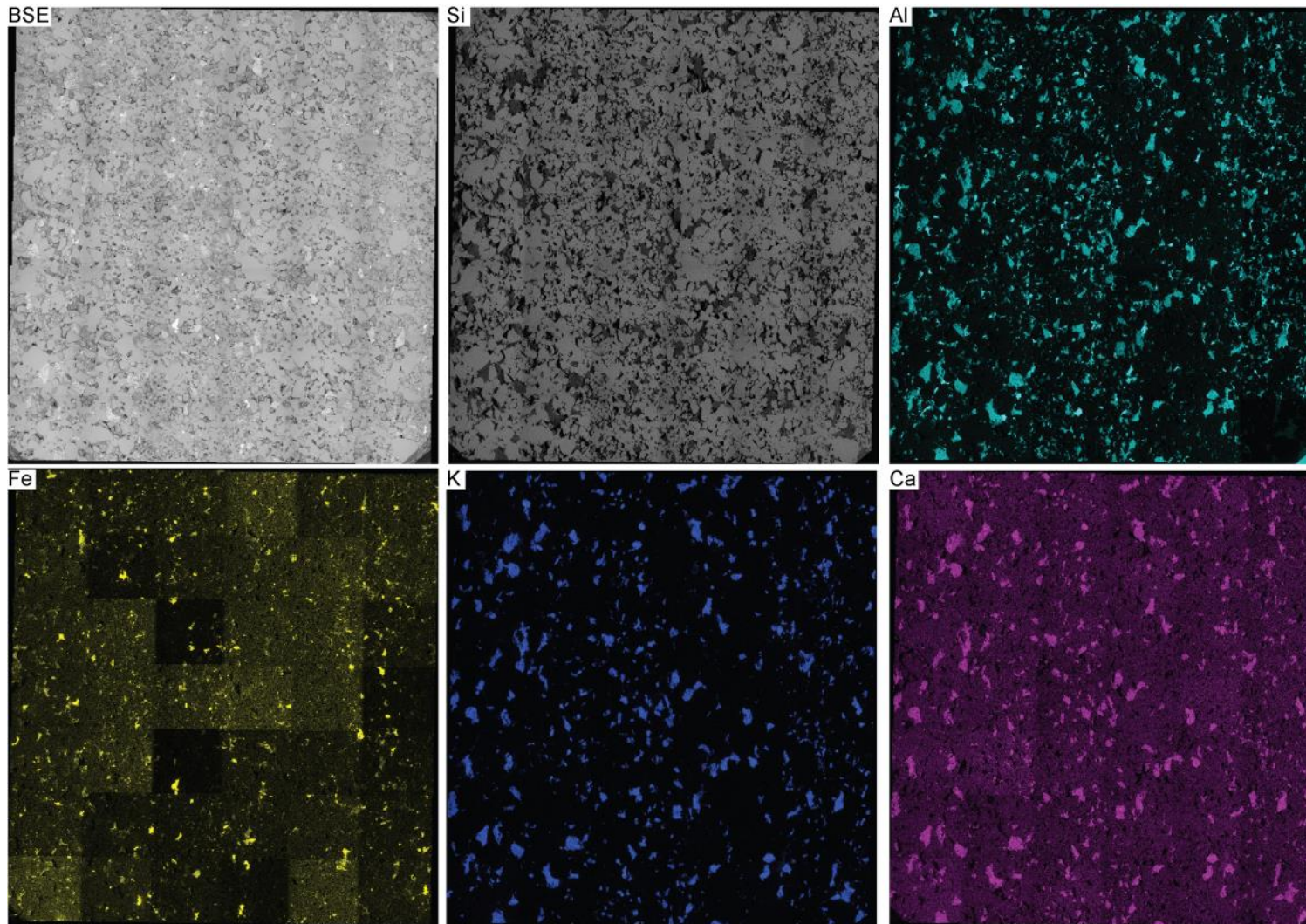


Figure 51 Mosaics of the surface of a disc belonging to H1-Plug4 imaged using the SEM in back scattered electron (BSE) and elemental mapping mode. Each image is composed of a matrix of 42 tiles stitched together in a single file of 8532×9055 pixels (27.05×28.70 mm; 1pixel = 3.17 microns).

After the preliminary image treatment the goal of the analysis is to quantify certain parameters of the various minerals occurring in the rocks. By applying simple mathematical operations to the elemental maps it was possible to create maps highlighting quartz, k-feldspar, kaolinite and calcite as separate datasets. Manual thresholding allowed isolating the mineral of interest; a particle analyser algorithm was then used to identify and geometrically characterize the grains according to the following geometrical descriptors:

- Equivalent circular diameter (d): defined as the diameter of a circle with the same area as the

$$\text{particle } (d = \sqrt{\frac{4 * Area}{\pi}});$$

- Shape factor (S): defined as the degree to which the particle is similar to a circle taking into account the smoothness of the perimeter. As the value approaches 0.0, it indicates an increasingly

$$\text{elongated shape, while 1 indicates a perfect circle } (S = \sqrt{\frac{4\pi Area}{Perimeter^2}}).$$

Ideally, before microstructural investigations, the surface of the samples should be prepared following standard petrographic polishing, but due to the friable nature of the samples collected from wells Harvey-3 and Harvey-4, it was not possible to achieve the fine polishing grade (1 μ m) achieved on the Harvey-1 samples. The effect of surface roughness is detrimental to reliable X-ray energy dispersive spectroscopy, as the take-off angle of the X-rays emission and path to the detector will be affected by the topography of the surrounding region (Figure 52).

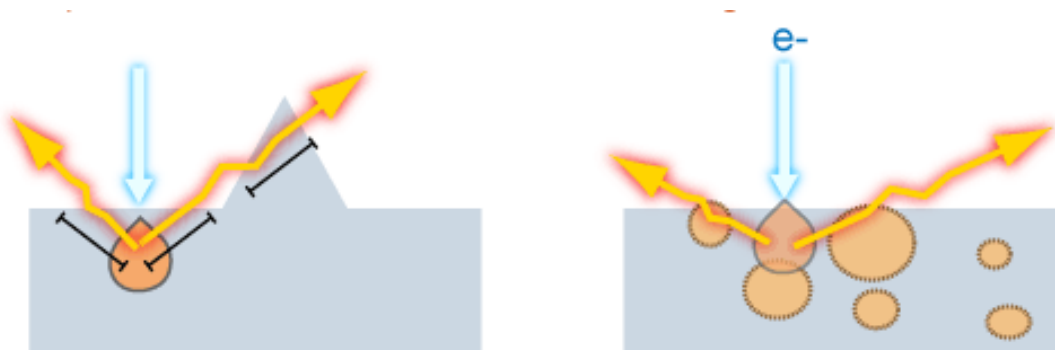


Figure 52 Schematic drawing illustrating the importance of proper sample preparation quantitative analysis. Left: rough sample surface affecting the propagation of X-rays emitted (yellow arrows) from the interaction volume (orange teardrop) excited by the incident electron beam (blue arrow). Right: smooth sample surface. Image modified from <http://www.ammrf.org.au/myscope/analysis/eds/quantitative/>.

Therefore, for the Harvey-3 and Harvey-4 specimens, the focus is on the comparison between BSE images of the sample surface before and after core flooding. No attempt was made to quantify mineral abundance and shape from the X-ray elemental maps due to the sample preparation limitations illustrated above.

Analytical Results

Harvey-1

Two sample assemblies composed of four plugs (two plugs per each assembly) from well Harvey-1 were selected. As indicated in Section 1, all plugs are macroscopically described as medium to very coarse grained cross bedded sandstone with significant grain size variation between beds and are representative of high energy fluvial channel fill and barforms depositional environment (Facies Ai and Aii according to the classification proposed by Delle Piane et al. 2013; Olierook et al. 2014). Position of the plugs with respect to the Harvey-1 cores is given in Figure 53 along the sedimentological logging, gamma ray, petrophysical and mineralogical logs. The depth of each plug can be found in Table 1.

Hyperspectral logging in the short wavelength infrared region reveals the presence of kaolinite as the only clay mineral at depth corresponding to those of the selected samples (Figure 53); this is also confirmed by quantitative mineralogy results obtained via X-ray diffraction analysis on samples taken at adjacent depths to those analysed here (Table 29). The main mineral constituents of samples representing facies Aii of the Wonnerup are quartz (> 70 % by mass); K-feldspar (> 8 % by mass) and kaolinite (> 5 % by mass) accessory minerals are calcite and berthierine (a non-swelling Fe-rich clay with kaolinite structure).

Depth (m)	Quartz	K-feldspar	Calcite	High-Mg calcite	Ankerite	Kaolinite	Berthierine	Facies
1916.38	70	14	---	1	---	13	2	Aii
1935.5	77	12	---		4	7		Aii
2496.22	83	9	---		---	6	3	Aii
2503.46	86	8	1		---	5	---	Aii

Table 29. XRD mineralogy obtained on samples from the Harvey -1 well at depths adjacent to those analyzed in this study and described as the same lithofacies. Values expressed as weight %.

The following analysis reports results obtained from two discs extracted from depths of 1924.7 (H1-Plug2) and 2505.4 m (H1-Plug4).

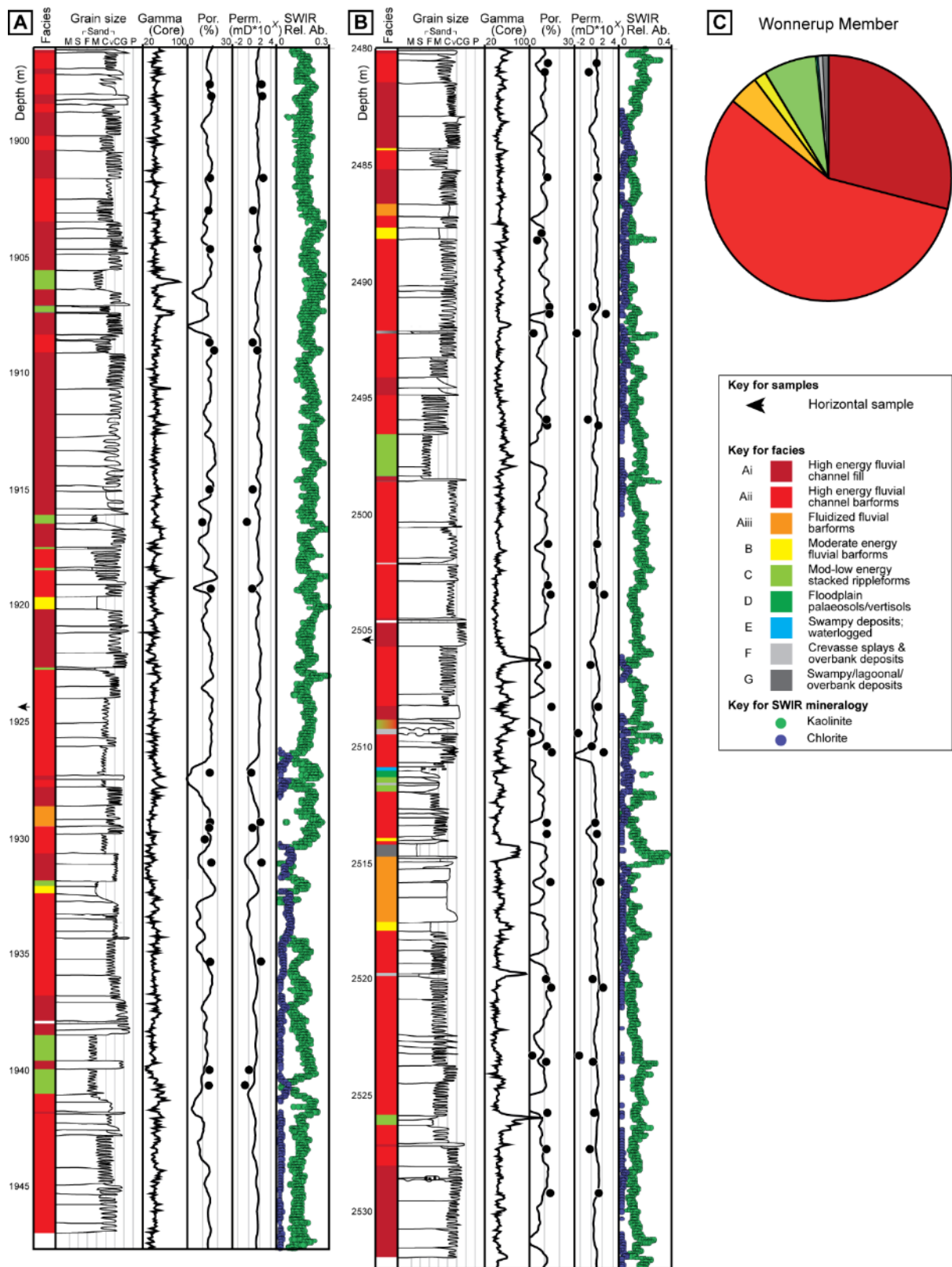


Figure 53. (A-B) Positions of selected plugs and distribution of lithofacies and rock properties in the Wonnerup Member cored intervals of Harvey 1: (A) Core 5, 1896-1847.7 m, and; (B) Core 6, 2480-2532.5 m. Gamma was taken at 5 cm intervals on whole core. Porosity (Por.) and permeability (Perm.) were determined from wireline logs (continuous lines) and from helium-injection on core plugs (black dots). Short-wavelength infrared (SWIR) spectra from the HyLogger were binned every 20 cm. (C) Pie chart showing the relative abundance of each facies of the Wonnerup Member. Modified after Olierook et al., 2014.

Unfortunately, it was not possible to have a reliable microstructural comparison of the disc cut from H1-Plug2 (depth 1924.84m) before and after flooding due to technical problems during the acquisition of the images. The long acquisition time required to collect the multiple tiles and X-ray information at a reasonable quality affected the stability of the electron beam in the SEM resulting in severe artefacts in the pre-flooding dataset. These, in turn, hindered to the procedure designed to automatically stitch and align the tiles for an unbiased comparison of microstructural features of the rocks. Nevertheless, a general description of the rock sample can be made based on the single tiles acquired pre-flooding, while the quantitative analysis is restricted to the post flooding dataset.

The sediment is composed of equant to slightly elongated quartz crystals making up the load-bearing framework of the rock; minor K-feldspar grains of similar shape and size as the quartz are also noted as well as occasional oxides. Quartz is primarily monocrystalline and 5-10% of total quartz is polycrystalline appearing in large aggregates typically of several mm in size. K-feldspar appears either intact or skeletal with kaolinite infill. Quartz and feldspars grains are of detrital origin and sub-angular to sub-rounded in shape indicating moderate distance from the sediment source (Figure 54).

Diagenetic alterations of the original deposit are recognised as i) quartz overgrowth cements along the grain boundaries of detrital quartz crystals; ii) kaolinite in form of microcrystalline coatings on detrital grains, as infills of feldspar skeletal grains and as heterogeneously distributed pore-occluding clots in the vicinity of skeletal feldspar grains; iii) Ti-oxides probably formed as a results of K-feldspar dissolution (Figure 54).

Statistical analysis of the grain size and shape of quartz and K-feldspar grains are reported in Table 30 and illustrated in Figure 55.

	Mean	Median	S.D.	Min	Max	Count	Mineral
d (μm)	189.27	153.77	144.59	17.52	1731.83	4977	Quartz
S	0.73	0.73	0.13	0.28	1.00	4977	
d (μm)	108.86	64.78	122.35	17.52	1299.89	1868	K-feldspar
S	0.77	0.83	0.23	0.09	1.00	1868	

Table 30. Summary of the image analysis results for the quartz and K-feldspar particles identified in the disc cut from H1-Plug2 (depth 1924.84 m). d = equivalent circular diameter; S = shape factor; S.D. = standard deviation.

Quartz grains have larger mean diameter and show a broader size distribution than the feldspar ones (Figure 55). The shape of the grains expressed as shape factor (S) show an inverse correlation with equivalent circular diameter indicating that the smaller grains are rounder and more equant than the larger ones for both quartz and K-feldspar (Figure 55 right).

The mean shape factor is 0.73 and 0.77 for quartz and k-feldspar respectively indicating a statistically similar shape of the two minerals. Feldspar particles show a broader range of S values extending to a minimum of 0.09 for the larger grains (Figure 55 right)

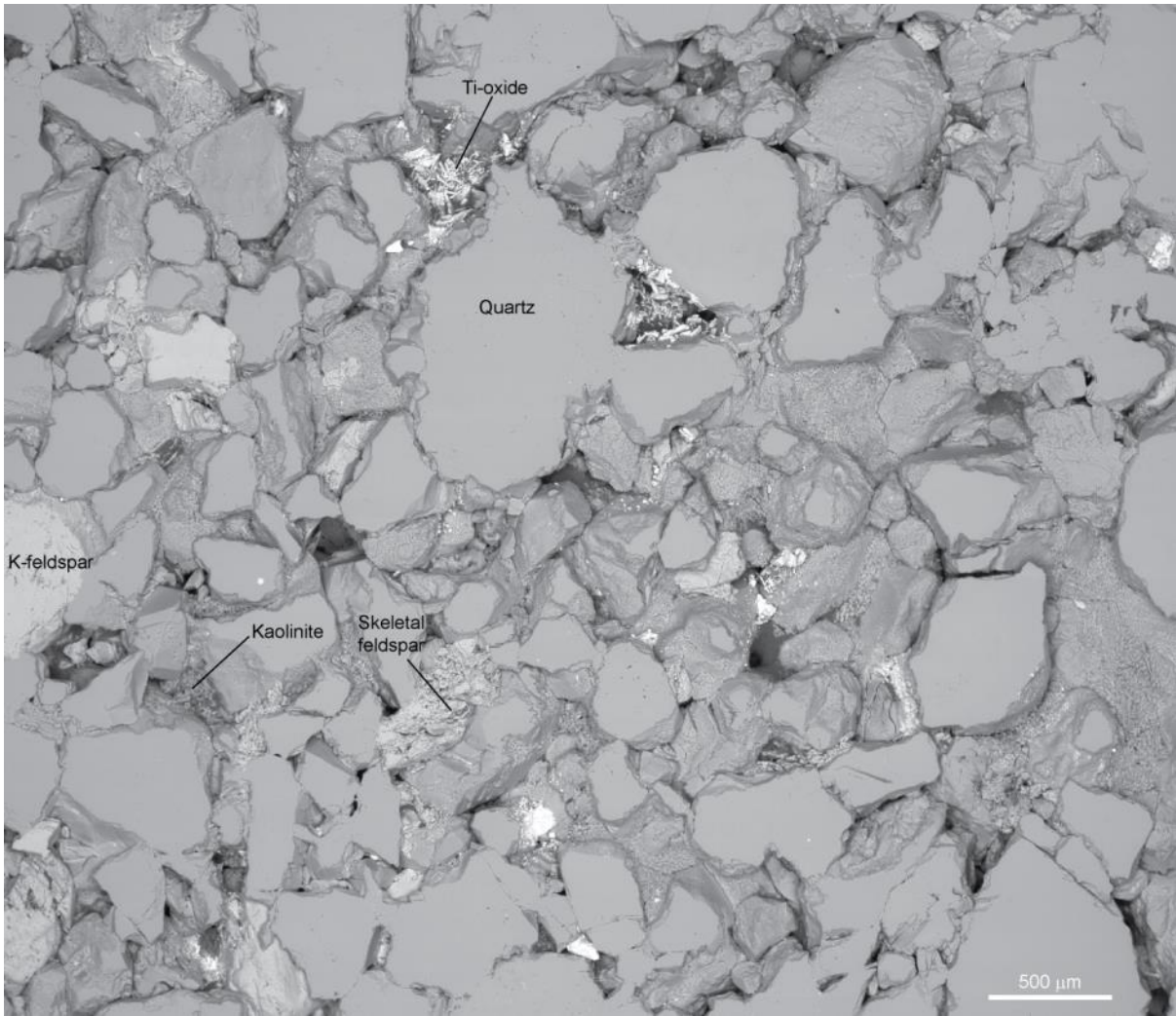


Figure 54. BSE image of the disc cut from H1-Plug2 (depth 1924.84 m) illustrating the main mineral phases of the sediment and their geometry.

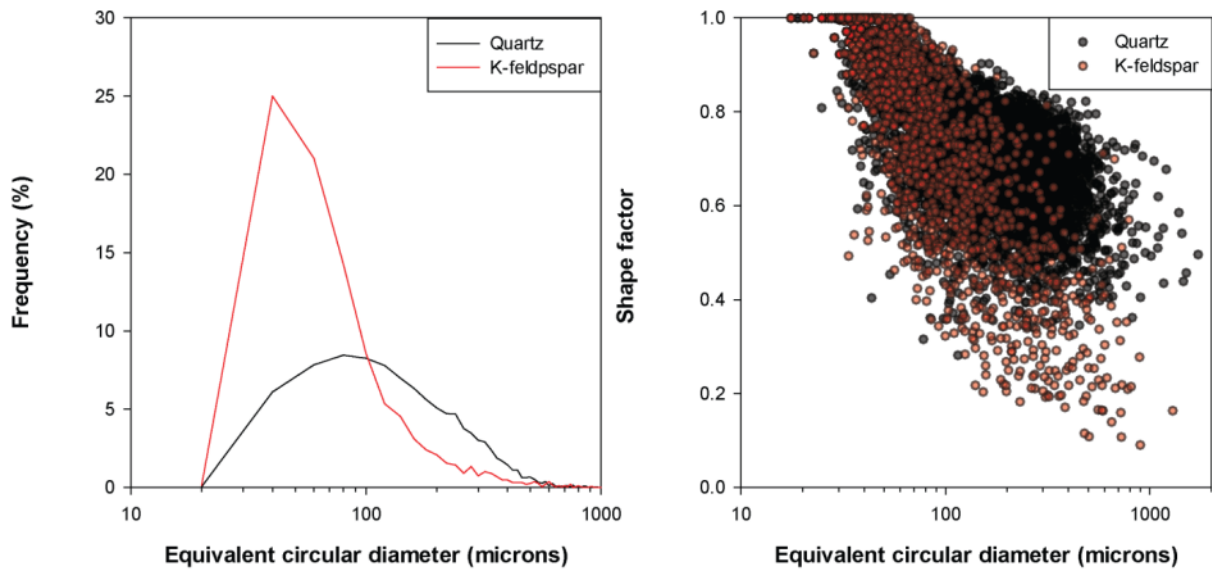


Figure 55. Grain size and shape of quartz and K-feldspar grains identified in the disc cut from H1-Plug2 (depth 1924.84 m). Left: Histogram of equivalent circular diameter of quartz and K-feldspar grains. Right scatter plot of the shape factor as a function of the grain size of quartz and feldspar grains.

The microstructure of the disc cut from the deeper H1-Plug4 is dominantly composed of equant to slightly elongated quartz crystals and minor K-feldspar grain of similar shape and size as the quartz; these two minerals make up the load-bearing framework of the rock. Quartz is almost exclusively monocrystalline and 5-10% K-feldspar appears either intact or skeletal with kaolinite infill. Quartz and feldspars grains are of detrital origin and sub-angular to sub-rounded in shape indicating moderate distance from the sediment source (Figure 56).

As seen in the disc cut from H1-Plug2, diagenetic alterations of the original sediments are recognised as i) quartz overgrowth cements along the grain boundaries of detrital quartz crystals; ii) kaolinite in form of microcrystalline coatings on detrital grains, as infills of feldspar skeletal grains and as heterogeneously distributed pore-occluding clots in the vicinity of skeletal feldspar grains; iii) small calcite (Figure 56).

Statistical analysis of the grain size and shape of quartz, K-feldspar, kaolinite and calcite grains identified from image analysis of the disc cut from H1-Plug4 before and after the flooding experiment are reported in Table 31 and Table 32, respectively and illustrated in Figure 57.

	Mean	Median	S.D.	Min	Max	Count	Mineral
<i>d</i> (μm)	125.80	75.96	133.38	5.06	1471.39	11784	Quartz
<i>S</i>	0.71	0.70	0.15	0.28	1.00	11784	
<i>d</i> (μm)	130.30	63.48	162.42	10.12	1132.56	1424	K-feldspar
<i>S</i>	0.77	0.84	0.22	0.13	1	1424	
<i>d</i> (μm)	48.99	34.86	43.72	10.73	427.07	1691	Kaolinite
<i>S</i>	0.81	0.88	0.20	0.14	1	1691	
<i>d</i> (μm)	32.74	29.06	18.36	8.76	351.58	6092	Calcite
<i>S</i>	0.88	0.94	0.16	0.17	1	6092	

Table 31. Summary of the image analysis results for the quartz, K-feldspar, kaolinite and calcite particles identified in the disc cut from H1-Plug4 (depth 2505.52 m) before flooding experiment. *d* = equivalent circular diameter; *S* = shape factor; S.D. = standard deviation.

	Mean	Median	S.D.	Min	Max	Count	Mineral
<i>d</i> (μm)	119.01	72.96	125.28	5.06	1231.66	12695	Quartz
<i>S</i>	0.72	0.71	0.14	0.31	1	12695	
<i>d</i> (μm)	120.01	60.60	146.60	10.73	1092.20	120.01	K-feldspar
<i>S</i>	0.77	0.85	0.23	0.11	1	0.77	
<i>d</i> (μm)	32.40	25.54	23.35	10.73	208.14	2119	Kaolinite
<i>S</i>	0.85	0.91	0.18	0.17	1	2119	
<i>d</i> (μm)	48.56	36.13	43.74	10.73	470.79	3315	Calcite
<i>S</i>	0.83	0.91	0.20	0.10	1	3315	

Table 32. Summary of the image analysis results for the quartz, K-feldspar, kaolinite and calcite particles identified in the disc cut from H1-Plug4 (depth 2505.52 m) after flooding experiment. *d* = equivalent circular diameter; *S* = shape factor; S.D. = standard deviation.

Similarly to what was observed in the disc from H1-Plug2, quartz and feldspar in the disc from H1-Plug4 have similar size and shape with mean values of equivalent circular diameter of 125.8 and 130.3, respectively. The spectrum of shape factor values is slightly broader in the feldspar than in the quartz grains as indicated by the minimal for the two minerals (0.28 and 0.13 respectively).

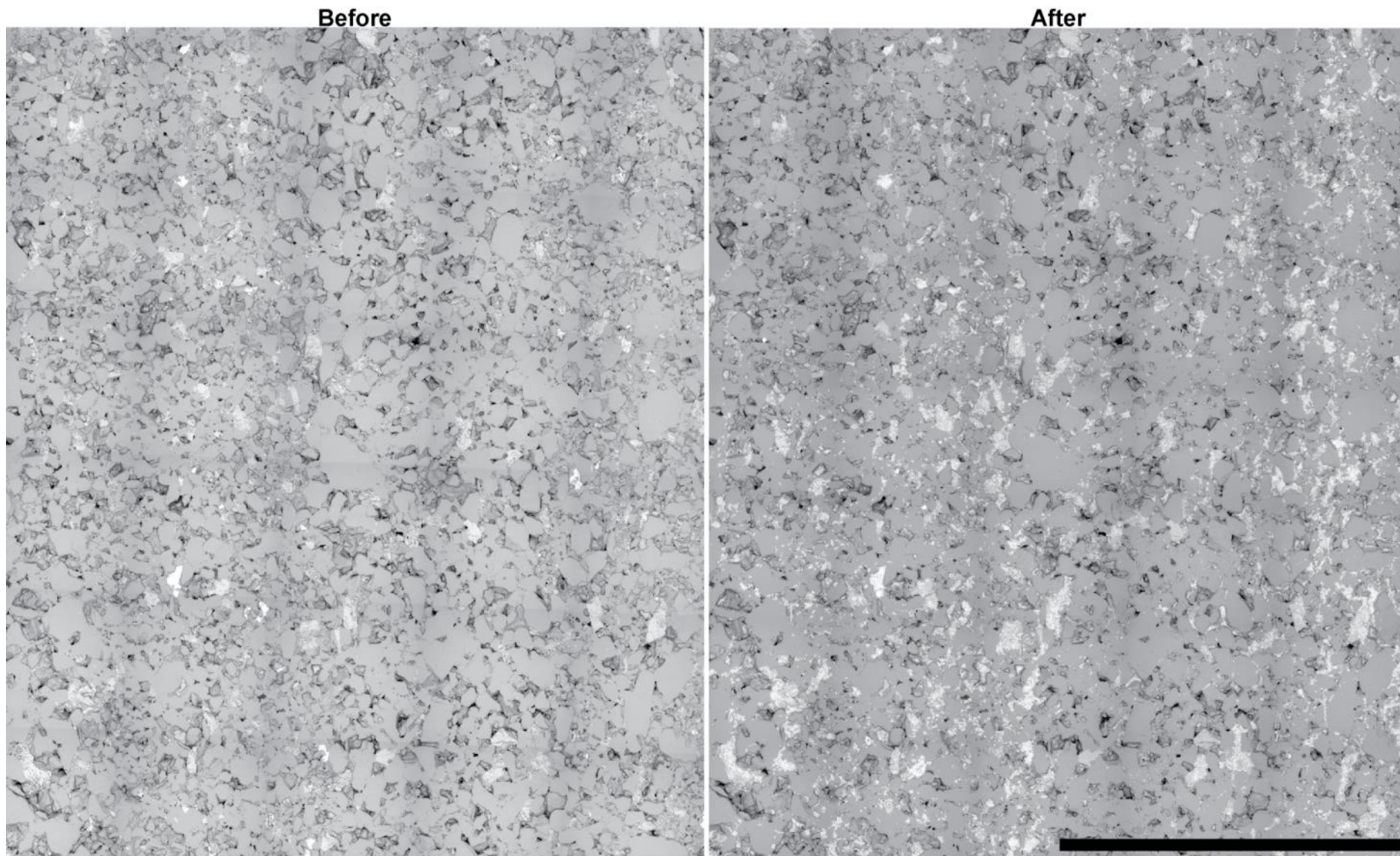


Figure 56. BSE images of the core surface before and after core flooding tests, sample is oriented so that bedding is vertical. Black scale bar is 1 cm (the disc cut from H1-Plug4; depth 2505.52 m)

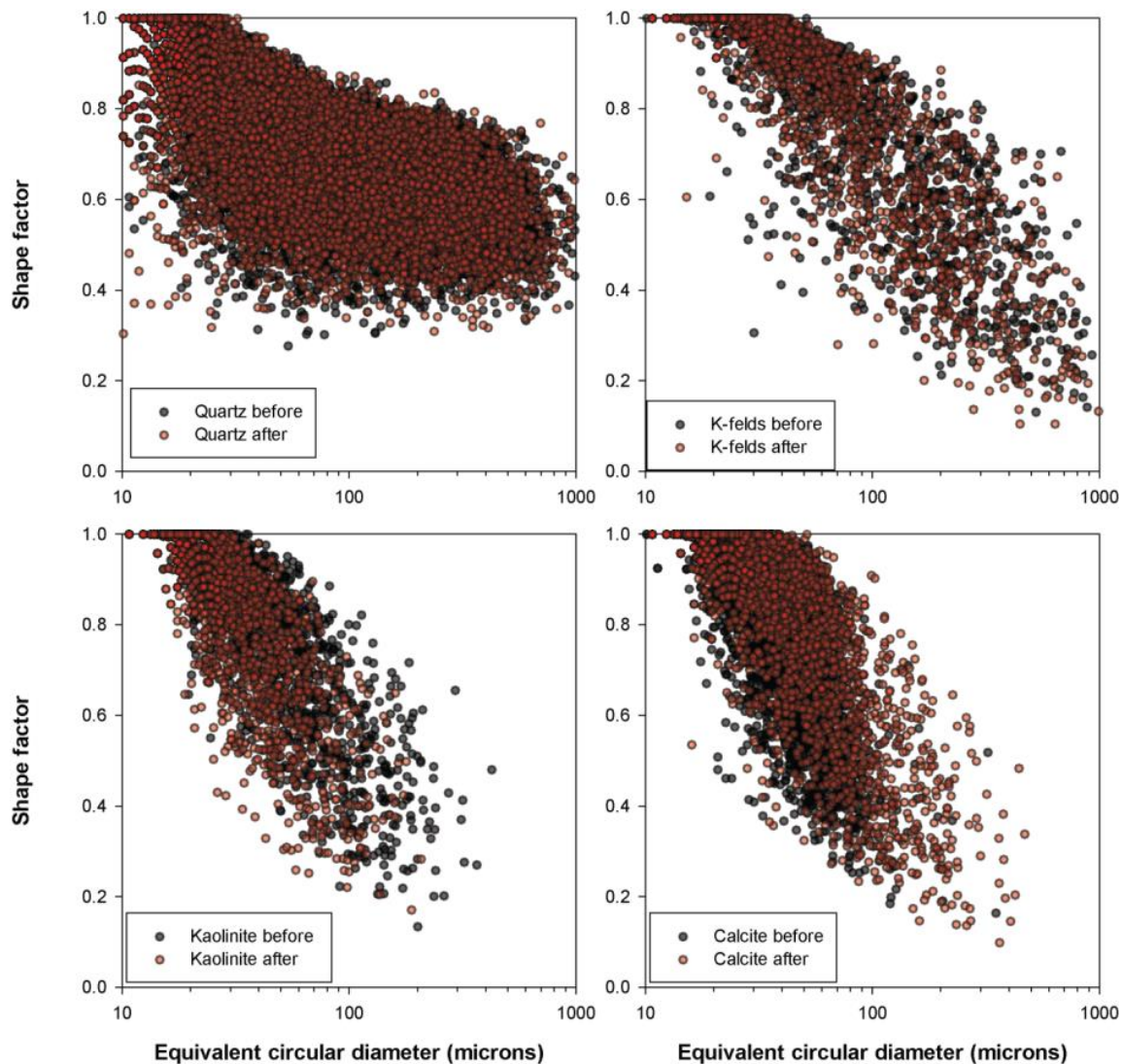


Figure 57. Scatter plots of the shape factor as a function of the grain size of quartz, feldspar, kaolinite and calcite grains before and after the core flooding tests on the disc cut from H1-Plug4 (depth 2505.52 m).

Grains of kaolinite and calcite have significantly lower mean d size than the detrital quartz and feldspar, this together with the observation of their spatial distribution allow their identification with respect to diagenetic origin.

Figure 57 shows cross plots of shape factors as a function of equivalent circular diameter for the four minerals and compares their spread before and after the flooding tests. While no significant changes can be observed in the quartz and feldspar grains, kaolinite and calcite show some visible differences in their distribution. Specifically, after flooding kaolinite grains are shifted towards smaller d values while calcite grains are shifted towards larger d values.

In summary, only one of the two discs from Harvey-1 cores was comprehensively characterized before and after flooding, and the analysis indicated that no significant change in shape or size is observed in the framework grains of the rock (i.e. detrital quartz and K-feldspar) while pore occluding mineral phases like diagenetic kaolinite and calcite show a decrease and an increase in the statistical distribution of grain size respectively, as a result of the flooding experiment (Figure 57 and Figure 58).

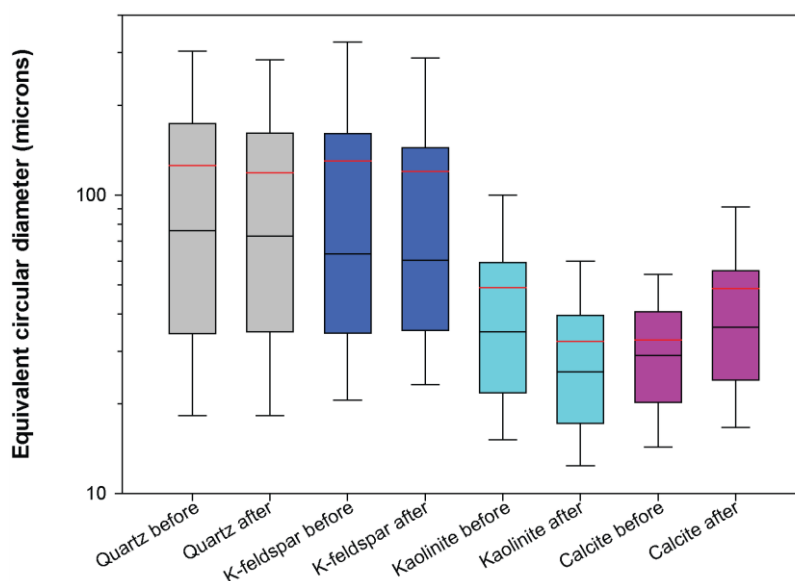


Figure 58. Box plot summarizing the distribution of the main minerals identified from the image analysis of the disc cut from sample H1-Plug4 (depth 2505.52 m). The boundary of the box closest to zero indicates the 25th percentile, and the boundary of the box farthest from zero indicates the 75th percentile. Error bars above and below the box indicate the 90th and 10th percentiles. The black and red lines within the box indicate the median and mean of the distribution respectively.

Harvey-3

One disc of sample H3-Plug1 from the Harvey-3 well (depth = 1459.40 m) was used for microstructural characterization before and after core flooding experiments. The core is described as medium to very coarse grained cross bedded sandstone with significant grain size variation between beds and is representative of high energy fluvial channel fill and barforms depositional environment, consistently with the samples from Harvey-1 described earlier.

As indicated earlier, ideally, before microstructural investigations, the surface of the samples should be prepared following standard petrographic polishing, but due to the friable nature of the samples from Harvey-3, it was not possible to achieve the fine polishing grade (1 μ m) achieved on the Harvey 1 samples described in the previous section. The effect of surface roughness is detrimental to reliable X-ray energy dispersive spectroscopy, as the take-off angle of the X-rays emission and path to the detector will be affected by the topography of the surrounding region (Figure 52).

As observed in the samples from the Harvey-1 well, the sediment is composed of equant to slightly elongated quartz crystals making up the load-bearing framework of the rock; minor K-feldspar grain of similar shape and size as the quartz are also noted as well as occasional oxides. Quartz is primarily monocrystalline and 5-10% of total quartz is polycrystalline appearing in large aggregates typically of several mm in size. K-feldspar appears either intact or skeletal with kaolinite infill. Quartz and feldspars grains are of detrital origin and sub-angular to sub-rounded in shape indicating moderate distance from the sediment source. Diagenetic alterations of the original deposit are recognised as i) quartz overgrowth cements along the grain boundaries of detrital quartz crystals; ii) kaolinite in form of microcrystalline coatings on detrital grains, as infills of feldspar skeletal grains and as heterogeneously distributed pore-occluding clots in the vicinity of skeletal feldspar grains; iii) Ti-oxides probably formed as a results of K-feldspar dissolution (Figure 59).

A comparison of the images collected before and after flooding allows for the visualization of some interesting microstructural modifications; it is observed that some of the detrital grains are either missing or appear cracked in the images acquired after flooding, this is probably due to the friable nature of the sample and the consequent inability to achieve a good polish. Rough surfaces in contact with each other under the stress imposed by the in-situ conditions during the experimental flooding probably resulted in localised grain crushing at joining asperities (Figure 59)

Another prominent feature of the images collected after flooding is the presence of enhanced pore connectivity in clay rich pore throats between detrital grains of quartz and feldspar (Figure 60 and Figure 61). The clay is most likely kaolinite as interpreted from its morphological features and the mineralogical data collected on equivalent samples from Harvey-1.

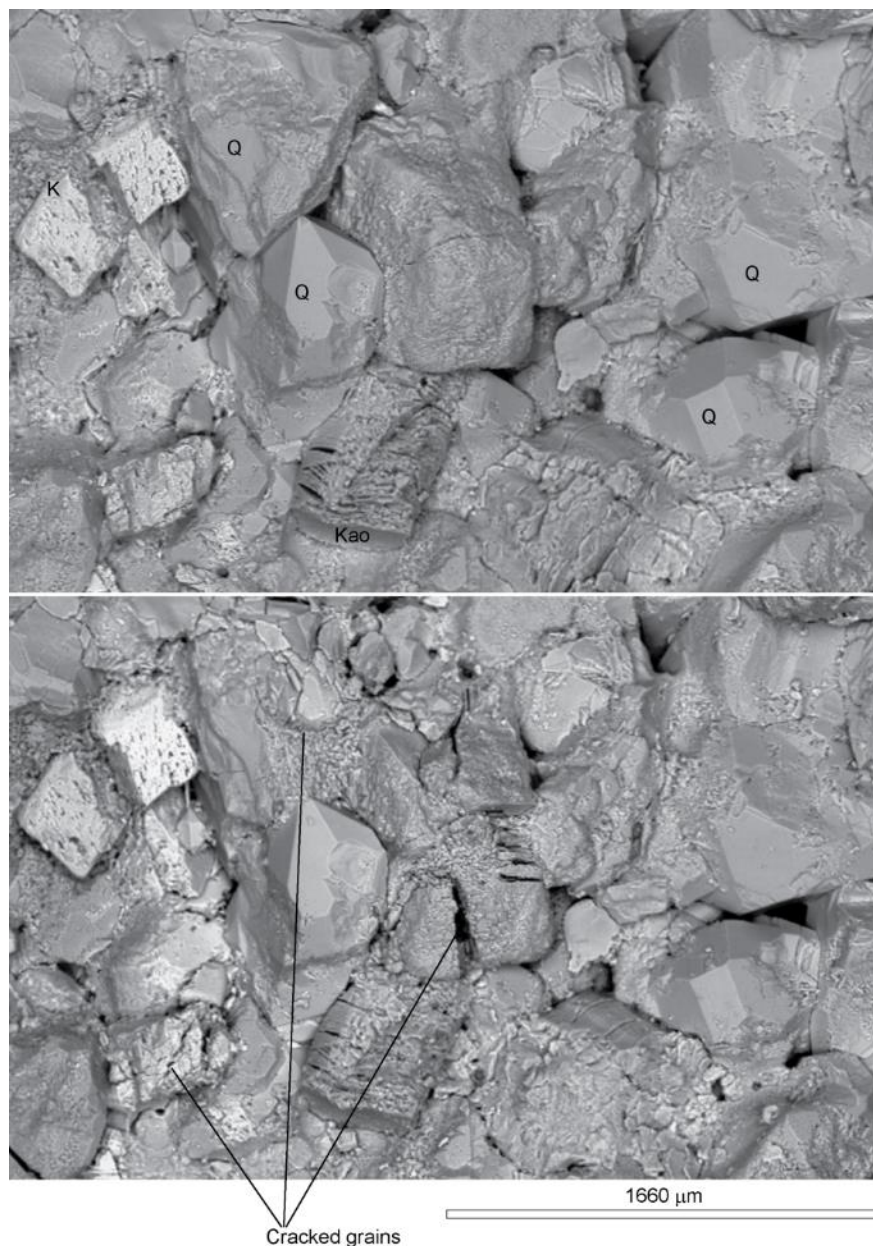
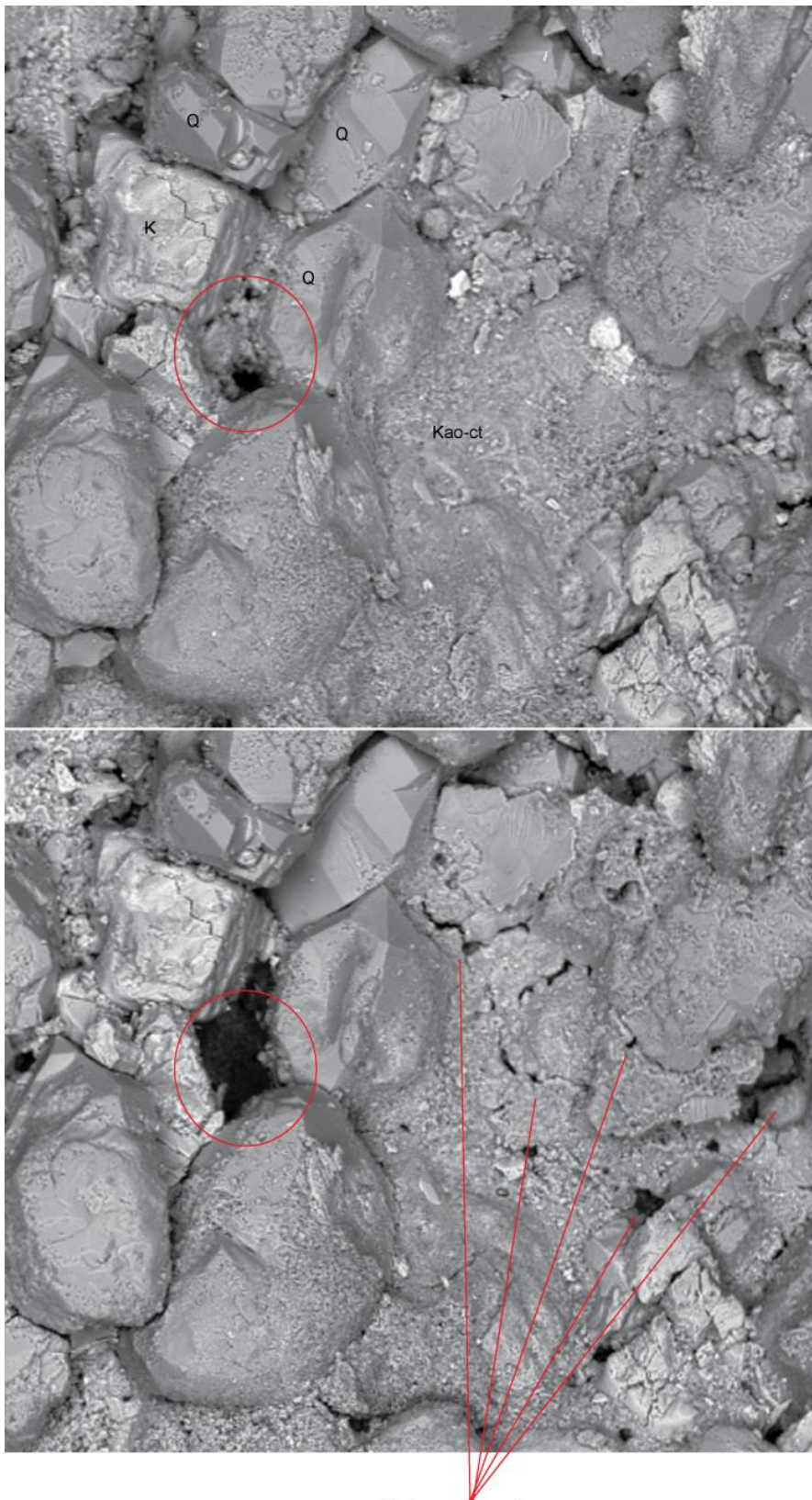


Figure 59. Detail of the disc cut from sample H3-Plug1 before (top) and after (bottom) core flooding test. Q = quartz; Kao = kaolinite; K = K-feldspar. Note the presence of cracked grains in the bottom image. These are probably due to high contact stresses at surface asperities during the core flooding experiment. Also note the euhedral shape of many of the quartz grains indicative of diagenetic cementation by quartz overgrowth.



Enhanced pore connectivity

Figure 60 Detail of the disc cut from sample H3-Plug1 before (top) and after (bottom) core flooding test. Width of the image is 2.5 mm. Q = quartz; Kao-ct= kaolinite coating; K = K-feldspar. Note the presence of enhanced connectivity in the bottom image mostly occurring in regions previously occupied by clays.

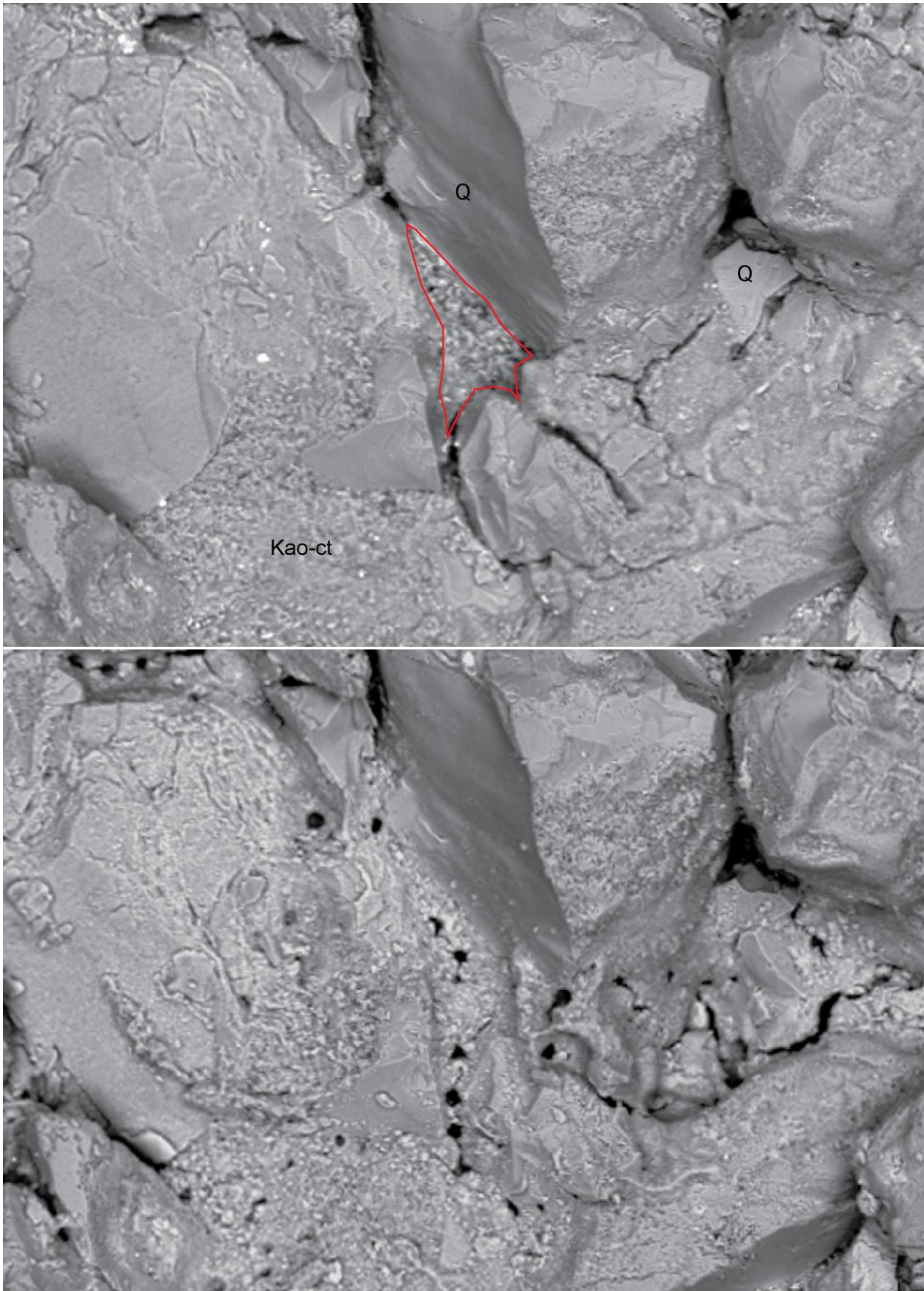


Figure 61: Detail of the disc cut from sample H3-Plug1 before (top) and after (bottom) core flooding test. Width of the image is 2.3 mm. Q = quartz; Kao-ct= kaolinite coating; K = K-feldspar. The red envelope in the top image delineates a pore throat between quartz grains. Note the presence of enhanced porosity in the bottom image mostly occurring in regions previously occupied by clays.

In summary, BSE mosaics were collected from a non-polished disk cut out from a sample retrieved from the Harvey 3 well at a depth of 1459.5 m (H3-Plug1). A comparison of the images before and after flooding allows the recognition of clay mobilization which could be linked to the core flooding test. Removal of fine-grained clay coatings and from pore bridging clay aggregates is non-ambiguously identified in the images presented above. The modifications of pore space and the fracturing of some of the detrital grains are expected to affect both the transport and elastic properties of the rock.

Harvey-4

Two discs of H4-Plugs1 and H4-Plug3 from the Harvey-4 well (depth = 1794.53 m and 1800.42, respectively) were used for microstructural characterization before and after core flooding experiments. The core material can be described as medium to very coarse grained cross bedded sandstone with significant grain size variation between beds and is representative of high energy fluvial channel fill and barforms depositional environment, consistently with the samples from Harvey 1 and 3 described earlier.

As also observed in the samples from the Harvey-1 and 3 wells, the sediment is composed of equant to slightly elongated quartz crystals making up the load-bearing framework of the rock; minor K-feldspar grain of similar shape and size as the quartz are also noted as well as occasional oxides. Quartz is primarily monocrystalline. K-feldspar appears either intact or skeletal with kaolinite infill. Quartz and feldspars grains are of detrital origin and sub-angular to sub-rounded in shape indicating moderate distance from the sediment source. In contrast with the sample from Harvey-3, pore space seems to be mostly occluded by clay minerals, and diagenetic quartz overgrowths appear less evident.

A comparison of the images collected before and after flooding allows for the visualization of some interesting microstructural modifications, overview mosaics are shown in Figure 62. It is observed that in the disc from H4-Plug1 there is an obvious mobilisation of clays which appear to be either removed or deposited in some of the pore throats found between detrital grains of quartz and feldspar (Figure 63). Overall, based on the images alone, it is hard to assess whether the total porosity is enhanced or diminished as a consequence of the flooding, but the measurements presented in Section 3 indicate a slight increase of porosity at the core scale.

A comparison of the SEM images collected on the disc from H4-Plug3 before and after flooding test reveals much less evidence of microstructural modifications as a consequence of the flooding tests. Figure 64 shows two regions of interests characterised by the presence of detrital quartz and feldspar and abundant pore occluding clays. In previous samples (H4-Plug1 and H3-Plug1 described earlier) such areas were observed to be preferential loci for evidence of fluid-rock interaction. In this case the images before and after flooding seem to be similar and no inference can be made on possible interaction between the fluids and the rock during the flooding tests.

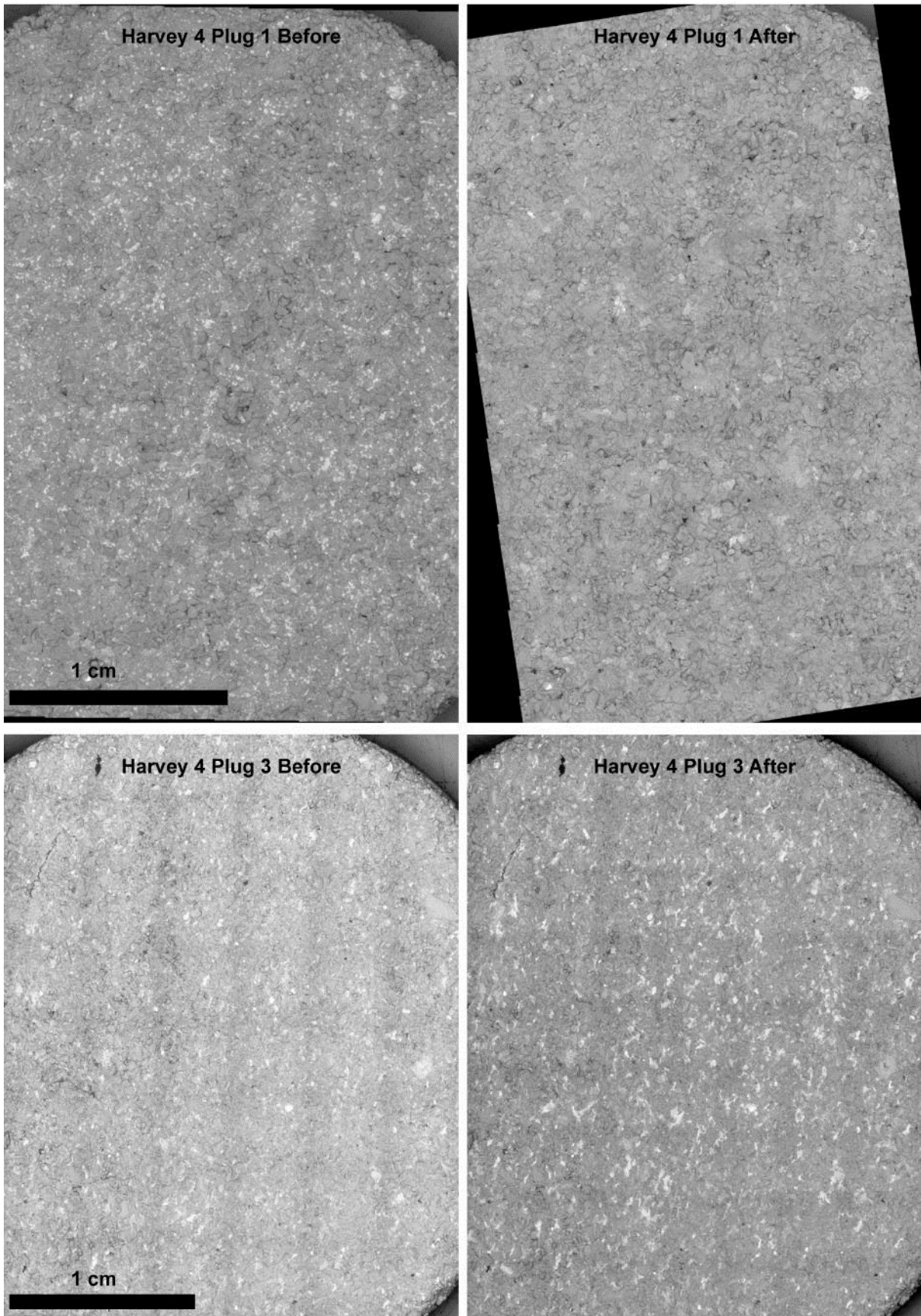


Figure 62. Mosaic of BSE images collected from the two analysed samples.

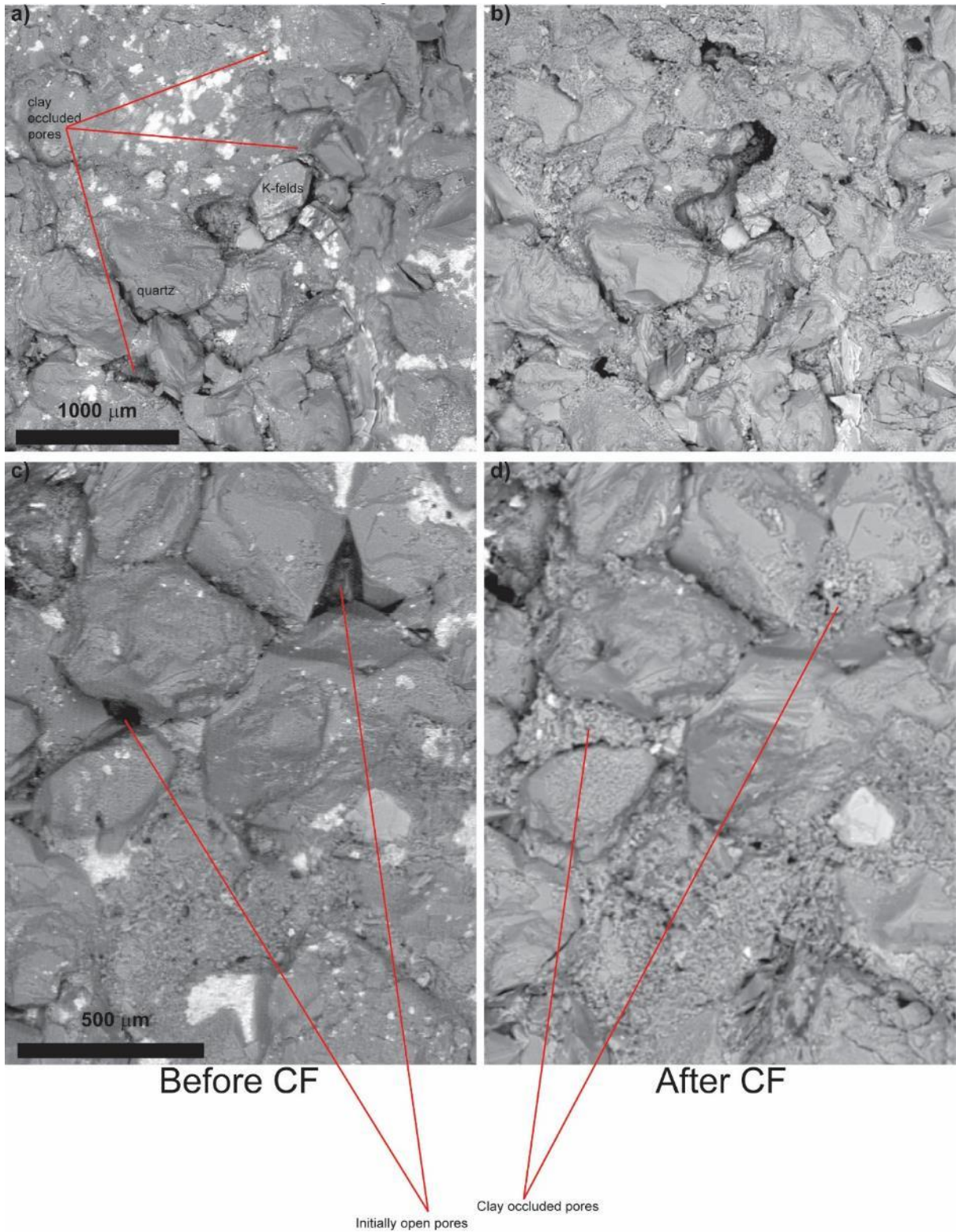


Figure 63. SEM images of regions of interest in disc from H4-Plug1 from well Harvey-4 (depth 1794.53 m) before (left) and after (right) flooding experiments. Salt precipitation (bright patches in the images) on the sample surface is evident in the images acquired before flooding; most of the salt appears to be removed in the images acquired after flooding test. a) and b) showing porosity enhancement by removal of pore occluding clays. c) and d) showing porosity reduction by pore occlusion.

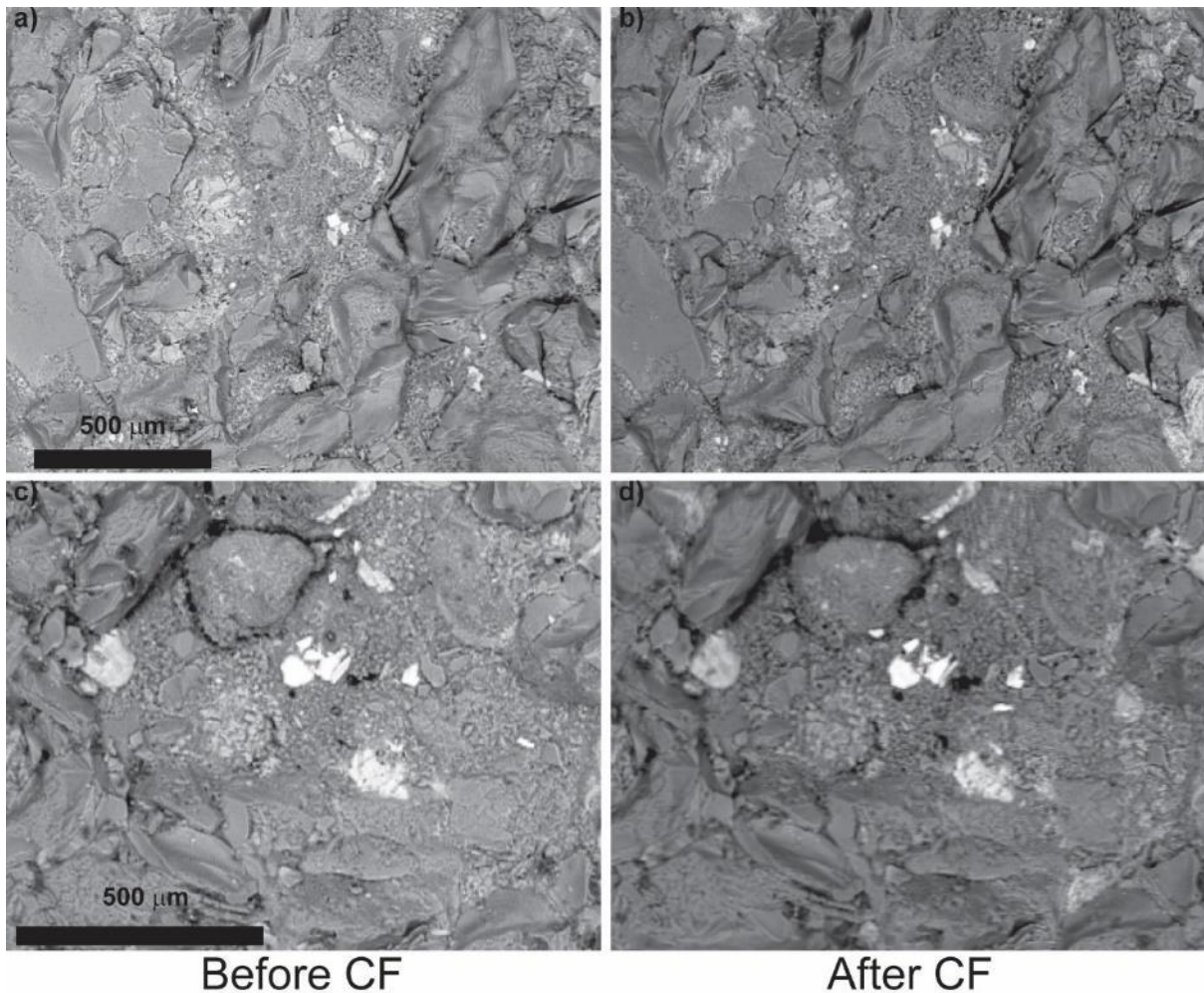


Figure 64. SEM images of regions of interest in disc from H4-Plug3 from well Harvey 4 (depth 1800.47 m) before (left) and after (right) flooding experiments. a) and b) showing a tight portion of the sample with abundant pore occluding clays. No significant change can be detected in the images acquired before and after flooding. c) and d) showing a clay rich region of the samples with an aggregate of oxides (possibly Ti-oxide) in the middle of the image (bright phase). As for the previous region of interest, no significant change can be detected in the images acquired before and after flooding.

Summary and Conclusions

BSE mosaics were collected from discs cut out of sample assemblies retrieved from wells Harvey-1, Harvey-3 and Harvey-4 and used for core flooding tests with CO₂ saturated brine as the pore fluid.

Mineralogy of the samples is summarised in Table 33: there is an overall consistency between samples from different wells showing a relatively simple mineralogy constituted of quartz, orthoclase, kaolinite and illite. Also evident is an anti-correlation between quartz and kaolinite and quartz and k-feldspar, which could be linked to slight variation in sediment source composition and diagenetic overprint.

An original, novel protocol has been developed to identify microstructural changes in sandstones subjected to core flooding. The protocol is centred around the acquisition of chemical and microstructural information at a resolution of around 3 microns over a sample area of a few cm, allowing the analysis of a statistically relevant grain population. Image analysis techniques have been employed to ensure an unbiased analysis of the acquired images on two samples extracted from the

Harvey-1 well. Only one of the two samples was comprehensively characterized before and after flooding, the analysis indicate that no significant change in shape or size is observed in the framework grains of the rock (i.e. detrital quartz and K-feldspar) while pore occluding mineral phases like diagenetic kaolinite and calcite show a decrease and an increase in the statistical distribution of grain size respectively, as a result of the flooding experiment.

Sample ID	Quartz	Kaolin	Orthoclase	Illite	Calcite	Berthierine	Ankerite
H1-Plug1	73.5	10	13	---	---	1	2
H1-Plug4	86	5	8	---	1	---	---
H3-Plug1	86.6	4.8	7.8	0.7	---	---	---
H4-Plug1	85.5	3.9	9.8	0.9	---	---	---
H4-Plug3	76	8.7	13.7	1.5	---	---	---

Table 33 Mineralogy of the studied samples as obtained from X-ray diffraction analysis. Values expressed as weight %.

In the remaining samples used for this study the quantitative approach could not be applied due to sample preparation issues (poor consolidation); nevertheless, a qualitative approach revealed microstructural modification in the samples that can be attributed to fluid-rock interaction occurring during the flooding tests. In particular, a comparison of the images before and after core flooding tests in samples from wells Harvey-3 and Harvey-4 (H4-Plug1) allows the recognition of clay mobilization from and in partially occluded pores. On the other hand, no obvious difference in the microstructure is noted in the deeper sample from well Harvey-4 (H4-Plug3) before and after flooding test.

In conclusion, the present study confirmed that the Wonnerup Member of the Lesueur Sandstone shows some degree of reactivity to carbonated formation water; the current results confirm what was speculated by Delle Piane et al. (2013) that clay mobilization could be responsible for the observed modification of petrophysical properties of samples from Harvey-1.

This study provides additional analytical data showing unequivocal microstructural evidence of clay mobilization within the samples pore space and supporting water chemistry analysis. Overall, the analytical results indicate that mineral dissolution is unlikely to play a dominant role at the time scale and physical conditions explored in this study. More details about this point will be presented and discussed in the upcoming section (Section 5) of the report.

Importantly, the fluid-rock interaction processes responsible for clay mobilization are active at the experimental time scale and, as demonstrated by the measurements conducted in the tasks pertaining to Section 3 of this report, which produce measurable modifications to the absolute permeability of rock which will, in turn, affect injectivity of the reservoir.

Notably, as also discussed in the previous section of this report, the permeability modifications induced by CO₂ saturated brine flooding is non monotonic: i.e. permeability decreases in some samples and increases in others; the cause of such discrepancy is not a 100% clear at the moment, but the difference in the original mineralogy and level of diagenetic pore space modification could play a role.

Section 5: Geochemical Analysis of Effluent Fluids

Contributors

Dr. Ryan Noble

Dr. David Gray

Dr. Linda Stalker

Methods and Analysis

Core flood experiment set up and core materials

The core-flood experimental set up is fully described in Section 2 of this report. As indicated earlier in Section 1, the cores can be described as medium to very coarse grained cross bedded sandstone with significant grain size variation between beds and are representative of high energy fluvial channel fill and barforms depositional environment (Facies Ai and Aii according to the classification proposed by Delle Piane et al. 2013). The main mineral constituents of samples representing facies Aii of the Wonnerup are quartz ($\text{SiO}_2 > 70\%$ by mass); K-feldspar ($\text{KAlSi}_3\text{O}_8 > 8\%$ by mass) and kaolinite ($\text{Al}_2(\text{Si}_2\text{O}_5)(\text{OH})_4 > 5\%$ by mass) accessory minerals are illite, calcite and berthierine (a non-swelling Fe-rich clay with kaolinite structure).

The produced brine eluents were collected in small volumes of 5mL in plastic vials. The samples were capped and stored in a refrigerator before undergoing a series of analyses. The flow conditions were 0.5 cm³/minute of CO₂ saturated brine. The Harvey 1-1924m (first sample assembly including core plugs 1 and 2, drilled from the depth of 1924m in Harvey-1) initially had 20 cm³ slug of CO₂ gas through at the start of the run and this is shown in the results with a short lag before solution chemistry typically changes as the CO₂-rich brine flows through the core. Additionally, as indicated in Section 2, an auto sampling malfunction overnight for this sample assembly occurred after brine sample H1089 (890 minutes and 445 cm³ of solution). This resulted in the experiment being reset with an approximately 24 hour delay and with an estimated 10 hour stagnation period and soaked in brine with no CO₂ and then 15 hours before pressure was restored to experimental conditions. Brine samples H1R001 are the continuation in this experiment and plotted from 900 minutes and 450 cm³ of volume in the following results. Harvey 3-1459m (the sample assembly including core plugs 1 and 2 drilled from the depth of 1459m in Harvey-3) was tested in October with the conducted over 1200 minutes with approximately 600 cm³ of fluid passing through the core. Harvey 4-1794m (first sample assembly from Harvey-4 including core plugs 1 and 2 drilled from a depth of 1794m in Harvey-4) and Harvey 4-1800m (second sample assembly from Harvey-4 including core plugs 3 and 4 drilled from the depth of 1800m in Harvey-4) were the most recent tests that were conducted over approximately 880 minutes with approximately 440 cm³ of fluid passing through the core.

Synthetic brine selection

In the earlier ANLEC R&D funded research projects difficulties working with such a simplistic synthetic brine (30,000 ppm NaCl) to flood samples from the SW Hub storage site was identified. The chemistry used in that previous project was chosen in the absence of a suitable formation fluid sample being collected during the drilling of Harvey-1. The data gathered from the single sample (Yalgorup formation at 856m) together with existing data from the Harvey and Binningup Lines of research bores (Deeney, 1989a and 1989b) was used to generate a brine that has a more balanced and representative chemistry with other species such as Ca, Mg or SO₄ or CO₃ added. The other potential issue with the NaCl brine approach is how it may impact on the behaviour of the clays as they are flooded.

A previous sample taken from the Harvey-1 well at 856m DRT in the Yalgorup Member has a total dissolved solids (TDS) value of 52,300 mg/L (influenced by drilling mud K contamination). Calculated values for the wireline logging reported in Delle Piane et al., (2013) are 40,000 mg/L NaCl equivalent for the Yalgorup Member and 30,000 mg/L NaCl equivalent for the Wonnerup Member. Results of

Conciadori et al. (2014) showed samples from the Yalgorup Member (903.62 m), the salinities range between 12000 and 30000 mg/L. Samples around 1900m of depth have a distribution between 2000 and 28000 mg/L, but there is a single data at higher salinity, 64000 mg/L.

Seawater has a TDS of 35,500 mg/L, similar to the general deeper groundwater at Harvey-1. However, comparing the most consistent results from the deeper regional water samples and the water sample from the wireline formation sampler and looking at major element ratios with seawater, the expected groundwater at Harvey will proportionally have more Ca, less K and Mg, slightly less SO_4 , with similar Na, Cl and HCO_3 . Given many of the other elements are low, an internal standard of Br as an anion and Sr as cations were included at a concentration 100 mg/L to test our ability to effectively measure minor elements in this saline brine. An internal standard of the transition metal Cu was also included at a similar concentration, although it was expected that reaction with clays and other mineral surfaces may immobilise this ion. Salinity was determined to be ~ 30000 mg/L and the end composition was calculated to be 31,400 mg/L. Major cation composition was targeted to be 1200 Ca, 600 Mg, 60 K, 9600 Na all in mg/L. The theoretical test solution should contain this composition with Na being slightly greater at 9647 mg/L once the 100 mg/L Sr internal standard was added as SrCl_2 . Major anion composition was targeted to be 17500 Cl, 2000 SO_4 , 125 HCO_3 , and 100 Br all in mg/L. The theoretical test solution should contain this composition 17012 Cl, 2522 SO_4 , 125 HCO_3 , and 123 Br all in mg/L.

Highly soluble salts AR grade chemicals were used to mix this brine. The species were added using the following compounds CaCl_2 , $\text{MgSO}_4 \cdot 7\text{H}_2\text{O}$, KBr, NaCl, NaHCO_3 , SrCl_2 and $\text{CuSO}_4 \cdot 5\text{H}_2\text{O}$.

Chemical analysis

Each sample collected at 10 minute intervals was analysed to include: major anions (Cl, SO_4 , Br, F and NO_3) by Ion Chromatography (IC), major element analysis (Al, B, Ca, Cr, Cu, Fe, K, Li, Mg, Mn, Na, P, S, Si, Sr and Z) by Inductively Coupled Plasma Optical Emission Spectroscopy (ICP-OES) and trace element analysis (Ag, As, Ba, Cd, Ce, Co, Cr, Cu, Dy, Er, Eu, Ga, Hf, Ho, La, Lu, Mo, Nb, Nd, Ni, Pb, Pr, Rb, Sb, Sc, Sm, Sn, Sr, Ta, Th, U, V, W, Y, Yb, Zn and Zr) by Inductively Coupled Plasma Mass Spectrometry (ICP-MS). All ICP-MS and OES analysis were conducted by LabWest Pty Ltd in Malaga. Samples were diluted 50x in 2% HNO_3 to reduce the salinity to approximately 1000 mg/L to ensure accurate determination. Alkalinity was determined by pH titration using a Metrohm Autotitrator in the NGL. A set volume of 2mL was diluted to 20 mL and titrated for HCO_3^- with a known concentration of acid (e.g. 0.01 M HCl) to an endpoint of pH = 4.3. Ion Chromatography was done by CSIRO, Kensington using a Thermo Dionex ICS-4000 with KOH capillary eluent generation. Samples were diluted 150x prior to analysis to reduce salinity. All preparation work was conducted in the National Geosequestration Laboratory (NGL).

The Harvey 4 fluid samples were collected in the same manner as the Harvey-1 and 3 fluid samples, but to reduce analytical costs the number of fluid samples analysed was reduced with the first 20 samples analysed and then every 4th sample after that. This decision was based on the observed patterns from the Harvey-1 experiments where most of the variation occurred in the early eluent samples (i.e. a first flush effect). Alkalinity analysis was limited by sample size and only attempted on the Harvey 4 samples. The analysis of HCO_3 (alkalinity) for the Harvey 4 samples were combined as composites of 4 samples to provide an average result over 40 minutes.

A total of 549 samples were analysed with the Harvey-1 experiments, 104 with the Harvey-3 experiment and a further 113 with the Harvey-4 experiment. Analytical blanks and duplicates were included every 30 samples, these are separate to the “blank” runs conducted for the core flood test as a whole as described in Section 2. Analyses were blank corrected, with robust detection limits added. Reproducibility was very good for nearly all analytes with an ionic charge balance average of $\pm 3\%$ and 99th percentile of 9.4%. The balance was slightly skewed from earlier analyses with the anions being slightly overestimated and cations being slightly underestimated in the Blank H3 results. This did not alter the results significantly. The average half absolute relative difference for duplicate tests in the latest Harvey-4 experiment across all analytes was 1.6%, with most <1%. These results are very similar to the reproducibility achieved in the Harvey 1 and 3 studies.

Elements Al, B, Ca, Cr, Cu, Fe, K, Li, Mg, Mn, Na, P, S, Si, Sr and Zn) were analysed by Inductively Coupled Plasma Optical Emission Spectroscopy (ICP-OES) at LabWest in Malaga. Trace elements (Ag, As, Ba, Cd, Ce, Co, Cr, Cu, Dy, Er, Eu, Ga, Hf, Ho, La, Lu, Mo, Nb, Nd, Ni, Pb, Pr, Rb, Sb, Sc, Sm, Sn, Sr, Ta, Th, U, V, W, Y, Yb, Zn and Zr) were analysed by Inductively Coupled Plasma Mass Spectrometry (ICP-MS) at LabWest in Malaga. Detection limits for ICP analyses are affected by salinity, with more saline samples having higher detection limits due to increased dilution requirements.

Modelling and mass balance

Geochemical modelling is useful in understanding the results from the core flood experiments. The modelling component of the study was conducted with the results from Harvey-1, 3 and 4. Modelling was done using React (Geochemist’s Workbench® Version 8.0) to conduct a static equilibrium model. This mixture was equilibrated, with resultant mineral and solution properties (Figure 65). For each sample, using XRD and solution data, the initial conditions, including porosity were simulated as closely as possible and the conditions shown in Table 34.

A slightly simpler mineral assemblage was required to be used as the larger number of minerals violated the phase rule for mineral equilibration, indicating that the observed mineral assemblages in the sediments were not in complete equilibrium with the present environment. For the modelling, Si, Ca, Mg, Al, K, HCO₃, pH and Fe were controlled by mineral equilibration, whereas dissolved Na and SO₄ were added to simulate the pore solution and Cl set by charge balance. In some cases, to get the model to run the inputted Na concentration had to be decreased (up to 50%) and SO₄ slightly decreased. These effects were simulated to check sensitivity of modelling with limited impact to the results.

To model initial conditions, CO₂ is added step-wise, up to 5x greater than the experimental conditions used in the core flood experiments. At each step the simulation is totally equilibrated (i.e., as if the solution contacted all parts of the rock – which is not realistic). This simulation is therefore the maximum amount of CO₂ the rock mass can “carry”. While the modelling is not dynamic and less representative of the CO₂ moving through preferential flow paths in the rocks, it does provide insight into the mineral assemblages and changes we can expect to occur over long time periods.

Table 34. Parameters used in modelling of the Harvey-1 1924m sample. Full details for all samples are provided in Appendix A.

Solid Phase %	Density	Harvey-1.1924	Notes or units
Quartz	2.648	73.5	
Kaolinite	2.594	10	
Orthoclase	2.557	13	Not end member, so split to 50:50 K:Na feldspar
Illite	2.763		
High Mg calcite	2.75	0.5	Combined and split between calcite and dolomite
Ankerite	2.87	2	
Berthierine	1.65	1	Used Chamosite – similar to Berthierine which was not in the database
Total Mineral %		100	
100 kg will have Vol ...		0.0382	m ³ using 2.648 g/cm ³ (minerals)
		0.0451	m ³ using 2.648 g/cm ³ (including water)
Porosity %		15.3	
H ₂ O		0.0069	m ³
H ₂ O		6.90	kg
Experiment Conditions			
Pore Pressure (Mpa)		19.28	
T (°C)		61	
CO ₂ mol/kg		1.219	
		8.4	No of total Moles - Experimental Conditions
		42.0	So simulation matches Core Flood Conditions at 20% reaction progress
Solution mg/L	For all experiments		
Ca	1200	8276	Set by solid equilibration with calcite
Mg	600	4138	Set by solid equilibration with illite
K	60	414	Set by solid equilibration with K-feldspar
Na	9647	66535	34000 - adjusted
SO ₄	2522	17397	13000 - adjusted
Cl	17012	117332	Charge Balance

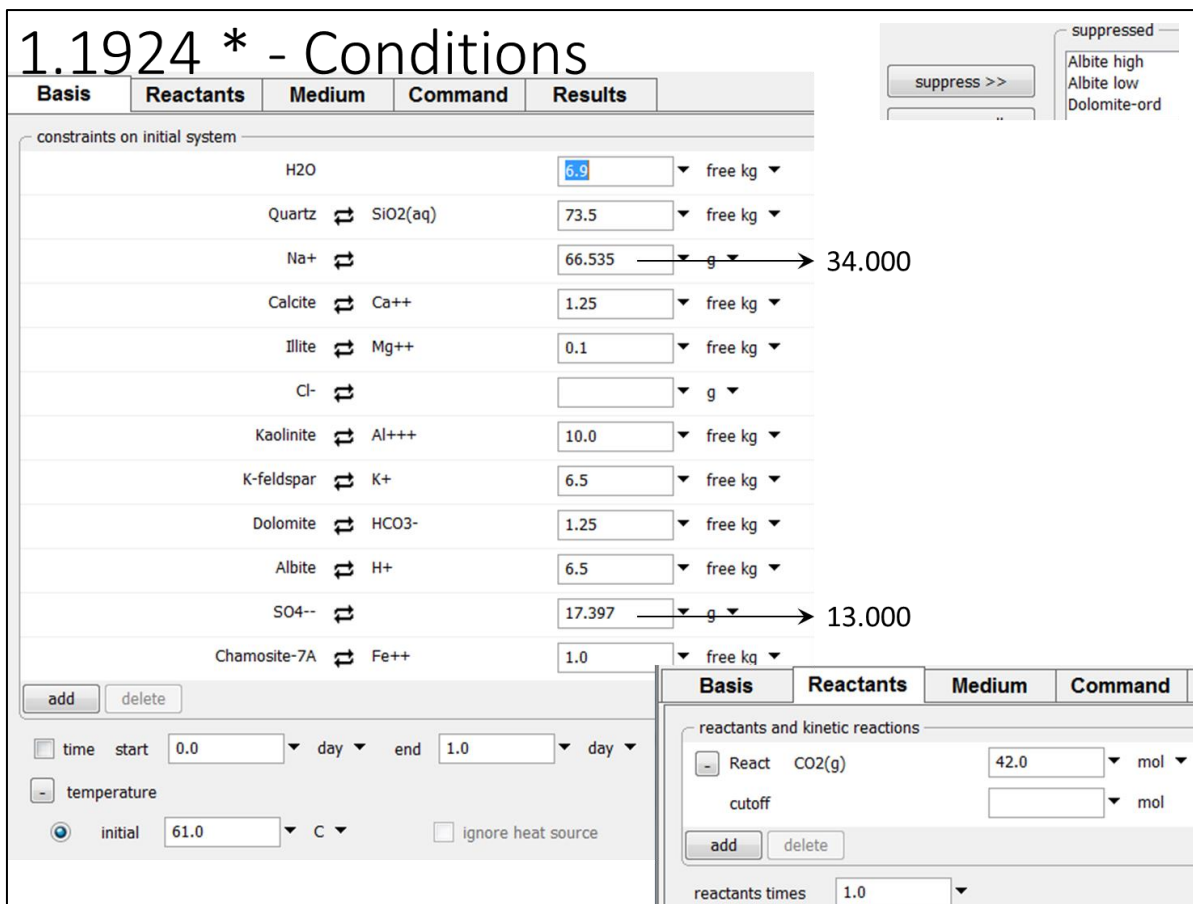


Figure 65. Example of the Static equilibrium model parameters (for Harvey-1 1924m). Note the variation in Na and SO₄ used to run the model which is also reflected in Table 34.

Mass balance data used the results of the core flood experiments to determine the net mobilisation of elements and relate that to the mass potentially removed from the core. The results used the same mineralogy reported in Section 4 (Table 33) of the report and checked against the mass potentially removed using the porosity changes and related bulk density shifts reported in Section 3.

Results

Data

An MS Excel spreadsheet of the data is submitted as a digital file with this report (Appendix A). This file also hosts additional spreadsheets of the results of the modelling and mass balance assessment (Appendix A). Many compounds showed similar trends and, for brevity, only representative graphs are shown with discussion on other similar element behaviours in the text. Appendix A and B show the data and figures for all Harvey-1, 3 and 4 eluents used. The results are reported in volume (cc) of eluent at a flow rate of 0.5 cm³ per minute. Although porosity, volume and density of the samples vary, the solution is in contact with the rock for approximately 100 minutes. An important consideration is that Harvey-1-1924m (the 1st sample assembly) had an initial 20 cc of scCO₂ come through the core at the start of the experiment. A few eluents from Harvey-1 and -3 were not analysed as they were used for other laboratory analysis, but those included in the analyses are presented in Table 35.

Table 35. Experiments, samples, duplicates and missing samples (due to particle size testing).

Sample tested	Sample ID	Number of samples	Missing samples	Duplicates	Blanks
Blank Teflon Tube	B001-B120	120		30d, 60d, 90d, 119d	#1-4
Berea Sandstone	BR001- BR119	113	BR031, 034, 046, 047, 059, 060	30d, 061d, 090d, 119d	#5-8
Harvey-1 1924 m (1 st Assembly)	H001-H089	83	H1 058, 059 060, 086, 087, 088	30d, 63d	#9, 10
Harvey-1 1924 m R (1 st Assembly-repeat)	H1R001- H1R119	114	H1-R 007, 008, 042, 119, 120	30d, 60d, 90d, 118d	#11-14
Harvey-1 2505 m (2 nd assembly)	H001- H3118	118		30d, 60d, 90d, 118d	#15-18
Blank Teflon Tube	H3B 001- H3B 119	119	H3B 059 was not analysed for anions	15d, 50d,95d	#1-3
Harvey-3 1459 m	H3 001- B119	119	H3B 059 was not analysed for anions	15d, 50d,95d	#4-6
Harvey-4 1794 m (1 st assembly)	H41 1 – H41 87	87		15d, 46d, 87d	#1-3
Harvey-4 1800 m (2 nd assembly)	H43 1 – H43 88	88		15d, 48d,	#4-6
Blank Teflon Tube	H4 B1 – H4B 36	36		15d	#7

Major elements

Concentrations of major ions in solution remained relatively stable throughout much of the experiment. Calcium, Mg, Na and K, changed little during the experiment, even after 75 cm³ of CO₂ saturated solution had passed through the core. Some changes in the eluent chemistry were observed as an initial flush effect where the Ca concentration is elevated in Harvey 3 1459m and the Harvey 4 1800m compared to their respective background levels (Blanks H3 and H4). The theoretical Ca concentration should have been closer to 1200 mg/L. Concentrations of eluent Ca was an average of approximately 1100 mg/L in the first Harvey 1 experiment, however in later experiments the eluted Ca concentration was generally lower between 650 and 800 mg/L (Figure 66). The blank experiment (no core material to react with and representing just the eluent interacting with the experimental apparatus (metal tubing etc.) showed the eluent used in the Harvey-1 experiment contained more initial Ca i.e. the results do not indicate greater precipitation of Ca in the Harvey 3 and 4 experiments compared to Harvey 1 core.

Variation in salinity has been shown to occur in these experiments. To adjust for variations in salinity concentration, Ca was adjusted for the Total Dissolved Solids (TDS) of the solution. This resulted in an observed loss of Ca from solution in the Harvey-3 core and significantly reduced the first flush effect observed for all experiments (Figure 66 and Figure 67), too. The first flush probably indicates a slight loss of Ca (and other elements from the core), although this was shown to be a net precipitation of Ca in the mass balance. With the solution containing Ca, the blank correction was made and showed the mass change of Ca from the core materials varied. Precipitation of Ca (and Mg), on a mass balance, should have occurred in all Harvey samples except Harvey-3 1459m (Table 36) as these elements were reduced in solution. Elements that were not present in the starting eluent were more easily assessed in the mass balance approach. Aluminium, Fe and Si are discussed later.

Table 36. Mass balance net change in grams of major elements. Black font indicates precipitation (net loss of an element from solution) and red indicates dissolution (gain of element in solution).

	Al	Ca	Fe	K	Mg	Si
Berea	0.00000	0.026	0.053	0.000	0.029	0.0007
Harvey-1.1924	0.00000	-0.117	0.026	0.003	-0.017	0.0039
Harvey-1.2505	0.00000	-0.009	0.011	0.002	-0.003	0.0005
Harvey-3.1459	0.00049	0.016	0.008	0.106	0.007	0.0014
Harvey-4.1794	0.00014	-0.233	0.010	-0.010	-0.105	0.0018
Harvey-4.1800	0.00015	-0.182	0.008	0.261	-0.071	0.0034

Magnesium shows similar trends to Ca (Figure 66 and Figure 68). A probability plot shows little separation of these results (Berea excluded) apart from the samples that are elevated in the first few volumes. There is little evidence to suggest further dissolution of Mg from the core materials (Figure 69): i.e., Mg eluted for the core tests is not significantly different from the starting eluent. The very strong first flush effect shown in Harvey-4 1800m is discussed in more detail later and related to mixing of previously evaporated eluent. Mg-bearing mineral phases are not greatly affected (precipitated or dissolved) in the cores tested (Table 36) and this is supported in the geochemical models shown later in this chapter.

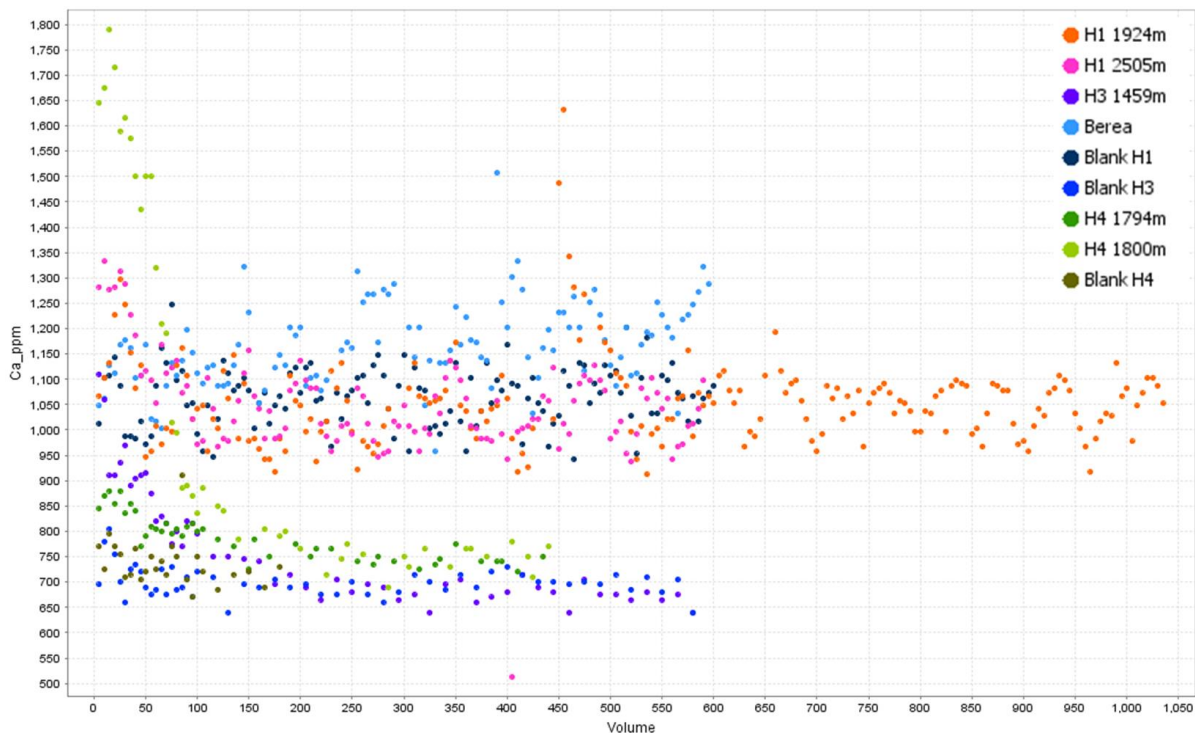


Figure 66. Calcium eluent in mg/L from the core flood experiments over volume eluted from the different rock samples or experiments (0.5 cm^3 solution per minute). Long-term differences in the trends relate to different eluent chemistry (batch effect), rather than solid-phase interaction.

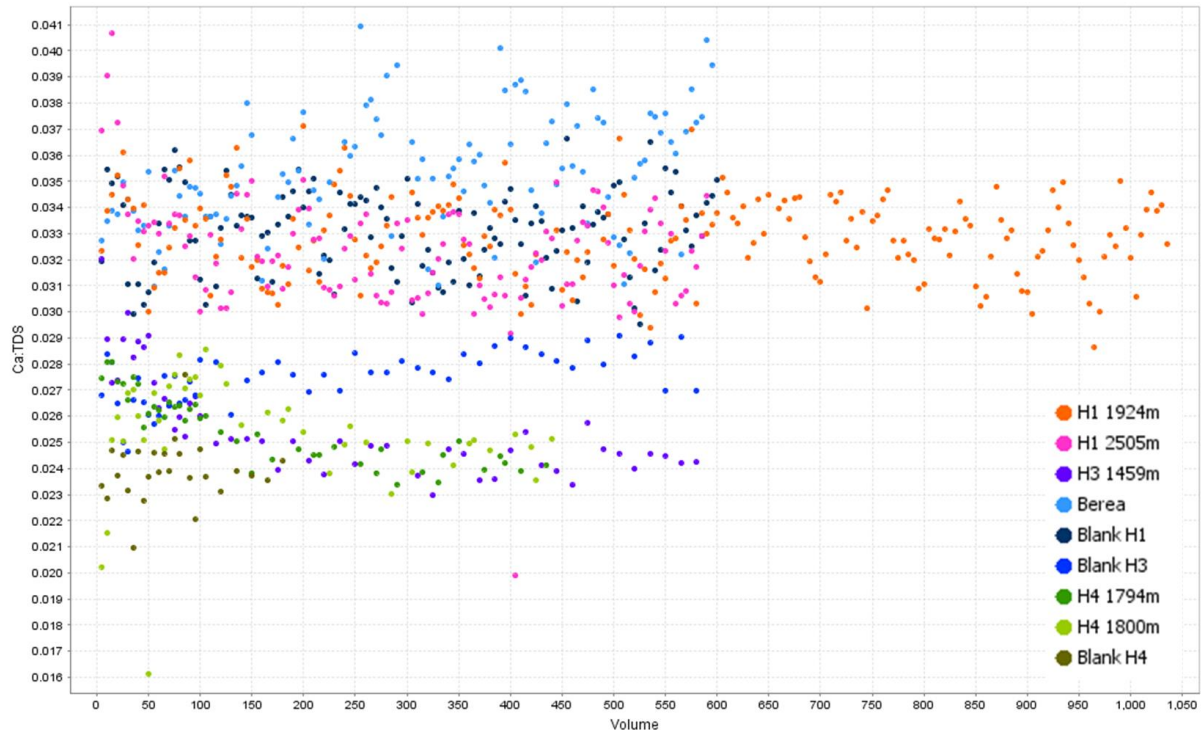


Figure 67. Calcium eluent concentration divided by total dissolved solids (TDS) from the core flood experiments over volume eluted from the different rock samples or experiments (0.5 cm³ solution per minute).

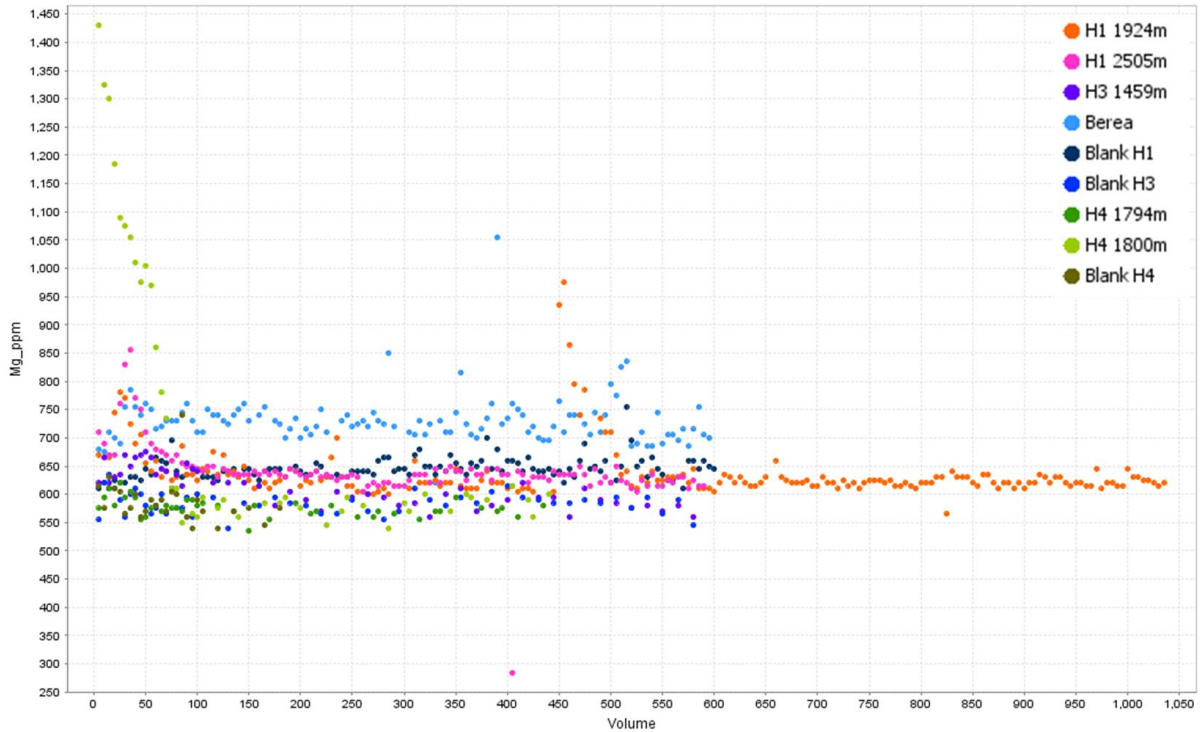


Figure 68. Magnesium eluent in mg/L from the core flood experiments over volume eluted from the different rock samples or experiments (0.5 cm³ solution per minute). Long-term differences in the trends relate to different eluent chemistry (batch effect), rather than solid-phase interaction.

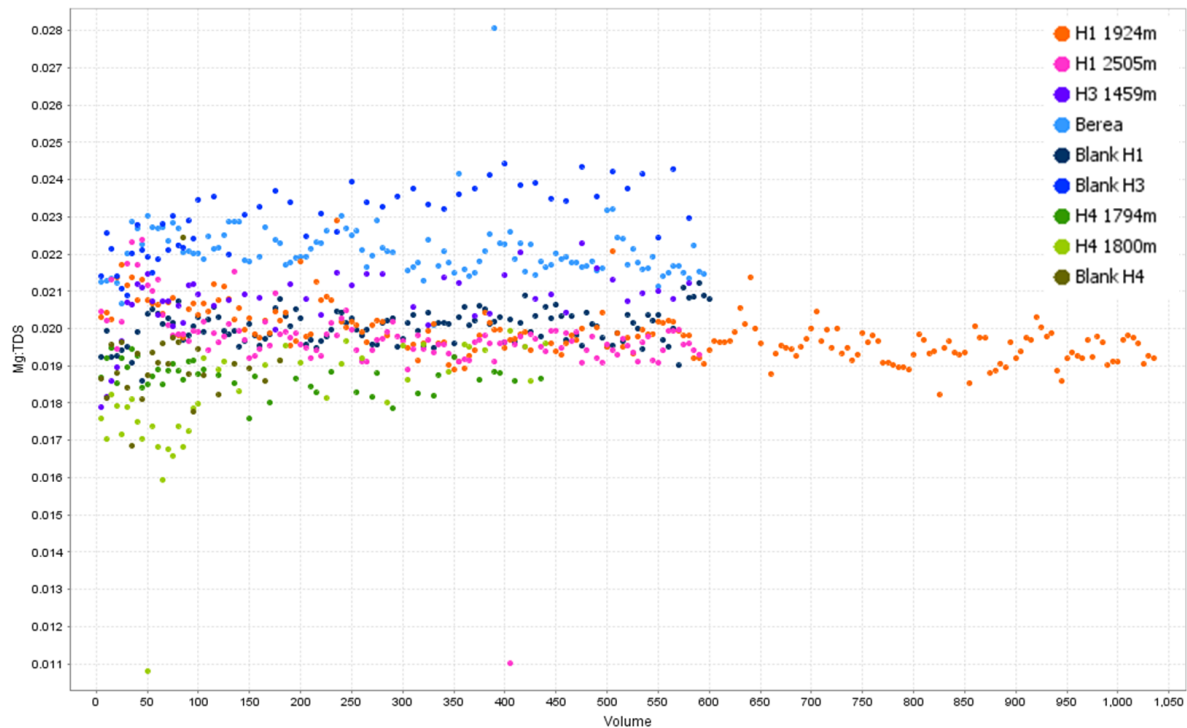


Figure 69. Magnesium eluent concentration divided by total dissolved solids (TDS) from the core flood experiments over volume eluted from the different core plugs or experiments (0.5 cm³ solution per minute).

In some tests, K has a strong first flush impact from the CO₂-rich brine (Figure 70): in particular, for the Harvey-3 (1459m) and Harvey-4 (1800m) much more K than the other samples tested is released in the early eluents.

Changes related to eluent chemistry are mainly observed in the “first flush effect” during the core flood experiments. The Harvey-4 results show a mixing trend of solutions, one highly saline and the other the more typical solution with the reactive CO₂ as shown with increased soluble Si, Al and Fe. It is believed this highly saline solution without the effects of CO₂ is a result of brine saturation for the previous NMR porosity testing and some subsequent drying creating pores with additional salt crystals. These crystals rapidly solubilise and migrate with the following eluent in the core flood experiments. In effect, the first flush is predominantly a salinity increase and then the effects of the CO₂ are observed later. The use of smoothing with TDS assists in recognising other trends in the data and not just an increase in all elements due to greater salinity.

The trend of increase K dissolution compared to other major cations is confirmed in the mass balance (Table 36). The deeper Harvey-1 sample (2505m) shows greater K mobilisation than Harvey-1 (1924 m) (inset Figure 70). This K increase in the eluent is likely due to minor dissolution of aluminosilicate phases that substitute K into the lattice structure or interlayers as well as K-feldspar minerals that were previously identified in the study of the Wonnerup facies (Section 4; Delle Piane et al., 2013). The mineralogy assessment was indicative of an increase in fine kaolinite particles post-flooding. The solution should have 60 mg/L K and clearly much more than this is eluted in the first half of the experiment from the Harvey-3 and 4 cores. What is quite unexpected is how Harvey-4 1794m shows no change in K and yet it is spatially close by (~6 m shallower). This demonstrates the variation in the Wonnerup formation material and how chemical changes are not well understood to be scaled up. This pattern of K mobility initially in many of the Harvey cores is weakly supported by other element chemistry such as Si and Fe (increased dissolution in Harvey-3 and Harvey-4 1800m) although their

patterns of elution do not match. The K increase in solution for Harvey-3 and 4 (1800m) may represent dissolution of other non-silicate, K-bearing phases, not identified. There was significant cracking and void increases observed in Section 4 for Harvey-3 and to some extent for Harvey-4 and this represents some physical evidence that supports the chemical changes seen here, with voids forming where dissolution of aluminosilicate phases have occurred. For the other samples, as occurred with Ca and Mg, this K dissolution is a relatively minor change with little net change of K occurring.

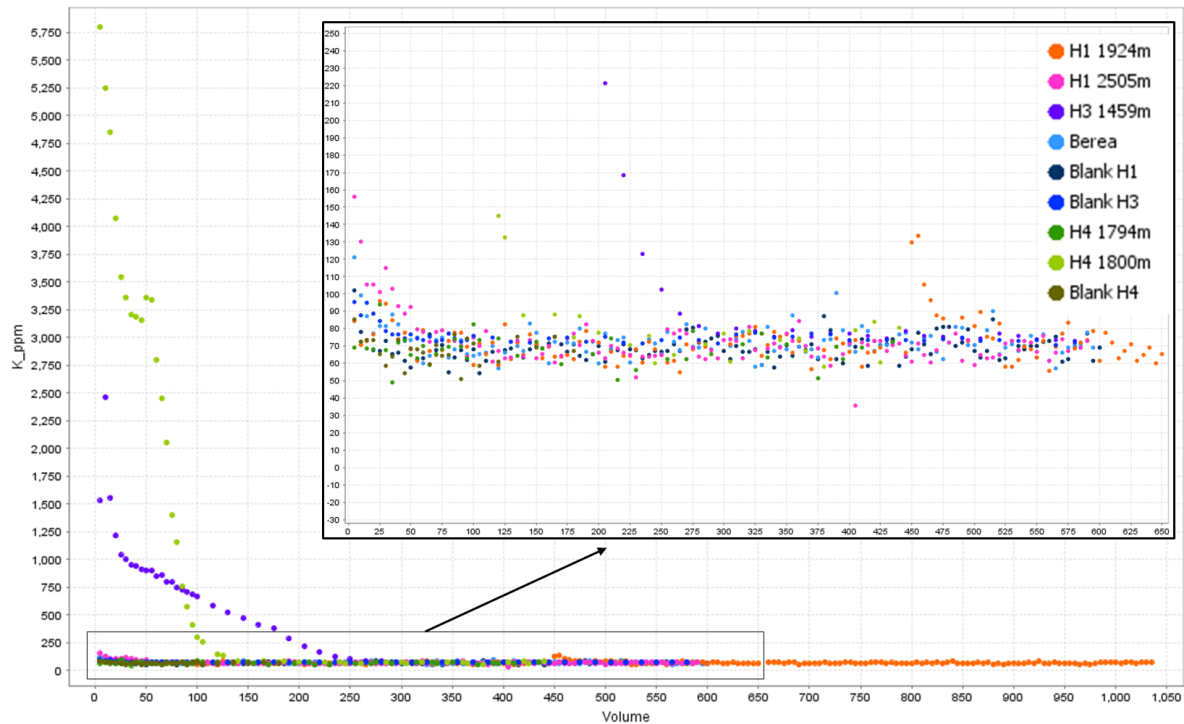


Figure 70. Potassium eluent in mg/L from the core flood experiments over volume eluted from the different rock samples or experiments (0.5 cm³ solution per minute).

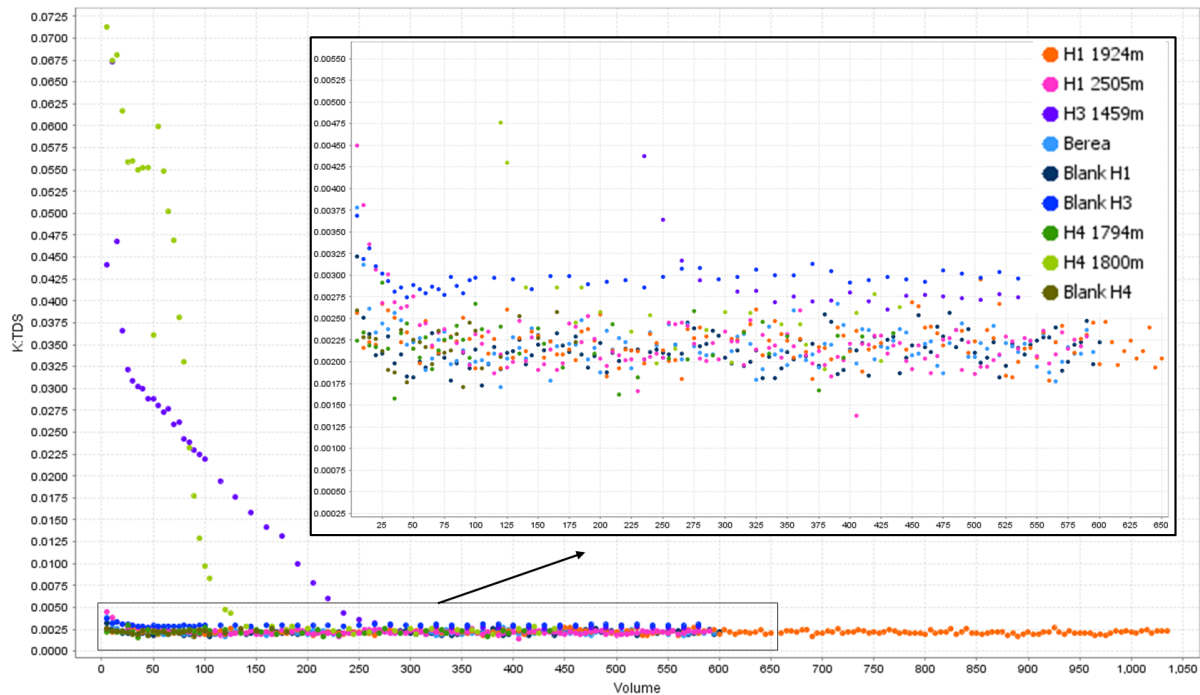


Figure 71. Potassium eluent ratio adjusted for Total Dissolved Solids (TDS) from the core flood experiments over volume eluted from the different rock samples or experiments (0.5 cm³ solution per minute).

The two element tracers used in these experiments were Br as an anion at 125 mg/L (Figure 72) and Sr as a cation at 100 mg/L. Bromide concentrations tend to slightly increase in eluents, when adjusted for TDS in all Harvey samples (Figure 73). Duplicate analyses of the Harvey 3 eluents confirmed these Br results. At present, the Br increase is not well understood, but potentially indicates a subtle Br release from the core materials. Strontium shows unusual chemistry with what appears to be a significant reduction in concentration (Figure 74 and Figure 75), for all core tests. The drop in Sr could be attributed to the solution being saturated with respect to strontianite (SrCO₃) minerals and minor precipitation occurring. This was not assessed using mineral saturation modelling as pH and alkalinity results were not measured for these samples with the current experimental set up. It is important to realise that although changes of 60 mg/L in eluent concentration would only be equivalent to the actual mass change in the core material of less than 0.01%. Observing these possible mineral phase changes is difficult. The mass balance approach was not applied to the Br or Sr results due to the low concentrations and no observed mineral phase that hosts either element.

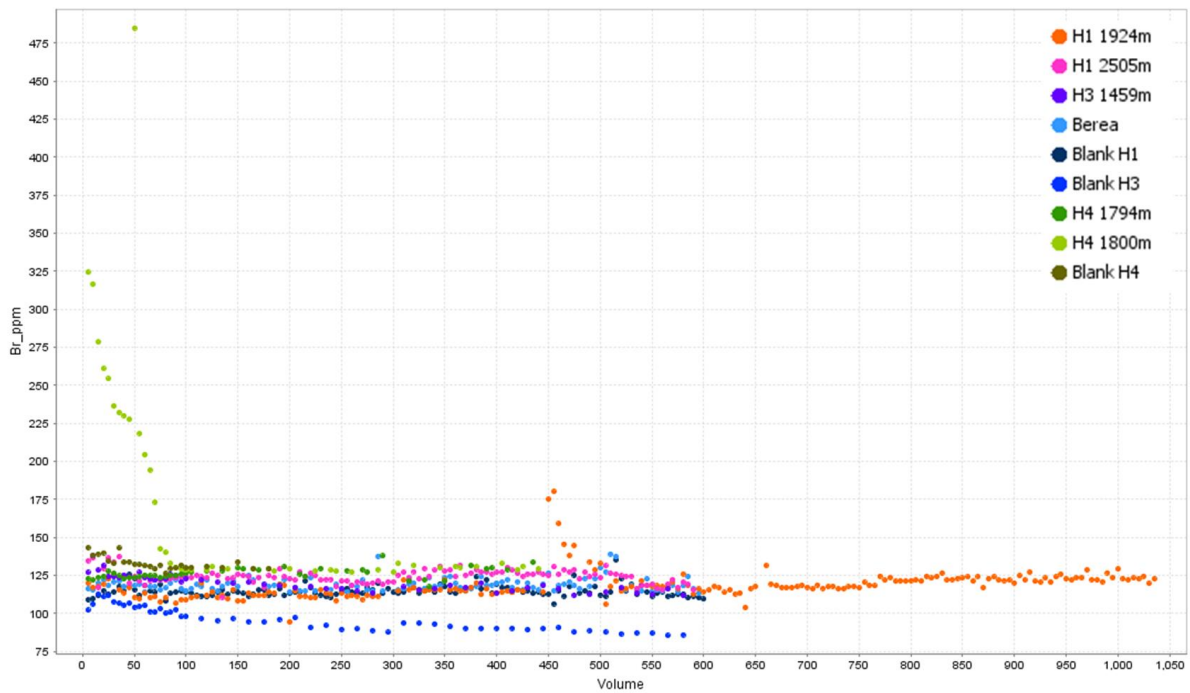


Figure 72. Bromide eluent in mg/L from the core flood experiments over volume eluted from the different rock samples or experiments (0.5 cm^3 solution per minute). Starting concentration was 125 mg/L (ppm).

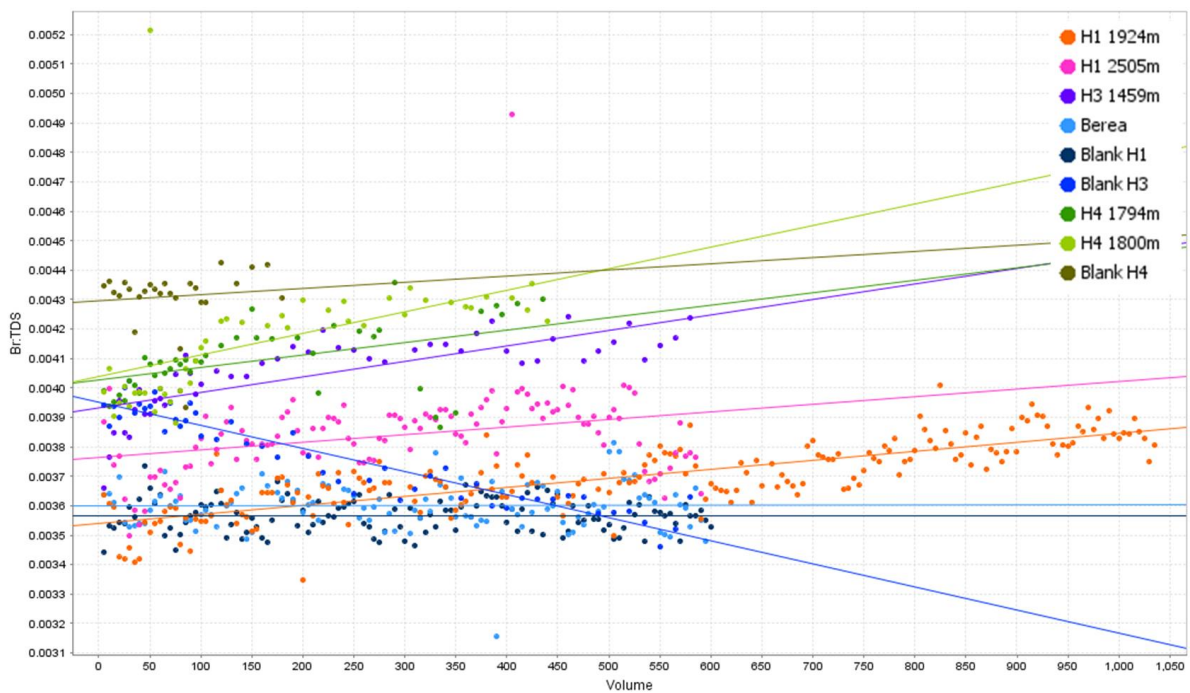


Figure 73. Bromide eluent ratio adjusted for Total Dissolved Solids (TDS) from the core flood experiments over volume eluted from the different rock samples or experiments (0.5 cm^3 solution per minute). Linear regression lines have been added for each core type.

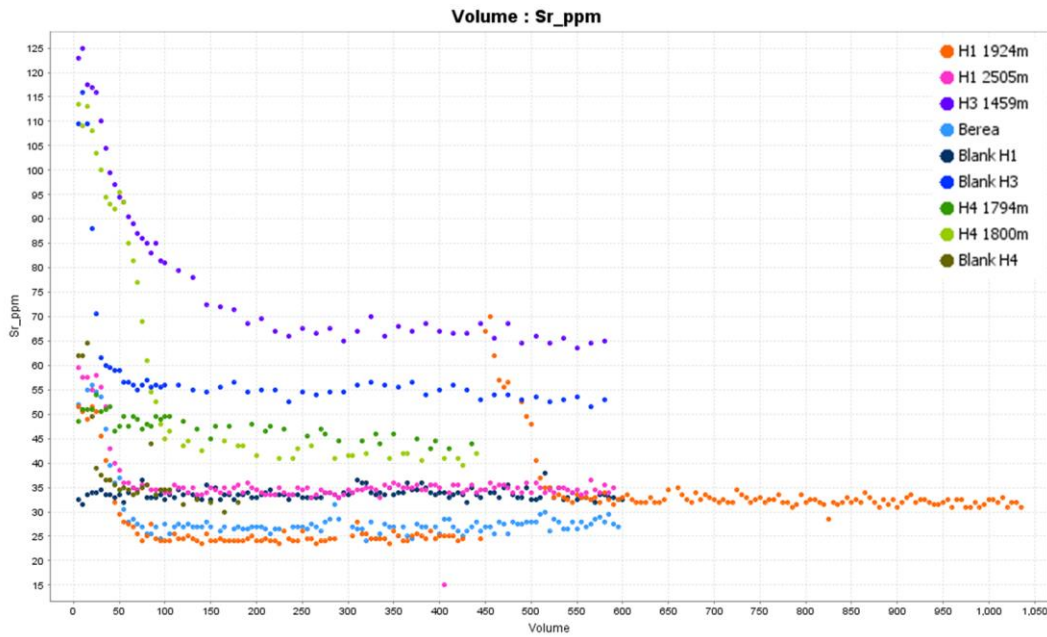


Figure 74. Strontium eluent in mg/L from the core flood experiments over volume eluted from the different rock samples or experiments (0.5 cm^3 solution per minute). Starting concentration was 100 mg/L (ppm).

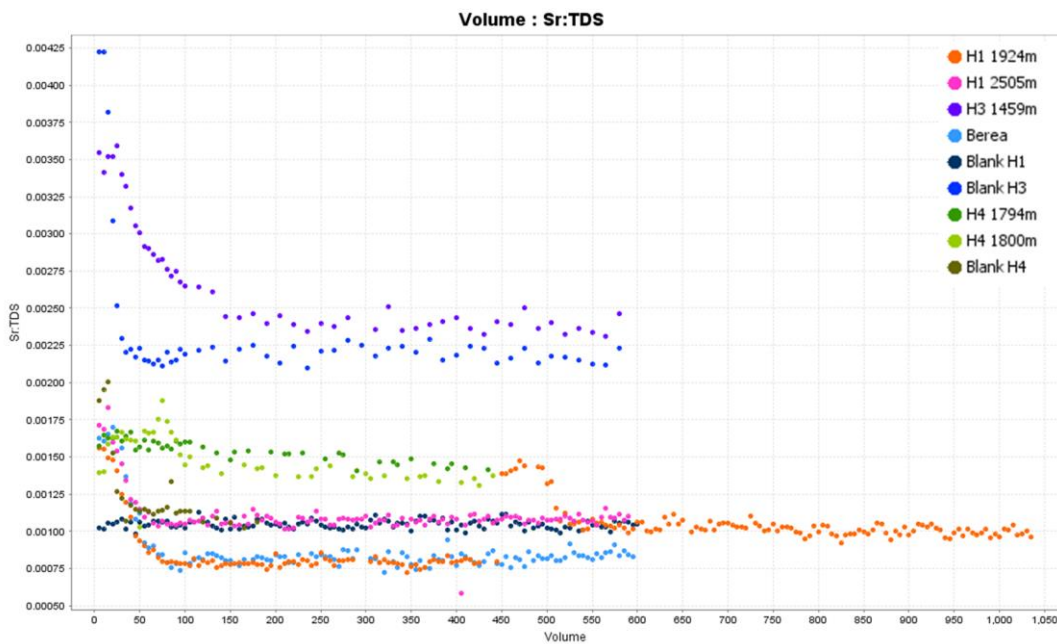


Figure 75. Strontium eluent ratio adjusted for Total Dissolved Solids (TDS) from the core flood experiments over volume eluted from the different rock samples or experiments (0.5 cm^3 solution per minute).

Trace elements

Transition metals and other trace elements were rapidly mobilised from the samples in a first flush effect for the Harvey-1 and 3 tests, but were not as evident in Harvey-4. Following any first flush the concentrations decreased and stabilised. This was evident in Cu and a number of trace metals and the major cations. Copper was used as a tracer with a starting solution concentration of 100 mg/L. As shown in Figure 76, the Cu had an initial rise (first flush) in Harvey-1 and 3 core flood eluents and then stabilised between 50 and 80 mg/L. This occurs in the blank, too, and is most evident in the Harvey-4

blank. Harvey-4 (1794 m and 1800m) increase to the stabilising concentration, indicating some very minor adsorption or precipitation of Cu is occurring, if anything. Adjustment for TDS (not shown) did not change the pattern observed in the eluent concentrations.

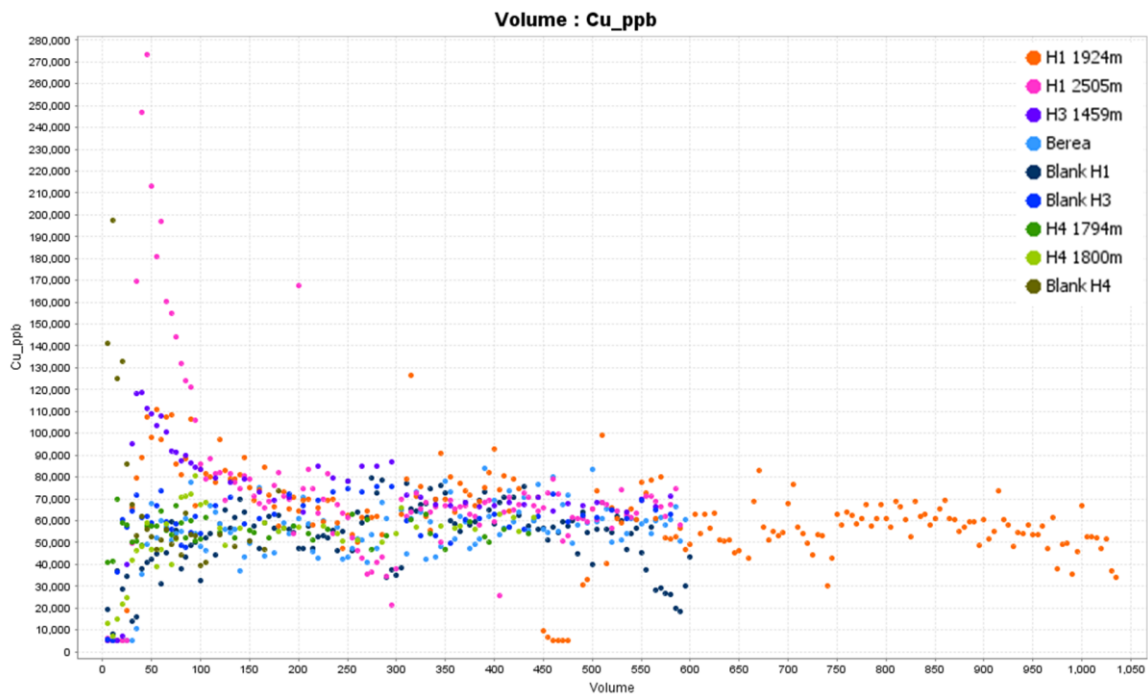


Figure 76. Copper eluent in $\mu\text{g/L}$ from the core flood experiments over volume eluted from the different core plugs or experiments (0.5 cm^3 solution per minute). Starting concentration was $100,000 \mu\text{g/L}$ (ppb).

Lead (Figure 77 and Figure 78) shows the same first flush pattern exhibited by other elements such as Be, Co, Cu, Li, Mn, Ni, Rb, Si, U and Zn. These all remained relatively stable throughout the experiments, however, the Harvey-3 core and Harvey-4 core (1800m) were different with a number of trace metals such as Pb showing the first flush and then a ramping up until the midpoint in the experiment before decreasing again (Figure 77 and Figure 78). The results for Harvey-3 (1459m) and Harvey-4 (1800m) imply a similar process to the other core flood experiments, but a distinctive, ongoing dissolution of some minor mineral phases. With only 6 m separating the two Harvey-4 cores the results are different and indicative of vertical variation in the Wonnepurup materials. The other consideration is that the Harvey-4 (1794m) sample is a true outlier. Harvey-4 (1794m) also shows more potential mass loss than any other core material tested in the total mass balance checks based on porosity and bulk density changes reported in Section 3, but this was not evident in the core flood eluent chemistry. The results of porosity changes were used to calculate mass change in Table 37 with full calculations provided in Appendix A. The patterns observed in the eluent chemistry do not match these calculations nor do the other mass balance calculations.

Table 37. Mass calculated changes after the CO_2 passes through the core. The results assume total core volume is constant from the initial plug and uses average bulk density over the length of the plugs as a ratio of each plug length to compensate for material removed during core cutting.

	BEFORE (g)	Check (g)	AFTER (g)	Net loss (g)
Harvey1.1924	327.63	327.69	324.36	3.34
Harvey1.2505	332.06	331.55	331.59	-0.04
Harvey3.1459	365.40	365.41	358.98	6.43
Harvey4.1794	373.46	373.46	364.35	9.11
Harvey4.1800	401.62	401.62	399.62	2.00

The Harvey-3 core was more friable compared to the Harvey-1 material influencing its permeability, but Harvey-4 (1800m) is not more friable than Harvey-4 (1794m) yet Harvey-4 (1800m) results indicate much greater dissolution of trace metals such as Pb. The Harvey-4 1800m core does have more clay and reduced permeability than the other cores tested. The increase in clay potentially could provide a greater source of Pb and other trace metals. Additional trace element mapping studies with LA-ICPMS may be valuable in showing $\mu\text{g}/\text{kg}$ chemical changes of trace elements for future studies.

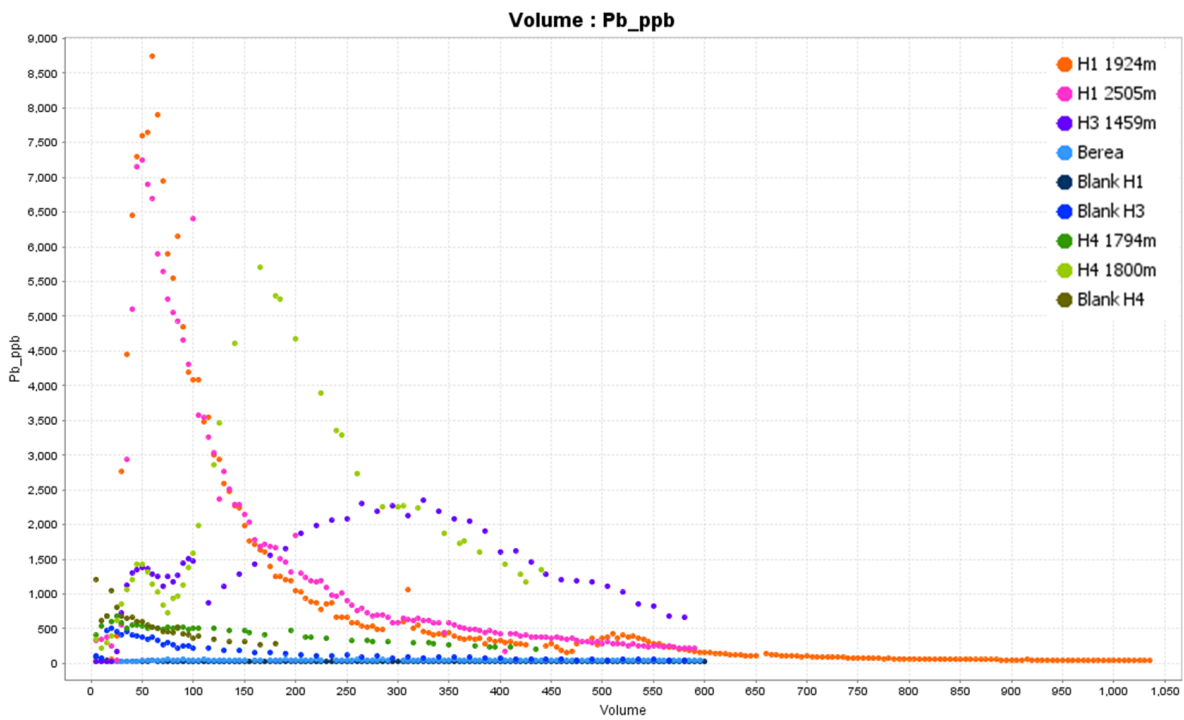


Figure 77. Lead eluent in $\mu\text{g}/\text{L}$ from the core flood experiments over volume eluted from the different rock samples or experiments tested (0.5 cm^3 solution per minute).

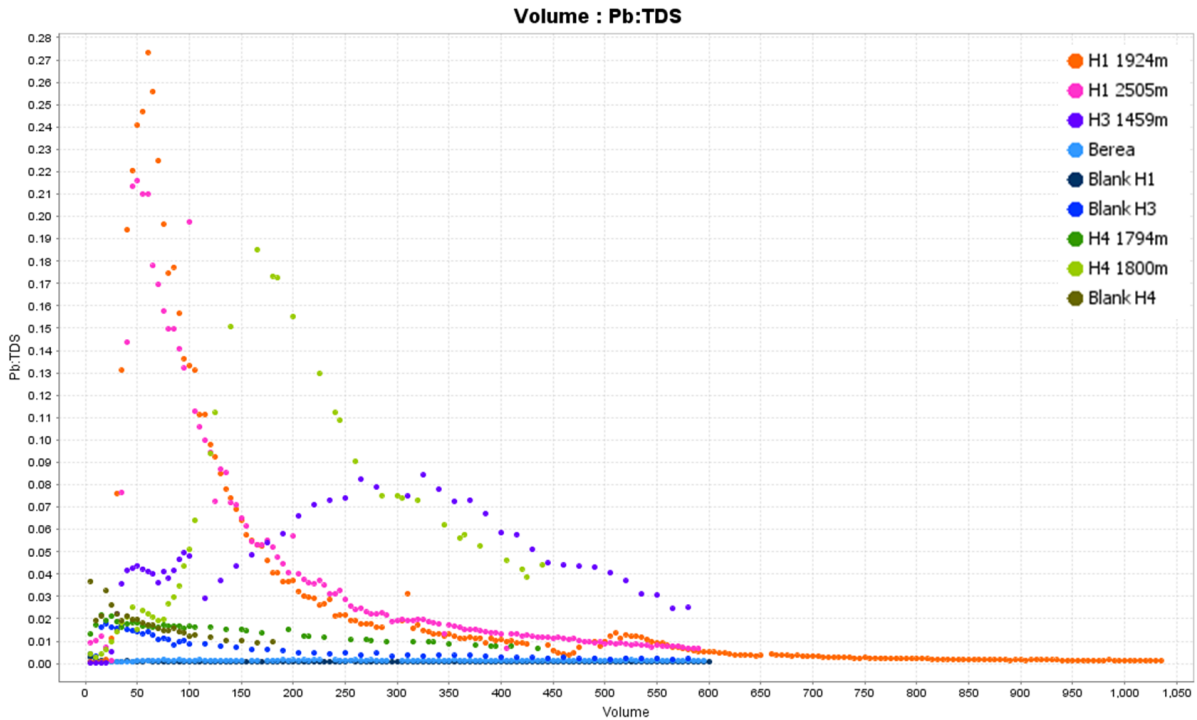


Figure 78. Lead eluent ratio adjusted for Total Dissolved Solids (TDS) from the core flood experiments over volume eluted from the different rock samples or experiments (0.5 cm³ solution per minute).

Rare Earth Elements (REE) showed a similar trend to the transition elements in the previous section. The exception to these previously observed patterns in other element elution was the Berea Sandstone that continued to liberate REE over the experiment. Neodymium is plotted as a representative REE in the experiment (Figure 79). This pattern is likely a result of the different mineralogy of the Berea Sandstone and particularly an increase in concentrations through minor dissolution of carbonates and possibly some other REE-bearing mineral phases. The pattern was unchanged when adjusted for TDS. It is important to realise that the REE concentrations are low and only 10-15x above the detection limits, but these patterns are believed to be representative.

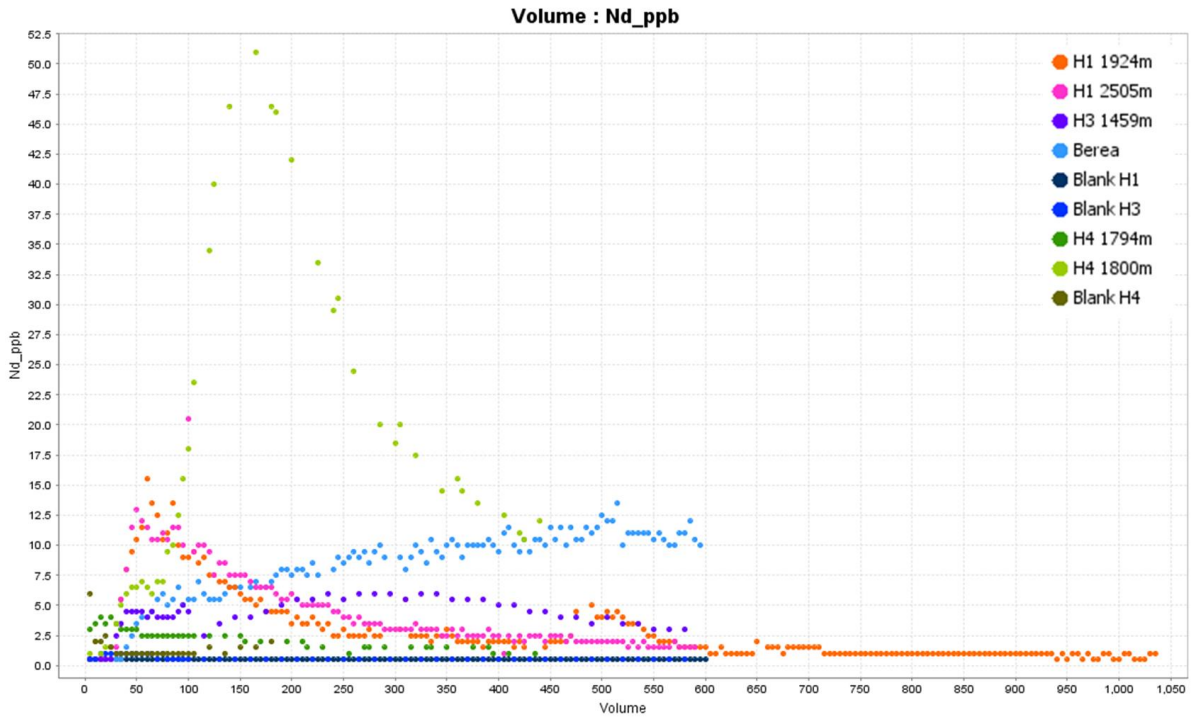


Figure 79. Neodymium (REE) eluent in µg/L from the core flood experiments over volume eluted from the different core plugs or experiments (0.5 cm³ solution per minute).

Elements that may have potential environmental toxic effects such as As and Se were observed to be at very low concentrations, close to detection limits, and stable throughout the experiment. Arsenic and Se were slightly greater in the Harvey-3 1459m core and Harvey-4 1800m core eluents. Principally, these experiments indicate the cores used did not have many As- or Se-bearing minerals. In effect, the result is a positive for future CO₂ injection as it implies concerns around toxic metal and metalloid mobility is unlikely and at low concentrations. These concentrations are just below the current drinking water guidelines for livestock for arsenic (500 ppb), but above the guideline trigger value for selenium (20 ppb; NHMRC, 2004). Given the salinity of the formation water at these depths this water would not be used for animal or human consumption regardless of CO₂ injection status.

Chromium and Mo were relatively abundant in the core flood eluents, but this occurred for all experiments including the blank. Nickel (Figure 80) shows the first flush in Harvey-4 1800m and the pattern is similar to other trace metal chemistry previously discussed, but is hard to distinguish as it is influenced by the stainless steel composition of the experimental apparatus tubing, too. As found in earlier studies by Stalker et al., (2013) these element concentrations are influenced by the corrosion of the SS 316L stainless steel tubing. The composition of the stainless steel is shown in Table 38. The chamber containing the rock plug is made of Hastelloy, which is primarily composed of Ni, Cr, Fe and Mo.

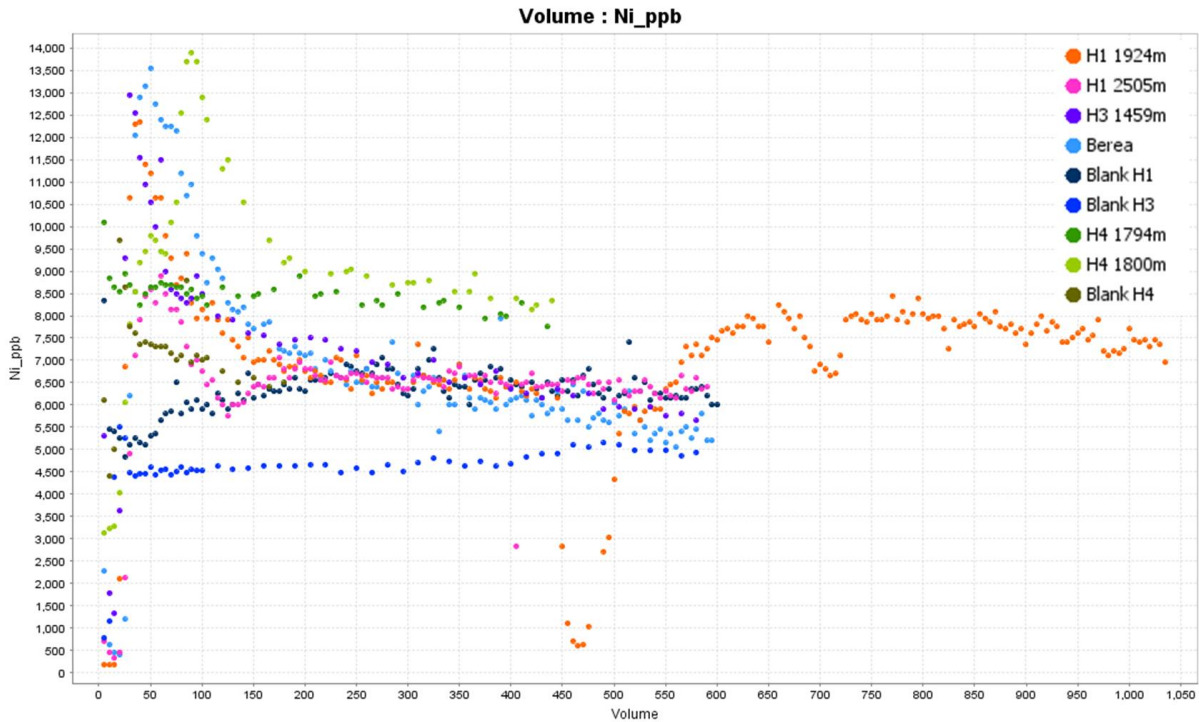


Figure 80. Nickel eluent in $\mu\text{g/L}$ from the core flood experiments over volume eluted from the different rock samples or experiments (0.5 cm^3 solution per minute).

Table 38 Composition ranges for 316L stainless steel (%) used in the core flood experiment (from <http://www.azom.com/article.aspx?ArticleID=2382>).

Steel type		C	Mn	Si	P	S	Cr	Mo	Ni	N
316L	Min	-	-	-	-	-	16.0	2.00	10.0	-
	Max	0.03	2.0	0.75	0.045	0.03	18.0	3.00	14.0	0.10

The trend for dissolved Fe in the eluents differs from all the other elements (Figure 81). Over time the Fe concentration increases and stabilises. Although the concentrations are low ($<150 \text{ mg/L}$), it would appear that some consistent dissolution of Fe oxides or Fe-substituted clays is occurring in the core from all Harvey and Berea samples. All core tests showed higher dissolved Fe than the blanks; which exhibit stable dissolution of the Hastelloy tubing across all experiments as shown by the overlapping and consistent probability plots for Blanks 1, 3 and 4 (Figure 82). The dissolution of Fe is greater in the Harvey-3 and Harvey-4 cores compared to the Harvey-1 cores. (Figure 81 and Figure 82). An accessory mineral berthierine (a non-swelling Fe-rich clay with kaolinite structure) was previously observed in the Wonnerup Aii facies (Delle Piane et al., 2013), but based on the mineralogy reported in Section 4 the Fe in Harvey-3 and -4 can only be sourced from illite. However, it is likely that there are minor minerals present in the core that were below detection limits for the XRD or not observed in the SEM analyses such as Fe-oxides. The Berea Sandstone used in these experiments was not analysed for mineral changes using electron microscopy, but composition from multiple publications of this rock was reported (Dawson et al. 2015) and shows minor Fe-bearing mineral phases may be present including ankerite ($\text{Ca}(\text{Fe},\text{Mg},\text{Mn})(\text{CO}_3)_2$), siderite (FeCO_3), hematite, chlorite, illite and smectite. The Dawson et al. (2015) study reported increases in Fe when subject to a CO_2 -rich brine and noted that carbonates were dissolved. Hematite was reported in trace amounts and was not shown to have

changed. Based on this finding it is most likely that ankerite and siderite are being dissolved to produce the Fe in solution from the Berea Sandstone core flood.

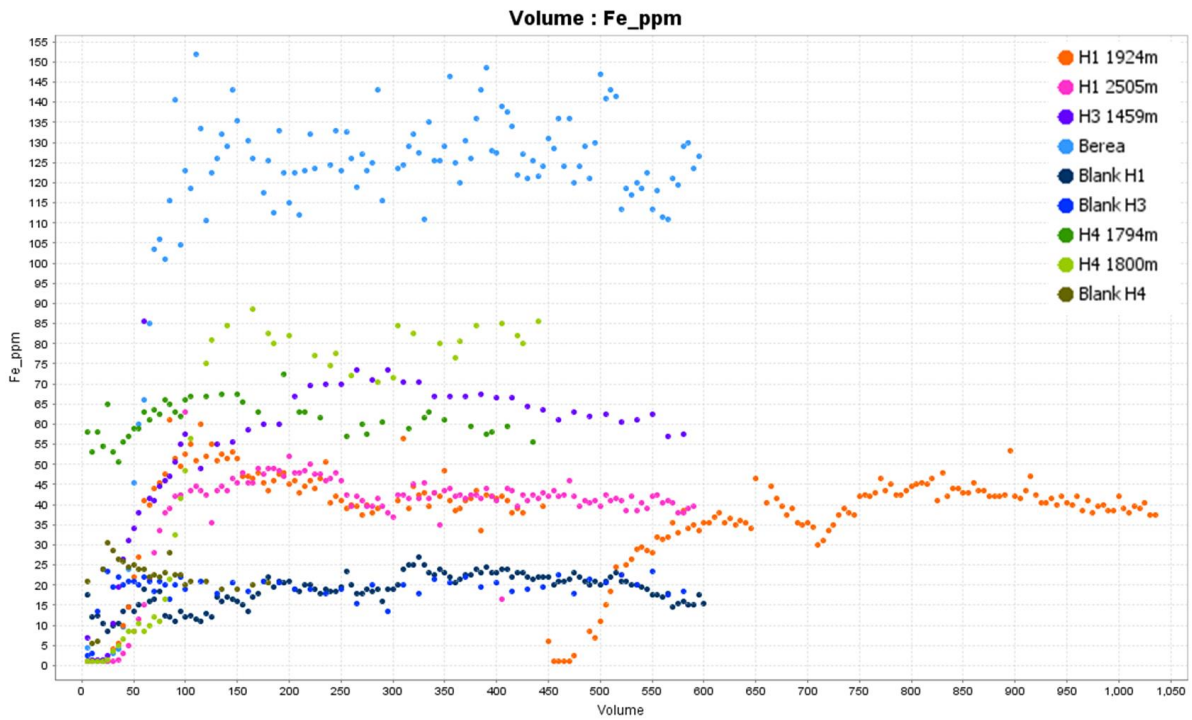


Figure 81. Iron eluent in mg/L from the core flood experiments over volume eluted from the different rock samples or experiments (0.5 cm³ solution per minute).

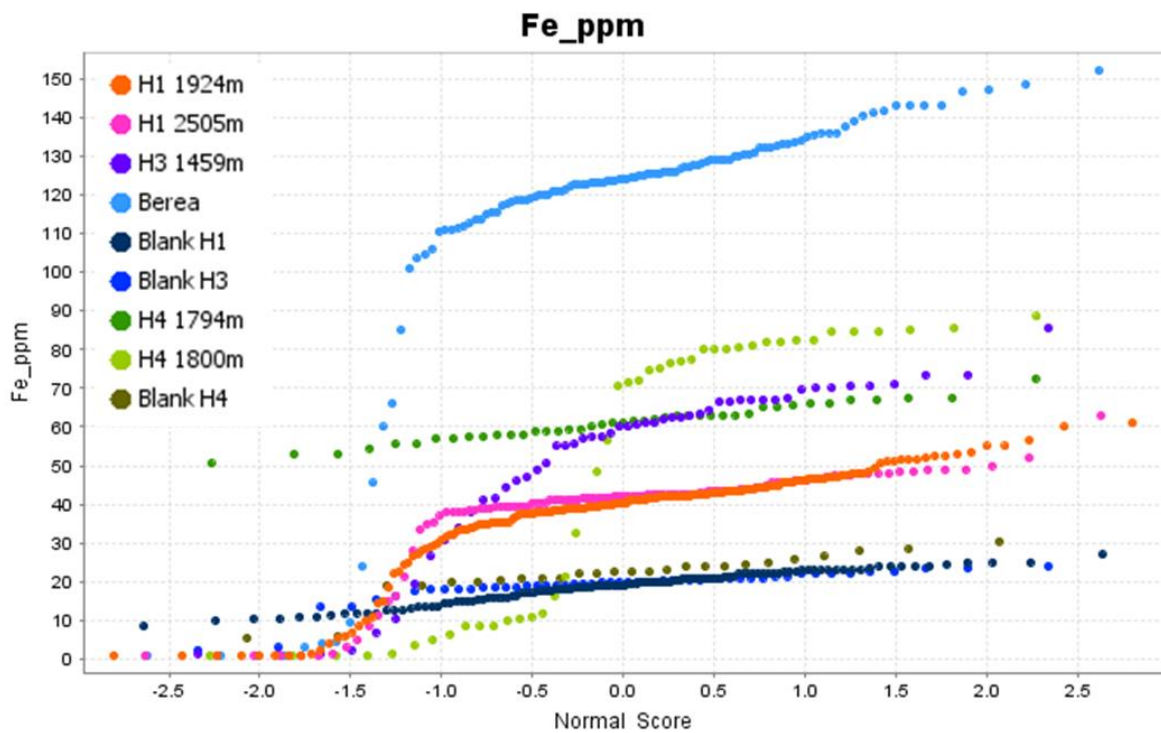


Figure 82. Probability plots of iron eluent in mg/L from the core flood experiments.

Using the results of the mass balance (g) dissolved with respect to the percentage and calculated weight of the mineral phases present, the percentage loss of the mineral phases was determined (Table 39). Only three of the observed minerals contain Fe, namely: illite - $K_{0.6}(H_3O)_{0.4}Al_{1.3}Mg_{0.3}Fe^{2+}_{0.1}Si_{3.5}O_{10}(OH)_2 \cdot (H_2O)$ which is quite common in the Wonnerup facies (Section 4); berthierine, an Fe-substituted aluminosilicate ($Fe^{2+}_{1.5}AlFe^{3+}_{0.2}Mg_{0.2}Si_{1.1}Al_{0.9}O_5(OH)_2$); and ankerite, an Fe-carbonate ($CaFe^{2+}_{0.6}Mg_{0.3}Mn^{2+}_{0.1}(CO_3)_2$). As ankerite and berthierine are Fe-rich, the amount of these phases needed to be dissolved to account for the dissolved Fe is small. In contrast, the amount of illite dissolved to produce this much Fe in solution is much greater. Nearly 25% of the illite would be dissolved in Harvey-3 and between 9 and 22% of the illite dissolved in Harvey-4 samples (for which illite is the only Fe-containing mineral observed) (Table 39). If no additional Fe-bearing minerals were present then those reported which comprise 1-2% of the total Harvey-3 and 4 cores, it is conceivable that this phase loss could be observed and future research should investigate the behaviour of Fe in this environment (Appendix A). The mass balance predicted loss of illite for Fe in solution does not match the Si, Al or K predicted losses of illite (Table 39). It is likely that there are trace additional mineral sources of Fe such as hematite in the Harvey rocks that were not detected by XRD. If hematite (Fe_2O_3) was present in these samples, only 0.01% to the total core mass would need to be hematite and dissolve to produce this concentration of Fe in the eluent.

Table 39. Percentage of core mineral phases dissolved based on mass balance approach using the eluent chemistry. Empty cells are minerals that do not contain that element or were not measured in that core using XRD (Table 33).

	Si					
	Qtz	Kaolinite	Orthoclase	Illite	Berthierine	Ankerite
Harvey-1.1924	0.0035	0.0026	0.0303		1.1428	
Harvey-1.2505	0.0004	0.0006	0.0059		0.1443	
Harvey-3.1459	0.0009	0.0017	0.0159	0.2119		
Harvey-4.1794	0.0012	0.0027	0.0162	0.2108		
Harvey-4.1800	0.0024	0.0021	0.0204	0.2231		
	Al					
	Qtz	Kaolinite	Orthoclase	Illite	Berthierine	Ankerite
Harvey-1.1924						
Harvey-1.2505						
Harvey-3.1459		0.0133	0.0176	0.2114		
Harvey-4.1794		0.0046	0.0040	0.0466		
Harvey-4.1800		0.0021	0.0028	0.0279		
	Fe					
	Qtz	Kaolinite	Orthoclase	Illite	Berthierine	Ankerite
Harvey-1.1924					2.46	2.43
Harvey-1.2505					1.07	
Harvey-3.1459				23.17		
Harvey-4.1794				21.36		
Harvey-4.1800				9.14		
	K					
	Qtz	Kaolinite	Orthoclase	Illite	Berthierine	Ankerite
Harvey-1.1924			0.001			
Harvey-1.2505			0.001			
Harvey-3.1459			0.052	69.0		
Harvey-4.1794			-0.004	-4.7		
Harvey-4.1800			0.067	71.9		

For the analyses of core before and after testing, the percentage loss of mineral phases associated with Al and Si was low, with a loss of <0.03% for the major mineral constituents such as quartz (SiO_2), kaolinite ($\text{Al}_2\text{Si}_2\text{O}_5(\text{OH})_4$) and orthoclase/albite (KAlSi_3O_8 / $\text{NaAlSi}_3\text{O}_8$) (Table 39). These results support the observed results of Section 4 where no net loss was observed even though some pores were altered (filled, opened) by clay mobility, and the quartz was unaltered.

It is important to monitor Al and Si as these are critical components of many minerals, including clays, and measured concentrations could indicate dissolution of clays. Unfortunately, once robust detection limits were applied to the data, nearly all Al was near or below detection limits. Presumably, the formation of minerals such as dawsonite as indicated by modelling in this report and Stalker et al., (2013) would precipitate much of any Al dissolved in mineral reactions and maintain soluble Al below detection. However, it is important to consider that the formation of dawsonite is debated under numerous conditions (Hellevang et al., 2014) and precipitation of other mineral phases could also account for the loss of Al. Silicon trends differ from Al, showing a slight first flush effect like most elements presented in this Section and dissolution when the brine was stagnant in the core of Harvey-1-1924m when the experiment was reset (after elution of 450 cm^3). Silicon concentration increases after the overnight “reset” of the experiment for Harvey-1 1924m. The Si trend for Harvey-3 1459m and Harvey-4 1800m cores are similar to that of the trace metals where Si was observed at an elevated level until a midpoint and then decreases to background levels (Figure 83). There is an initial flush of high dissolved Si for the Harvey-4 1794m test and then a more stable but reduced Si dissolution occurring later. The increased Si is possibly a result of increased acid attack on the rock minerals, the destruction of illite (or possibly K-feldspar) and potentially the formation of dawsonite ($\text{NaAlCO}_3(\text{OH})_2$) or kaolinite which is feasible in the early experimental conditions based on the modelling results. The formation of dawsonite will remove Al, Na and CO_2 from solution, but given the high concentrations in solution this change would be difficult to observe. Silicon will be released from Al-Si clays. Harvey-4 1800m contains more clays than Harvey-4 1794m (Section 4). The Harvey-3 and Harvey-4 (1800m) core flood showed much greater K dissolution, but this was not correlated to the Si (Figure 70 and Figure 83). The release of Al is a rate limiting element in the formation of dawsonite. However, a loss of Al (below detection) and a slight increase of Si (and K) does potentially represent this reaction in the core flood eluents (Figure 83). In later experiments, the analyses gave better detection of Al, indicating that some Al is present for both Harvey-3 and 4 samples, compared to the background (Figure 84).

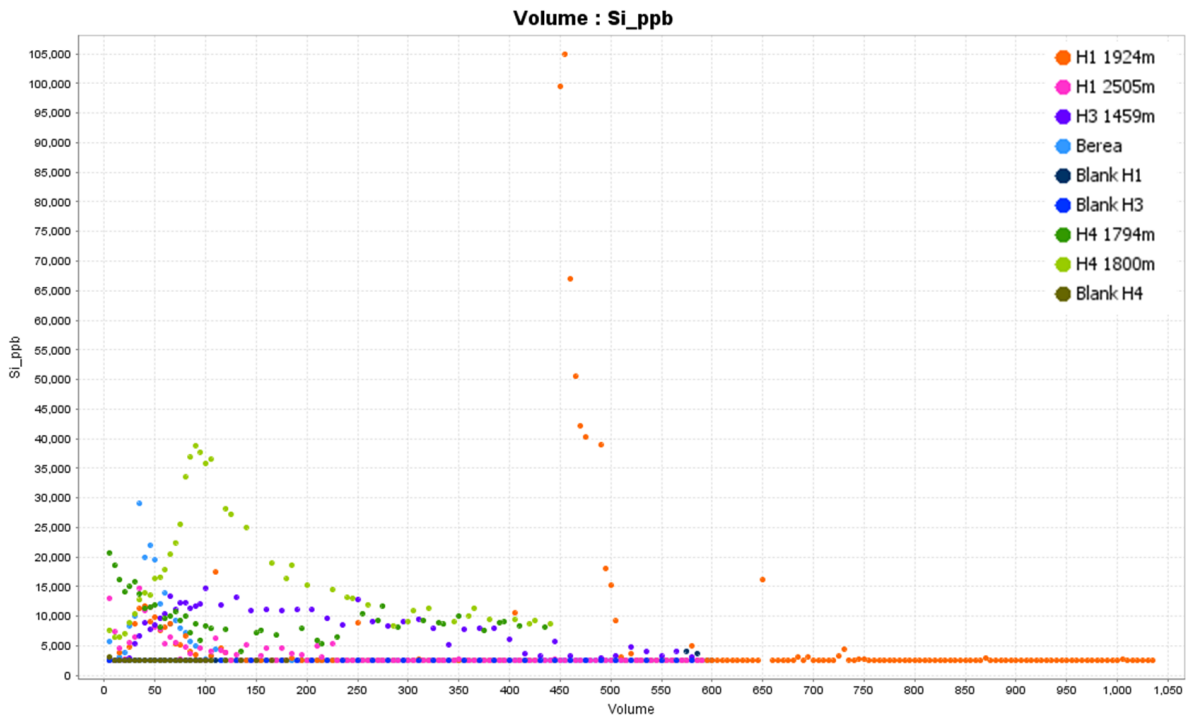


Figure 83. Silica eluent in $\mu\text{g/L}$ from the core flood experiments over volume eluted from the different core plugs or experiments (0.5 cm^3 solution per minute).

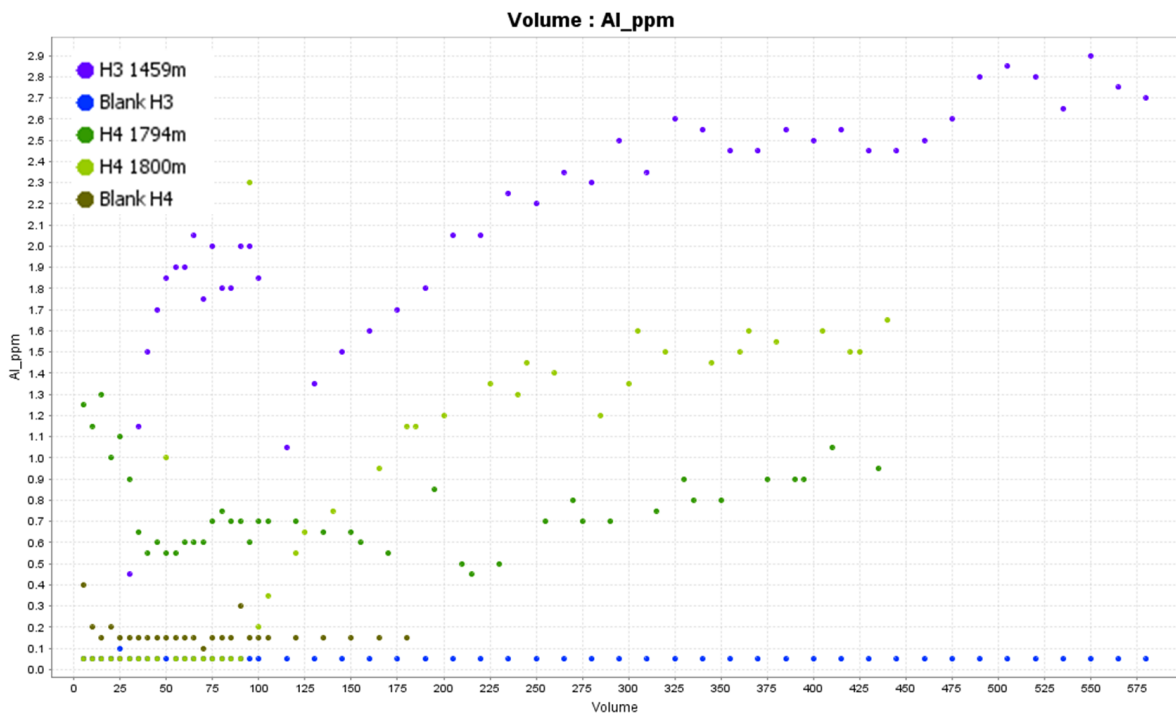


Figure 84. Aluminium eluent in mg/L from the core flood experiments over volume eluted from the different core plugs or experiments (0.5 cm^3 solution per minute).

Modelled injection of CO_2

Modelled results showed increased CO_2 injection caused significant changes in mineral and fluid compositions as the reaction progressed. For context, it is important to note that the conditions associated with our core flood experiments are at the 20% or 0.2 reaction progress mark in the

following plots (e.g. Figure 85). Another important consideration is that kinetic barriers at this relatively low temperature, and other effects such as inability of fluids to migrate into (and react with) the mineral mass from the pore space, could strongly reduce the degree of reaction in the real world, and the speed of these effects. Finally, while many minerals are observed in the rock samples from Harvey 1, 3 and 4, the initial equilibration of the model will remove meta-stable minerals and cannot incorporate various solid solution species, so end member minerals are used. Our chemical modelling assumes the solution and rock mass react fully. These modelling results should be seen as an indication only.

Modelled fluid chemistry

As more CO₂ is put into the system (pressure is increased above realistic levels) major mineral conversions occur. CO₂ fugacity starts at close to atmospheric levels (an underestimate by the modelling) and is 0.1 atm CO₂ at our approximate standard experimental conditions (0.2 reaction progress; Figure 85). With major increases in CO₂ fugacity the system is potentially over pressurised. After 'saturation' at approximately 0.7 reaction progress the CO₂ rises linearly (note Figure 85 is a log plot of fugacity) to ~ 100 atm. Increased CO₂ leads to higher TDS (Figure 86)

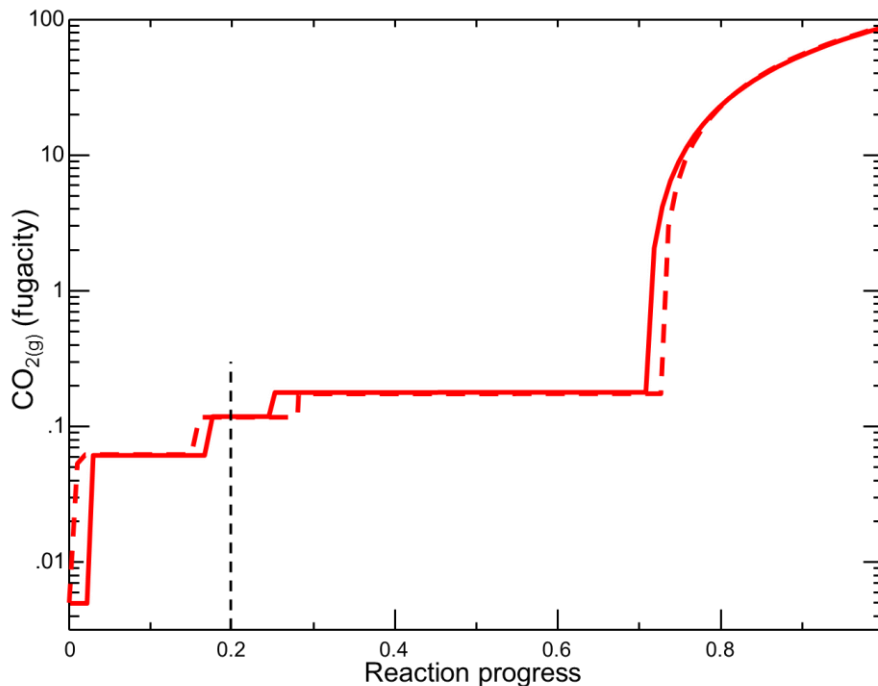


Figure 85 CO₂ fugacity increasing as the reaction progresses. The black dashed line represents the approximate conditions for the core flooding experiment, with the red dashed line showing the changes related to a reduced Na, SO₄ and Cl starting composition of the brine.

The water component in solution is diluted as the CO₂ increases. As CO₂ is hydrolysed $\text{CO}_2 + \text{H}_2\text{O} \rightleftharpoons \text{HCO}_3^- + \text{H}^+$ this produces acid, resulting in the potential breakdown of minerals, and decrease in pH (Figure 87). These reactions are indicative of what may occur at mineral boundaries and indicators of what we may expect in terms of fluid changes as solution passes through the cores. In some scenarios the models could not run without an approximate 50% dilution of the Na, SO₄ and Cl input. To test the sensitivity of the modelling with this required change we ran the reduced solution input as well. The dashed line represents the changed initial solution on the following plots. It is evident that the models

are robust and the trends do not change with decreased Na, SO₄ and Cl. In Figure 86, the dashed line is for the lower initial Na/Cl/SO₄ and shows a later inflexion point compared to the original parameters (Figure 86). In this plot there is a minor increase in salinity until CO₂ 'saturation' when the rock mass has little capacity to incorporate further CO₂ and it remains in the solution (Figure 86).

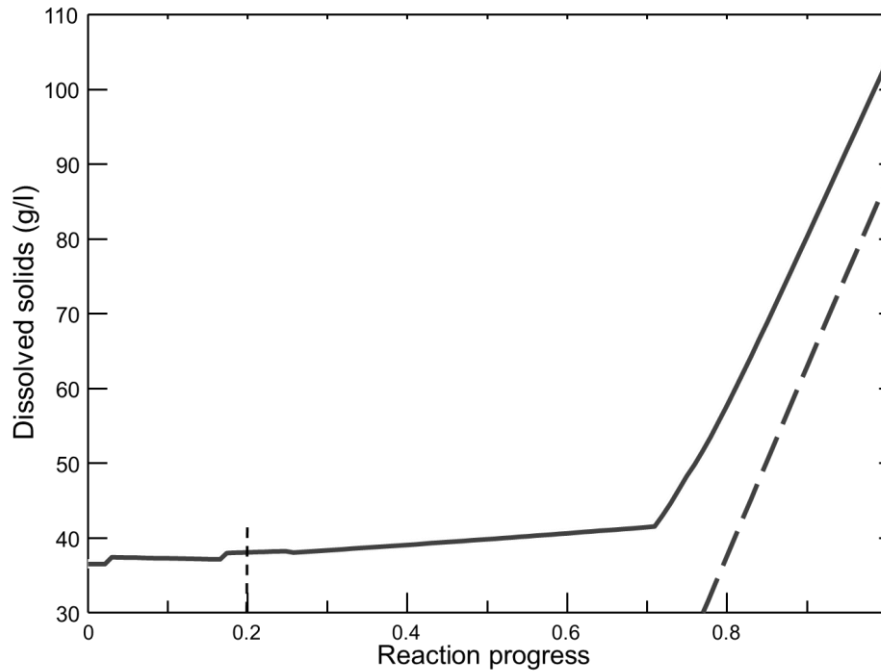


Figure 86 Total dissolved solids as influenced by increased CO₂ reactant. The solid line shows the results for the standard conditions reported in Table 34 and reduced Na, SO₄ and Cl in the dashed line. These results are for Harvey-1 1924m.

The pH is slightly influenced by a lower salinity (Figure 87). Solution pH remains neutral to beyond the experimental conditions with CO₂ addition. The pH then drops to just below 7, before significantly dropping after the 'saturation' point which is reflected in Figure 86 and Figure 87. Interestingly, the ~50% lower Na/Cl model had slightly higher pH, though the trends were very similar.

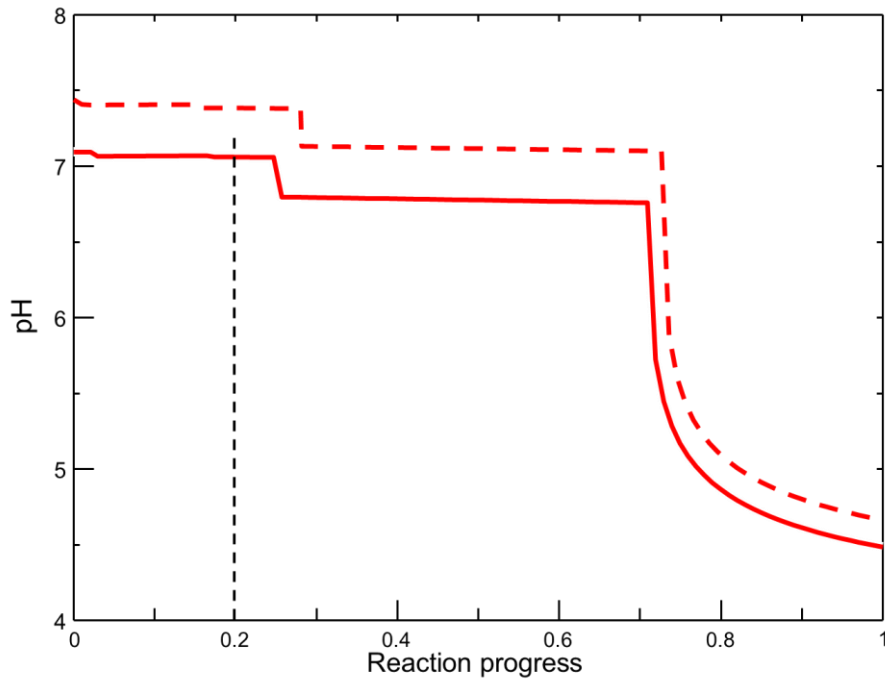


Figure 87 Production of carbonic acid and loss of neutralising capacity in the rock results in reduced pH conditions as the reaction progresses.

Na and Cl remain stable until CO₂ 'saturation'. At this stage, small amounts of the Na are being subsumed into dawsonite and removed from solution, although this is minor relative to the CO₂ being added. The lower Na and Cl used in the sensitivity testing clearly shows the lower dissolved Na and Cl in the results (dashed lines in Figure 88). The lower TDS brine reduces the dissolved Na available for incorporation into dawsonite after 'saturation' point, and so there is a slightly higher rate of CO₂ into solution, but the differences are very small (Figure 88).

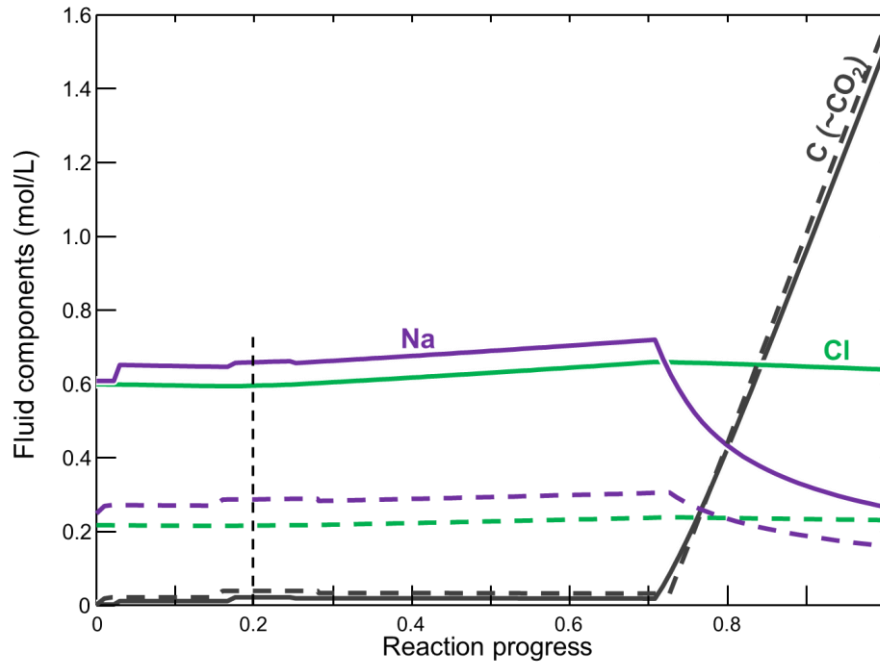


Figure 88. Major cations and anions released into solution from the injection of CO₂ into the Harvey-1 1924m rocks. The dashed line represents the sensitivity testing of lower salinity brine

Other elements Ca, K, Mg and Fe (Figure 89 and Figure 90) are released into solution after the 'saturation' point, due to pH lowering. Slightly less cation release occurs for the lower TDS test. Increases in concentration of elements such as Cl are related to the decrease in the water content. Dissolved Na significantly decreases, due to incorporation in dawsonite. Once dissolved CO₂ increases, Ca and Mg increase although some of the Ca released is reprecipitating as anhydrite (CaSO₄) in the very later stages of the modelled reactions which is more noticeable in the loss of SO₄ from the fluid (Figure 90). Potassium and some Fe are also liberated from mineral phases which is observed in the core flood experiments, however, this metal mobilisation takes place at much greater pCO₂ and conditions (reaction progress 0.7) compared to the plots where the conditions of the core flood experiments are at 0.2 reaction progress.

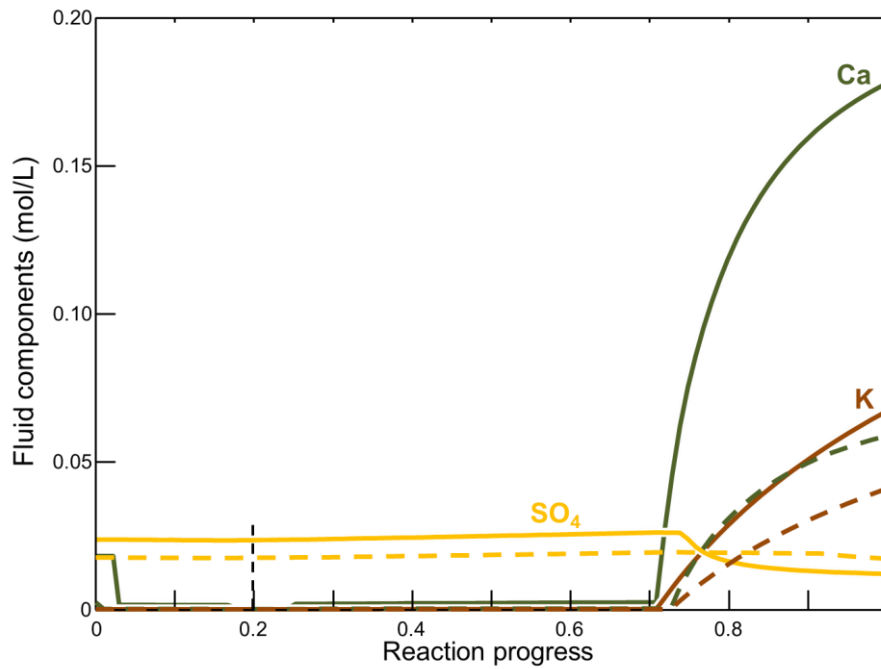


Figure 89 Minor cations and anions released into solution from the injection of CO₂ into the Harvey-1 1924m rocks. The dashed line represents the sensitivity testing of lower salinity brine.

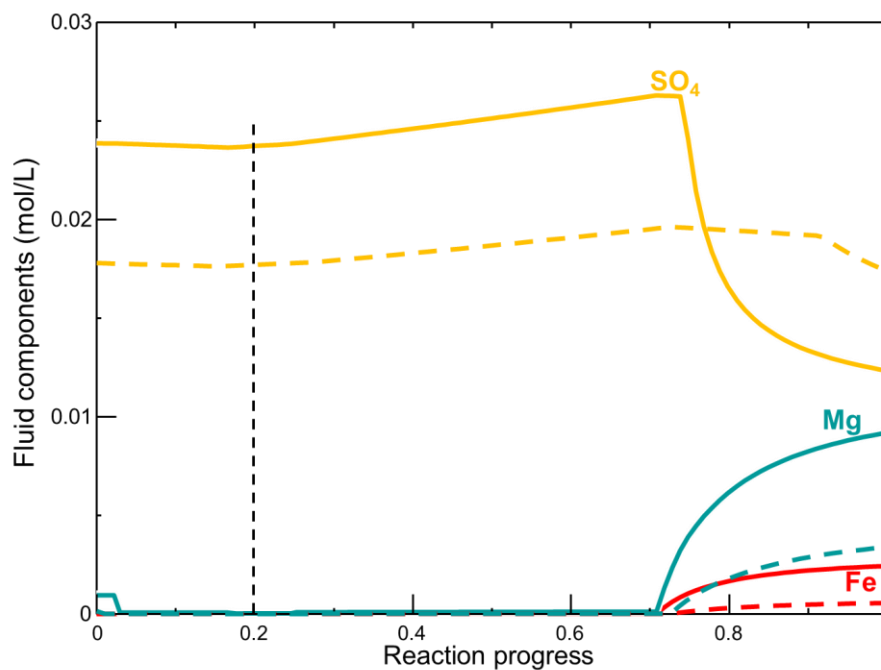


Figure 90 Other trace cations and anions released into solution from the injection of CO₂ into the Harvey-1 1924m rocks. The dashed line represents the sensitivity testing of lower salinity brine.

Modelled mineral dissolution and precipitation

Quartz and muscovite are not depleted during CO₂ addition. The quartz content slightly increases due to release of Si from side-reactions and this pattern for the major mineral components is unchanged regardless of the brine salinity tested (Figure 91). The main reactions are dominated by CO₂ which is consumed by the conversion of albite then paragonite (a Na end member mica) to dawsonite, kaolinite and minor quartz, siderite and anhydrite (Figure 91, Figure 92 and Figure 93). Released Si goes to quartz

and kaolinite, and Al goes into kaolinite and dawsonite. Paragonite is still stable at the normal CO₂ level. Once paragonite is consumed, the mixture is semi-‘saturated’, as only Na from solution can be used (albeit with difficulty) to form dawsonite. As dawsonite formation reduces, there is little capacity for the rock to adsorb CO₂ and it remains in solution (Figure 85). The formation of dawsonite is consistent with coal seam gas observations where dawsonite is precipitated in fractures (Golab et al. 2006).

Although little Fe exists in these mineral phases, any Fe that is released is precipitated as siderite. Other carbonate minerals remain relatively stable e.g. dolomite and calcite (Figure 93). The experimental pressure increase decreases pH by protonation, but does not change the actual CO₃²⁻ so many minerals remain stable with just CO₂ partial pressure increased e.g. dolomite saturation remains constant and we observe this in the models, as well as the mass balance and in the mineralogy that shows now significant change to the carbonate cements post core flood.

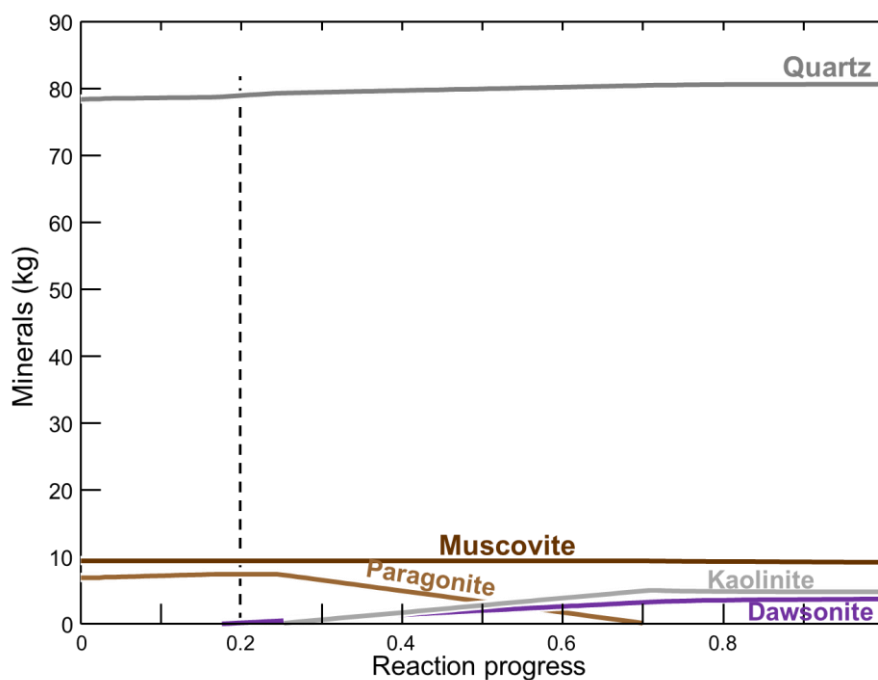


Figure 91. Reaction modelling progress for major minerals showing the destruction or weathering of paragonite (mica) and the formation of kaolinite and the precipitation of dawsonite as CO₂ is added to the Harvey-1 1924m rock mass. Note the quartz and muscovite are only slightly changed and remain relatively stable to other mineral transformations.

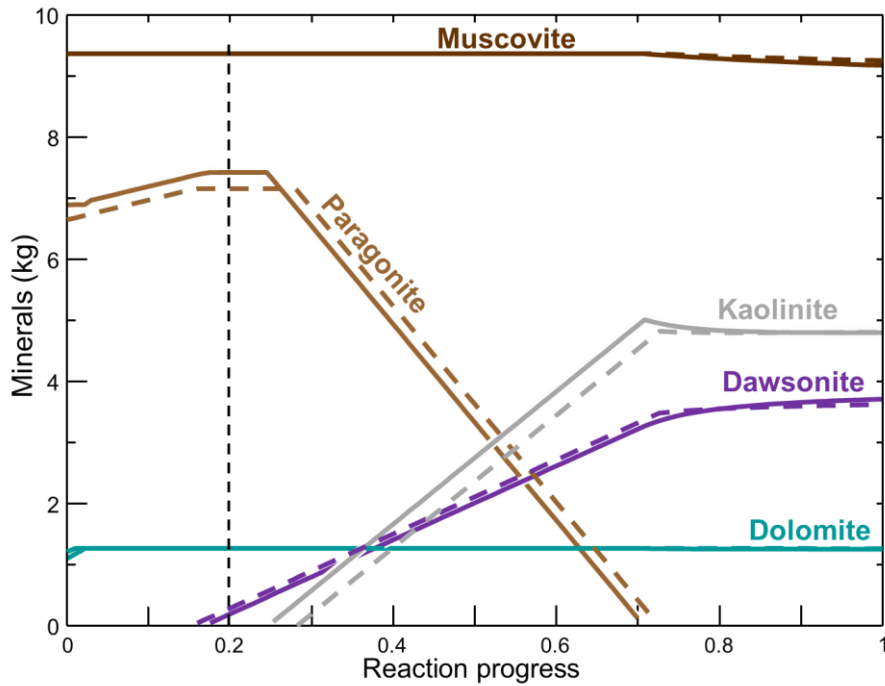


Figure 92. Reaction modelling progress for minor minerals showing the destruction or weathering of paragonite (mica) and the formation of kaolinite and the precipitation of dawsonite as CO₂ is added to the Harvey-1 1924m rock mass. The dashed lines show the reactions related to the reduced starting brine salinity.

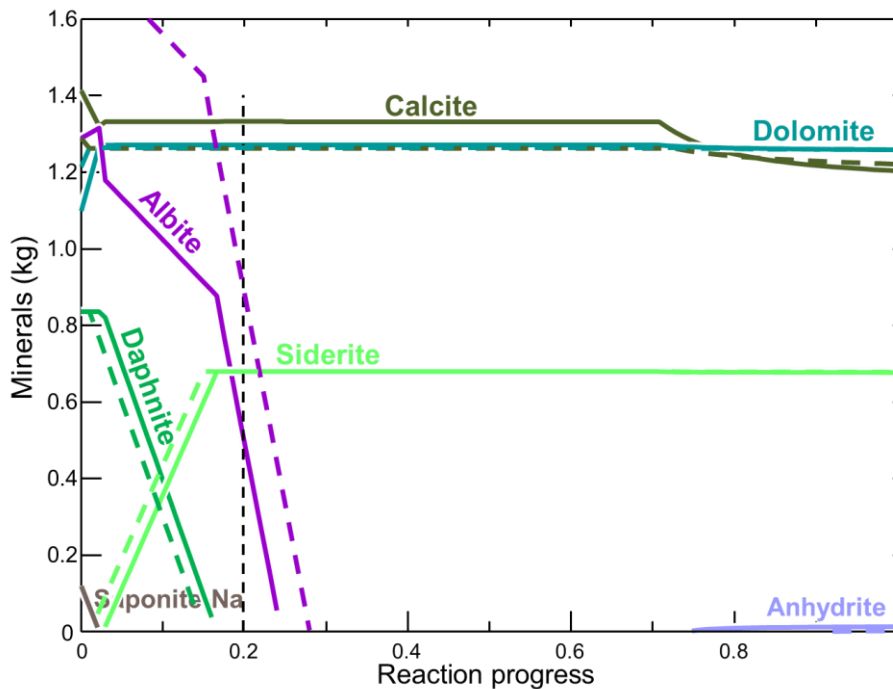


Figure 93. Reaction modelling progress for trace minerals showing the destruction of albite and daphnite and the formation of siderite and anhydrite as CO₂ is added to the Harvey-1 1924m rock mass. The dashed lines show the reactions related to the reduced starting brine salinity.

The results presented in the modelling section are for Harvey-1 1924m conditions. The mineralogy was similar, but not identical for the other cores tested and the modelled reactions of these materials are also similar. More plots and the modelled data are provided in Appendices A and B. Changes are

relatively minor, for example Harvey-1 2505m reaches the ‘saturation’ point at 0.6 instead of 0.7 as was the case in Harvey-1 1924m, but the reactions all progress in the same pattern. The Harvey-3 1459m and Harvey-4 1794 m tests achieve ‘saturation’ much earlier than Harvey-1 (and Harvey-4 1800 m) due to the reduced mineral buffering capacity and as a result CO₂ increases in solution, pH drops and the mineral conversions occur earlier (Figure 94). The mineral changes are similar, though with alunite also forming later and some loss of dolomite and calcite (Figure 95). The modelling for Harvey-3 1459m was one scenario that required the reduced saline brine starting solution to progress, but the previous sensitivity testing shows that this is unlikely to greatly alter the results.

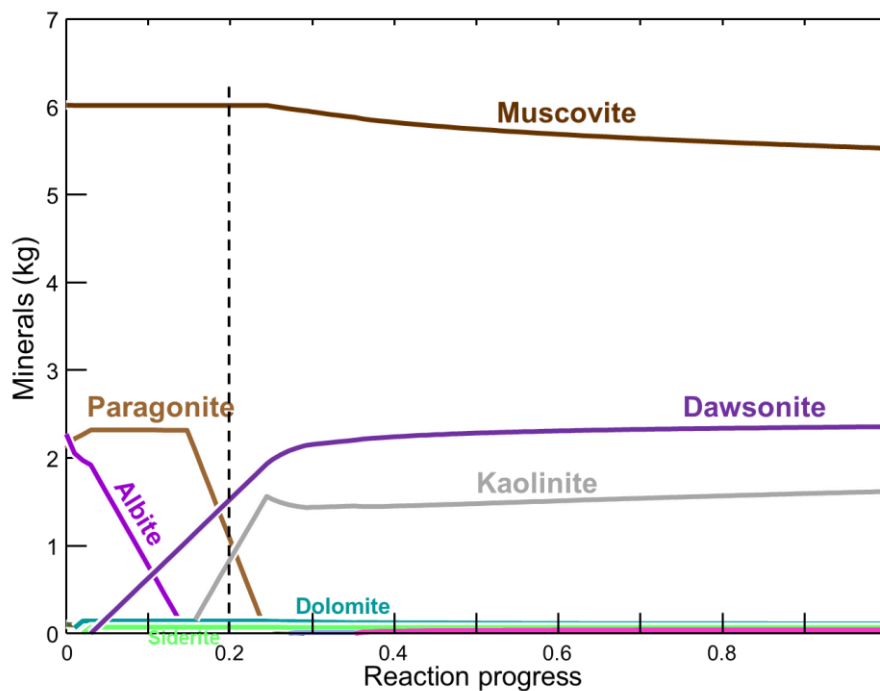


Figure 94. Reaction modelling progress for minor minerals as CO₂ is added to the Harvey-3 1459m rock mass. The dashed lines shows the equivalent experimental conditions used in the core flood tests. Compare to Figure 92.

The Harvey-4 1794m sample differed from the other samples slightly with the mineralogy, but the major common end reaction products were quartz, muscovite and dawsonite. In this model there was no kaolinite and more albite initially.

The chemical modelling is useful in delineating the potential reactions and the influences these will have on the formation mineralogy and the groundwater chemistry. They are also useful in understanding the results from the core flooding experiment. In particular, the rocks theoretically have some capacity to maintain circum-neutral conditions from our modelling or in carbonate rocks (Wilke et al., 2012) although other experimental studies have shown acidic conditions occur with silicate minerals (like the Wonnerup formation) and become even more acidic with gaseous impurities of SO₂ and NO₂ (Wilke et al., 2012; Dawson et al., 2015). The emulation of these systems could be improved by better groundwater chemistry and mineral information, and by moving from static to reaction-path modelling

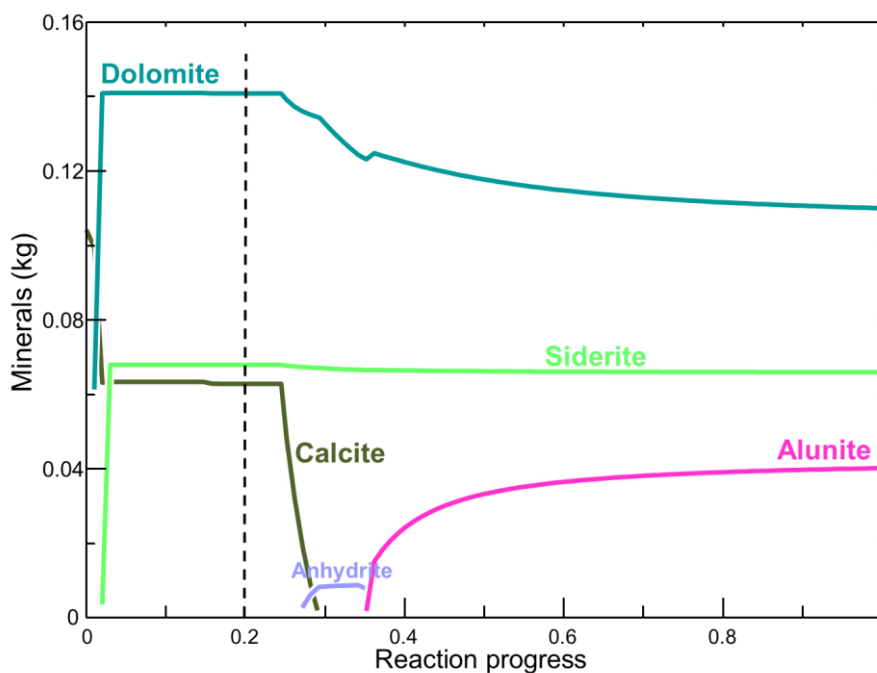


Figure 95. Reaction modelling progress for trace minerals as CO₂ is added to the Harvey-3 1459m rock mass. The dashed lines shows the equivalent experimental conditions used in the core flood tests. Compare to Figure 93.

With respect to the core flood experiments the modelled changes correspond to the liberation of Fe, K and some Si which was observed, however, the increase in soluble Ca and Mg was not observed. Both these observations were also confirmed in the mass balance evaluation (Table 36). The concentrations are lower in the core flood experiments compared to the model, but given the kinetic (reactive surface area) effects it seems representative, especially considering mineral transformations were not observed in the mineral study component of this report (Section 4). The fate of most trace elements is not shown in modelled results as the inputted mineralogy (and to a lesser extent the thermodynamic database) does not contain these compounds.

Summary

Changes related to eluent chemistry are mainly observed in the “first flush effect” during the core flood experiments. Initially this was thought of as acidic brine (carbonic acid) interacting with the core. This may occur, and certainly K seems to show this effect to some extent, but the more recent experiments of Harvey-4 core show a mixing trend of solutions, one highly saline and the other the more typical solution with the reactive CO₂ as shown with increased soluble Si, Al and Fe. The highly saline solution without the effects of CO₂ is a result of brine saturation for the previous NMR porosity testing and some subsequent drying creating pores with additional salt crystals. These crystals rapidly solubilise and migrate with the following eluent in the core flood experiments. In effect, the first flush is predominantly a salinity increase and then the effects of the CO₂ are observed later. The later observed solubilised Al, Si and other elements are representative of the CO₂ attack on mineral phases and agree with modelling results. The CO₂ is most likely buffered quickly and then material is not greatly changed.

The use of a mass balance approach showed that any measured chemical change will only relate to a small (< 0.03%) change in the total mineral phases, consistent with the lack of observed mineral

changes in SEM analysis (Section 4). There may be significant changes related to Fe minerals, but at their low concentrations it is unlikely these changes will be observed with broad SEM analysis of the core cross sections. Future research should investigate specific mineral mapping or targeted analysis of mineral phases.

The friable nature of the Harvey-3 core and the related increase in clays in the Harvey-4 1800m core may also change the solution migration patterns and retard the flush effect resulting in a greater lag i.e., the elevated chemical signature extends for greater time/volume. Harvey 3 and Harvey-4 1800m were certainly more reactive possibly due to the increased clay content whereas Harvey-4 (1794m) was much less reactive. The increased reactivity related to clay content matches the modelling results where the silicate minerals are the more reactive phases compared to the dominant quartz mineralogy. The Harvey-4 1794m core had increased porosity and better permeability which may explain why the core flood eluent seemed to stabilise more rapidly than the Harvey-4 1800m sample.

The Harvey-3 and 4 core appears to show less resistance to the dissolution of K and Si compared to Harvey-1. The overall mass balance for the cores with pre and post flood changes related to porosity do not match the eluted elements. For example, most mass was lost from Harvey-4 1794m and then Harvey-3 core. While Harvey-3 exhibited significant element mobility, Harvey-4 1794m was much less reactive. These results contradict the lack of perceived changes in the mineralogical and physical core testing (Sections 3 and 4), however, it is important to realise that the changes observed in the core flood eluent are very small with respect to the overall core mass and volume.

The use of smoothing the data by dividing by TDS was highly valuable to understand geochemical changes in the core. Potassium and Si are useful indicators of clay and K-feldspar dissolution. Iron (and REE for the Berea) show different trends to the rest of the data for all experiments.

The release of Al is the rate limiting element in the formation of dawsonite. The loss of Al (below detection) and a slight increase of Si (and K) does potentially represent this reaction in the core flood eluents, and later experiments showed that some Al is present for both Harvey-3 and 4 samples compared to the background. These results match the general modelling conditions that indicate it is unlikely the formation of dawsonite is occurring and this is confirmed in the mineralogy studies. Rapid mineral precipitation would lead to rapidly decreased permeability and this was not observed in the chemical, mineralogical and physical studies of the Wonnerup core materials when subject to CO₂ saturated flooding.

Conclusions

Below is a summary of the main results and conclusions arising from the work carried out to date:

- The percentage loss of mineral phases associated with Al and Si was insignificant, with a loss of <0.03% for the major mineral constituents such as quartz (SiO₂), kaolinite (Al₂Si₂O₅(OH)₄) and orthoclase/albite (KAlSi₃O₈ or NaAlSi₃O₈). These results support the observed results of the mineralogical assessment where a net loss was not observed even though some pores were altered (filled, opened) by clay mobility and the quartz was unaltered.
- Nearly 25% of the illite would be dissolved in Harvey-3 and between 9 and 22% of the illite dissolved in Harvey-4 samples *if* the source of Fe was solely from the minerals observed in the XRD and SEM analyses. However, it is unknown, but more likely that trace Fe-oxides are

present in the Wonnerup formation rocks contribute to the dissolved Fe measured. Future research should study the behaviour of Fe in this environment.

- The Harvey-4 1800m core has greater dissolution of K and Si compared to Harvey-1 and -3.
- Most geochemical changes are mainly observed in the “first flush effect” that may be a remnant of salt remobilisation rather than the acid attack in minerals from CO₂ saturated brine. The acid attack is minor, buffered rapidly and better reflected in the mobilisation of Si and Fe.
- The friable nature of the Harvey-3 core like the increased clay content of Harvey-4 1800m may also change the solution migration patterns and retard the flush effect resulting in a greater lag i.e. the elevated chemical signature extends for greater time/volume and the sharp first flush is not as prominent.
- Aluminium availability is a likely rate limiting step for the formation of minerals such as dawsonite. Potassium and Si are useful indicators of clay and K-feldspar dissolution whereas Fe and REE show unusual trends dissimilar to other elements.
- Elements that may be a concern for environmental toxicity (e.g. arsenic, selenium) were consistently at low concentrations, with minimal mobility and should not cause any persistent problems for CO₂ injection into the rock types tested.

Modelling shows the experimental conditions are unlikely to result in major mineralogical and fluid changes which is confirmed in the results of the core flood eluent chemistry and the mineralogical studies.

Section 6: Micro Computed Tomography (Micro-CT) Imaging

Contributors:

Dr. Stefan Iglauer

Dr. Maxim Lebedev

Introduction

In order to investigate any pore-scale changes which may occur to the Harvey-1 and Harvey-4 rock samples after undergoing the flooding procedure, two sets of experiments were conducted using an X-ray micro-CT imaging technique.

Harvey-1 Samples

Experimental procedure

Ex-situ imaging

Two small cylindrical micro-plugs (length 10mm, diameter 5mm) were drilled from H1-Plug1 (Plug 1 of Harvey-1). One of the micro-plugs was cut from an off-cut piece of this core plug and was imaged in a dry state with a micro-computed tomograph (Xradia VersaXRM 500T) at high resolution ($3.43 \mu\text{m}$)³ in 3D. This would provide information about the state of this core plug before being flooded.

After flooding core Plug 1 (Section 2 of the report), a second micro-plug was cut from it to undergo the micro-CT imaging (Figure 96). This second micro-plug was drilled from a flooded segment of this core plug and as close as possible to the location of the first micro-plug imaged before. This second micro-plug was imaged after cleaning with tap water.



Figure 96. Schematic of the 1st sample assembly of Harvey-1 showing the location of the micro-CT samples.

In-situ imaging

A third micro-plug (length 10 mm, diameter 5 mm) was also drilled from an off-cut piece of Plug1 and mounted into an X-ray transparent cell (Figure 97a). This cell is the heart of the micro-CT core-flood apparatus (Iglauer et al. 2011; Rahman et al. 2016), which is integrated into the micro-CT scanner (Figure 97b). The micro-plug was then subjected to 15 MPa confining pressure, and the whole flow system was vacuumed for 24 hours. The system was subsequently flooded with dead (not CO₂ saturated) brine at a Darcy flow rate of 7.3×10^{-6} m/s, so that the micro-plug was fully saturated with dead formation brine. Subsequently the whole flow system was heated isothermally to 45°C, and once the desired temperature was reached the pore fluid pressure was increased to 10 MPa. The micro-plug was then micro-CT imaged in-situ fully saturated with dead brine at a high resolution of ($3.43 \mu\text{m}$)³. Finally 40 PV of live (CO₂ saturated) brine were pumped through the micro-plug at a Darcy flow rate of 7.3×10^{-6} m/s, and the plug was imaged again in-situ after flooding at a high resolution of ($3.43 \mu\text{m}$)³.

Experimental results

Ex-Situ coreflooding

Qualitative analysis

The greyscale microCT images (which represent 3D maps of the relative radiodensity, Golab et al. 2013) were filtered with a non-local means filter (Buades et al. 2005) to remove salt-and-pepper noise

and segmented with a watershed algorithm (Schlüter et al. 2014). Selected axial slices through the plugs (raw images) are shown in Figures 98 (before flooding) and 99 (after flooding).

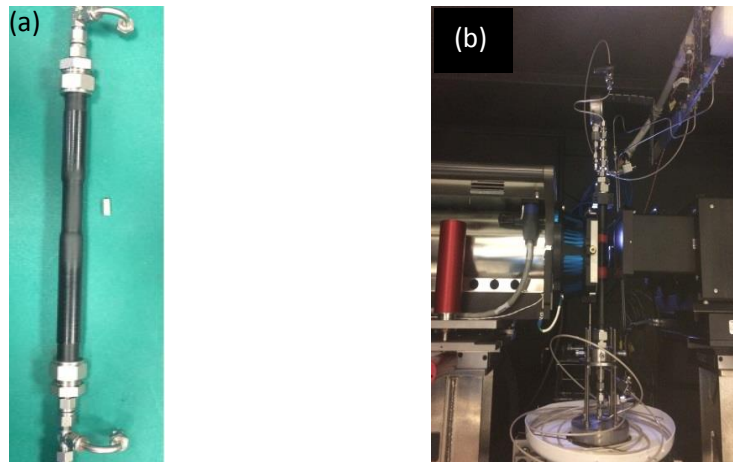


Figure 97. a) X-ray transparent Hassler cell; b) micro-CT setup in scanner: the x-ray source is located on the left, the detector on the right.

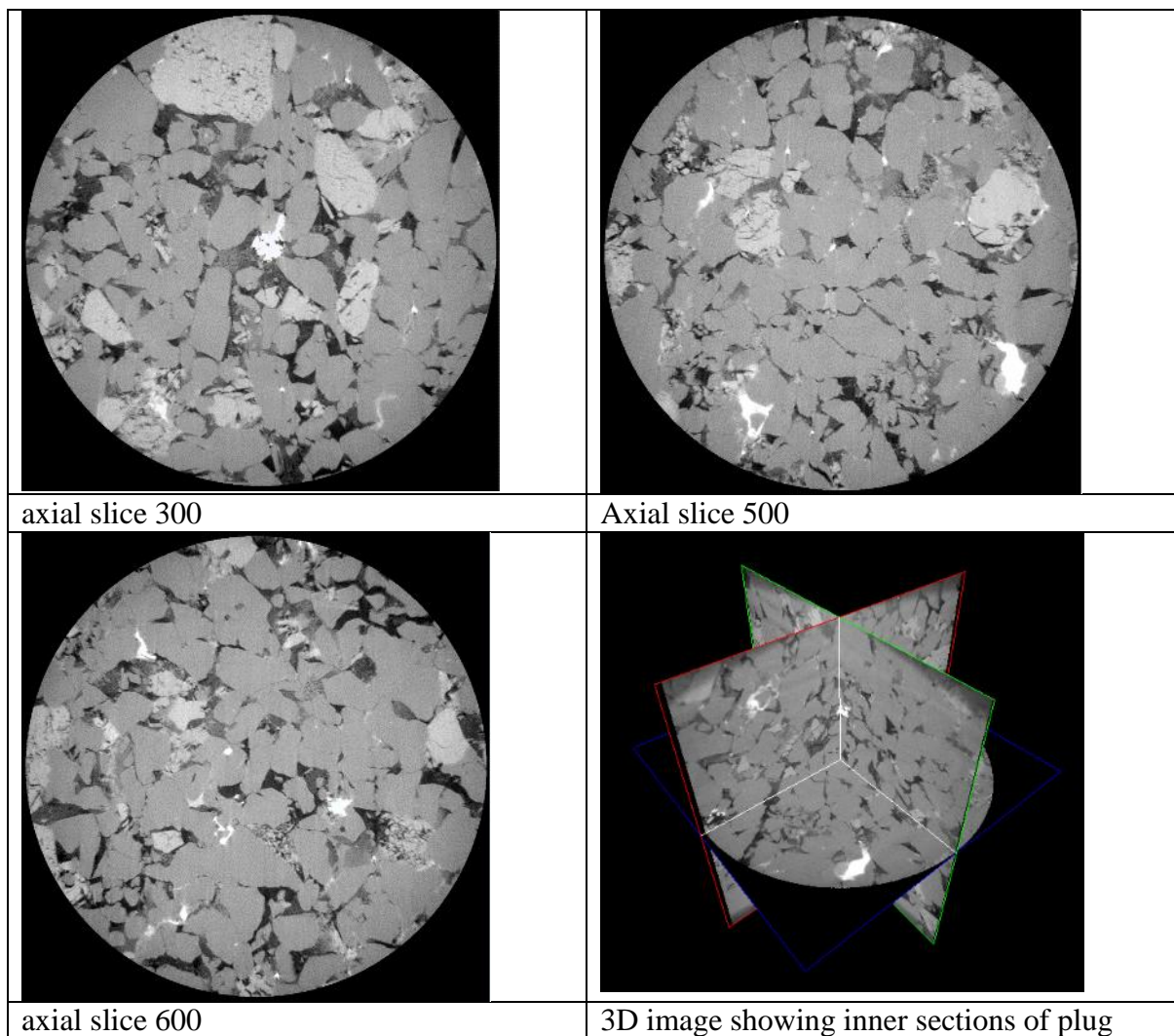


Figure 98. Selected axial slices through the pre-flood plug (ex-situ). The diameter of the shown circles is 3.43mm.

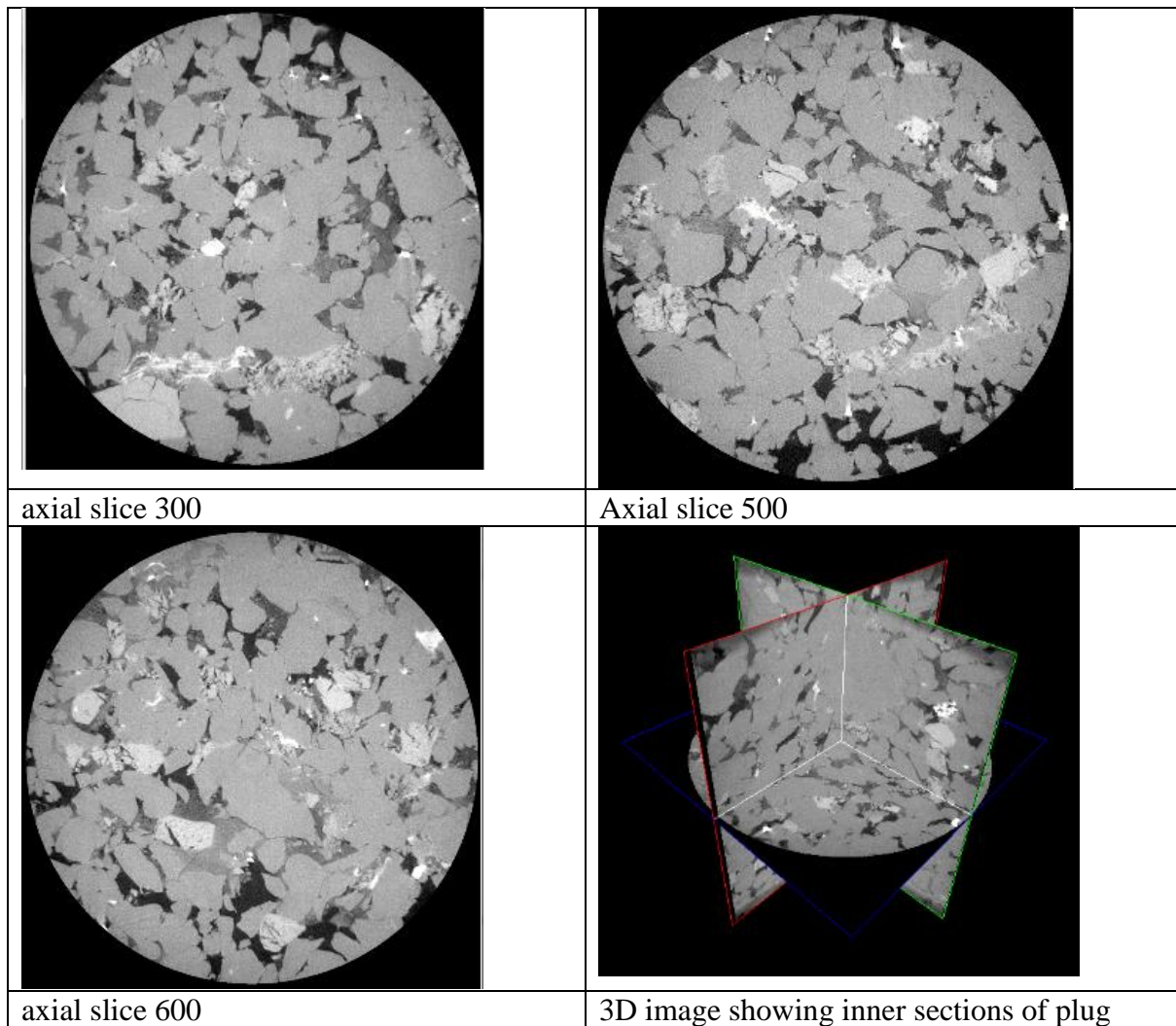


Figure 99. Selected axial slices through the post-flood plug (ex-situ). The diameter of the shown circles is 3.43mm.

In Figure 100 2D slices through the dry plug are displayed, where each phase has been identified (raw image: pore: black, kaolinite: dark grey, quartz: medium grey, feldspar: light grey, TiO₂: white/segmented image: pore: light blue, kaolinite: dark blue, quartz: red, feldspar: green, TiO₂: yellow). The minerals were identified in a two-step process:

1. The relative radiodensity (i.e. the relative greyscale) was ranked and compared with the density of each material and its chemical composition (Table 40). Note that higher densities can be approximately correlated with higher relative radiodensities, i.e. lighter grey values.
2. The images were compared with the SEM images and EDS data.

Based on this information the phases were assigned to a specific mineral (De Boever et al. 2015).

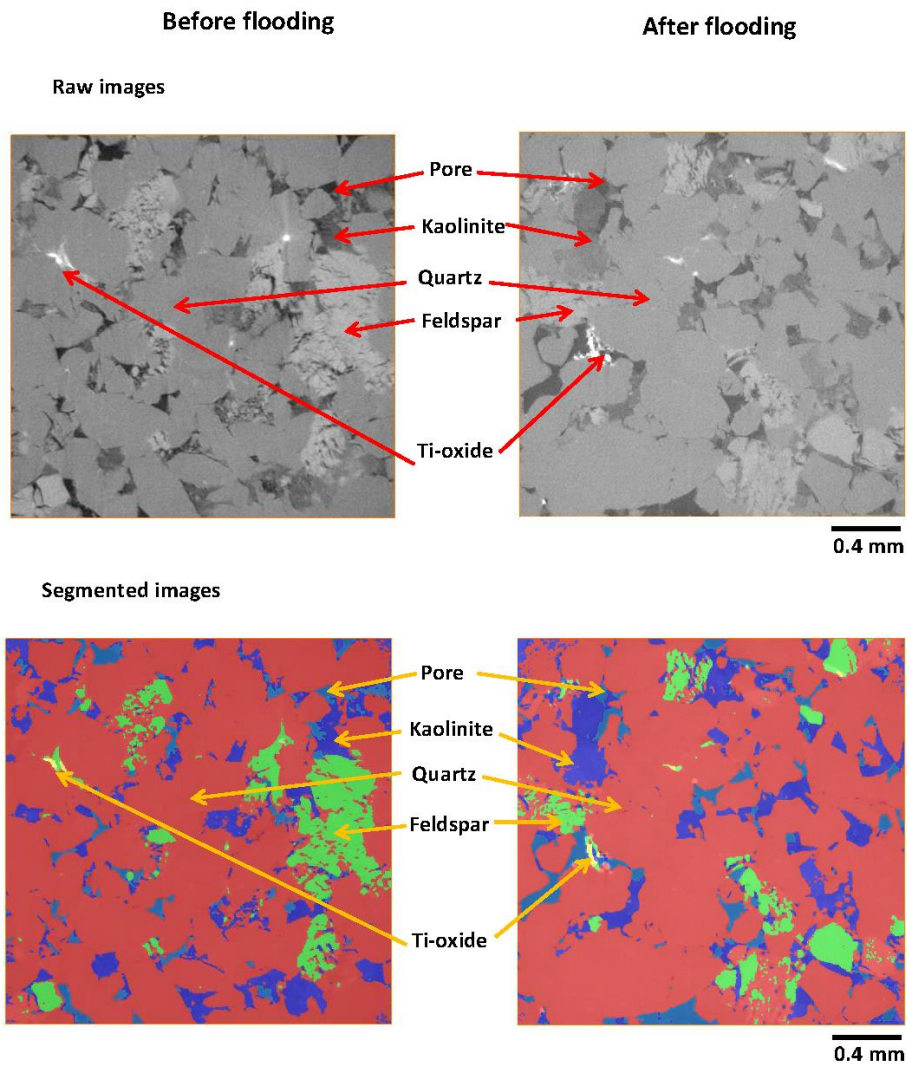


Figure 100. 2D slices through the Harvey 1 (ex-situ) rock before (left) and after (right) flooding. Raw slices are shown on the top, segmented on the bottom, the mineral and void phases are indicated.

Table 40. Physical properties of the mineral phases identified.

Phase	Greyscale*	Colour in segmented image	Mineral	Chemical composition	Density [kg/m ³]
1	Black	Light blue	Void	-	0
2	Dark grey	Dark blue	Kaolinite	Al ₂ Si ₂ O ₅ (OH) ₄	2600**
3	Medium grey	Red	Quartz	SiO ₂	2650
4	Light grey	Green	Feldspar	K/Na/Ca _{0.5} AlSi ₃ O ₈	2560-2780
5	White	Yellow	TiO ₂	TiO ₂	3780**

*corresponds to the relative radiodensity

**probably has nanoporosity and thus a lower bulk density

***Anatase

3D visualizations of the different void and mineral phases are shown in Figure 101. These 3D visualizations show that the different phases are distributed rather homogeneously, both, before and after flooding. Furthermore, pore space, TiO₂ and feldspar volume fractions decreased, this is further quantified below.

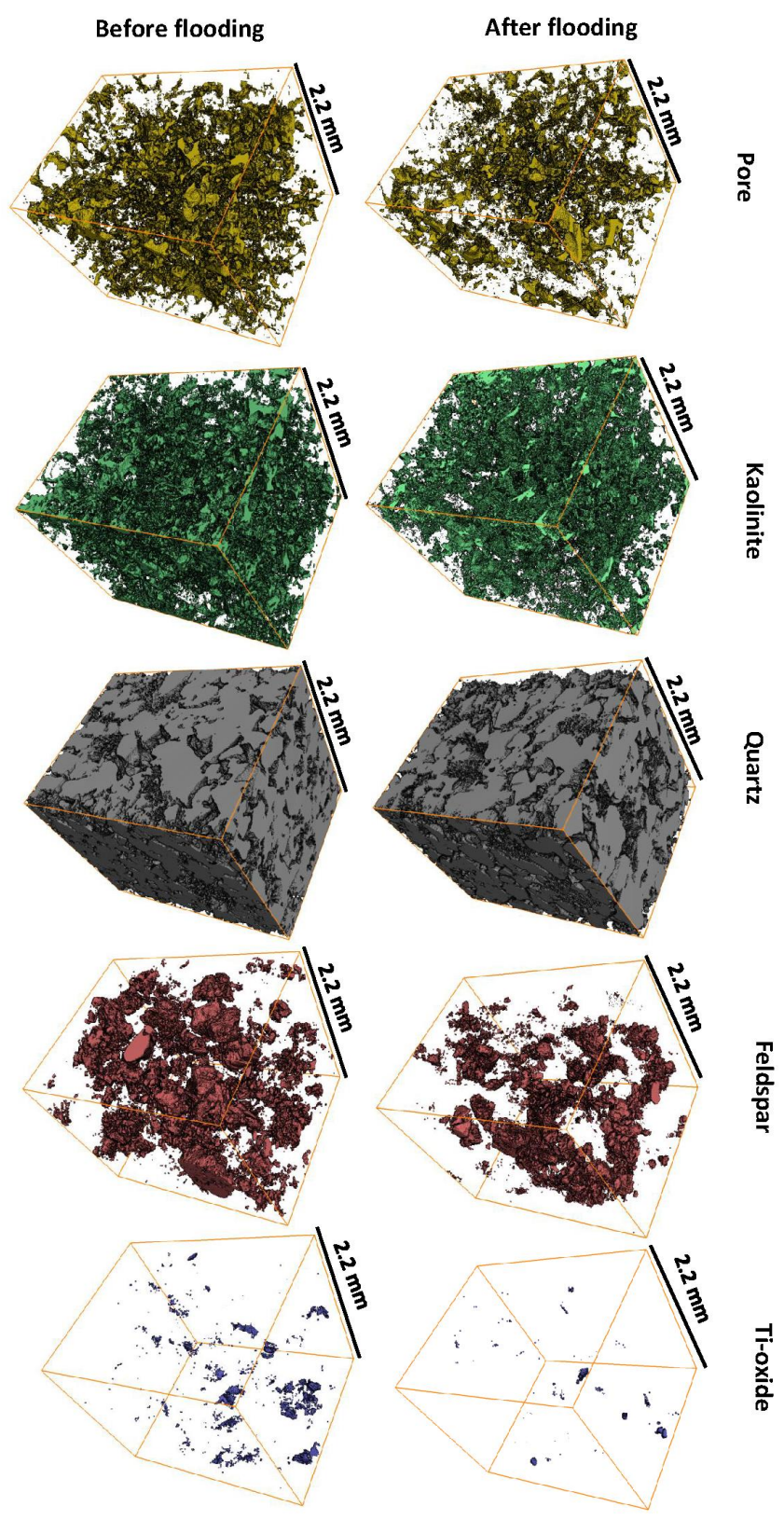


Figure 101. 3D visualizations of the different mineral and void phases for Harvey 1 (ex-situ), before (left) and after (right) flooding.

Quantitative analysis

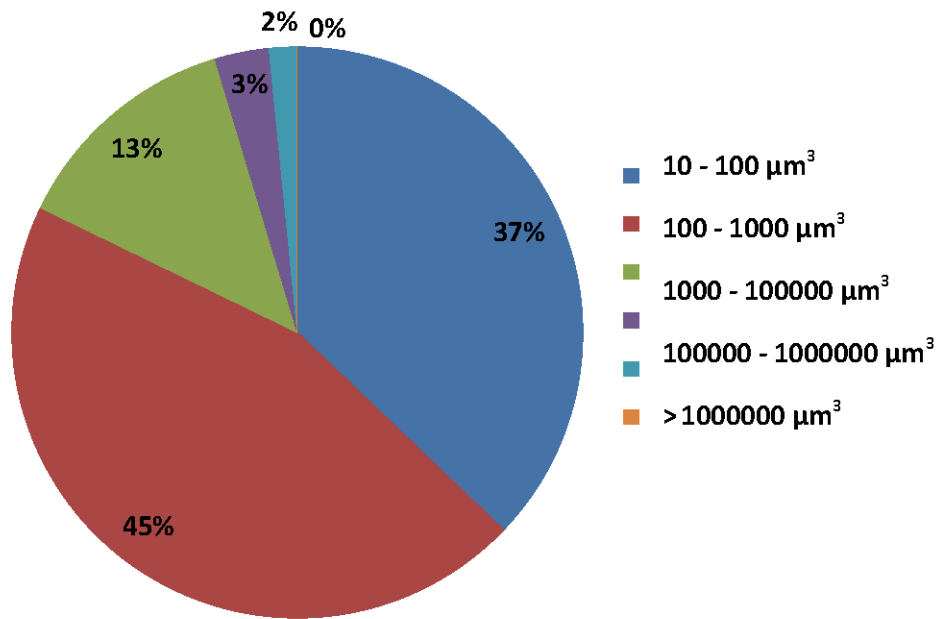
Subsequently, the volume fractions of each phase (including the void phase) were determined by counting the number of voxels of the specific phase and dividing this number by the total number of voxels, Table 41. While the quartz and kaolinite volume fractions slightly increased, the feldspar and TiO₂ volume fractions decreased slightly. These changes may be caused by the flooding, however, note that two different plugs are compared here and these changes might also be caused by natural rock heterogeneities.

Table 41. Volume fractions for segmented mineral and void phase, Harvey 1 ex-situ.

	Before flooding	After flooding
Pore	6.56 %	5.85 %
Kaolinite	10.07 %	11.26 %
Quartz	75.43 %	78.60 %
Feldspar	7.58 %	4.15 %
High density (Ti-oxide)	0.36 %	0.14 %

The pore size distributions were also measured on the microCT images (Figure 102). A clear increase in the frequency of pores with sizes smaller than 100 μm^3 was observed (an increase from 32% to 60%), while the frequency of large pores (> 1000 μm^3) decreased significantly (from 5% to 2%).

Pore size distribution for Harvey 1 ex-situ before flooding



Pore size distribution for Harvey 1 ex-situ after flooding

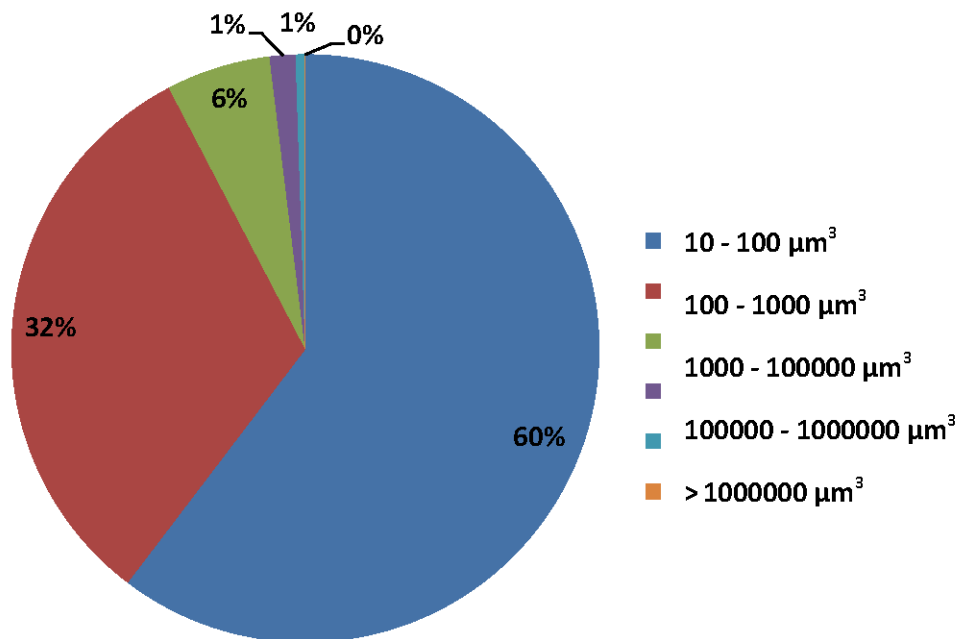


Figure 102. The pore size distribution for Harvey 1 ex-situ before (top) and after (bottom) flooding.

In-Situ coreflooding

Qualitative analysis

Again microCT images before and after live brine flooding were acquired. Figure 103 shows the core plug filled with dead brine at 10 MPa pore pressure and 15 MPa confining pressure imaged in-situ at 318 K; and Figure 104 shows the plug after flooding at 10 MPa pore pressure, 15 MPa confining pressure and 318 K imaged in-situ. The in-situ images have a significantly higher noise-to-signal ratio; however, the images are consistent with the ex-situ images shown in Figures 98 and 99.

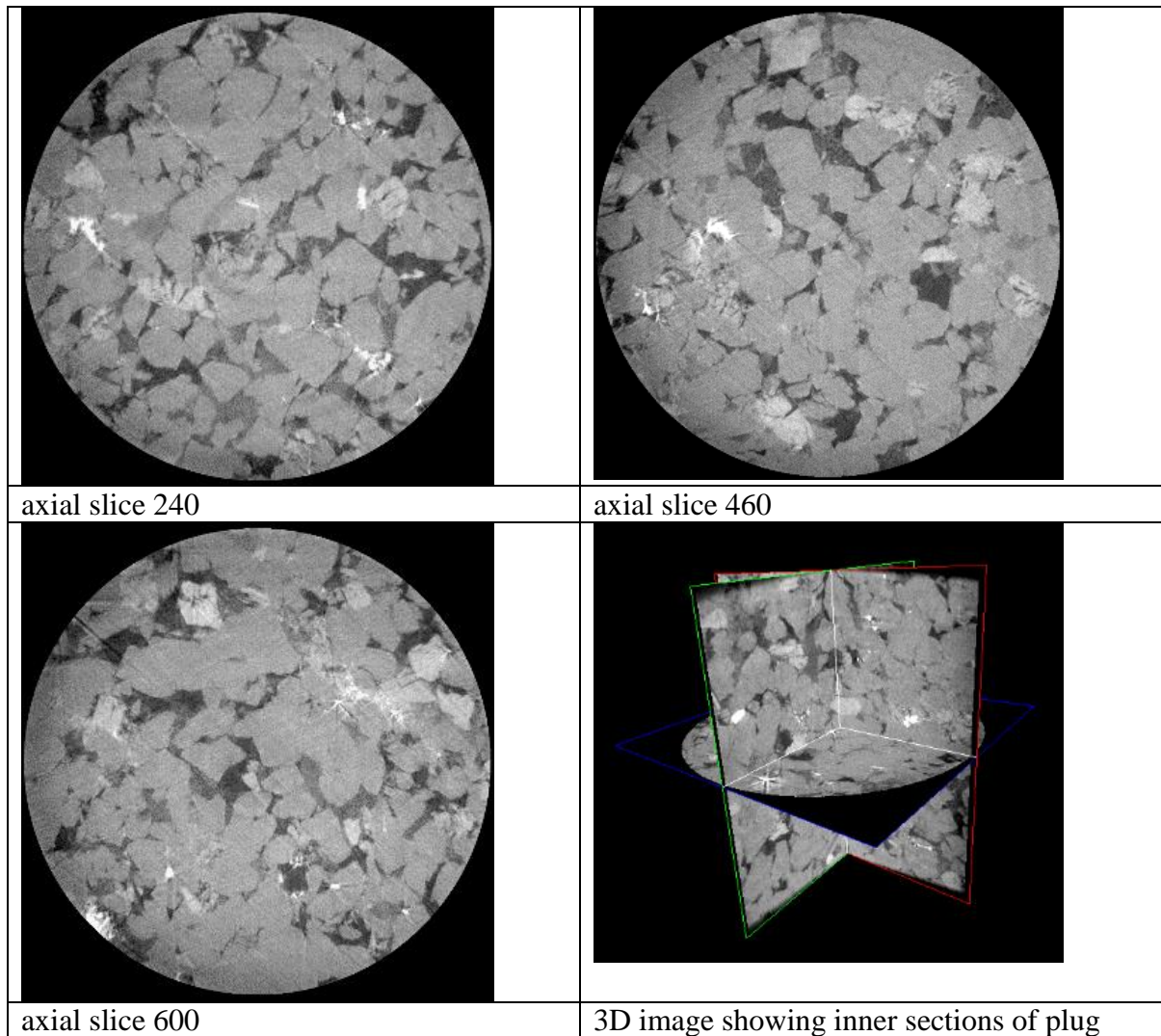


Figure 103. Selected axial slices through the pre-flood plug fully saturated with dead brine (in-situ). The diameter of the shown circles is 3.43mm.

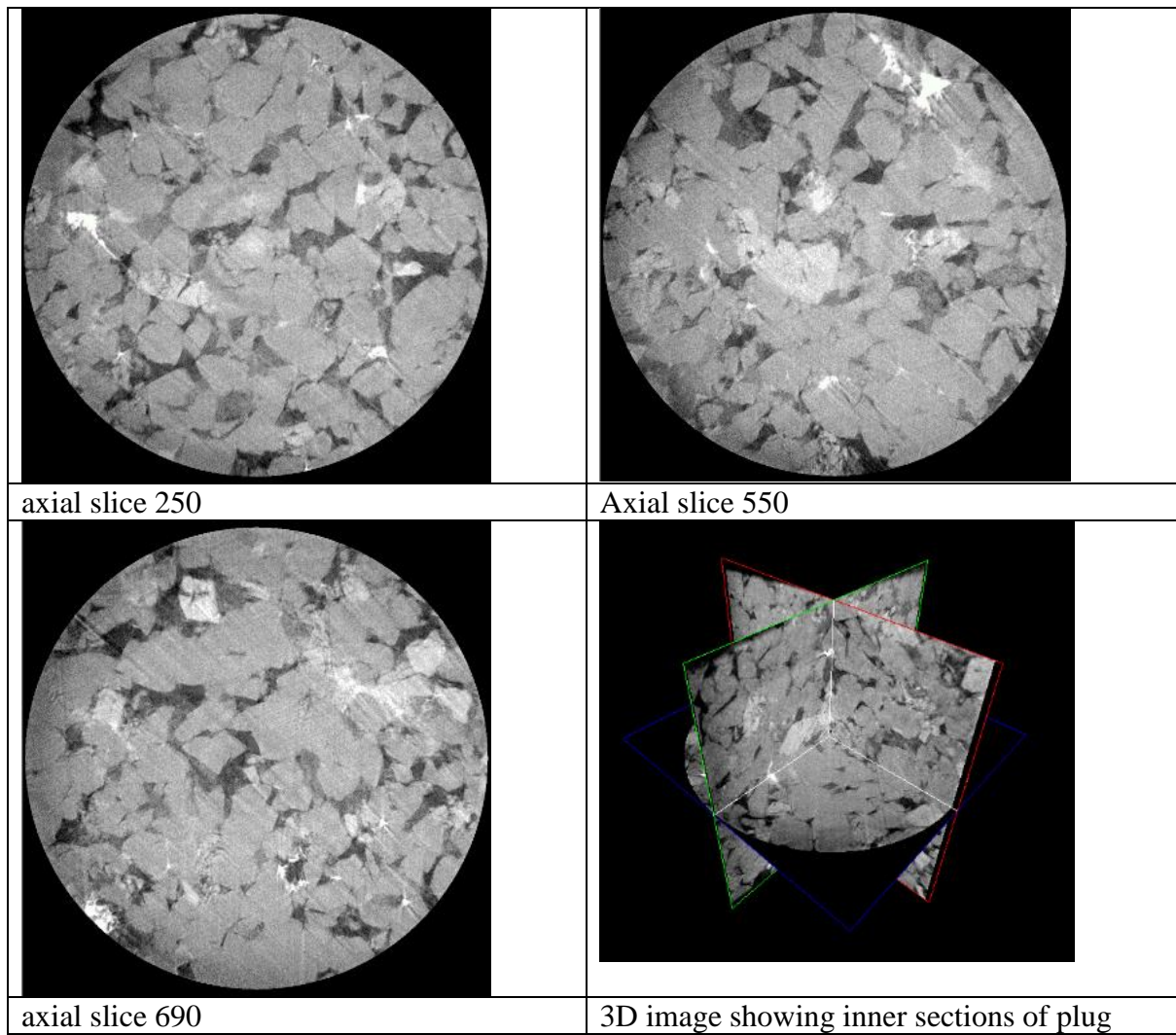


Figure 104. Selected axial slices through the plug flooded with 40 PV of live brine (in-situ). The diameter of the shown circles is 3.43mm.

The Harvey 1 in-situ images were analysed in the same way as the Harvey 1 ex-situ images, see above. The images are visualized in Figures 105 (2 D slices) and 106 (3D images). As expected mineral and void distributions are similar to those in the ex-situ plug.

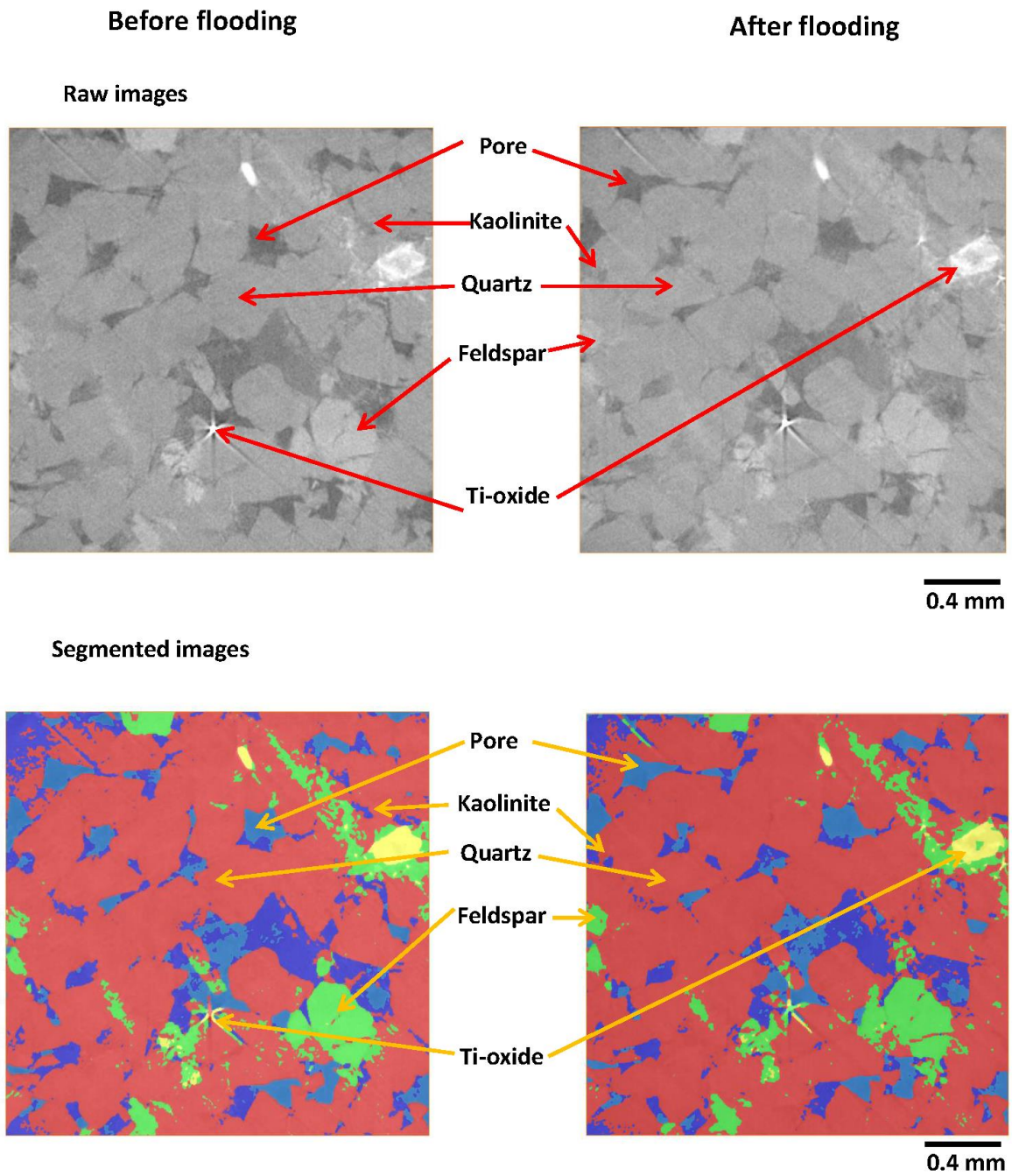


Figure 105. 2D slices through the Harvey 1 (in-situ) rock before (left) and after (right) flooding. Raw slices are shown on the top, segmented on the bottom, the mineral and void phases are indicated.

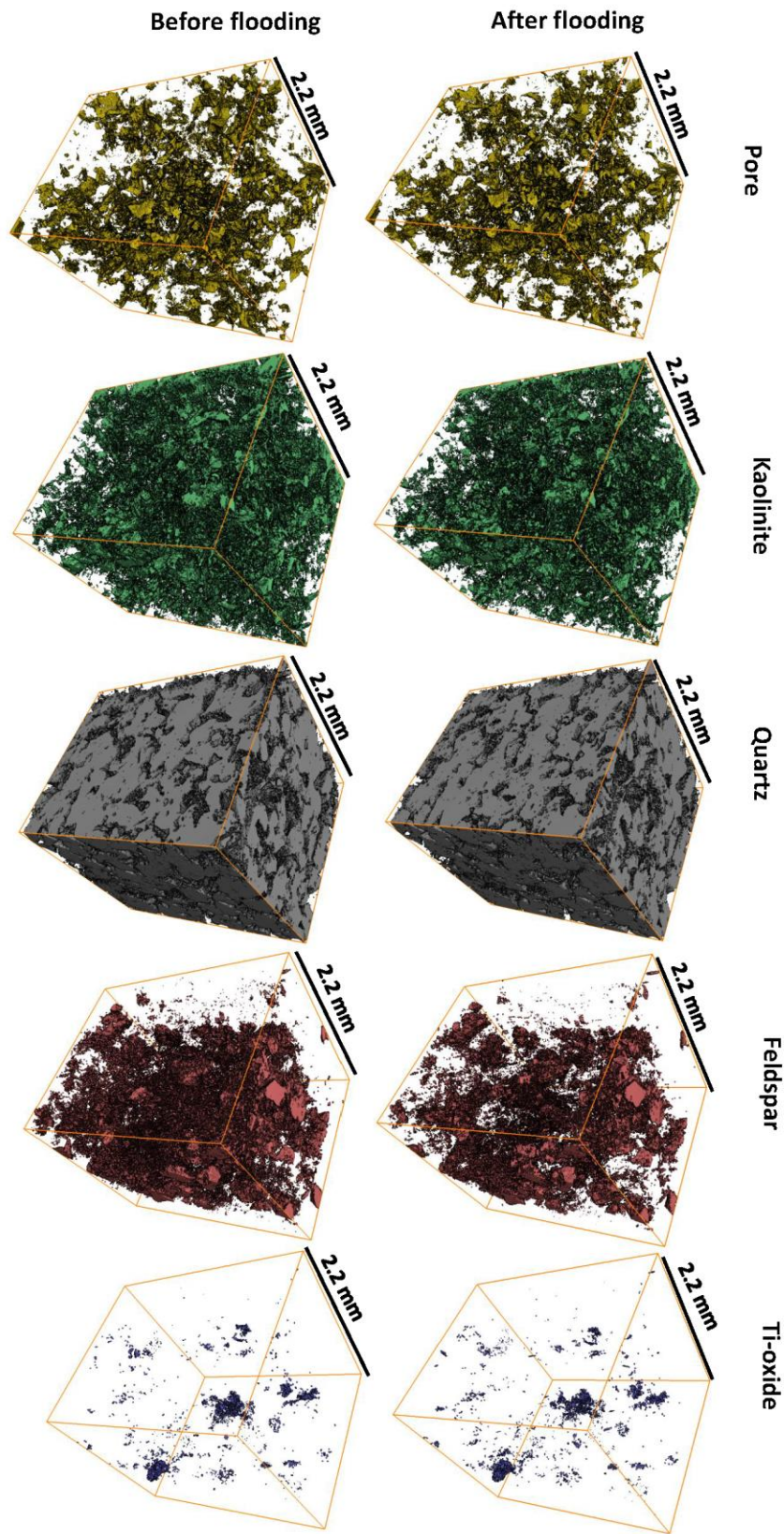


Figure 106. 3D visualizations of the different mineral and void phases for Harvey 1 (in-situ), before (left) and after (right) flooding.

Quantitative analysis

The volume fractions measured are tabulated in Table 42. Again pore space and feldspar fractions decreased, and quartz volume fraction increased, while the kaolinite fraction decreased, and TiO₂ was essentially not affected. As here the same plug was imaged these results are not convoluted by natural rock heterogeneity.

Table 42. Volume fractions for segmented mineral and void phases, Harvey 1 in-situ.

	Before flooding	After flooding
Pore	5.86 %	5.70 %
Kaolinite	12.91 %	10.75 %
Quartz	72.71 %	76.13 %
Feldspar	8.12 %	7.00 %
High density (Ti-oxide)	0.40 %	0.42%

The pore size distributions were again extracted from the 3D images (Figure 107a and b), however, they did not change significantly due to flooding. This is consistent with the coreflood results, where no change in permeability was measured.

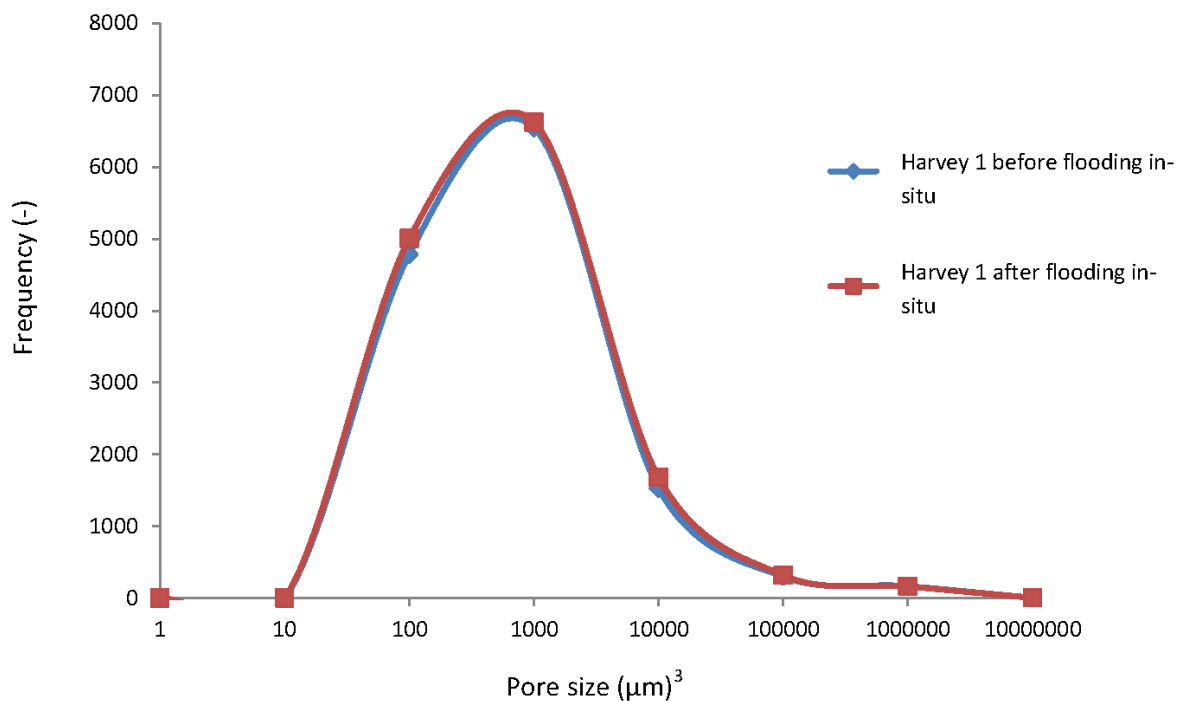
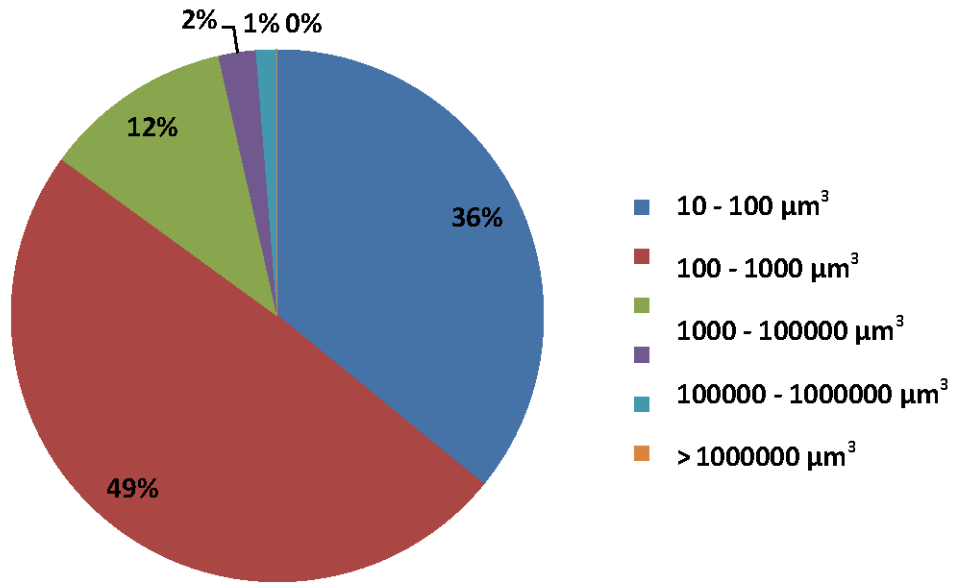


Figure 107a. The pore size distribution for Harvey 1 in-situ before and after flooding.

Pore size distribution for Harvey 1 in-situ before flooding



Pore size distribution for Harvey 1 in-situ after flooding

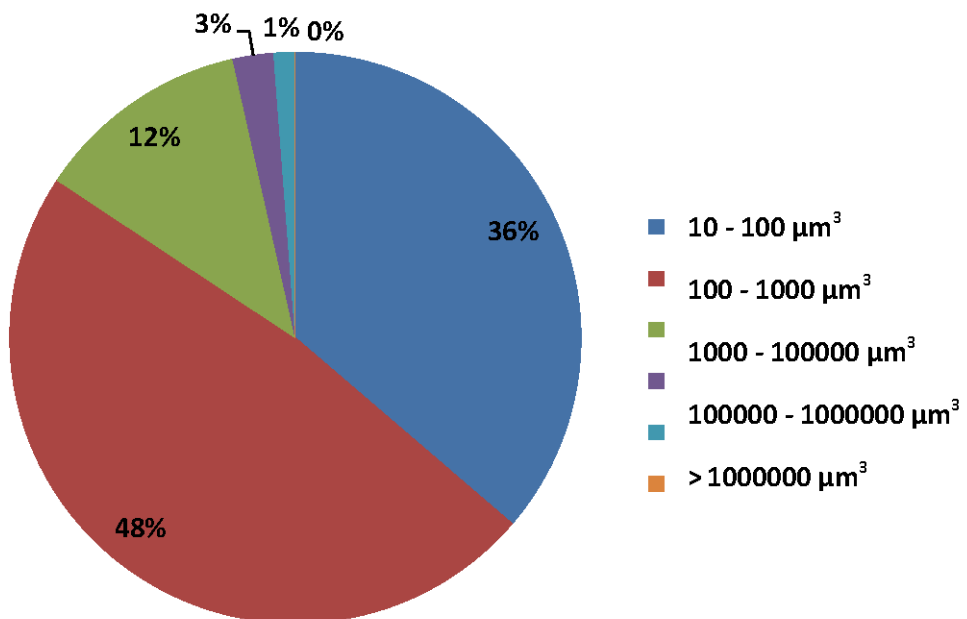


Figure 107b. The pore size distribution for Harvey 1 in-situ before (top) and after (bottom) flooding.

Conclusions

MicroCT imaging revealed that the Harvey 1 core (H1-Plug1) consists of various minerals which were homogeneously distributed in the rock material in 3D. Furthermore, the rock has a complicated pore structure with fine material located in the intergranular space. When comparing with the SEM results we conclude that this clay material is kaolinite. The porosity was relatively low (5.8% on average), and porosity decreased after flooding by 0.2% on average. Moreover, the volume fraction of feldspar decreased and the volume fraction of quartz increased. However, the kaolinite response was mixed: in the ex-situ experiment kaolinite concentration increased, while it decreased in the in-situ experiment; this mixed response is probably due to natural (slight) heterogeneities in the two different core plugs (also recall that in the ex-situ experiment two different core plugs were used). This natural heterogeneity and associated clay distribution is probably also responsible for the fact that a clear change in pore size distribution was measured in the ex-situ plug (probably caused by rock heterogeneity), while no change was observed in the in-situ plug. This result is consistent with the coreflood experiment, where no change in permeability was measured.

Harvey-4 Samples

Experimental procedure

Ex-situ imaging

In a similar fashion to the core samples prepared from Harvey-1 plug, two small cylindrical micro-plugs (length 10mm, diameter 5mm) were drilled from H4-Plug4 (Figure 108). One of the micro-plugs was cut from an off-cut piece of this core plug and was imaged in a dry state with the micro-computed tomograph at high resolution ($3.43 \mu\text{m}$)³ in 3D. This would provide information about the state of this core plug before being flooded.

After flooding H4-Plug 4, a second micro-plug was cut from it to undergo the micro-CT imaging. This second micro-plug was drilled from a flooded segment of this core plug and as close as possible to the location of the first micro-plug imaged before (Figure 108).



Figure 108. Schematic of the 2nd Harvey-4 sample assembly showing the location of the micro-CT samples.

In-situ imaging

Similar to the procedure for Harvey-1, a third small core plug (length 10 mm, diameter 5 mm) was drilled from an offcut piece of H4-Plug 4 and mounted into an X-ray transparent cell (Figure 97b). The micro core plug was then subjected to 15 MPa confining stress, and the whole flow system was vacuumed for 24 hours. The system was subsequently flooded with dead (not CO₂ saturated) brine at a Darcy flow rate of 7.3×10^{-6} m/s, so that the plug was fully saturated with dead brine. Subsequently

the whole flow system was heated isothermally to 45°C, and once the desired temperature was reached the pore fluid pressure was increased to 10 MPa. The plug was then micro-CT imaged in-situ fully saturated with dead brine at a high resolution of $(3.43 \mu\text{m})^3$. Finally 40 PV of live (CO₂-saturated) brine were pumped through the core plug at a Darcy flow rate of 7.3×10^{-6} m/s, and the plug was imaged again in-situ after flooding at a high resolution of $(3.43 \mu\text{m})^3$.

Experimental Results

Ex-situ imaging

Qualitative analysis

Selected axial slices through the plugs are shown in Figures 109 (before flooding) and 110 (after flooding). The pore structure is clearly complicated and pores are partially filled with fine material. Furthermore, a range of CT numbers can be identified which indicates that the core consists of several different minerals, consistent with the SEM-EDS measurements. Figures 111 (2D) and 112 (3D) visualize the different minerals (kaolinite = dark blue, quartz = red, feldspar = green, TiO₂ = yellow) and void space (light blue). Again, as in the Harvey 1 plugs, these phases were rather homogeneously distributed in 3D.

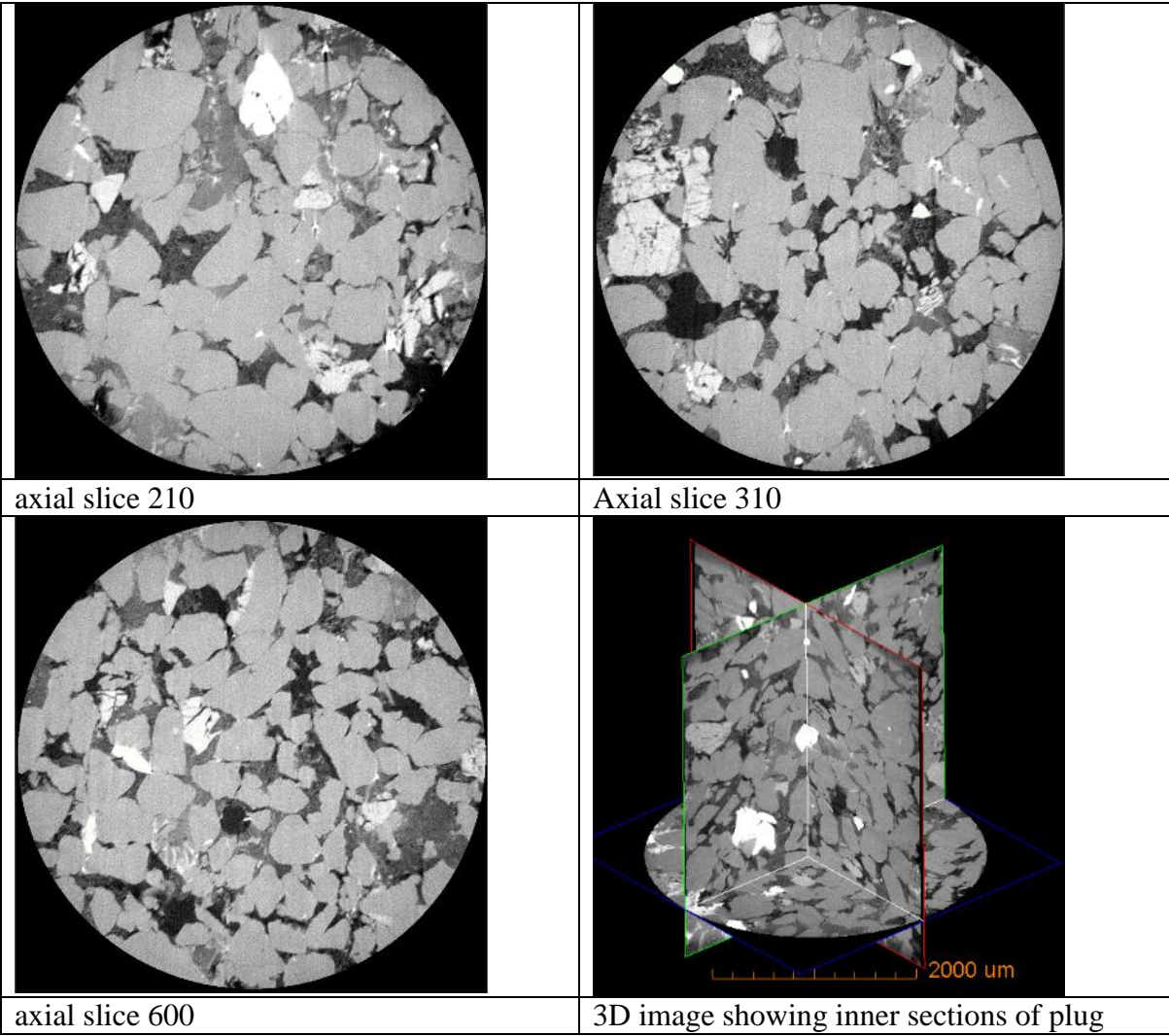


Figure 109. Selected axial slices through the non-flooded Harvey-4 plug (ex-situ). The diameter of the shown circles is 3.43mm.

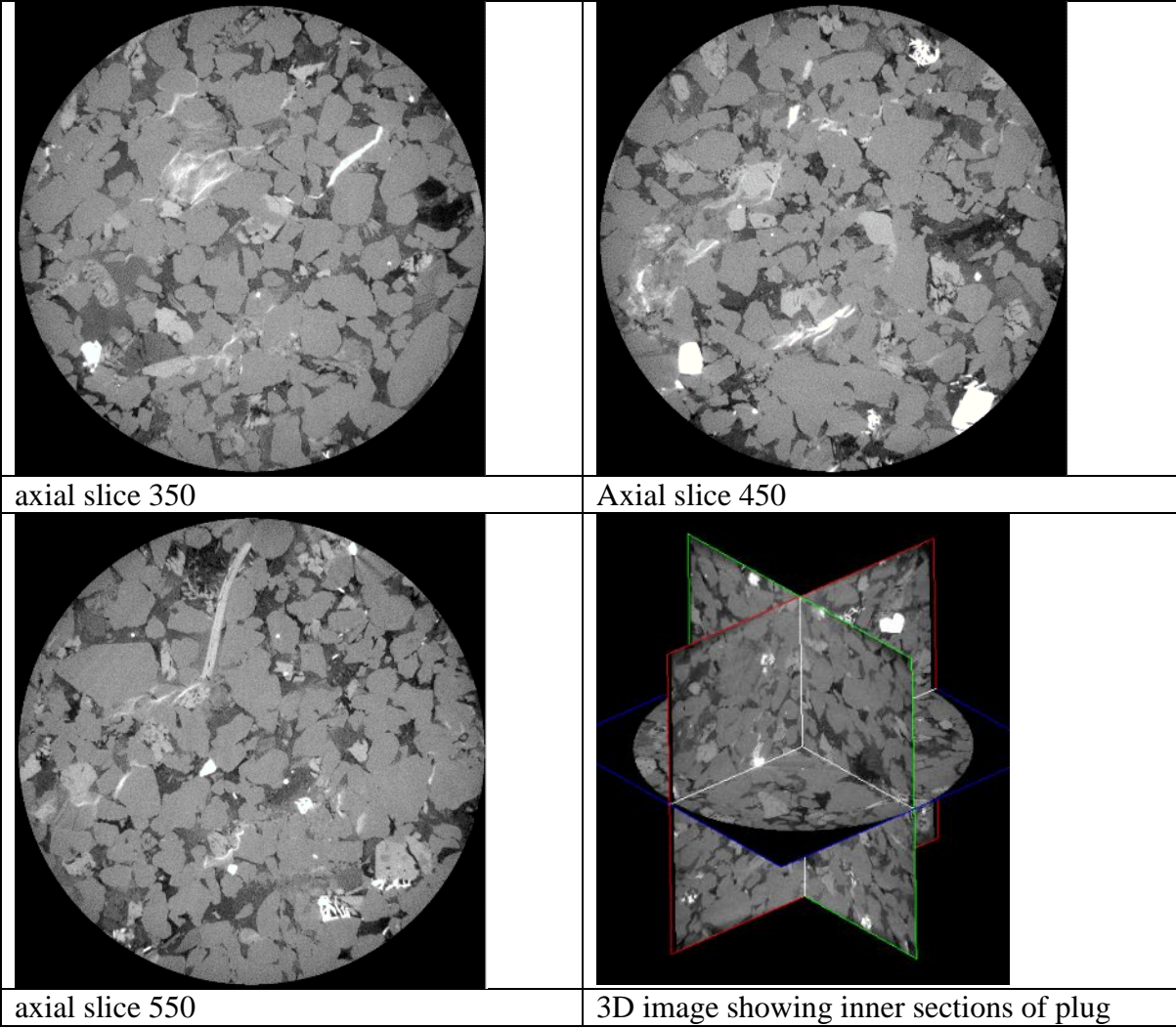


Figure 110. Selected axial slices through the Harvey 4 plug flooded with live brine (ex-situ). The diameter of the shown circles is 3.43mm.

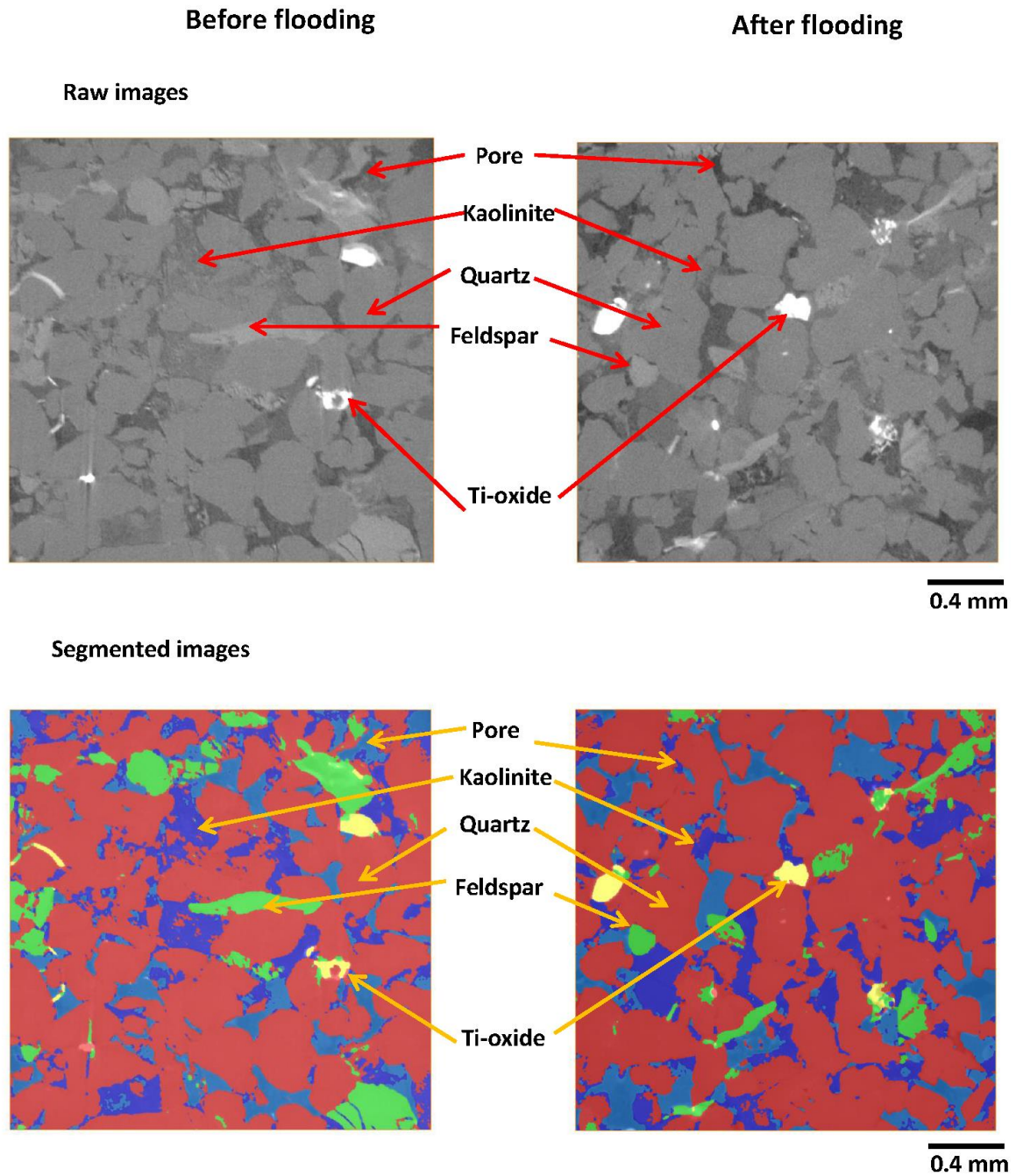


Figure 111. 2D slices through the Harvey 4 (ex-situ) rock before (left) and after (right) flooding. Raw slices are shown on the top, segmented on the bottom, the mineral and void phases are indicated.

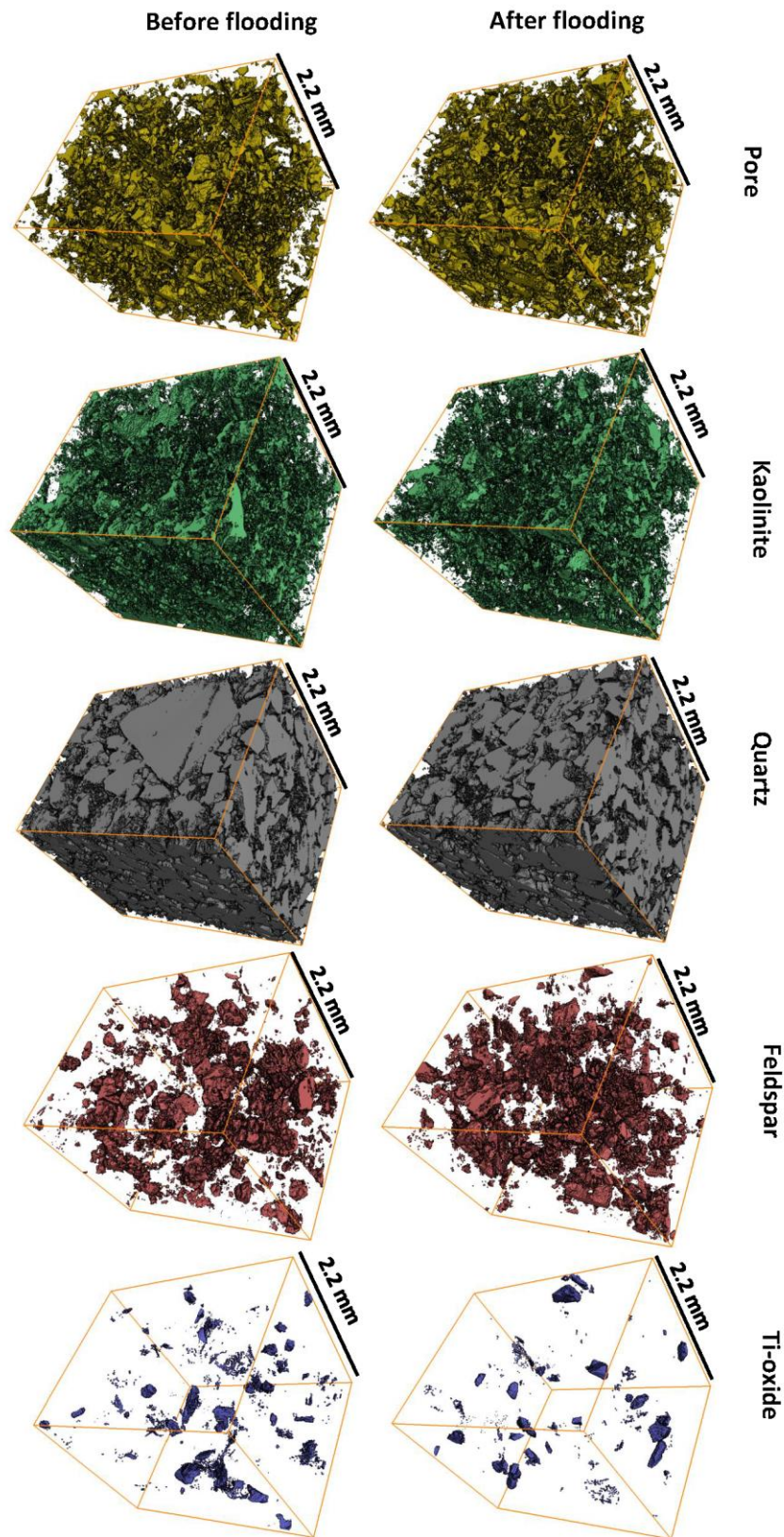


Figure 112. 3D visualizations of the different mineral and void phases for Harvey 4 (ex-situ), before (left) and after (right) flooding.

Quantitative analysis

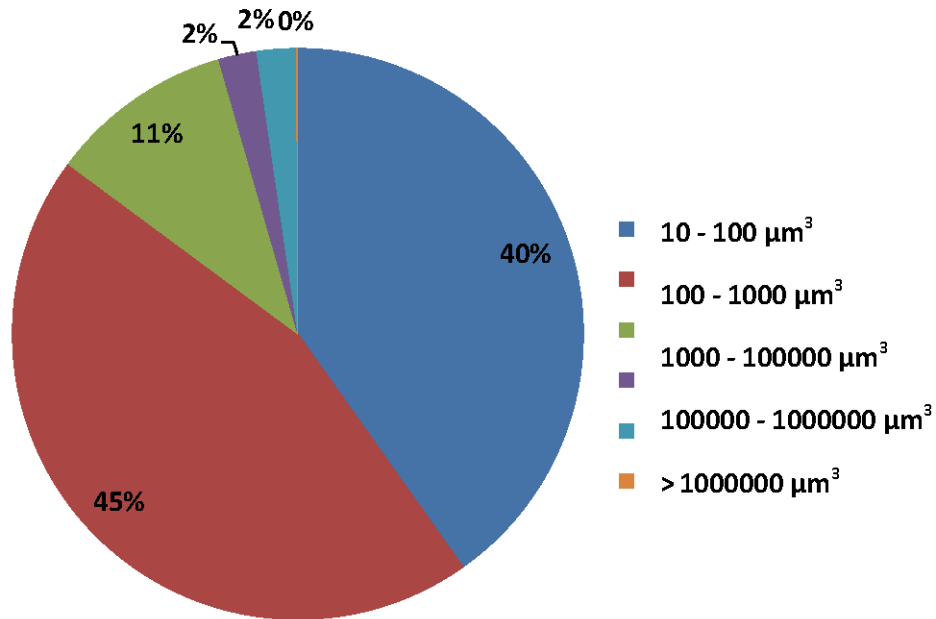
The volume fractions measured are tabulated in Table 43. Now porosity and feldspar volume fractions increased, while kaolinite, quartz and TiO₂ concentrations decreased. These differences are caused by flooding and/or natural rock heterogeneity.

Table 43. Volume fractions for segmented mineral and void phases, Harvey 4 ex-situ.

	Before flooding	After flooding
Pore	12.93 %	15.62 %
Kaolinite	14.46 %	11.60 %
Quartz	66.62 %	65.90 %
Feldspar	4.86 %	6.06 %
High density (Ti-oxide)	1.13 %	0.82 %

Furthermore, the pore size distribution changed significantly (Figure 113): the frequency of small pores increased significantly, while the frequency of large pores significantly decreased. Again this difference is caused by live brine flooding and/or natural rock heterogeneity.

Pore size distribution for Harvey 4 ex-situ before flooding



Pore size distribution for Harvey 4 ex-situ after flooding

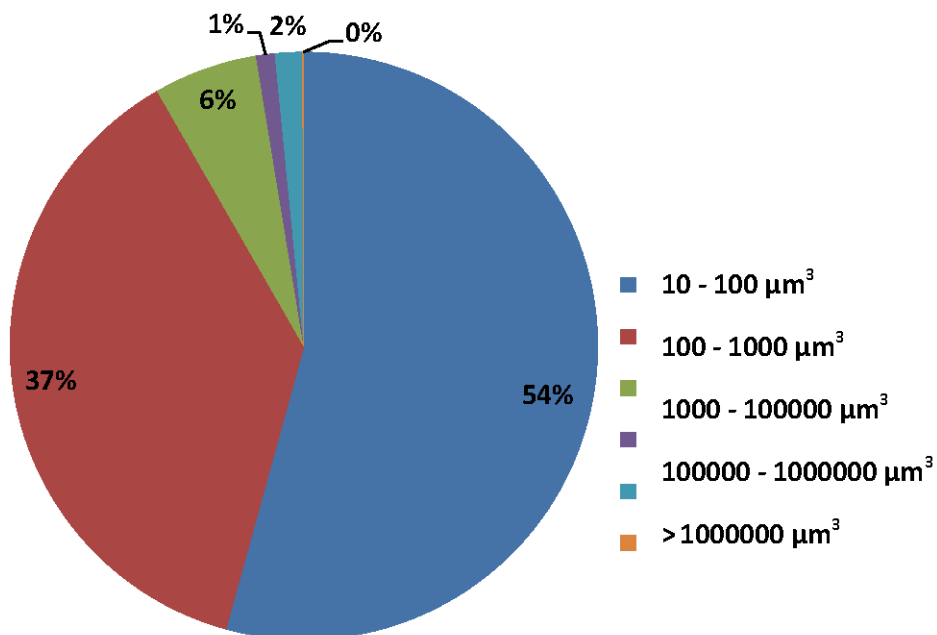


Figure 113. The pore size distribution for Harvey 4 ex-situ before (top) and after (bottom) flooding.

In-situ imaging

Qualitative analysis

Again microCT images before and after live brine flooding were acquired. Figure 114 shows the core plug filled with dead brine at 10 MPa pore pressure and 15 MPa confining pressure imaged in-situ. The in-situ image has a significantly higher noise-to-signal ratio; however, the image is consistent with the ex-situ image shown in Figure 109. Also the image of the plug, which was flooded with live brine (Figure 115), is consistent with the image shown above in Figure 110 for the ex-situ live brine flood. Figures 116 (2D) and 117 (3D) again visualize the spatial positions of the different void (light blue) and mineral (kaolinite = dark blue, quartz = red, feldspar = green, TiO₂ = yellow) phases. The minerals were again rather homogeneously distributed in 3D, before and after flooding with live brine.

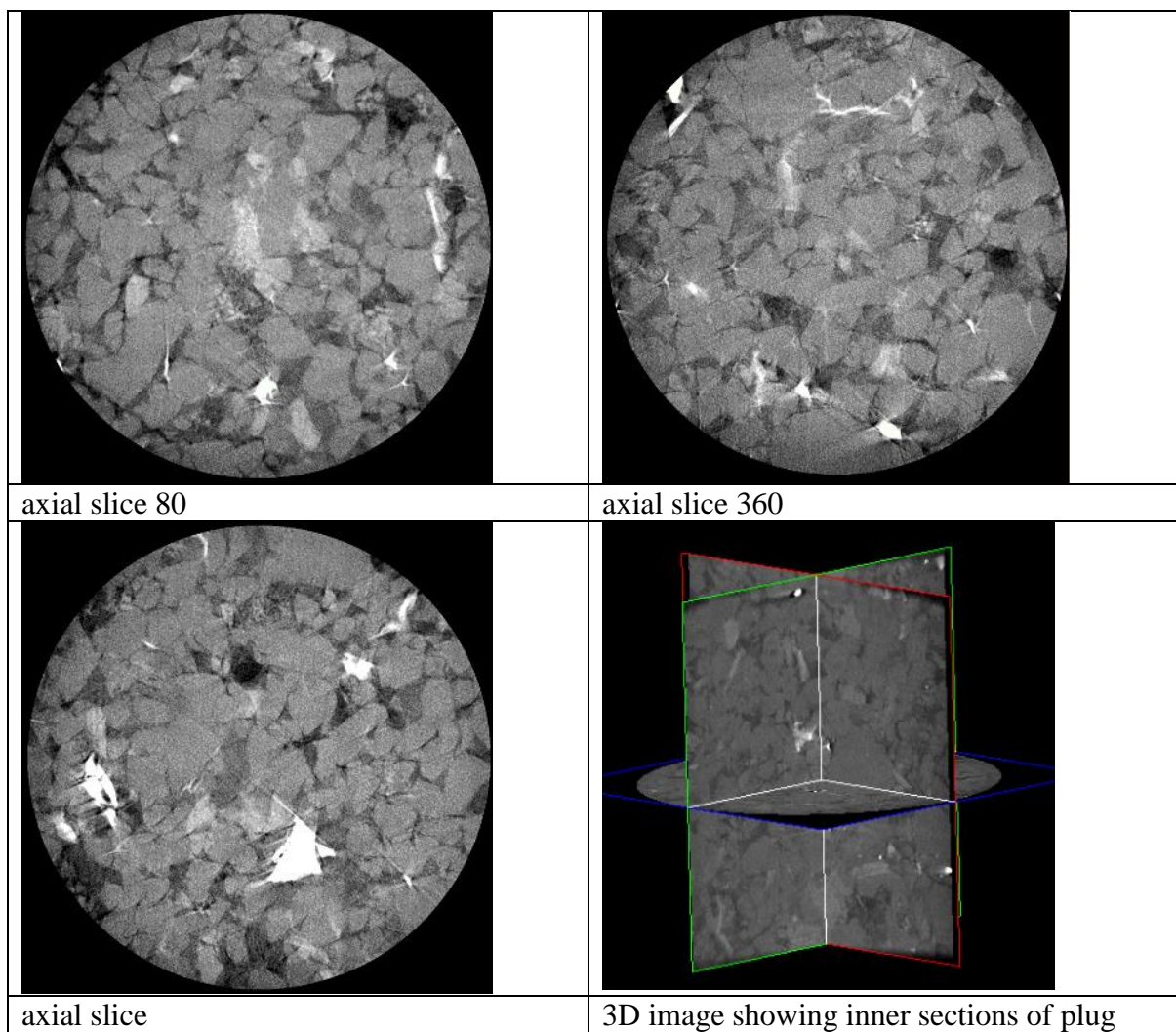


Figure 114. Selected axial slices through the Harvey-4 plug fully saturated with dead brine (in-situ). The diameter of the shown circles is 3.43mm.

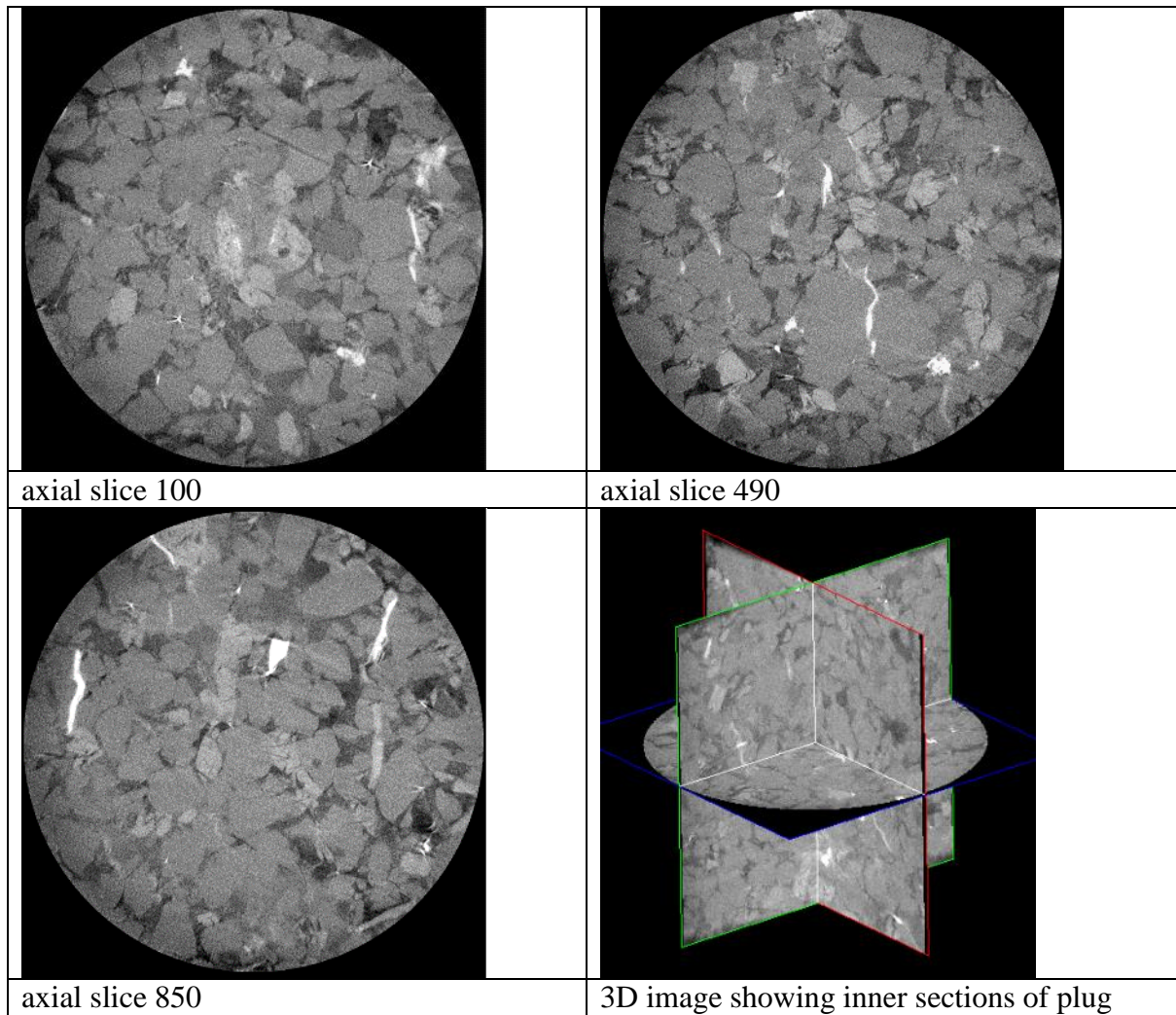


Figure 115. Selected axial slices through the Harvey-4 plug flooded with 40 PV of live brine (in-situ). The diameter of the shown circles is 3.43mm.

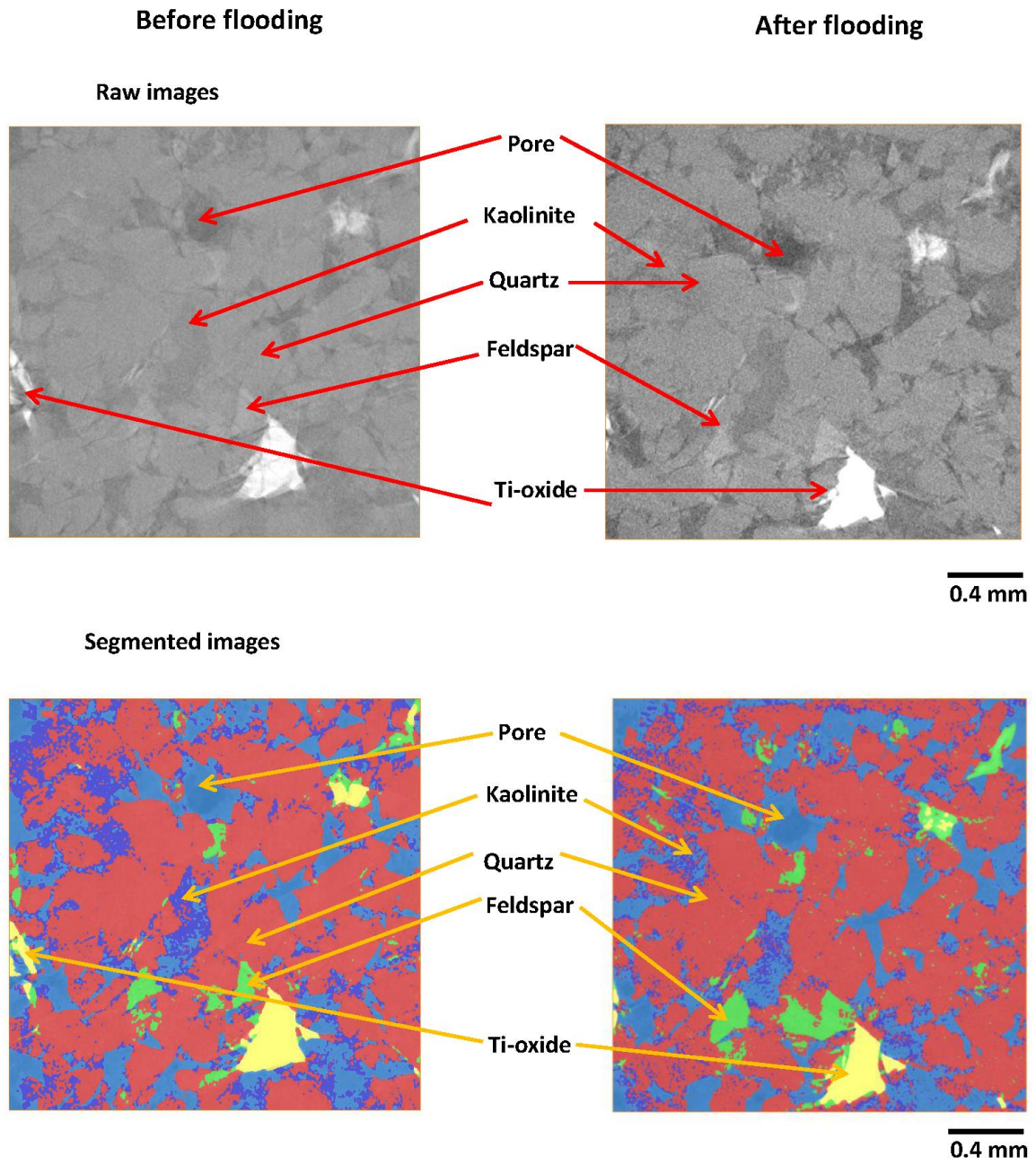


Figure 116. 2D slices through the Harvey 4 (in-situ) rock before (left) and after (right) flooding. Raw slices are shown on the top, segmented on the bottom, the mineral and void phases are indicated.

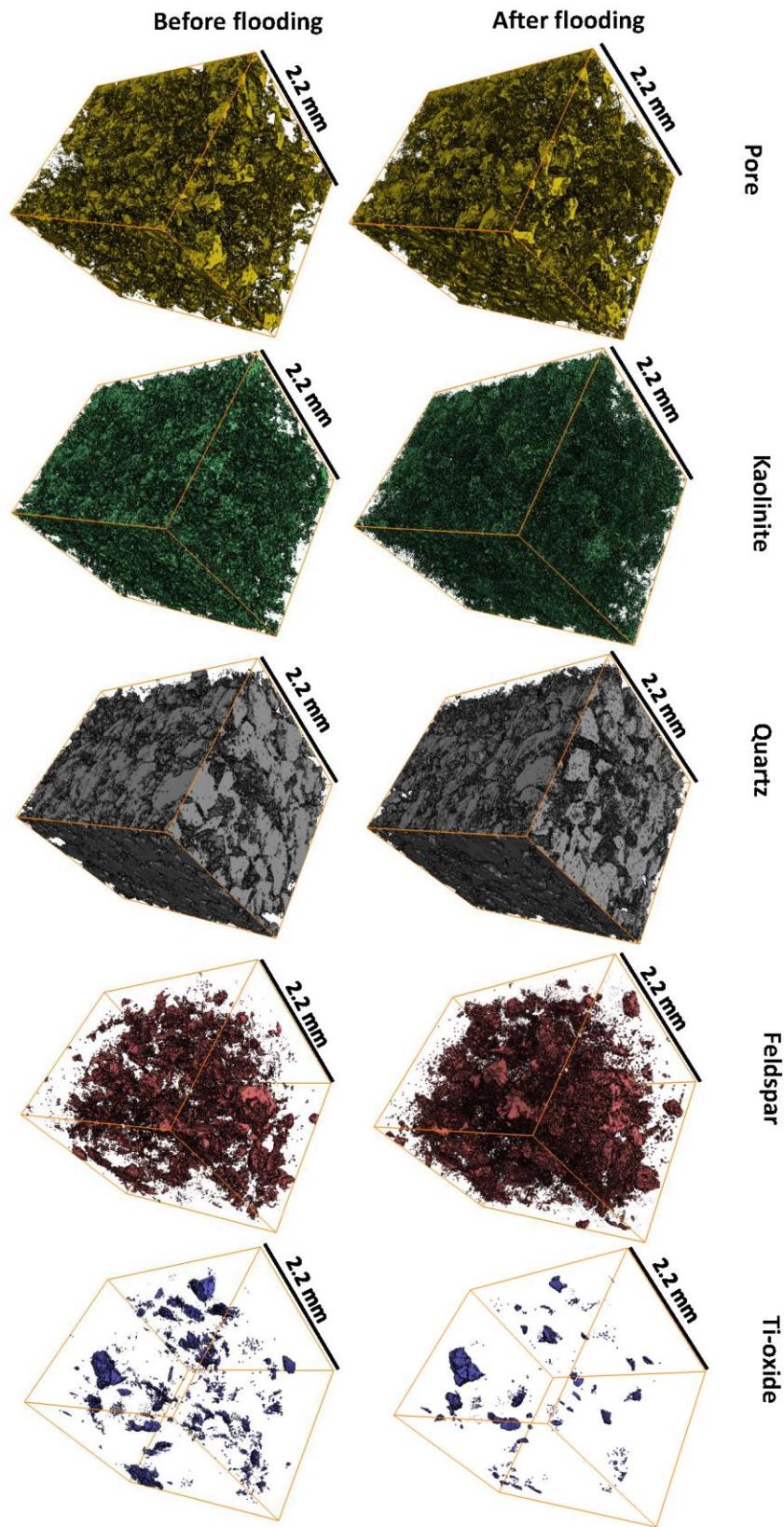


Figure 117. 3D visualizations of the different mineral and void phases for Harvey 4 (in-situ), before (left) and after (right) flooding.

Quantitative analysis

The volume fractions measured are tabulated in Table 44. Porosity and feldspar volume fractions increased, while kaolinite and quartz concentrations decreased.

Table 44. Volume fractions for segmented mineral and void phase, Harvey 4 in-situ.

	Before flooding	After flooding
Pore	9.81 %	11.86 %
Kaolinite	10.92 %	8.89 %
Quartz	72.52 %	71.05 %
Feldspar	5.84 %	7.44 %
High density (Ti-oxide)	0.91 %	0.76%

The pore size distribution also changed markedly, Figure 118a and b. The number of pores increased dramatically due to flooding, consistent with the increased porosity. As in this in-situ experiment this result is not convoluted with natural sample heterogeneity we conclude that this is a significant change.

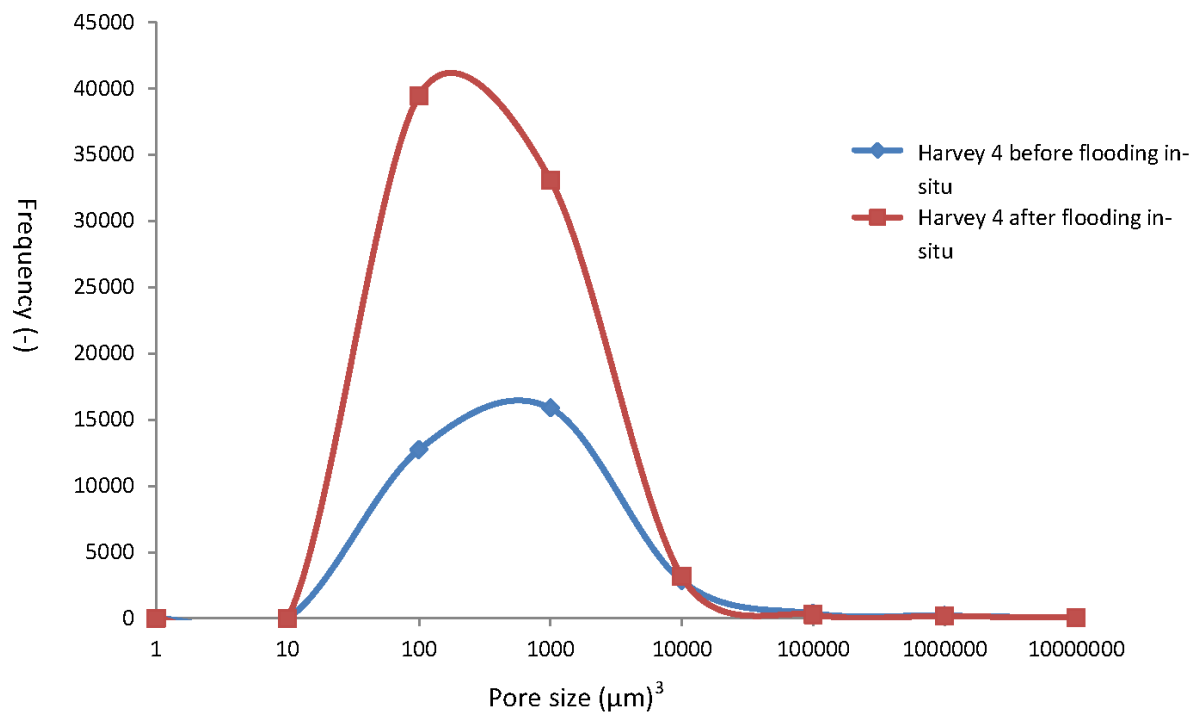
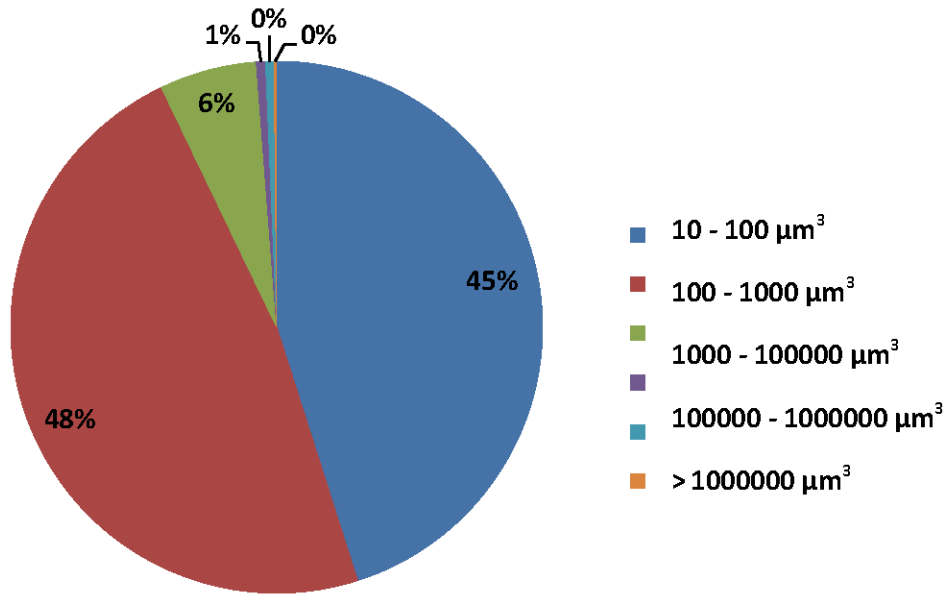


Figure 118a. The pore size distribution for Harvey 4 in-situ before and after live brine flooding.

Pore size distribution for Harvey 4 in-situ before flooding



Pore size distribution for Harvey 4 in-situ after flooding

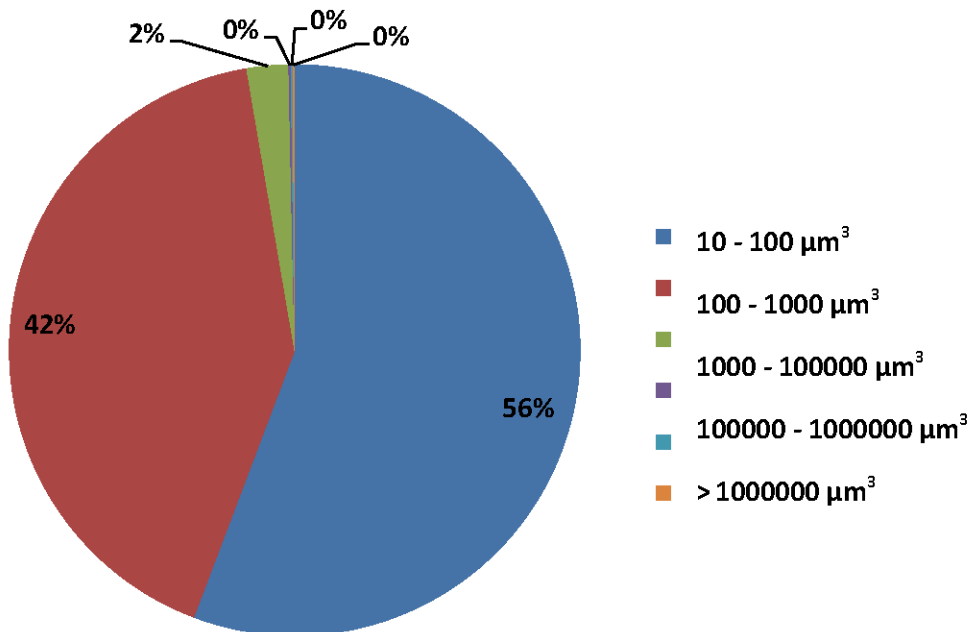


Figure 118b. The pore size distribution for Harvey 4 in-situ before (top) and after (bottom) live brine flooding.

Conclusions

MicroCT imaging revealed that the Harvey 4 core (H4-Plug4) consists of various minerals which were homogeneously distributed in the rock material in 3D. Furthermore, the rock has a complicated pore structure with fine material located in the intergranular space. When comparing with the SEM results we conclude that this clay material is kaolinite. The porosity increased significantly from 9.8% to 11.9% (in-situ test) after flooding. Moreover, the volume fractions of kaolinite and quartz decreased, while the feldspar volume fraction increased.

Furthermore, the pore size distribution changed significantly: while the number of small pores increased after flooding, the number of the largest pores decreased substantially, to the extent that all pores larger than $1000 \mu\text{m}^3$ were closed in the in-situ experiment. This is even evident in the ex-situ test which is convoluted by natural rock heterogeneity (as two different plugs were used); and this is consistent with the corefloods where a permeability decrease was measured, as the largest pores essentially determine the permeability (Dullien 1992).

Overall Conclusions

MicroCT imaging revealed that the Harvey 1 (H1-Plug1) and Harvey 4 (H4-Plug4) cores consist of various minerals (quartz, kaolinite, feldspar, TiO_2 as identified by comparing with the SEM-EDS results), homogeneously distributed in 3D space. Both cores had a complicated pore structure with fine material located in the intergranular space, which was identified as kaolinite when comparing with the SEM-EDS results. In addition, the pore size distributions and porosities of the plugs were measured via microCT before and after live brine flooding.

The response to live brine flooding was different: while the pore size distribution of the Harvey 1 plug did not change significantly, it did change significantly in the Harvey 4 plug. Consistent with this is a significant increase in porosity in the Harvey 4 plug, while porosity did not change significantly in the Harvey 1 plug. After flooding more small pores were counted in the Harvey 4 plug, while the number of large pores decreased dramatically, and all pores larger than $1000 \mu\text{m}^3$ disappeared in the in-situ test. This is consistent with the coreflood experiments where a permeability decrease was observed for the Harvey 4 plug, but not the Harvey 1 plug.

We conclude that only in-situ tests should be used as otherwise natural rock heterogeneity (which is significant in the Harvey rock) significantly convolutes the response of live brine flooding.

Overall we conclude that the Harvey rock material has a tendency to reduce its permeability when flooded by live brine due to the closure of the largest pores.

Section 7: Summary, Conclusions and Recommendations

Contributors

Dr. Ali Saeedi

Dr. Claudio Delle Piane

Dr. Lionel Esteban

Dr. Ryan Noble

Dr. David Gray

Dr. Stefan Iglauer

Dr. Maxim Lebedev

Dr. Linda Stalker

This project was defined to address some of the uncertainties identified by the previously completed research (Projects 7-1111-0199 (Delle Piane et al., 2013), 7-1111-0200 (Stalker et al., 2013) and 3-1110-0122 (Evans et al., 2013)) about the in-situ fluid-rock interactions at the SW Hub CO₂ storage site. In the previous projects, a number of samples from well Harvey-1 were flooded to reveal that the permeabilities of the post-flood samples were significantly less than their original pre-flood values. Such changes, if they were to occur in the field, could have serious implications for the required level of injectivity in the injection wells at the SW Hub site. While based on the limited evidence available at the time, some speculation was made about the root cause of such changes, there was an increasing need to do a more thorough work and reduce the uncertainty imposed on the real achievable well injectivities. There was a need also realised to identify and characterise the fluid-rock geochemical reactions which may occur at the in-situ conditions in the SW Hub. Previously, only one rock sample had been tested from Harvey-1 for geochemical reactions and, moreover, the core-flood procedure used to do that single experiment had a number of critical deficiencies.

In order to achieve the objectives set, the current work has employed a purpose-designed workflow built upon the previous experiences. Such a workflow included six steps as outlined below:

- I. Core sample collection and preparation: this involved cutting 38 mm (1.5") diameter core plugs and core discs from the available whole-cores followed by trimming and polishing the relevant surfaces. The order for subsampling and analyses were developed to obtain relevant information before and after flooding to maximise data acquisition.
- II. Petrophysical evaluation: an extensive list of petrophysical measurements were conducted on the rock samples including porosity and permeability measurements, NMR spectrometry, Medical X-ray CT imaging, and electro-acoustic measurements both before and after flooding
- III. Microstructural analysis: a detailed microstructural study was performed on the core samples using a specially designed SEM (Scanning Electron Microscopy) imaging and data analysis technique before and after flooding.
- IV. Core-flooding: the samples underwent a specially designed core-flood procedure which makes it possible to collect fluid samples continuously throughout the duration of the experiment. Furthermore, three "blank" experiments were also conducted to quantify the background contamination of the experimental equipment. A known material (Berea Sandstone) was also analysed by the same procedure for comparative purposes.
- V. Geochemical evaluation: the fluid eluent collected during the core-flood experiments were chemically analysed to evaluate the chemical reactions which had occurred between the rock and fluid during the core-flood experiments. In addition, static, thermodynamic modelling was used to simulate the fluid-rock geochemical interactions under in-situ conditions to determine differences if observed.
- VI. Steps II and III were repeated on the rock samples after the core-flood experiments.

The rock samples tested in this work came from wells Harvey-1, Harvey-3 and Harvey-4 as these are the three wells drilled into the primary injection/storage area of the SW Hub. Also, the samples all belonged to the Wonneurp Member. The Wonneurp is considered to be the main injection/storage interval in the SW Hub.

The earlier outlined workflow and the analysis techniques all were found to be very effective in achieving the objectives of this work. In the first phase of the study, the new samples tested from well Harvey-1, all showed reductions in their post-flood permeabilities, no appreciable change in their post-flood porosities and shift in their NMR T2 spectra, consistent with the observations made previously for similar samples. However, this time, reliable evidence could be generated from the petrophysical and microstructural studies to confirm that fines migration is responsible for the majority of the observed petrophysical alterations of the rock after flooding.

In the second phase of the work, two core plugs from well Harvey-3 were prepared and tested using the same workflow as above. However, some major discrepancies were observed between the results obtained from Harvey-1 and Harvey-3 samples. The post-flood Harvey-3 samples showed significant improvement to their permeability despite the fact that they had come from the same formation. The analysis of the X-ray CT images also revealed some differences between the post-flood samples from Harvey-3 and those belonging to Harvey-1. However, the above observed discrepancies were explained once the microstructural images generated using the SEM analysis for the pre- and post-flood samples were compared. The images revealed extensive removal of clay particles from the major flow paths inside the samples resulting in enhanced pore connectivity and hence the improved overall sample permeability.

The last stage of the project used four core samples from well Harvey-4 for the planned experimental work. The results from these samples indicated a behaviour somewhat in between that observed from Harvey-1 and Harvey-3 samples. Some Harvey-4 samples showed slight enhancement to their permeability while others showed some reduction and the rest did not reveal appreciable changes. The SEM images generated for the Harvey-4 samples indicated a combination of what was observed in Harvey-1 and Harvey-3.

The difference in the responses of the three sets of samples to the flooding process may find support in the nature of the samples and their diagenetic features. The rock samples from Harvey-1 were consolidated and well cemented while most of the samples from the other two wells were friable and weakly cemented. Such differences between the three sample sets is believed to have influenced their transport properties. For example, while in Harvey-3 samples the clay fines were mobilised in a manner similar to Harvey-1 samples, this time around the fines were flushed out of the samples due to their special pore structure dictated by their degree of cementation. Overall, the diagenetic factors seem to control the fluid-rock interactions at the pore scale and subsequently have a strong effect on the way samples respond to flooding.

The effect of diagenesis on the way samples react to core-flood experiments when flooded with a CO₂-brine fluid system had already been observed in a previous study (Project 3-1110-0122 (Evans et al., 2013)). In that study, a sample from the Wonnerup taken from well Pinjarra-1 and subjected to core-flood process showed significant enhancement to its permeability. The Wonnerup is buried at deeper depths (~3 km) at the Pinjarra-1 well compared with the Harvey wells. Therefore, the rock materials have undergone a greater degree of diagenetic alteration due to burial, compared with the Harvey samples, making them far tighter and richer in carbonate cement. It is believed that the carbonate cement had reacted with the injection fluids during the CO₂-brine flooding resulting in enhanced permeability of the Pinjarra-1 sample.

Combining the results achieved in this work and those obtained in other projects it may be concluded that the Wonnerup exhibits a great degree of spatial diagenetic alteration. Such alterations have the potential to change the way the formation rock reacts to a CO₂-rich injection fluid during injection. Therefore, depending on the type of the rock constituents of a particular interval chosen for fluid injection in any of the wells, reduced injectivity may or may not present a problem over time. The best way to address this issue and narrow the uncertainty is to characterise the intervals of interest with respect to their fluid-rock interactions using a workflow similar to that used in this project.

The geochemical analysis of the fluid samples collected during the core-flood experiments have also revealed some similarities and differences in the way fluid-rock reactions may occur in rock samples from different wells. Overall such analyses have indicated that chemical reactions between the carbonated brine and the rock (mineral dissolution/precipitation) are very limited at the time scale and physical conditions investigated in this study. Therefore, the petrophysical alterations caused to the rock samples is believed to be merely due to the dislodgment and transport of the fine clay particles within the pore space of the rock. The variation in the concentration of various chemical species during each experiment show that most changes in the water composition occur in the “first flush effect” although the more important geochemical reactions show Si and Fe mobilised later in the experiment. The first flush is dominantly the result of a remnant of salts (left from the previous core analysis e.g. NMR measurements) rather than the acid attack of the minerals by the CO₂-saturated brine whose effect is considered to be minor. The computer modelling shows that the experimental conditions used are unlikely to result in major mineralogical and fluid changes which is confirmed in the results of the core-flood eluent chemistry.

This research work has been very insightful about the fluid-rock interactions which may occur in the Wonnerup (i.e. the primary injection/storage zone in the SW Hub) and how they may or may not impact on the well injectivities. However, it is believed that there are still areas which require further investigation to narrow down the remaining uncertainties even further, a list of which is provided below:

- The effect of salt precipitation (salting out effect) on the near wellbore region and well injectivity: salt is expected to be precipitated out of the resident brine as CO₂ (mainly in dry state) is injected into the underground storage site. Since the water may be continuously imbibed into the dried out zone from the aquifer, the salt volume may keep building up over time posing a risk to the injectivity of the CO₂ injection wells. A coupled experimental-numerical study would be required to assess the impact of such phenomenon should this occur in the injection wells at the SW Hub. A pristine water sample from the study area would be particularly beneficial to this component of the work.
- The effect of injection rate variation on the results achieved in this work: it is well documented in the literature that the intensity of the fines migration phenomenon depends on the rate of fluid injection. The flow-rate used in this work (0.5 mL/min) was dictated by the desire to give the rock and fluid adequate time to interact for geochemical analysis. Also to keep all the analysis consistent, the flow-rate could not be changed between different experiments. Therefore, it would be highly beneficial to investigate the effect of flow-rate variation on the degree of formation damage caused by the fines migration. Also, as indicated earlier, no significant geochemical reactions are expected to have occurred between the rock and fluids at the conditions already applied during this work. It would be beneficial to examine the

absence/presence of reactions and their intensity, in particular, if the injection rate is changed.

- The impact of soak periods during injection start up could also be investigated using this workflow. During the start-up of any project there tend to be periods where the pumps are not working and there is sporadic injection and waiting periods. In our work, this has had significant impact on mineral dissolution rates. The question is whether this would become significant during the start-up period. Use of the start-up timing at some of the new CCS sites (e.g. Boundary Dam) could be simulated in a core-flood sense and compared with this work to see if there are quantitative impacts to geochemistry or fine mobilisation in the future. The effect of variation in the brine salinity on the results achieved in this work: the composition of the resident or injection brine is expected to alter the fluid-rock interactions. A coupled experimental-numerical investigation could shed light on the extent to which brine salinity could control the in-situ reactions.

References

- Archie, G.E., 1942. The electrical resistivity log as an aid in determining some reservoir characteristics. *Trans. AIME*, 146(1):54-62.
- Arps, J.J.: "The Effect of Temperature on the Density and Electrical Resistivity of Sodium Chloride Solutions," *Petroleum Transactions, AIME*, 1953.
- Barbera, G., G. Barone, P. Mazzoleni, and A. Scandurra, 2012. Laboratory measurement of ultrasound velocity during accelerated aging tests: Implication for the determination of limestone durability. *Construction and Building Materials*, 36:977-983.
- Bennion, B. and Bachu, S., 2005. Relative permeability characteristics for supercritical CO₂ displacing water in a variety of potential sequestration zones in the Western Canada sedimentary basin, SPE 95547, The SPE annual technical conference and exhibition. Society of Petroleum Engineers, Dallas, Texas, USA.
- Bona, N., E. Rossi, S. Capaccioli, and M. Lucchesi, 2008. Electrical measurements: Considerations on the performance of 2-and 4-contact systems. In *International Symposium of the SCA, Abu Dhabi, UAE*.
- Brich, F., 1960. The velocity of compressional waves in rocks to 10 kbars: Part 1. *Journal of Geophysical Research*, 65:1083-1102.
- Chouteau, F.M. and Beaulieu, S., 2002. An investigation on application of the electric resistivity tomography method to concrete structures. In *Geophysics 2002. The 2nd Annual Conference on the Application of Geophysical and NDT Methodologies to Transportation Facilities and Infrastructure*.
- Christaras, A., 2003. P-wave velocity and quality of building materials. In *Proc Int Symp Industrial Minerals and Building Stones*, pages 295-300.
- Clennell, B., 1997. *Tortuosity: a guide through the maze*. Geological Society, London, Special publications, 122: 299-344. Doi: 10.1144/GSL.SP.1997.122.01.18.
- Clennell, M. B., Dewhurst, D. N., Siggins, A. and Raven, M. D., 2006. Shale Petrophysics: Electrical, dielectric and Nuclear Magnetic Resonance studies of shales and clays. *Transactions, SPWLA 47th Annual Logging Symposium*, June 4-7, paper KK, 13pp.
- Coates, G. R., Marschall, D., Mardon, D., Galford, J., 1998. A new characterization of bulk-volume irreducible using magnetic resonance. *The Log Analyst*, 39, 51-63.
- Coates, G.R., Peveraro, R.C.A., Hardwick, A., Roberts, D., 1991. Magnetic resonance imaging log characterized by comparison with petrophysical properties and laboratory core data. *Proceedings – SPE Annual Technical Conference and Exhibition, Vol. Omega*, 627-635.
- Conciadori M, Bourdet J and Delle Piane C., 2014. Diagenesis and palaeo-fluid circulation in the Lesueur Sandstone, Perth Basin, Australia. CSIRO report number EP149172.
- Daigle, H. and Dugan, B., 2009. Extending NMR data for permeability estimation in fine-grained sediments. *Mar. Petrol. Geol.*, 26, 1419-1427.

- Dawson, G.K.W., Pearce, J.K., Biddle, D. and Golding, S.D., 2015. Experimental mineral dissolution in Berea Sandstone reacted with CO₂ or SO₂-CO₂ in NaCl brine under CO₂ sequestration conditions. *Chemical Geology*, 399, 87-97.
- Deeney, A.C., 1989a. Hydrogeology of the Binningup borehole line, Perth Basin: Western Australia Geological Survey, Professional Papers, Report 25, P. 7-16.
- Deeney, A.C., 1989b. Hydrogeology of the Harvey borehole line, Perth Basin: Western Australia Geological Survey, Professional Papers, Report 26, P. 59-68.
- Delle Piane, C., Olierook, H.K.H., Timms, N.E., Saeedi, A., Esteban, L., Rezaee, R., Mikhaltsevitch, V., Lebedev, Maxim. 2013. Facies-based rock properties distribution along the Harvey 1 stratigraphic well. CSIRO Report Number EP133710.
- Dunn, K.J., Bergman, D.J. and Latorraca, G.A., 2002. Nuclear Magnetic Resonance: Petrophysical and Logging Applications. Pergamon, Amsterdam, 293pp.
- Evans, B., Saeedi, A., Reza, R., Rasouli, V., Lebedev, M., Iglauer, S., Liu, K., 2014. Predicting CO₂ injectivity properties for application at CCS sites. Final Report to ANLECR&D, Project 3-1110-0122.
- Garrouch, A. and Sharma, M., 1992. Techniques for the measurement of electrical properties of cores in the frequency range 10 hz to 10 mhz. In international symposium for the Society of Core Analysts, Oklahoma City, Oklahoma.
- Golab, A.N., Carr, P.F., Palamara, D.R., 2006. Influence of localised igneous activity on cleat dawsonite formation in Late Permian coal measures, Upper Hunter Valley, Australia. *International Journal of Coal Geology*, 66, 4, 296-304.
- Grunewald, E., & Knight, R. 2011. A laboratory study of NMR relaxation times in unconsolidated heterogeneous sediments. *Geophysics*, 76(4), G73-G83.
- Guéguen, Y. and Palciauskas, V., 1992. Introduction à la physique des roches. Hermann.
- Hellevang, H., Aagaard, P. and Jahren, J., 2014. Will dawsonite form during CO₂ storage? *Greenhouse Gas Sci. Technol.*, 4:191-199.
- Hidajat, I., Mohanty, K.K., Flaum, M., Hirasaki, G., 2004. Study of vuggy carbonates using NMR and X-ray CT scanning. *SPE Reservoir Evaluation & Engineering*, 88995.
- Hurlimann, M.D., Flaum, M., Venkataramanan, L., Flaum, C., Freedman, R. and Hirasaki, G.J., 2003. Diffusion-relaxation distribution functions of sedimentary rocks in different saturation states. *Mag. Res. Imaging*, 3-4, 305-10.
- Izgec, O., Demiral, B., Bertin, H. and Akin, S., 2008. CO₂ injection into saline carbonate aquifer formations I: laboratory investigation *Transport in porous media*, 72(1): 1-24.
- Johnson, J.F. and Cole, R., 1951. Dielectric polarization of liquid and solid formic acid¹. *Journal of the American Chemical Society*, 73(10):4536-4540.
- Jones S. C., 1972, A rapid accurate unsteady-state Klinkenberg permeameter, *SPE* 3535, 383-397.

- Jorand, R., Fehr, A., Kock, A., Clauser, C., 2011. Study of the variation of thermal conductivity with water saturation using nuclear magnetic resonance. *J. Geophys. Res.*, 116, B08208.
- Josh, M., Esteban, L., Delle Piane, C., Sarout, J., Dewhurst, D.N. and Clennell, M.B., 2012. Laboratory characterization of shale properties. *J. Petrol. Sci. Engin.*, vol. 88-89, 107-124; doi: 10.1016/j.petrol.2012.01.023.
- Kahraman, S. and Alber, M., 2006. Predicting the physico-mechanical properties of rocks from electrical impedance spectroscopy measurements. *International Journal of Rock Mechanics and Mining Sci-ences*, 43(4):543-553.
- Kleinberg, R. L., C. Flaum, C. Straley, P. G. Brewer, G. E. Malby, E. T. Peltzer III, G. Friederich, and J. P. Yesinowski. 2003b, Seafloor nuclear magnetic resonance assay of methane hydrate in sediment and rock, *J. Geophys. Res.*, 108(B3), 2137, doi:10.1029/2001JB000919.
- Kleinberg, R. L., C. Flaum, D. D. Griffin, P. G. Brewer, G. E. Malby, E. T. Peltzer, and J. P. Yesinowski (2003a), Deep sea NMR: Methane hydrate growth habit in porous media and its relationship to hydraulic permeability, deposit accumulation, and submarine slope stability, *J. Geophys. Res.*, 108(B10), 2508, doi:10.1029/2003JB002389.
- Lataste, J., C. Sirieix, D. Breyse, and M. Frappa, 2003. Electrical resistivity measurement applied to cracking assessment on reinforced concrete structures in civil engineering. *NDT & E International*, 36(6): 383-394.
- Lebedev, M., Toms-Stewart, J., Clennell, B., Pervukhina, M., Shulakova, V., Paterson, L., Muller, T.M., Gurevich, B. and Wenzlau, F., 2009. The Leading Edge, January 2009, Special section: Rock Physics, pages 24-27.
- Lowe D., 2004. Distinctive Image Features from Scale-Invariant Keypoints", *International Journal of Computer Vision* 60(2): 91-110
- Machado, V.F., Azeredo, R.B.V., Ramos, P.F., Coutinho, M.R., Carneiro, S.R., 2008. A NMR permeability model based on partial least square (PLS) regression analysis for a low permeability gas sand in Santos Basin. In: *International Symposium of the Society of Core Analysts*, 29.10-2.11.2008. UAE, Abu Dhabi.
- Martinez-Martinez, J., D. Benavente, and M. Garcia-del Cura, 2011. Spatial attenuation: the most sensitive ultrasonic parameter for detecting petrographic features and decay processes in carbonate rocks. *Engineering Geology*, 119(3):84-95.
- Mavko, G. and Nolen-Hoeksema, R., 1994. Estimating seismic velocities at ultrasonic frequencies in partially saturated rocks. *Geophysics*, 59, 2, 252-258.
- Mayr, S. and Bukhardt, H., 2006. Ultrasonic properties of sedimentary rocks: effect of pressure, saturation, frequency and microcracks. *Geophys. J. Intern.*, 164, 1, 246-258.
- Olierook, H.K.H., Delle Piane, C., Timms, N.E., Esteban, L., Rezaee, R., Mory, A.J., Hancock, L., 2014. Facies-based rock properties characterization for CO₂ sequestration: GSWA Harvey 1 well, Western Australia. *Marine and Petroleum Geology*, 50: 83-102.

- Perrin, J.-C. and Benson, S.M., 2010. An experimental study on the influence of sub-core scale heterogeneities on CO₂ distribution in reservoir rocks. *Transport in porous media*, 82(1): 93-109.
- Preibisch, S., Saalfeld, S., & Tomancak, P., 2009. Globally optimal stitching of tiled 3D microscopic image acquisitions. *Bioinformatics*, 25(11), 1463-1465.
- Saeedi, A. and Rezaee, R., 2012. Effect of residual natural gas saturation on multiphase flow behaviour during CO₂ geo-sequestration in depleted natural gas reservoirs. *Journal of Petroleum Science and Engineering*, 82–83: 17-26.
- Saeedi, A., 2012. *Experimental Study of Multiphase Flow in Porous Media during CO₂ Geo-Sequestration Processes*. Springer Thesis. Springer Publishing, Heidelberg, Germany.
- Saeedi, A., Rezaee, R. and Evans, B., 2012. Experimental study of the effect of variation in in-situ stress on capillary residual trapping during CO₂ geo-sequestration in sandstone reservoirs. *Geofluids*, 12(3): 228-235.
- Saeedi, A., Rezaee, R., Evans, B. and Clennell, B., 2011. Multiphase flow behaviour during CO₂ geo-sequestration: Emphasis on the effect of cyclic CO₂-brine flooding. *Journal of Petroleum Science and Engineering*, 79(3-4): 65-85.
- Sarout, J. and Gueguen, Y., 2008. Anisotropy of elastic wave velocities in deformed shales: Part 1—experimental results. *Geophysics*, 73(5):D75-D89.
- Schindelin, J., Arganda-Carreras, I., Frise, E., Kaynig, V., Longair, M., Pietzsch, T., & Cardona, A., 2012. Fiji: an open-source platform for biological-image analysis. *Nature methods*, 9(7), 676-682.
- Shevnin, V., A. Mousatov, A. Ryjov, and O. Delgado-Rodriquez, 2007. Estimation of clay content in soil based on resistivity modelling and laboratory measurements. *Geophysical Prospecting*, 55(2):265-275.
- Stalker, L., Noble, R., Gray, D., Trefry, C., Varma, S., Ross, A., Sestak, S., Armand, S., Gong, S., 2013. Harvey 1 geochem report. *Geochemical Characterisation of Gases, Fluids and Rocks in the Harvey-1 Data Well*. Final Report to ANLECR&D Project 7-1111-0200 EP135208, 110 p.
- Tiab, D. and Donaldson, E.C., 2004. *Petrophysics*. Gulf Professional Publishing, Elsevier, Burlington, Massachusetts.
- Timur, A., 1968. An Investigation of Permeability, Porosity and Residual Water Saturation Relationships, paper presented at SPWLA 9th Annual Logging Symposium, Society of Petrophysicists and Well Log Analysts, 23–26 June.
- Walbrecker, J. O., Hertrich, M., & Green, A. G. 2011. Off-resonance effects in surface nuclear magnetic resonance. *Geophysics*, 76(2), G1-G12.
- Wellington, S.L., and Vinegar, H.J. 1987. X-ray computerized tomography. *Journal of Petroleum Technology*. Vol. 39, pp 885-898.
- Wilke, F.D.H., Vasquez, M., Wiersberg, T., Naumann, R. and Erzinger, J., 2012. On the interaction of pure and impure supercritical CO₂ with rock forming minerals in saline aquifers: An experimental approach. *Applied Geochemistry*, 27, 1615-1622.

Winkler, E.M., 1994. Stone in architecture: properties, durability; with 63 tables. Springer.

Wulff, A.M. and Bukhardt, H., 1997. Mechanisms affecting ultrasonic wave propagation in fluid-containing sandstones under high hydrostatic pressure. *J. Geophys. Res.*, 102, B2, 3043-3050.